ESTIMATING BODY AND SURFACE WAVES USING VIRTUAL SOURCES AND RECEIVERS

JOHN GONZALEZ

Thesis submitted in fulfilment of
the requirements for the degree of
Doctor of Philosophy

School of Geosciences
University of Edinburgh
2012

Declaration

I declare that this thesis has been composed solely by me and that it has not been submitted, either in whole or in part, in any previous application for a degree. Except where otherwise acknowledged, the work presented is entirely my own.

John Gonzalez
2012

Abstract

This research is focused on the application of both new and established seismic interferometry techniques to a single area: the Altiplano in the Andes region. This area has already been widely studied in terms of its geological evolution. Nevertheless, a single accepted theory has not yet been developed to explain why the topography of the Andes incorporates such a large area of low relief at this altitude. The Altiplano is therefore an interesting zone to study.

This research introduces and analyses new concepts and methodologies, such as retrieving surface and body waves between earthquakes by using interferometry. Nevertheless, several factors, such as the quality of recordings, the separation between sources, and the velocity gradient of the medium, had to be taken into account for body and surface wave retrieval.

This research also analysed the retrieval of body waves by means of seismic interferometry applied to coda wave arrivals. Results show that due to the attenuation of S waves produced by the zone of partial molten material, when using S coda waves, seismic interferometry does not achieve the objective of wave retrieval. On the other hand, P coda waves gave good results. Also, the combined methodology of interferometry by cross-correlation and convolution was shown to account for the behaviour of the retrieved waves and provided an indication of how the distribution of sources affects the Green’s functions estimates for body waves in this area.

Another point covered by this research was the analysis of passive recordings in order to retrieve surface and body waves. Results indicate that surface and body waves could be retrieved. However, in order to retrieve body waves, special circumstances are required, such as lateral continuity of the Moho, a relative strong Moho impedance contrast, and simplicity of the geologic structure because these factors will contribute to a strong signal like that obtained in critical reflections making interferometry results more successful.

Finally, the novel concept of source-receiver interferometry was proven to be useful with a real data set for the first time in the Andes region. This was undertaken using two different approaches: (i) deterministic sources, and (ii) passive noise recordings. Both approaches demonstrated that surfaces waves could be retrieved between sources and showed good approximation and coherent results when compared to real recordings.

In general, this thesis shows that each methodology attempted has points in favour and points against its application. It is therefore not a straightforward matter to choose which methodology is the best to apply in a given case study. The general advice inferred is to conduct a pilot project in order to test all methodologies available, assess which one works best, and then apply it to the whole area and the full data set.

Future studies in the Altiplano should concentrate on factors such as, for example, interferometry by deconvolution in order to account for factors such as diffusion, bending waves, elastodynamics or irregular illumination as well as to concentrate on the nature of the changes detected by seismic interferometry.

Acknowledgements

Este doctorado ha sido posible gracias al esfuerzo sostenido de mi persona y de aquellos que me apoyaron durante todo este tiempo. Primeramente al gobierno Venezolano con su programa de becas "Misión Ciencia" que financió mis estudios y estadía por cuatro años en este país. A mi tutor, Andrew Curtis, el cual me guió hacia la culminación de esta meta y que aunque algunas veces sentí que me trataba injustamente, es sin duda alguna un buen hombre. A la familia, la cual nunca nos abandona y siempre está ahí para hacernos sentir apoyados y queridos. Gracias a mis viejos, a mi suegra, a Moraima, a Nancy, a Amarilis-Luis-Ana-David, a Rubén Reinoso, y a mi tía Dulce. A Begoña y su esposo Charlton, por ayudarnos cuando lo necesitamos, por compartir con nosotros, por las tapas, por España, por hacernos felices. Begoña, gracias por ser la mejor amiga de Yanka. A Amanda cuyas clases de inglés me ayudaron a poder mejorar mi manera de comunicarme. A Iván Vasconcelos cuyas discusiones y sugerencias, al comienzo de este proyecto, sirvieron para impulsar y guiar los primeros pasos de esta investigación. A mis compañeros de oficina del ático que de una u otra forma me acompañaron, ayudaron y compartieron durante todo este tiempo la meta común del doctorado. Gracias a Angeleena, Heather, Ruth, Simon, David, y Tom. A mis jurados Johan Robertsson y Arash JafarGandomi, cuyas correcciones después del examen oral mejoraron notablemente la calidad de esta tesis. A todos los amigos que hemos hecho durante todo este tiempo y que nos han hecho felices con su amistad. Gracias a Blanca, Anna, Luis, Alessandro, los pichus(Ana-David), Carolyn, Cristina, Elena, Samira.

Finalmente, la contribución más importante de todas la hizo mi esposa, amiga y compañera de la vida, Yankari Moreno cuyo sacrificio ha sido total durante todo este tiempo, desde dejar a su familia para seguirme, pasando por la grave quemadura que sufrió en su mano, hasta la pérdida de su amado padre, don Rafael Moreno. Yankari es sin duda esa gran mujer que todo hombre desea a su lado y que yo tengo la fortuna de tener. Yanka, ¡gracias!, tú me has apoyado y amado desde que nos conocimos y me has dado el regalo más grande que una mujer le puede dar a un hombre. Juan, hijo, te amo.

Contents

List of Figures

List of Tables

Chapter 1

INTRODUCTION

1.1 Chapter plan

This chapter is divided into seven sections:

Section 1.2 presents a historical introduction to the field of seismic interferometry, and the original motivation for this current research, retrieving body waves using seismic interferometry. It also describes the difficulties associated with this problem.

Section 1.3 provides a general introduction to the geology of the Altiplano. The idea behind this section is to highlight the geological features which directly affect interferometric calculations, e.g. the zones of partially melted material which in turn affect the propagation of S waves and therefore, as will be seen, affect the effectiveness of seismic interferometry.

Section 1.4 explains the main sources of bias and difficulties encountered when acquiring and recording the seismic data for this project. The main points playing against the acquisition of data were the extremely harsh environmental conditions in the zone that affected geophone functioning, as well as human supervision of and intervention with the geophones.

Section 1.5 sets the aims of this research in relation to the more general frame of seismic interferometry. It is important to point out that, by the time these aims were set, usual seismic interferometry applications had already demonstrated the application of seismic interferometry to surface waves. The aims of this current research are new in the sense that they propose turning sources into virtual receivers, in order to estimate information about the medium and analysing the extent to which the results obtained from seismic interferometry reflect what a real geophone would record if put in the same place as the virtual source.

Section 1.6 outlines and briefly explains the different methodologies used in this research project. One of the aggregate values of this current work is that it has used various different and new seismic interferometry methodologies for the same study area evaluating and rating each one. As will be seen from each chapter, each methodology had its own particular advantages and disadvantages and different information was estimated with each one. Finally, in section 1.7 a summary of the undergraduate that served as a pilot project within this PhD project is given.

1.2 General introduction to the field of interferometry and to the problem of body wave retrieval by means of seismic interferometry

Seismic interferometry is the process of cross-correlating convolving or deconvolving seismic traces recorded at different locations on the surface of the earth, with the purpose of simulating data from virtual (imagined) sources or receivers.

The foundations of seismic interferometry can be traced back to the field of physics (Callen and Welton, 1951). The work by Callen and Welton (1951) showed that the Nyquist relation can be extended to general dissipative systems which in turns means that they found the theoretical basement for the relationship between fluctuations (or electronic noise) and irreversibility, a concept related to interferometry as will be explained later in this chapter. This electronic noise is known as the Johnson-Nyquist noise and is generated by the thermal agitation of charged particles inside the electrical conductor. In equilibrium, this noise is independent of the voltage applied. Quantum and statistical arguments (Callen and Welton, 1951) give to the known Nyquist relation:

$$\langle V^2 \rangle = \left({}^{2}\!/_{\pi}\right) KT \int R(\omega)\, d\omega \quad (1.1)$$

Where:

K is the Boltzmann constant

T is the temperature

R(ω) is the resistance

ω is the frequency of perturbation
$\langle V^2 \rangle$ is the mean square value of the spontaneously fluctuating force.

This equation, derived by Nyquist, relates the voltage fluctuation (a property of a system in equilibrium) to the electrical resistance (a parameter) related to an irreversible process.

The actual birth of seismic interferometry *per se* is clearly identified with Claerbout’s work on the synthesis of a layered medium from its acoustic transmission response (1968). Claerbout (1968) showed that the autocorrelation of an impulse transmission response of a horizontally layered medium, bounded by a free surface, yields the reflection response of this medium. In other words, Claerbout showed how the Green´s function (i.e. the impulse response to a point source) on the Earth’s surface could be obtained by autocorrelating traces generated by sources on the other side of the medium. Claerbout’s theory was rigorously proven for a 1D medium, and validated by testing with synthetic data (Claerbout, 1968), but it was not known whether this idea could be extended to a 3D situation.

This result implies that, for example, if one would measure the response on the Earth’s surface of a band-limited, white noise source in the subsurface, the autocorrelation would give the impulsive reflection response (i.e. the response from a virtual source at the surface) convolved with a band-limited delta function. This indicates that noise observed at the surface can be turned into a signal containing interpretable information about the subsurface.

The assumption that this would also work in 3D media is known as Claerbout’s conjecture. Claerbout and his students conjectured for 3D media that the cross-correlation of the transmission response, observed at a number of different locations, gives the reflection response that would be recorded at one of the locations if there had been a source at the other. They named this method “daylight imaging”, which implies a random distribution of point sources that emit incoherent seismic energy.

After the introduction of Claerbout's conjecture, researchers realised that it concurred with existing geophysical data. Ironically, in the field of solar seismology, correlating solar records had already provided a convincing demonstration of the daylight imaging method well before Earth-based seismic experiments could do the same. Duvall *et al.* (1993) discovered a procedure similar to Claerbout's daylight imaging method, using the cross-correlation of solar vibration data to infer information about the Sun's internal structure.

They showed that it is possible to extract time-distance information from acoustic waves, via temporal cross-correlations of the intensity fluctuations on the solar surface. Rickett and Claerbout (1999) presented virtual shot gathers, obtained by correlating vibration records of the Sun's surface, to empirically demonstrate the validity of Claerbout's conjecture.

Earthquake data also show agreement with Claerbout's conjecture and the work of Scherbaum (1987a, 1987b) presented the first test of Claerbout's idea on real data. First, Scherbaum derived a theory to calculate a single station inversion, by adapting Claerbout's formulation to include the case of oblique incidence. His theory allowed the imaging of subsurface impedance structures from the recordings of SH wave records. Next, Scherbaum applied the theory he had derived to a subsurface site structure of Swabian Jura, South West Germany. Scherbaum's results showed a high degree of similarity between theoretical inverted impedance and a P-wave velocity log coming from a nearby exploration well.

Daneshvar *et al.* (1995) also reported some initial results, with acoustic daylight imaging (synthesising a non-homogeneous medium from its acoustic transmission response, obtained from passive measurements at the surface of noise sources that occur at depth) on Earth. Daneshvar *et al.* (1995) derived a method of processing seismic signals, generated by micro-earthquakes, to image the local subsurface structure beneath a recording station. This technique used the autocorrelation of the vertically travelling earthquake signals to generate pseudo reflection seismograms that could be interpreted for subsurface structure.

Other fields of geosciences also showed agreement with Claerbout's conjecture. Cole (1995) was the first person to test Claerbout's conjecture on both synthetic and real data. His data was very noisy and he did not arrive at any solid conclusions. Derode *et al.* (1995) performed the first experiment showing the reversibility of transient acoustic waves through high-order multiple scattering by means of an acoustic time-reversal mirror (time-reversal signal processing is a technique for focusing waves. A time-reversal mirror is a devise that focuses waves using the time-reversal method). This work demonstrated that reversibility could be used to focus a wave back onto its source; even in the presence of high-order multiple scattering.

Rickett and Claerbout (1996) confirmed the consistency of Claerbout's conjecture by numerical experiments, using synthetic data from simple 1D and point diffractor models. In all cases, the kinematics of observed events was as expected.

Meanwhile, in the early 1990s, Fink pioneered an initial independent field of research, making use of the invariance of the wave equation to time reversal. Through various physical-modelling tests using ultrasonic transducers, Fink (1997) showed that strongly scattered wave-fields could be time-reversed and back-propagated through the complex medium to result in a focused wavefield. Because of this, renewed interest arose in the use of multiple scattered coda waves. The term "coda" refers to any concluding event, summation or section, e.g. sound waves that travel through a medium are scattered multiple times by heterogeneities in the medium and generate slowly decaying (late-arriving) wave trains, called coda waves.

Schuster (2001) explained the Claerbout conjecture by means of stationary phase arguments. The method extends the daylight imaging concept of Rickett and Claerbout (1999) to arbitrary distributions of sources and arbitrary reflectivity distributions, and validates Claerbout's conjecture. Schuster's method can also be used to: migrate free-surface multiples and peg-leg multiples in CDP data; perform imaging on unknown source locations; and generalise the receiver-function imaging method used by seismologists.

Researchers from the fields of ultrasonic and seismology realised that the cross-correlation of signals at two different receivers in an acoustic diffuse field yielded the response at one of the receiver positions as if there were a source at the other. Lobkis and Weaver (2001) showed that the Green’s function of a medium emerged by cross-correlation of the recordings from two receivers in a diffuse acoustic field. Campillo and Paul (2003) used Lobkis and Weaver´s (2001) approach to reconstruct surface wave responses between two stations from recordings of distant earthquakes.

Because the above work relies only on the general properties of diffuse waves, its results have potential applications in other fields. For example, Weaver and Lobkis (2002) showed that the cross-correlation of ultrasonic signals at two different receivers, in an acoustic diffuse field, yields the response at one of the receiver positions as if there were a source at the other.

Wapenaar *et al.* (2002) proved that the Claerbout conjecture was correct if it was assumed that uncorrelated noise sources in the subsurface (evenly distributed along a single surface) were present and the medium parameters were lossless, 3D non-homogeneous and source-free. They used the reciprocity theorem (*A reciprocity theorem relates the sources and wavefields in two acceptable physical and/or computational states. One specific result is the source receiver reciprocity, which states that the acoustic field due to a sound source at point A and the sound pressure received at any other point B is the same as that which would be produced at A if the source were placed at B, this can be generalised for multiple sources and receivers*) to derive different relations between transmission and reflection responses for a 3D inhomogeneous medium. One of these relations proved Claerbout’s conjecture.

Snieder *et al.* (2002) showed how seismic interferometry could be used to extract subsurface information from earthquake coda i.e. the long “ringy” part of the earthquake record that is thought to be dominated by multiply-scattered events. Snieder *et al.* (2002) determined the temporal changes that are evident in a medium from incoherent waves. They used the phrase “coda wave interferometry” for the interferometric measurement of temporal changes in the medium from strongly scattered waves.

Derode *et al.* (2003a, 2003b) showed the relation between time reverse acoustic and seismic interferometry by demonstrating that the Green´s function retrieval (equivalent to seismic interferometry) by cross-correlation can be derived from time reversed acoustics. The derivation is valid for open systems and for arbitrary inhomogeneous lossless media. In a first paper Derode *et al.* (2003a), proposed a physical interpretation of the emergence of the Green’s function in a heterogeneous medium, based on time-reversal symmetry.

They found that the impulse response could be retrieved from either the causal or anticausal part of the sum of field-field correlation, provided that the sources are placed so that they would form a perfect time-reversal device (a device that can focus waves using a principle of the wave equation known as reciprocity). They also showed the role of multiple scattering for the reconstruction of the Green´s function. By which it is meant that, when the time-reversal criterion is not fulfilled, the time-reversal experiment works better through a multiple scattering medium than through a homogeneous one.

Ultrasonic experimental results were presented to illustrate that the exact Green’s function of a heterogeneous medium can be retrieved from the cross-correlation of the fields received by two passive sensors. In a second paper, Derode *et al.* (2003b) argued that the recovering of Green’s functions was also possible in an open, multiple-scattering medium. They proposed a criterion based on reciprocity, time-reversal symmetry and the Helmholtz-Kirchhoff theorem: if sources are placed as if they are to form a perfect time-reversal device, then the Green’s function can be recovered by summing the cross-correlations. This was validated by Derode *et al.* (2003b) using numerical experiments.

Draganov *et al.* (2003) tested the theory developed by Wapenaar *et al.* (2002), using numerically modelled data in laterally varying media. This theory is based on seismic reciprocity and formally generalises Claerbout´s relation between transmission and reflection responses to 3D non-homogeneous acoustic and elastic media. Wapenaar's derivation assumed that there were no reflectors below the buried noise sources and that these sources were regularly distributed in the subsurface.

Draganov *et al.* (2003) investigated how restrictive this assumption was by performing numerical modelling with reflectors above, as well as below, the sources and with irregular distributions of sources. They found that the assumptions were not as restrictive as expected, especially if there is a random distribution of sources.

Roux and Fink (2003) provided a new way to measure the Green's function between two points in an acoustic channel, without emitting a pulse from either of the two points. Their theoretical approach was based on mode propagation in a monochromatic regime. They showed that the Green's function between points A and B could be obtained from a set of secondary sources in the guide by averaging either the correlation or the convolution of the signals received in A and B.

Schuster (2004) showed how cross-correlation of seismic responses from man-made or natural sources, either at the surface or in the subsurface, can be used to form an image of the subsurface. Bakulin and Calvert (2004) produced the first practical application of seismic interferometry in an exploration setting. They used a 4D VSP data set, recorded in a 45^0 slanting well with 50 instrumented 3C geophones 8m apart. A single surface shot line directly above the well was used to construct 2D images. The work of Bakulin and Calvert (2004) demonstrated the feasibility of seismic interferometry redatuming a concept meaning the relocation of sources and/or receivers from the acquisition level to another depth level.

From the earlier work described above, it is clear that seismic interferometry, daylight imaging, virtual source imaging and reverse-time acoustics can be related by the summation of correlated data. These, apparently different, approaches were unified by Wapenaar (2004), who proved the generalisation of Claerbout's conjecture for 3D acoustic and elastodynamic media, without making assumptions about the randomness of the medium. This was an important result because it established a good mathematical basis upon which seismic interferometry could be rigorously developed.

After Wapenaar´s proof in 2004, the field developed rapidly. Malcon *et al.* (2004) demonstrated the validity of Lobkis and Weaver’s (2001) approach, using ultrasonic laboratory measurements in highly heterogeneous rocks. Shapiro *et al.* (2005) and Sabra *et al.* (2005a, 2005b) made use of interferometrically constructed impulse responses to carry out tomographic velocity inversion. Van Manen *et al.* (2005, 2006, 2007) showed how constructing impulse responses interferometrically on a computer provides an efficient and flexible numerical waveform modelling scheme, for heterogeneous, lossless acoustic or elastic media.

Snieder *et al.* (2006b) provided an explanation of the mechanism of impulse response (the impulse response function of a dynamic system is its output, when presented with a brief input signal, called an impulse) reconstruction by cross-correlation for direct inter-receiver arrivals and for singly-reflected waves. Halliday *et al.* (2007) showed that interferometrically constructed surface wave seismograms could be subtracted from real traces: thus, traces could be obtained with ground-roll removed to reveal body wave energy.

Wapenaar and Fokema (2006) give an overview of the representation of the Green’s functions in terms of cross-correlation. In this research, Green’s function means the response of an impulsive point source in a medium. The representation of the Green’s function is derived making no assumptions relating to the diffusivity of the wavefield. Nevertheless, these representations are only valid for application in seismic interferometry after a number of approximations such as the effect of scatters or considering monopole sources only. They consider the acoustic and elastic case.

Wapenaar *et al.* (2006d) used and extended the original idea of Snieder *et al.* (2006) that uncorrelated sources would eliminate errors, such as spurious multiples. Spurious multiple is the term resulting from the product of singly-reflected waves from different reflectors. It has been named spurious multiple because terms depend on the product of reflection coefficients as in the case of real multiples. Spurious multiples are caused by factors such as limitations in the geometrical aperture of correlated sources.

Vasconcelos *et al.* (2006) provided the theoretical basis for performing interferometry by deconvolution, and demonstrated the feasibility of deconvolution interferometry using numerical examples with impulsive sources. It was shown that deconvolution interferometry artifacts (one term of the Taylor expansion of the integral equation that is necessary to perform interferometry by deconvolution and gives rise to a spurious event that does not correspond to any physical phenomena) are not mapped onto the image space, and that deconvolution interferometry proved to be able to properly image the subsurface structure without the need for an independent estimate of the source pulse. Interestingly, this cannot be accomplished by using correlation-based interferometry.

Mehta *et al.* (2007) estimated near-surface properties of the Earth from passive recordings in a vertical borehole. Gaiser *et al.* (2008) investigated multicomponent applications of interferometry for processing OBC data. They used interferometry to retrieve pseudo-source data on the seabed containing PP, PS and SS wave reflections, as well as seabed surface waves.

Curtis *et al.* (2009) showed, for surface waves, that interferometry could be used between two well-recorded sources to construct an artificial, or virtual, sensor from any energy source. This idea, of transforming sources into virtual receivers, is explored in detail in this thesis in chapters 2 and 5, with positive results. Curtis and Halliday (2010) showed that it was also possible to perform interferometry between a source and a receiver.

They showed that the source-receiver Green’s function could be constructed without using the measured source-receiver signal. Curtis and Halliday (2010) used this latter form of interferometry to derive a formal link between interferometry and imaging theory. This new kind of interferometry was tested for the first time on real data by Duguid *et al.* (2011) and for the first time in the Altiplano in chapter 5.

To conclude this section, it is useful to mention some important points concerning the problem of body wave retrieval by interferometry. Moreover, these points were responsible for driving this current research project in the beginning. The reason for this is the fact that most of the successful applications of seismic interferometry have been carried out for surface waves, and relatively little is known about the retrieval of body waves.

This is mainly because stations are usually located on the surface implying that surface waves will be an order of magnitude stronger than body waves. Additionally, as explained by Wapenaar (2004, 2006c), in order to retrieve the correct body wave part of the Green's function a distribution of sources at depth is needed.

Despite the drawbacks of these considerations, some research has been successful in this matter. Roux *et al.* (2005) demonstrated the presence of P waves in the noise correlation functions. Mizayawa *et al.* (2008) extracted P and S waves produced by human activity. More recently, Tonegawa *et al.* (2009) retrieved body waves from S coda. In different research work, Tonegawa *et al.* (2010) also retrieved body waves travelling between sources using the stationary phase method. Zhan *et al.* (2010) retrieved body waves for SMS body waves for post-critical reflections.

This thesis tests, first, the validity of the interferometric method for surface waves in a complex medium (Altiplano), and second, body wave retrieval. Points investigated include: the influence of the medium, assessing the validity of seismic interferometry in the Altiplano region and the comparison of results obtained with other methods such as receiver functions and the retrieval of body waves in Green's functions, in the presence of discontinuities and scattering below the surface.

To summarise, development of the field of seismic interferometry is relatively new. Even though the extraction of the impulse responses of a system from noise was known in the early 1950s, the basis of seismic interferometry was only established in the late 1960s. Furthermore, despite the fact that, from the late 1960s until 2004, geophysical data agreed with Claerbout’s conjecture, it was not until 2004, after rigorous mathematical proof of Claerbout’s conjecture that a renewed interest in seismic interferometry arose. Developments in seismic interferometry up to the present include: tomography; ground roll removal; and multicomponent applications, among others. Seismic interferometry continues to be a promising, as well as a growing, field within geophysics.

1.3 The geology of the Altiplano (West-Central South America, the Andes)

This section is focused on important points concerning the geology of the area of study and how these features affect the quality of the data and the interferometric results. The main point to be considered here are the zones of partial melted material, the Altiplano low velocity zone and the geometry of the subducting slab.

The objective of this introduction is to give a short summary of important research work that has been conducted in the area and that has contributed to the understanding of the main geological features affecting interferometry. Chapter 4 gives a more in-depth introduction to the geological features of the area, as well as a summary of the geophysical surveys that have been conducted. The idea then, is to shorten this introduction and give the reader the key points related to the geology of the area, as well as to explain how these key points affect interferometry.

The Altiplano is the most extensive area of high plateau on Earth outside of Tibet, with an average elevation of around 3800 m. It is part of an area composed of five major sub-parallel morpho-structural units, as can be seen in Figure 1.1:

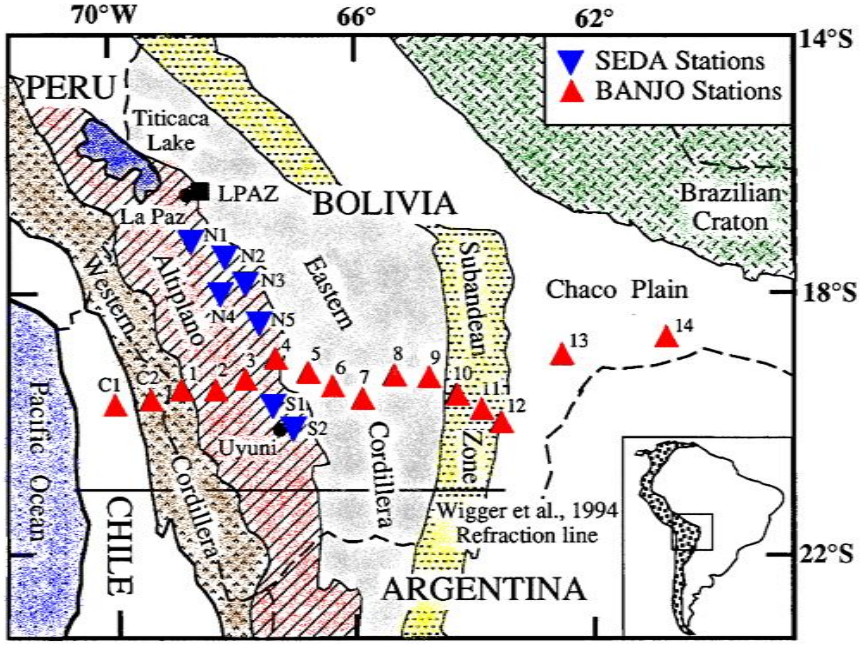

Figure 1.1 Map of the Altiplano showing geophone deployment for the BANJO and SEDA projects as well as morpho-tectonic units. Taken and adapted from Beck *et al.* (1996).

The five major units are: the Western Cordillera, characterised by an active volcanic arc whose peaks reach an elevation of up to 6000 m; the Altiplano, the current area of study; the Eastern Cordillera, a mountain range characterised by folding and thrusting; the sub-Andean zone, an active thin-skinned series of mountainous foothills formed due to contractional tectonics; and the Chaco plain, a large morphological unit whose main characteristics are the lack of relief and long term tectonic stability, underlaid by the Brazilian craton.

The first ideas concerning the subsurface structure of the Altiplano region came from the research of Beck *et al.* (1996) and Baumont *et al.* (2001) who found that the crustal thickness varied between 70 and74 km in the western Cordillera and between 32 and 38 km in the Chaco plain. This description of the Moho is also consistent with the work by Giese *et al.* (1999) who found that crustal structure changed considerably in the region, from east to west.

Another important geological feature potentially affecting the interferometric results for this area is that of the partial melting zones (across the Altiplano, with a minimum depth of 16 km and a maximum depth of 31 km, see Wölbern *et al.* 2009). These zones prevent S waves from travelling through the medium and this, in turn, affects the calculations.

Exactly how these partial melting zones affect results, and what alternatives could be used to circumvent this problem, are considered in chapter 3 of this current work. The first research proposing zones of partial melting for the Altiplano was that of Brasse *et al.* (2002) and this idea was also supported by Haberland *et al.* (2003).

Finally, the complex velocity structure of the area also played a decisive role in the interferometric results. The area is characterised by strong and rapid velocity changes making the task of ray tracing and velocity determination difficult. As an example of this complex variation in velocity of the area, Schmitz and Kley (1997) found that high velocities existed between the upper and the middle crust of the Eastern Cordillera, with an underlying, thick, low velocity zone.

More recently, Heit *et al.* (2008) found high velocities on the west of the profile indicating cold material from the fore-arc. They related this velocity anomaly between the fore-arc and the volcanic arc to the presence of fluids. A strong, low velocity anomaly was seen across the entire Altiplano plateau and also between the inter-Andean and sub-Andean regions. This, along with a strong high velocity anomaly, is thought to be caused by the Brazilian shield.

As will be seen, every geological feature affects the Altiplano in a different manner and also, depending on the approach, the interferometric results that were obtained. For example, the geological feature playing a part in chapter 2 is the velocity field, while in chapter 3 it is the zone of partial melting; in chapter 4, it is the structure of the subducting slab and the thickness of the crust and in chapter 5 the attenuation.

1.4 The data set

The data used in this current project come from recordings made by a temporal deployment of geophones conducted by the German Research Centre for Geosciences (GFZ in Potsdam) as part of a passive source experiment. The work was carried out under the framework of the collaborative research programme *"Deformation Processes in the Andes"*, whose objective was to obtain a better understanding of the lifting process in the Altiplano-Puna plateau in the Central Andes.

The experiment consisted of two profile lines, with the narrowest station-spacing ever implemented in the Central Andes. This narrow spacing permitted a much higher resolution than in previous studies and, thereby, allowed the seismic interfaces to be mapped in far greater detail than before (Wölbern *et al.*, 2009).

As shown in Figure 1.2, the temporal deployment of receivers consisted of two parallel lines, hereafter referred to as the northern and southern profiles. The northern profile, located in the Altiplano plateau, included a total of 59 seismological stations that were deployed from March 2002 to January 2004. It had a total length of 600 km and station spacing of approximately 10 km. The southern profile, located in the Puna plateau, consisted of 19 seismological stations, and was deployed from July 2002 to January 2004. It had a total length of 200 km and a station spacing of 10 km.

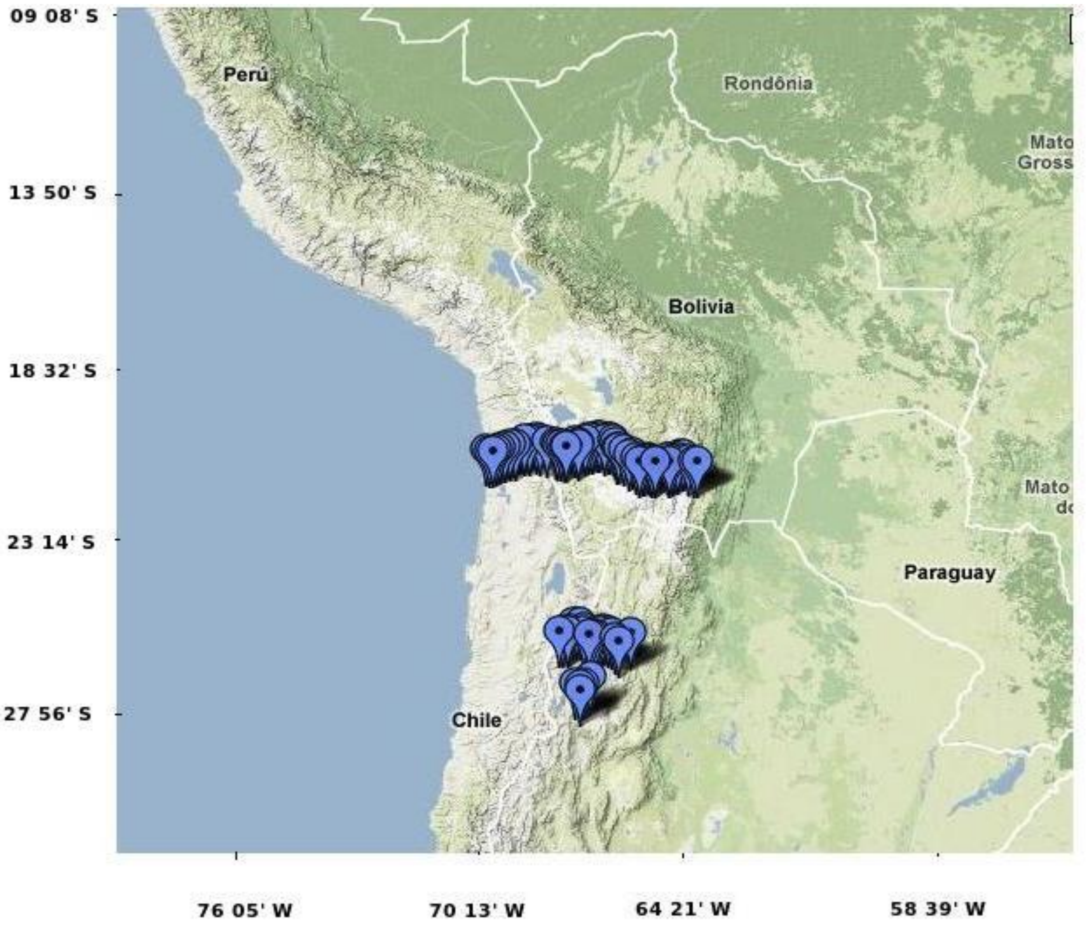

Figure 1.2 Deployment of receivers. Taken from www.http://geofon.gfzpotsdam.de/geofon/new/netabs/rf_map.kml

The deployment of the three component geophones was such that, of the 59 stations in the northern profile, nine were equipped with Guralp CMG-3ESP/120 broad-band seismometers and SAM digitisers. Three stations consisted of CMG-40T seismometers with Reftek recorders. The remainder operated with short period 1 Hz Mark L43-D seismometers using Reftek or EDL recorders.

Data were recorded with a sampling frequency of 100 Hz for the northern profile and 50 Hz for the southern profile. In general, the complex structure of the area caused strong attenuation that significantly affected the recorded data. Indeed, for every geophone, the frequency content of the recorded data depended on its location and, in some parts, attenuation led to a complete lack of S wave energy [as documented previously in Wölbern *et al.* (2009)]. Additionally, problems such as recording noisy signals and de-phasing in the origin time of the seismograms, due to GPS reading problems, made it clear that there was a real need for data pre-processing before application of the interferometric algorithms could take place.

Acquisition of data from both profiles was affected by factors such as hardware, software, weather and vandalism. As a consequence, not all the stations were operative during the time the array was deployed. Figure 1.3 shows geophones that were active during the period of time earthquakes took place.

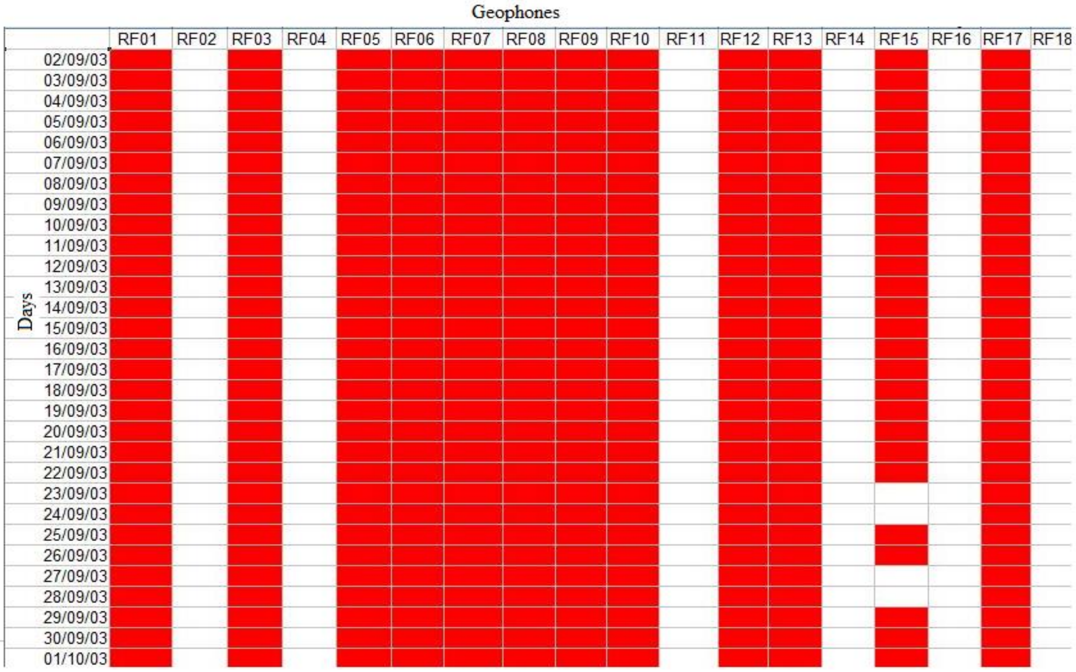

Geophones

Days	RF01	RF02	RF03	RF04	RF05	RF06	RF07	RF08	RF09	RF10	RF11	RF12	RF13	RF14	RF15	RF16	RF17	RF18
02/09/03	🟥		🟥		🟥	🟥	🟥	🟥	🟥	🟥		🟥	🟥		🟥		🟥	
03/09/03	🟥		🟥		🟥	🟥	🟥	🟥	🟥	🟥		🟥	🟥		🟥		🟥	
04/09/03	🟥		🟥		🟥	🟥	🟥	🟥	🟥	🟥		🟥	🟥		🟥		🟥	
05/09/03	🟥		🟥		🟥	🟥	🟥	🟥	🟥	🟥		🟥	🟥		🟥		🟥	
06/09/03	🟥		🟥		🟥	🟥	🟥	🟥	🟥	🟥		🟥	🟥		🟥		🟥	
07/09/03	🟥		🟥		🟥	🟥	🟥	🟥	🟥	🟥		🟥	🟥		🟥		🟥	
08/09/03	🟥		🟥		🟥	🟥	🟥	🟥	🟥	🟥		🟥	🟥		🟥		🟥	
09/09/03	🟥		🟥		🟥	🟥	🟥	🟥	🟥	🟥		🟥	🟥		🟥		🟥	
10/09/03	🟥		🟥		🟥	🟥	🟥	🟥	🟥	🟥		🟥	🟥		🟥		🟥	
11/09/03	🟥		🟥		🟥	🟥	🟥	🟥	🟥	🟥		🟥	🟥		🟥		🟥	
12/09/03	🟥		🟥		🟥	🟥	🟥	🟥	🟥	🟥		🟥	🟥		🟥		🟥	
13/09/03	🟥		🟥		🟥	🟥	🟥	🟥	🟥	🟥		🟥	🟥		🟥		🟥	
14/09/03	🟥		🟥		🟥	🟥	🟥	🟥	🟥	🟥		🟥	🟥		🟥		🟥	
15/09/03	🟥		🟥		🟥	🟥	🟥	🟥	🟥	🟥		🟥	🟥		🟥		🟥	
16/09/03	🟥		🟥		🟥	🟥	🟥	🟥	🟥	🟥		🟥	🟥		🟥		🟥	
17/09/03	🟥		🟥		🟥	🟥	🟥	🟥	🟥	🟥		🟥	🟥		🟥		🟥	
18/09/03	🟥		🟥		🟥	🟥	🟥	🟥	🟥	🟥		🟥	🟥		🟥		🟥	
19/09/03	🟥		🟥		🟥	🟥	🟥	🟥	🟥	🟥		🟥	🟥		🟥		🟥	
20/09/03	🟥		🟥		🟥	🟥	🟥	🟥	🟥	🟥		🟥	🟥		🟥		🟥	
21/09/03	🟥		🟥		🟥	🟥	🟥	🟥	🟥	🟥		🟥	🟥		🟥		🟥	
22/09/03	🟥		🟥		🟥	🟥	🟥	🟥	🟥	🟥		🟥	🟥		🟥		🟥	
23/09/03	🟥		🟥		🟥	🟥	🟥	🟥	🟥	🟥		🟥	🟥				🟥	
24/09/03	🟥		🟥		🟥	🟥	🟥	🟥	🟥	🟥		🟥	🟥				🟥	
25/09/03	🟥		🟥		🟥	🟥	🟥	🟥	🟥	🟥		🟥	🟥		🟥		🟥	
26/09/03	🟥		🟥		🟥	🟥	🟥	🟥	🟥	🟥		🟥	🟥		🟥		🟥	
27/09/03	🟥		🟥		🟥	🟥	🟥	🟥	🟥	🟥		🟥	🟥				🟥	
28/09/03	🟥		🟥		🟥	🟥	🟥	🟥	🟥	🟥		🟥	🟥				🟥	
29/09/03	🟥		🟥		🟥	🟥	🟥	🟥	🟥	🟥		🟥	🟥		🟥		🟥	
30/09/03	🟥		🟥		🟥	🟥	🟥	🟥	🟥	🟥		🟥	🟥		🟥		🟥	
01/10/03	🟥		🟥		🟥	🟥	🟥	🟥	🟥	🟥		🟥	🟥		🟥		🟥	

Figure 1.3 Red colours mean that the station was active. This plot shows how geophones worked for the northern profile

The earthquakes that were to be used for each calculation depended on the requirements of the task to be implemented. It is estimated that around 16,000 natural earthquakes took place worldwide during the length of time in which the deployment of geophones were active (International Seismological Centre). It is clear that, for every calculation, the events to be used have to be retrieved from the recordings made by active geophones. Usually, criteria for retrieving data is based on factors such as location of event, magnitude, the station that record the earthquake, the component registered by the geophone, and any other interesting factors such as the source mechanism.

1.5 Aims of the research

The aims of this project are:

1) To investigate whether it is possible to use seismic interferometry to construct an artificial or virtual sensor from any energy source that can then be used to detect surface and/or body waves.
2) To assess to what extent this virtual receiver emulates the response of a real sensor placed at the same location.
3) To establish a methodology for retrieving surface and body waves in a complex area, such as the Altiplano, and delineate the advantages and disadvantages of that methodology.

1.6 Research methodology

In this section, the research methodology as well as a mathematical introduction of seismic interferometry and the corresponding equations applied in this piece of research are given. The first concept to be introduced is that of reciprocity theorems. Reciprocity theorems are important for seismic interferometry because they describe properties of wave propagation. They have been used for demonstrating source-receiver reciprocity (Lord Kelvin, 1878), modelling wave propagation (Fokkema and van den Berg, 1993) and removing multiple reflections produced by the Earth free surface (Fokkema and van den Berg, 1993; Berkhout and Verschuur, 1997). More importantly, reciprocity theorems have been used to derived Green´s functions (Wapenaar *et al.*, 2002; Wapenaar and Fokkema, 2006; Wapenaar *et al.*, 2006e) demonstrating that the cross-correlation of the two receivers recordings can be used to retrieve the wave propagating between these receivers as if one of them acts as a source. In this chapter, reciprocity theorems of the correlation and convolution type will be introduced as the mathematical background over which interferometry calculations of this thesis are based.

The governing equations of acoustic interferometry are as explained by Schuster (2009). These equations are known as the reciprocity equations of the correlation and convolution type which in the far-field approximation reduces to the equation used in different fields of interferometry such as the virtual source method (Calvert *et al.*, 2004), reverse time acoustic (Lobkis and Weaver, 2001), and daylight imaging (Rickett and Claerbout, 1999).

For systems that are invariant under time-reversal the correlation method requires random sources on a bounding surface only (see Figure 1.4) The correlation method has the disadvantage of the requirement of volume distribution of sources when the time-reversal symmetry is broken, for example by diffusive or strongly attenuating systems.

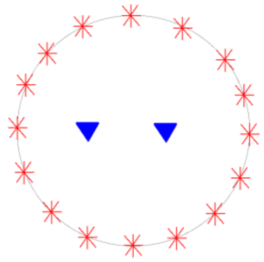

Figure 1.4 Geometrical set up necessary for interferometry by cross-correlation

Consider a situation where only one of the receivers is enclose by a surface of sources as in Figure 1.5. In this case, paths have to be summed instead of subtracted as in the case of Figure 1.4. The operation suitable for that is convolution.

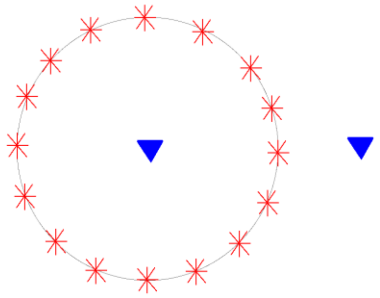

Figure 1.5 Geometrical set up necessary for interferometry by convolution

The geometrical set up of our case implies that we need to use a combination of cross-correlation and convolution, depending on the relative positions of the reference receiver, the earthquake event and the receivers used to cross-correlate or convolve with the reference receiver. The situation is summarised in Figures 1.6, 1.7 and 1.8.

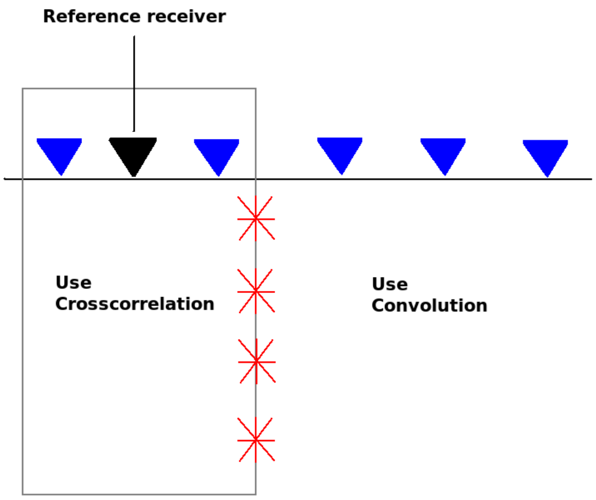

Figure 1.6 For this work, geometry is such that we need to use cross-correlation in one part of the array and convolution in the other part

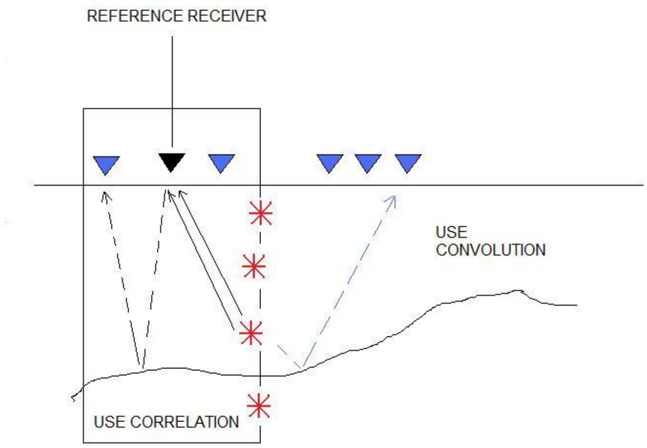

Figure 1.7 Represent a primary reflection. Solid lines represent direct arrivals. Dotted lines represent multiples.

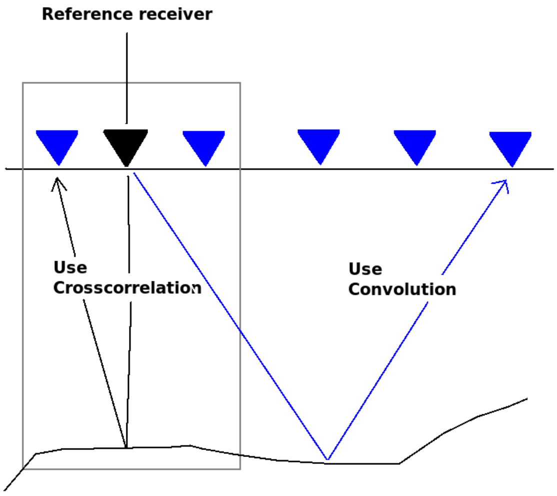

Figure 1.8 Final ray-paths (obtained using correlation or convolution) between the virtual source (reference receiver) and the respective geophones.

The reciprocity equation of the correlation type is the fundamental equation of standard correlational acoustic interferometry. The far field approximation of this equation reduces to that used in daylight imaging, reverse time acoustics, the virtual source method and interferometric imaging. The reciprocity equation of correlation type is: (Schuster, 2009)

$$G(B|A) - G^*(A \mid B) = \int_S G^*(X \mid B)\frac{\partial G(X|A)}{\partial n_X} - G(X \mid A)\frac{\partial G^*(X|B)}{\partial n_X} d^2x \quad (1.2)$$

Where: $\frac{\partial G^*(X|B)}{\partial n_x} = \hat{n} \cdot \nabla G^*(X \mid B)$ for B and A not on the boundary of integration.

In this equation, the integrands are composed of the multiplication of one spectrum by the conjugate of another, which become correlations in time under an inverse Fourier transform. The integrands in this equation are a product of a Green's function for monopole source and the conjugate of another from a dipole source. This means that the spectral phases are subtracted. The subtraction of phases is equivalent to subtracting travel times. This is illustrated in Figures 1.7 and 1.8. Consider the dotted and solid black lines in Figure 1.7. After cross-correlation, the resulting path is the subtraction of the two paths to be correlated. The result is the black line shown in Figure 1.8.

The reciprocity equation of convolution type is: (Schuster, 2009)

$$G(B|A) - G_0(A \mid B) = \int_S G_0(X \mid B) \frac{\partial G(X|A)}{\partial n_X} - G(X \mid A) \frac{\partial G_0(X|B)}{\partial n_X} d^2x \quad (1.3)$$

The integrands in this equation are a product of a Green’s function for monopole source and the conjugate of another from a dipole source. This means that the spectral phases are added together. Adding phases is equivalent to adding travel times as illustrated in Figures 1.7 and 1.8. In this case, consider the dotted and solid blue lines in Figure 1.7, after convolution the resulting travel path is the sum of the two paths. See the blue solid line in Figure 1.8

In chapter 2, a new idea within seismic interferometry, that of retrieving body waves between sources, is presented. Usual forms of interferometry retrieve surface or body waves between receivers. In chapter 2, using reciprocity between sources and receivers, waves travelling between sources were retrieved using deterministic wavefield sources, in order to perform interferometric calculations.

In chapter 2, inter-source Green’s functions by transforming one energy source into a virtual receiver is calculated. This is an idea first introduced by Hong and Menke (2006). It also employs the theory of stationary phase approximation introduced by Snieder (2004), which allows the calculation of the Green’s function by focusing on only those geophones situated along the extensions of the propagation path of the source-receiver pair that is being considered. Then it is possible to replace the assumption of a boundary of receivers or sources surrounding the pair virtual source-receiver by only a fraction of that boundary.

In chapter 2, sources and receivers are considered in a 3D setting (not only 2D as is usual for surface wave propagation). For this reason, paths connecting the pair of sources to the geophones at surface were calculated in a systematic way using a ray tracing algorithm. Results obtained in chapter 2 are in agreement with previous research results concerning the velocity structure of the area. Conclusions draw from chapter 2 imply that, in order to better estimate the velocity structure in a complex area, like the Altiplano studied here, it is better for events and virtual receivers to be as near as possible, in order to avoid distortions and interpretation pitfalls in the interferometric calculations.

The following discussion is an outline and does not intent to be a comprehensive review of the method proposed by Snieder (2004). For a more detailed discussion, the reader is encouraged to review the original paper. Snieder's (2004) work is an alternative way to understand why the correlation of wave recorded at two receiver locations gives the ballistic wave Green´s function between the receivers.

Snieder (2004) started by analysing the waves that travel from a given scatter to two receivers and then calculating the correlation of the waves recorded at two receivers over a time window of length T. Snieder (2004) continued his analysis by applying the following assumptions:

1) Sufficient time/event averaging is carried out so that the cross terms in the sum of the correlation of wave recorded at two receivers over a time window of length T can be ignored.
2) Variations in the power spectrum are uncorrelated with phase.
3) There are many scatters per wavelength.

Then the following equation is obtained:

$$C(\omega) = \overline{|S(\omega)|^2} \int \frac{exp\,[i\omega\,(r2-r1)/c]}{r1r2} ndxdydz \quad (1.4)$$

where:

C(ω) is the power spectrum of the correlation of the recorded signal.

r_1 and r_2 are the distances from the scatter S to the receivers considered.

n is the scatter density.

c is the velocity of wave propagation.

Snieder (2004) applied the stationary phase approximation technique to equation 1.4 which yielded the following equation:

$$C(\omega) = 2\pi\overline{|S(\omega)|^2}\frac{c}{-i\omega}\int_{-\infty}^{\infty}\frac{e^{ik(|R-x|-|x|)}}{||R-x|-|x||}ndx \quad (1.5)$$

With the same nomenclature as in equation 1.4 and with R the distance between the two receivers considered.

Equation 1.5 gives an oscillatory term between receivers that can be ignored leading to the following equation:

$$C(\omega) = 8\pi^2\overline{|S(\omega)|^2}\left(\frac{c}{i\omega}\right)\times\left(-\frac{e^{ikR}}{4\pi R}\int_{-\infty}^{0}ndx - \frac{e^{-ikR}}{4\pi R}\int_{R}^{\infty}ndx\right) \quad (1.6)$$

Equation 1.6 demonstrates that the correlation of waves recorded at two receivers is equal to the Green´s function of the scattered waves propagating along those receivers. This is the result of the process of constructive interference of waves that propagates between the receivers.

In chapter 2, the cross-correlation of the wavefields was interpreted in the same manner as Tonegawa *et al.* (2010) where the cross-correlation of the wavefield gives the direct P-waves propagating between two sources. The normalised frequency domain of the correlation of the ith station is given by:

$$C^i(\omega) = \frac{u^i(\omega)\cdot v^i(\omega)}{|u^i(\omega)||v^i(\omega)|} \quad (1.7)$$

where:

$u^i(\omega)$ and $v^i(\omega)$ are the wavefield generated by the two sources, for the case considered here u and v are the impulsive pulses.

Equation 1.7 gives the time difference between the two pulses. In the time domain and after stacking over M stations equation 1.7 transforms to:

$$\varphi(t) = \frac{1}{M}\sum_{i=1}^{M}C^i(t) \quad (1.8)$$

where φ(t) gives the information on the travel time between the two sources considered.

Body wave retrieval using coda waves is studied in chapter 3. The methodology in chapter 3 is based in a modified procedure introduced by Tonegawa *et al.* (2009). New research outcomes from the chapter include the introduction of a combined procedure of cross-correlation and convolution that operates based on the relative position of the earthquakes, virtual sources and geophones at the surface. Chapter 3 constructs Green's functions between pairs of receivers by means of seismic interferometry.

P waves and coda P waves, S waves and coda S waves and complete seismograms with all possible combinations of pairs of this are used, in order to calculate, by means of interferometry, the seismograms that would be obtained if a reference receiver or virtual source was in fact a real source. Seismic events with a depth of more than 100 km were used to compute the cross-correlation functions (CCF) with a time length of 300 s and a frequency band of 0.2-3.0 Hz. It was necessary to pre-process the data before the interferometric calculations, which is extensively explained in chapter 3.

The methodology included choosing a geophone on the surface in such a way that the considered events were symmetrically located around that fixed geophone, in order to approximate equipartitioning of energy. Then, for every earthquake, the cross-correlation function between the fixed geophone and another geophone located in the line of receiver, at a distance *d* from the fixed geophone, was calculated. This operation was performed for all possible geophone pairs. Finally, for all earthquakes, all possible pairs with approximately equal inter-receiver distances were stacked.

In an analogous way to that of Tonegawa *et al.* (2009), the processed wavefields are correlated and then stacked over all sources using the equation:

$$C_{1,2}^{i}(\omega) = u_1^i(\omega) \cdot u_2^i(\omega) \quad (1.9)$$

Where 1 and 2 represent receivers 1 and 2, $C_{1,2}^{i}(\omega)$ is the frequency domain representation of the temporal cross-correlation C for an ith event, and $u_1^i(\omega)$ and $u_2^i(\omega)$ are the processed wavefield. In the case of convolution, first the processed wavefields are flipped over and then equation 1.9 is applied.

Stacking over all sources is made using the equation:

$$\langle C_{1,2}(\omega) =\rangle \frac{\sum_{i=1}^{M} \omega_i C_{1,2}^{i}(\omega)}{\sum_{i=1}^{M} \omega_i} \quad (1.10)$$

Where M is the number of events, and ω_i is the weighting factor applied to the wavefield before summation.

This process of weighting in equation 1.10 is the way to homogenise the condition of incidence in order to have equal partitioning of the energy for the different incident angles, this condition is necessary in order to avoid ghost phases as explained by Nakahara (2006).

Results from chapter 3 demonstrate that the zone of partially melted material prevented the interferometric retrieval of waves from S coda. Nevertheless, P coda could be used to fulfil the objective instead.

The feasibility of retrieving body, or surface waves, in the case of strong Moho reflections, is investigated in chapter 4. This idea comes from the work of Mori and Helmberger (1996), who found that large amplitude SMS phases were caused when large Moho reflections were present. The methodology used in chapter 4 makes use of passive seismic recordings over a continuous six-month period in which earthquake signatures were suppressed in order to ensure that the only contributions were produced by noise sources. The methodology was based on a noise interferometry procedure introduced by Bensen *et al.* (2007), by which the earthquake signature is removed from the data by the application of a weighting factor to each sample of the data by this procedure: if x_i is the raw seismogram and $\hat{x}_i$ is the processed seismogram (bandpass filtered), the temporal weight applied in order to remove the earthquake signature is given by:

$$\hat{w}_n = \frac{1}{2N+1} \sum_{i=n-N}^{n+N} |\hat{x}_i| \quad (1.11)$$

Where 2N+1 is the width of the normalisation window and n is the number of samples considered within the window.

The data consisted of continuous recordings of six months of noise data, between March 2003 and August 2003, which were downloaded in segments of one day in which earthquakes signatures were suppressed using equation 1.11 in order to ensure that the only contributions were produced by noise sources, and then cross-correlations were calculated and stacked by using the following equation:

$$\langle C_{1,2}(\omega)\rangle = \sum_{i=1}^{M} C_{1,2}^{i}(\omega) \quad (1.12)$$

Where 1, 2 are geophones 1 and 2 and M is the time segment considered.

Chapter 4 also presents the analysis of data for two different profile lines, located in the Altiplano and Puna plateaux respectively. Results are in agreement with previous knowledge of the geology of the zones. For the Altiplano plateau, facts such as changes in the velocity of propagation of the waves were observed, due to a low velocity zone and different velocities of propagation, depending on the direction of propagation. For the Puna plateau, two different wave packets were observed; one was thought to be from body waves reflected at the Moho, or a refracted wave travelling along the subducting slab.

Chapter 5 presents the results of applying a new kind of interferometry, known as source-receiver interferometry, to surface waves in the Altiplano. Source-receiver interferometry was first introduced by Curtis (2009) and transforms real sources or receivers into virtual ones. This can be thought of as turning a real-source real-receiver pair into virtual-receiver virtual-source pair, respectively. This source-receiver interferometry procedure is a second-order interferometric method - that is to say, two steps of interferometry are applied to the data. In this current situation, these two steps could have been cross-correlation or convolution and, for that reason, the tests conducted in this chapter evaluated the quality of the data and results for the two steps of the interferometric calculation involved.

It is important to review the mathematical background of this new kind of interferometry. The starting point will be the acoustic unified representation theorem that combines correlation and convolution (Curtis and Halliday, 2010)

$$\begin{aligned}
&p(x_2) = \int_V G(x,x_2)q(x)dV - \frac{-1}{j\omega\rho}\int_S \Big\{\big[\int_V G^*(x',x)q(x')dV'\big]n_i\partial_i G(x_2,x) - \\
&n_i\partial_i\big[\int_V G^*(x',x)q(x')dV'\big]G(x_2,x) + \\
&\Big[\frac{-1}{j\omega\rho}\int_{S'}\{p(x')n_{i'}\partial_{i'}G^*(x',x) - n_{i'}\partial_{i'}p(x')G^*(x',x)\}dS'\Big]n_i\partial_i G(x_2,x) - \\
&n_i\partial_i\Big[\frac{-1}{j\omega\rho}\int_{S'}\{p(x')n_{i'}\partial_{i'}G^*(x',x) - n_{i'}\partial_{i'}p(x')G^*(x',x)\}dS'\Big]G(x_2,x)\Big\}dS \qquad (1.13)
\end{aligned}$$

Where:

p is the acoustic pressure, q is the source distribution, G is the Green's function representing the pressure at x due to a volume injection-rate density source at location x', ω is the angular frequency and ρ is the density at the source location.

Curtis and Halliday (2010) used equation 1.13 to derive an interferometric integral that describes the construction of a real-source to real-receiver wavefield, using the geometry of figure 1.9 (a) equation 1.13 simplifies to:

$$\begin{aligned}
&G(x_2,x_1) + G^*(x_2,x_1) = \\
&\frac{1}{j\omega\rho}\int_S\Big\{\Big[\frac{-1}{j\omega\rho}\int_{S'}\{G(x',x_1)n_{i'}\partial_{i'}G^*(x',x) - \\
&n_{i'}\partial_{i'}G(x',x_1)G^*(x',x)\}dS'\Big]n_i\partial_i G(x_2,x) - \\
&n_i\partial_i\Big[\frac{-1}{j\omega\rho}\int_{S'}\{G(x',x_1)n_{i'}\partial_{i'}G^*(x',x) - n_{i'}\partial_{i'}G(x',x_1)G^*(x',x)\}dS'\Big]G(x_2,x)\Big\}dS
\end{aligned}$$

(1.14)

Curtis and Halliday (2010) simplified equation 1.14 by the application of the Sommerfeld radiation condition which states for a scalar field that the energy radiated from the sources must scatter to infinity. This means that no energy may be radiated from infinity into the field. This translates into the following equation:

$$\pm jkG = n_i\partial_i G \qquad (1.15)$$

Equation 1.15 is valid if waves travel perpendicular to the boundaries. Then equation 1.14 simplifies to:

$$G(x_2,x_1) + G^*(x_2,x_1) \approx \frac{4k^2}{(\omega\rho)^2}\int_S\int_{S'} G(x',x_1)G^*(x',x)G(x_2,x)dS'dS \qquad (1.16)$$

Chapter 5 assesses two independent methodologies, one of them being the use of events recorded by geophones (active sources) to perform the interferometric calculations, and the other using passive recordings made by the geophones deployed in this project. In order to do this, a methodology introduced by Bensen *et al.* (2007), which suppressed earthquake signatures, was followed. The methodology that was used in chapter 5 consisted of an implementation of equation 1.16

Equation 1.16 in essence means interferometry by convolution, then interferometry by cross-correlation. In the current case, the two steps of interferometry were performed by cross-correlation due to the relative position of sources and receivers, as will be described in chapter 5. This methodology was introduced by Curtis *et al.* (2010), and uses surrounding sources and receivers to reconstruct source to receiver wavefields. Possible canonical geometries are shown in Figures 1.9 and 1.10.

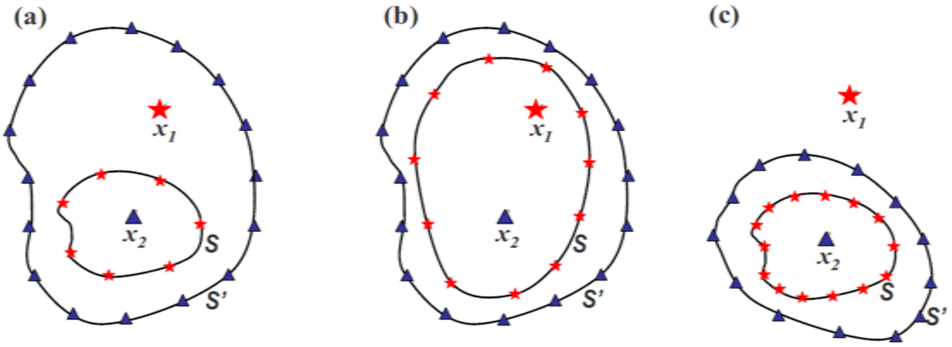

Figure 1.9 Canonical geometries for inter-receiver interferometry. Triangles represent receivers, stars represent sources. S and S' are closed lines in two dimensions, surfaces in three dimensions. Figure taken from Curtis *et al.* (2010).

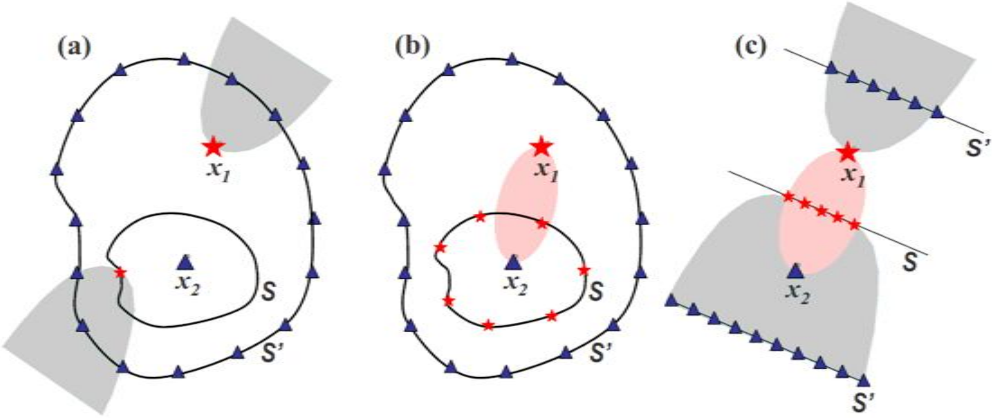

Figure 1.10 Regions of stationary phase within the interferometric integrals, corresponding to the geometry shown in Figure 1.9 (a). Key as in Figure 1.9. Shaded hyperbolae show stationary phase regions for correlational interferometry, while ellipses show the same for convolutional interferometry. Figure taken from Curtis *et al.* (2010).

In chapter 5, active sources, as well as passive recordings, were used to test the theory. Both methodologies showed consistent results when compared with those from other fields of geosciences. Nevertheless, for the second step of interferometry, the methodology using active sources showed better quality results than those of passive sources.

Chapter 6 summarises the findings and draws general conclusions about the area of study, the methodologies used and seismic interferometry in general. The aim of the research is discussed, as well as its contribution to existing knowledge, outlining how the results can be used and, further, pointing out the need for possible routes of further research.

Table 1.1 summarises which interferometry method was used in each chapter.

Chapter	Interferometry method used
02	Seismic interferometry combined with source-receiver reciprocity making use of the concept of stationary phase. Principal mathematical operation is cross-correlation. Eq.1.7 and 1.8
03	Coda wave interferometry. Principal mathematical operation: a combined method of cross-correlation and convolution. Eq.1.9 and 1.10
04	Ambient seismic noise interferometry. Principal mathematical operation: cross-correlation. Eq. 1.11 and 1.12
05	Source-receiver wavefield interferometry. Principal mathematical operation: two steps of interferometry calculation which includes correlation and/or convolution. Eq 1.9, 1.10 and 1.16

Table 1.1 Summary of the interferometric method used in each chapter

Other methodologies were also considered, such as that of constructing seismic virtual shots from interferometry. The idea of constructing seismic images from earthquake body waves can be found in the works of Bostock and Rondenay (1999); Nowack *et al.* (2003); and Nowack *et al.* (2006). In this current work, the intention was to use P and/or S coda waves in order to construct virtual shots, and then process these shots as a 2D line.

The goal was to transform certain arrivals in the earthquake record to surface data, which could then be processed to reconstruct the reflectivity distribution. As shown in Figures 1.11 and 1.12, the cross-correlation of the wavefield observed at two receivers describes the wavefield that would be recorded at one receiver if there were a source at the other. Taking this information into account, one can construct virtual shots.

By constructing interferometric virtual shots one can study the influence of every deterministic phase and coda wave in relation to the seismic interferometric image. Also, this test could allow one to answer questions concerning the resolution of the deployment as well as to identify the phases that contribute to the final images.

The methodology that should be used to accomplish this task includes the realisation of a seismic processing sequence that has to be implemented in SU (free seismic processing software package supported by the Centre for Wave Phenomena, Colorado School of Mine), and use of the velocity model for P and S waves, for example, from the work of Heit (2005).

The plan was also to include different components in the recording, to perform interferometric imaging and, in this way, take into account the elastic (P and S) character of body waves (geophones used for the Andes project consisted of three components). Unfortunately, this method did not provide positive results due to the fact that not all geophones where active during the time the survey was acquired.

This means that the spatial distribution of active geophones was irregular as can be seen in Figure 1.3. This fact created voids or holes of information, which in turn badly affects the quality of the tests conducted for this particular methodology. Therefore, no results will be presented in this thesis concerning this point.

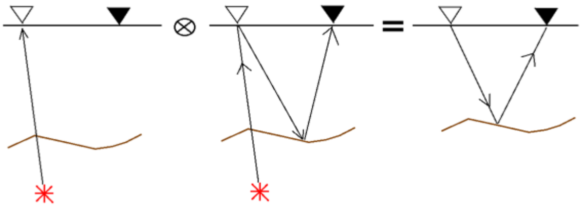

Figure 1.11 The principle of seismic interferometry. The cross-correlation of the wavefield observed at two receivers describes the wavefield that would be recorded at one receiver if there were a source at the other.

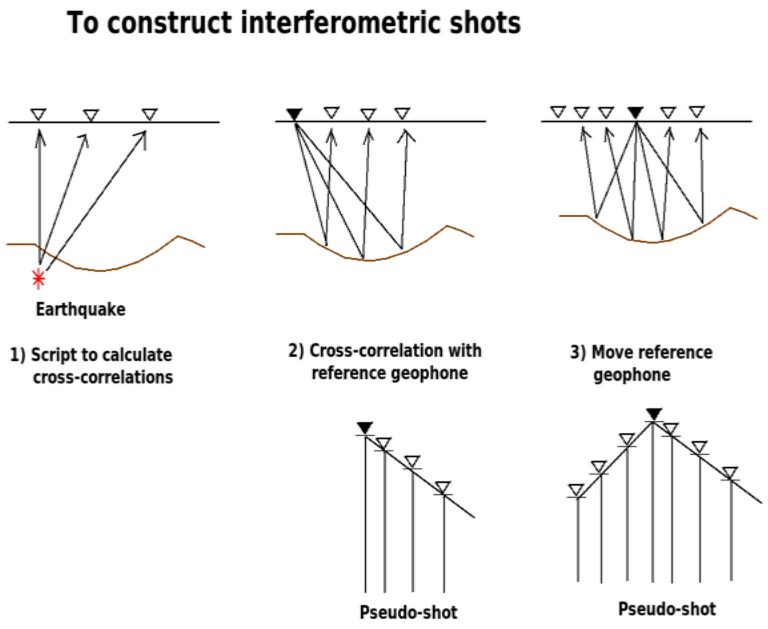

Figure 1.12 The process of constructing interferometric virtual shot recordings. First, an earthquake is recorded, and then cross-correlations with a reference receiver are calculated: the reference receiver acts as a pseudo shot, these pseudo shots can then be processed.

1.7 Surface wave interferometry (undergraduate project)

At the same time as this PhD project was starting to explore the possibility of retrieving body waves using seismic interferometry, a pilot project study with an undergraduate student, during a period of three months, was taking place. The intention of this pilot project was to explore the suitability of the application of seismic interferometry in the retrieval of surface wave in the Andes. This section will show and discuss the results of the supervision of this pilot project conducted by Kirsten Mauchline as part of her undergraduate training. Kirsten’s work was supervised by Prof. Andrew Curtis, John Gonzalez and Dr. Heather Nicholson.

The importance of this study for the seismic interferometry community resides in the fact that the novel technique of turning earthquakes into virtual receivers (Curtis *et al.*, 2009) was implemented for the first time in an area of high geological complexity that showed a clear indication of direct surface wave arrivals and moveout, related to inter-source distance, at the considered receiver stations. Also, interferometric results were shown to be compatible with previous velocity studies conducted in the area. The intention of this chapter is to add new and complementary information to the work undertaken by the undergraduate student as well as to summarise the findings and methodology of this piece of research.

The original data for the undergraduate project was chosen such that the depths of the events were less than 100 km and with sufficient distance from the receiver line used, to perform interferometric calculations, such that regular surface waves were expected. The original set of available data consisted of 54 events as shown in Figure 1.13. Of these, the student chose those which were the most suitable, based on the criteria listed below. The final choice made is depicted in Figure 1.14

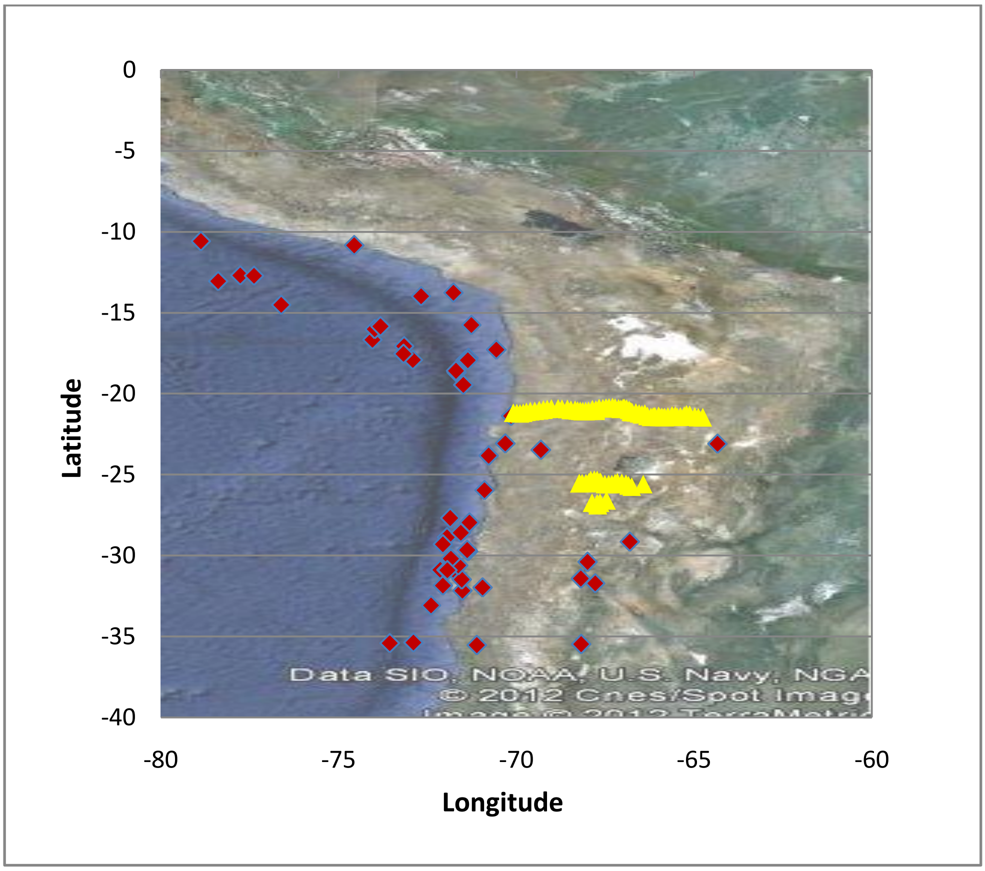

Figure 1.13 Original set of earthquakes for the undergraduate project

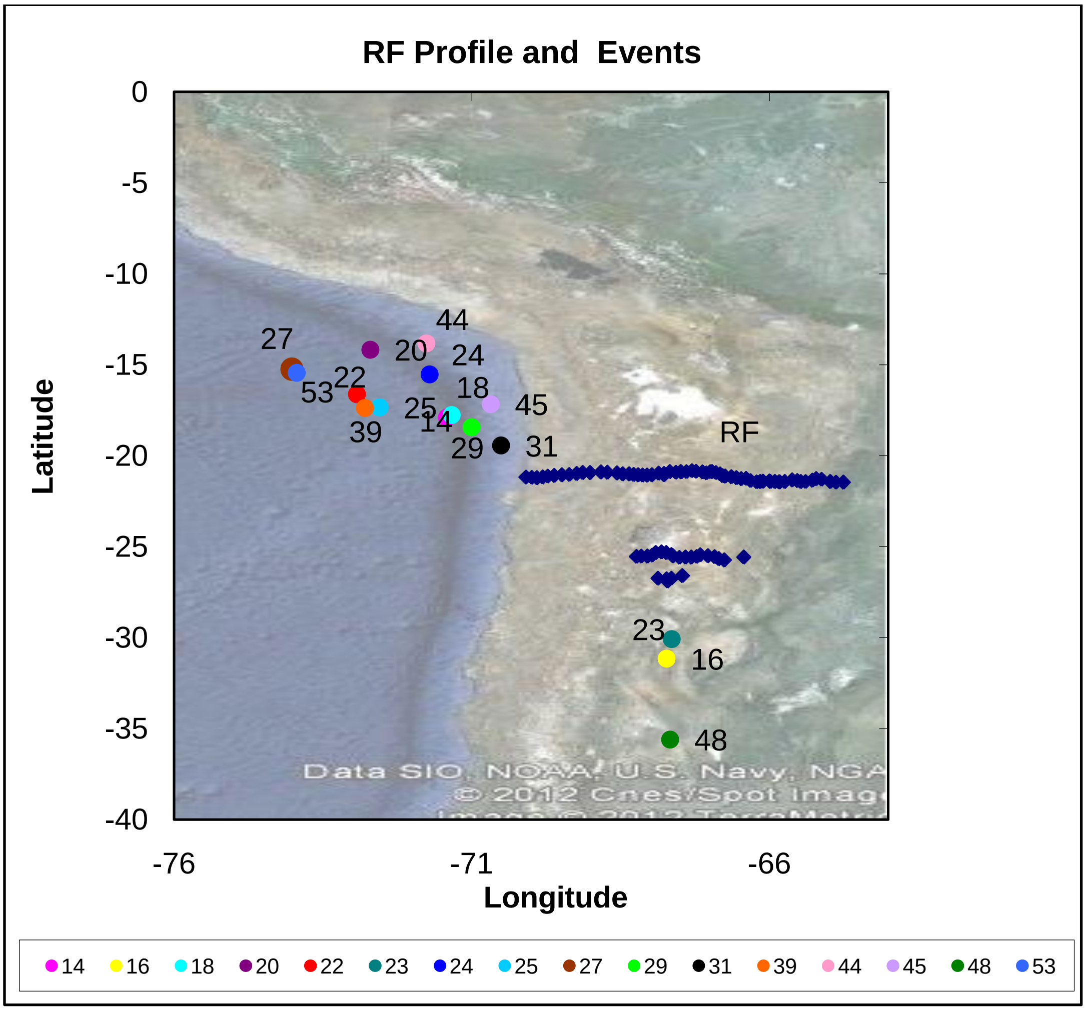

Figure 1.14 Final set of events chosen by the undergraduate student. Taken from Mauchline (2010)

Only four events were chosen from those available (Figure 1.14), based upon the following criteria: clarity of the direct surface wave arrival, availability of the fault plane solution, good signal to noise ratio and arrival time being within an expected range. Also, events were selected to ensure alignment with geophones, i.e. to ensure that the extension of their inter-source paths (between two events) extrapolates to the interior of the line of the receivers of interest, as this is necessary for inter-event interferometry to work (Curtis *et al.*, 2009). Events are shown in Figure 1.15.

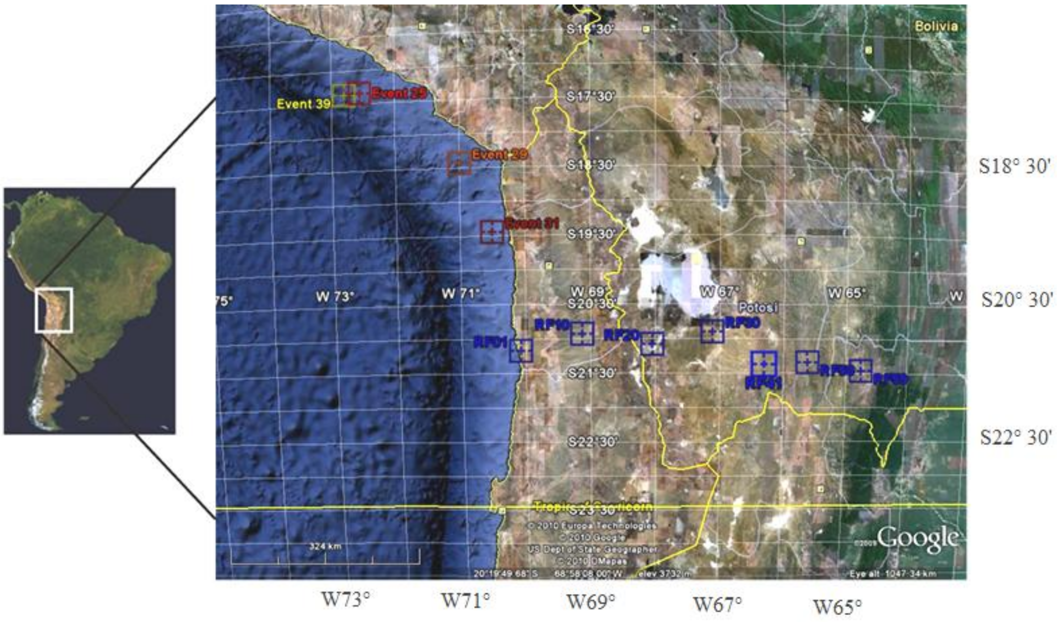

Figure 1.15 shows the four events to which interferometry was applied. Reproduced from the work of Mauchline (2010)

Once the data was downloaded from the GEOFON web server of GFZ, the subsequent processing steps included: raw data decompression; bandpass filter analysis in the region of 0.2-3.0 Hz frequency band suggested by the work of Wölbern *et al.* (2009); linear trend removal; application of a taper filter to the signal in order to smooth endings after cutting coda waves (to simplify the signal and the cross-correlation result); correcting the header for origin time; windowing the parts of the events which were of interest; normalisation; application of the interferometric operation (cross-correlation); placing a stack over the receiver of interest; and, QC of the results as will be explained and outlined in the discussion section. It is important to mention that this undergraduate project used the vertical component of the three-component recording available for the geophones in the project.

Software SAC (Seismic Analysis Code) from PASSCAL was used to perform all the processing steps. The program rdseed was used to decompress the data into seed format which is compatible with SAC. All visual inspections were made using the program PQLII from PASSCAL because this is more versatile than SAC for plotting and visualisation, and is easier to use. Interpretations of surface wave arrivals were carried out using the routine “envelope” from SAC that calculates the envelope function of a signal. This helped distinguish useful signals from the background level.

A series of tests were carried out, where variables such as the method of normalisation before correlation, the weighting of the receivers contributing to the final interferometric result, and the surface wave velocity encountered, were varied. In all cases it was shown that the theory of stationary phase approximation, already outlined in this chapter, held.

Regarding the normalisation method used before cross-correlation, the amplitude normalised data approach has already been proven to be successful in turning earthquakes into virtual receivers (Bensen *et al.*, 2007). Meanwhile, the one-bit normalisation, as explained by Bensen *et al.* (2007), did not give a good result because the relative amplitude of the signal needed to be retained.

A summary of the most relevant results obtained are shown in Figures 1.16 and 1.17 in which a roughly linear moveout can be observed. From these figures, it is important to mention that a better signal is obtained for the Green’s function between events 31 and 39 when a sub-set of receivers along the ray-path extension were considered. This can be seen in Figure 1.17

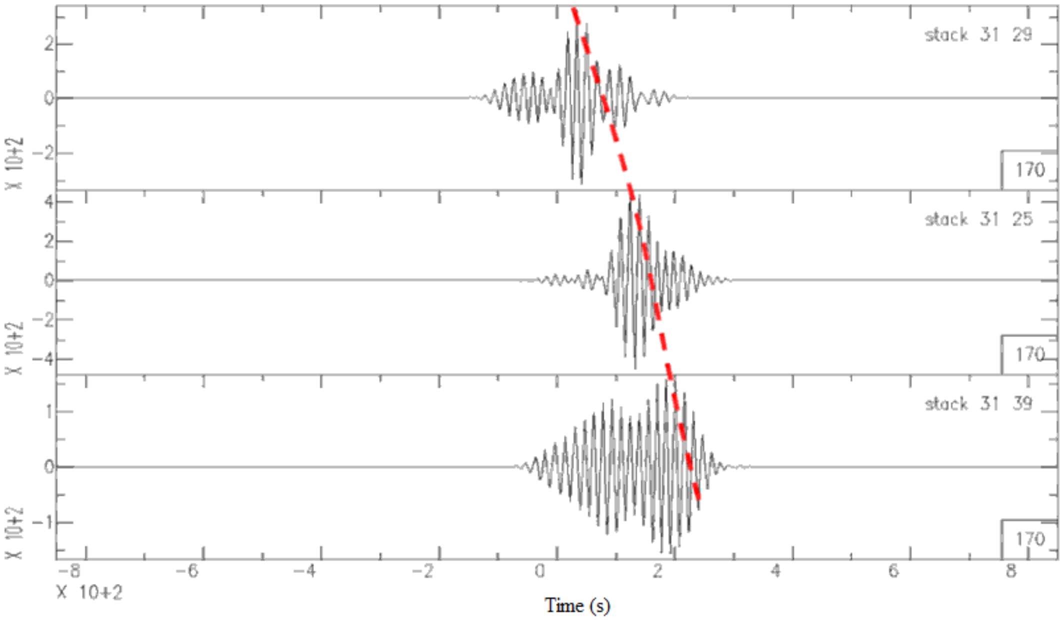

Figure 1.16 Taken from Mauchline (2010). Amplitude normalised functions for the three receiver pairs from the smallest inter-event separation 31-29 (top) to the largest inter-event separation 31-39 (bottom). The red dashed line indicates the moveout and the group surface waves arrive later with increasing travel distance.

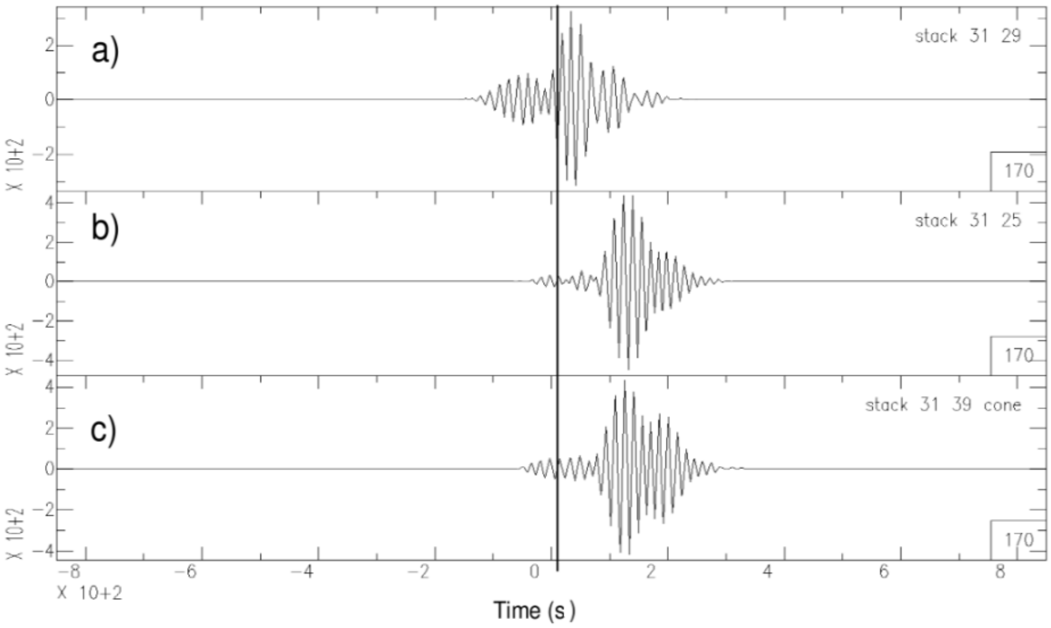

Figure 1.17 Taken from Mauchline (2010). The three final approximate Green's functions for the selected event pairs: a) 31-39 the resultant stack of all the possible cross-correlations; b) 31-25 the resultant stack of all the available receiver cross-correlation; and c) 31-39 the resultant stack only considering a subset of receivers located around the inter-source line whose cross-correlation created a symmetrical moveout. The black line marks the origin time of the earthquake at t=0.

Using the three pairs of travel times obtained from the inter-source surface wave Green's functions estimated using seismic interferometry, the group velocity was calculated. Waves were assumed to travel along the great circles paths between the two pairs of events, and then distance was calculated using a Java script developed by Chris Veness. The script uses the Haversine formula and can be accessed at the following web page:

http://www.movable-type.co.uk/scripts/latlong.html

The haversine formula is an equation for calculating the distance between two points on a sphere knowing their longitudes and latitudes and is given by:

$$haversin\left(\frac{d}{r}\right) = haversin(\emptyset_2 - \emptyset_1) + cos\emptyset_1 cos\emptyset_2 haversin(\lambda_2 - \lambda_1) \quad (1.17)$$

where haversin is the haversine function given by:

$$haversin(\theta) = sin^2\left(\frac{\theta}{2}\right) \quad (1.18)$$

and where:

d is the distance between the two points (along a great circle of the sphere)

r is the radius of the sphere,

$\phi_1 and\ \phi_2$ are the corresponding latitude of point 1 and latitude of point 2.

$\lambda_1\ and\ \lambda_2$ are the longitude of point 1 and longitude of point 2.

The results of the group velocity calculation are summarised in Table 1.2

Event pair	Group Travel Time (s)	Inter-source Distance (km)	Group Velocity (km/s)
31-29	30	124.2	4.14
31-25	130	317.3	2.44
31-39	130	333.7	2.57

Table 1.2 Reproduced from Mauchline (2010). Group travel times, inter-event distance and group velocities for each event pair.

Even though this is only an example with a small number of events, the contrast of velocity depending on the direction of its propagation is evident. In Figure 1.15, it can be seen that the path of event 31-29 is almost parallel and close to the coast, in contrast with events 31-25 and 31-39 whose paths are more towards the ocean. The result of this anisotropic behaviour is consistent with previous studies in the area. For example, the velocity anomaly is consistent with the distribution in the Moho model from Nataf and Richard (1996), and also with the low velocity anomalies present in the work of both Trampert and Woodhouse (1996) and also Ekstrom *et al.* (1997). For example, Figure 1.18 shows the estimated Rayleigh-wave group-velocity map at 100s period presented in percentage deviation from the average velocity versus period, the lateral variation of velocity presented for the Altiplano region is also observed from the results of this study.

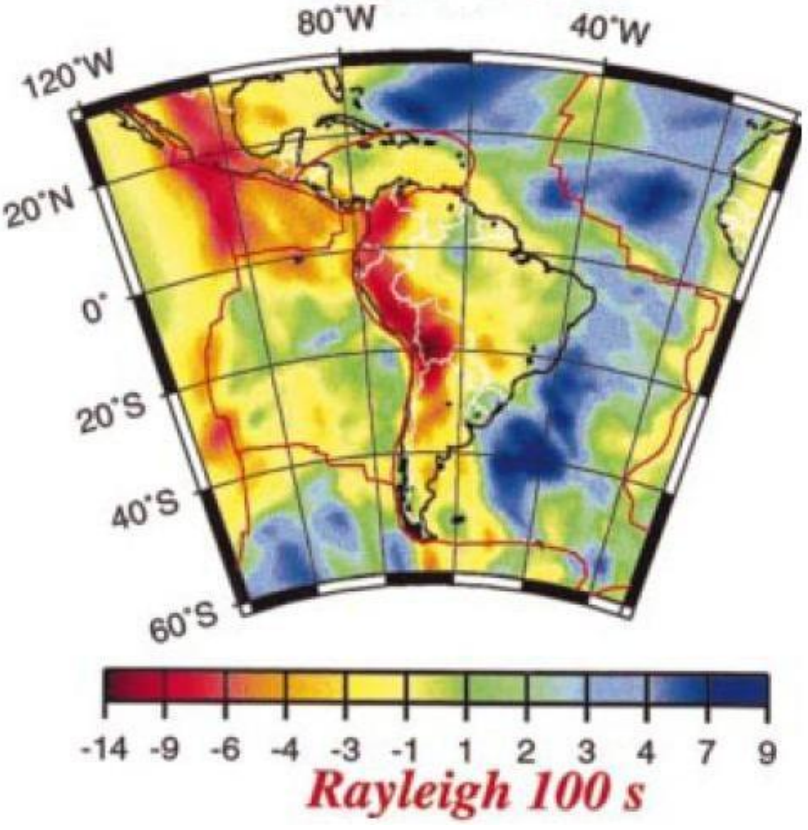

Figure 1.18 taken from Vdovin *et al.* (1999). Estimated Rayleigh-wave group-velocity map at 100s period presented in percentage deviation from the average velocity at this period.

Another piece of research that is compatible with the results described in this section is that of Vdovin *et al.* (1999). These researchers studied the dispersion characteristics of surface waves propagating across South America and its surrounding oceans; obtaining, as a final product, group velocity maps for Rayleigh and Love waves.

Referring back to the work of Vdovin *et al.* (1999) figure 8 (a) pp. 332, we can observe a strong variation for the Rayleigh wave group velocity along the coast and a mild variation of velocity in the sea area for frequencies of 20s, 30s and 50s. These are all consistent with the velocity variations found in Table 1.2 [Vdovin *et al.*, (1999)]. However, please note that we found about 40% deviation from the mean, where Figure 1.18 shows about 20% deviation between fast and slow anomalies in our locations. This is mainly due to the fact that their inversion is regularised (damped or smooth) which reduces amplitudes and ours is not.

One possible interpretation of this anisotropic behaviour could be explained by the presence of the roots of the Alpes which in turns influence the crustal thickness. Crustal thickness will determine how velocities vary within a region, for example, the magnitude of the low velocity features observed from Bolivia, Peru and north Altiplano are related to crustal thickness as explained by Vdovin *et al.* (1999).

One way to further this undergraduate project would be to analyse more events in order to consider a wider zone of calculation and comparison. Also, if a comparison with, for example, the Love waves map velocities from the work of Vdovin *et al.* (1999) was desired, it would be important to take note of the horizontal components of the recordings.

As far as we are aware, seismic interferometry using real data from a seismic passive experiment has not previously been applied in areas of partially molten material. This makes this project interesting from the point of view of understanding interferometry in such environments.

As it will be seen from chapter 3 of this thesis, the zone of partial melted material in the Andes zone is an important factor affecting interferometry because S waves do not propagate through this molten area and coda wave interferometry did not prove to be successful for retrieving body waves.

This undergraduate project revealed that interferometric studies were possible in the Altiplano plateau, but at the same time highlighted the potential setbacks that could be encountered. As was confirmed thereafter in this PhD project, geophysical and geological factors as well as technical problems were of crucial significance when considering the application of interferometry theory.

Finally, it is important to mention that this piece of research used only vertical component recordings that, when used to calculate inter-source group velocities, agreed with the velocity model of Vdovin *et al.* (1999) for Rayleigh waves.

Chapter 2

INTER-SOURCE BODY WAVE RETRIEVAL

2.1 Summary

This chapter is concerned with a relatively new idea within seismic interferometry: retrieving body waves between sources. Interferometry is usually used to retrieve surface or body waves between receivers. Here, using reciprocity between sources and receivers, waves travelling between sources were retrieved by using recordings of those sources at a boundary of receivers to perform interferometric calculations. Also, the concept of stationary phase approximation was used in order to simplify the calculation algorithms.

Most results presented in this chapter are in agreement with previous information about the velocity structure of the area in which the data was collected. Others represent new information about the velocity characteristics of the Altiplano.

Results presented in this chapter show the Green's functions calculated between the two sources considered. This Green's function shows wave arrivals whose times are in agreement with the expected times calculated by a 2D ray tracing algorithm. This agreement is an indication that the interferometry method is working.

In conclusion, in order to better estimate the velocity structure in a complex area such as that in the current study, it is better for events and virtual receivers to be as close together as possible in order to avoid distortions and interpretation pitfalls in the interferometric calculations caused by the strong velocity contrast present in the Altiplano (Heit, 2005).

2.2 Introduction

Usual forms of interferometry retrieve surface wave Green´s functions by using seismic coda (Campillo and Paul, 2003) or by the use of ambient seismic noise

(Shapiro *et al.*, 2005). Retrieving body waves is also possible using coda and ambient seismic noise (Roux *et al.*, 2005; Miyazawa *et al.*, 2008; Nishida *et al.*, 2008; Tonegawa *et al.*, 2009; Zhan *et al.*, 2010). Other approaches use wavefields, generated by active seismic sources, to retrieve waves propagating between two receivers - including direct and reflected waves. (Bakulin and Calvert, 2006; van Manen *et al.*, 2006; Wapenaar and Fokkema, 2006a).

The seismic interferometry concept of retrieving waves between two receivers has been extended to the concept of waves travelling between two sources by making use of source-receiver reciprocity (Aki and Richards, 1980). In this respect, important contributions regarding the retrieval of waves between two sources comes from the works of Hong and Menke (2006) and Curtis *et al.* (2009). Hong and Menke (2006) based their work on the coda wave interferometry of Campillo and Paul (2003) concerning the retrieval of dispersive surface waves seismograms travelling between two stations by using only the coda of recorded seismograms, extended by means of the usual cross-correlation technique and using the principle of spatial reciprocity, in order to retrieve waves travelling between pairs of events. Hong and Menke (2006) used seismicity along the fault plane of the San Jacinto fault in southern California to simulate the case where geophones are placed along the fault plane. In doing so, they estimated the seismic velocities and properties of the fault plane.

Curtis *et al.* (2009) used earthquakes located near the Earth’s surface to show that the strain information obtained from inter-earthquake interferometry was consistent with the information provided by instruments. Curtis *et al.* (2009) computed cross-correlations of the geophone responses, requiring only the recorded seismogram at each receiver. This approach is different from the methodology of Hong and Menke (2006), in which the wavefields were summed over receivers before computing the cross-correlations. The procedure of Hong and Menke (2006) produced less accurate seismogram approximation as shown in the work of Curtis *et al.* (2009) because accurate construction of seismogram, using coda wave, requires much longer time series. Curtis *et al.* (2009) approach is different because it is based on the representation theorems of Wapenaar and Fokema (2006) and van Manen *et al.* (2006), and hence is valid using the complete earthquake seismograms, not only the coda.

The theory of stationary phase, introduced by Snieder (2004), is key to the problem of retrieving waves travelling between sources. In fact, in the work of Curtis *et al.* (2009) retrieval of surface waves travelling between two sources was achieved by using the theory of stationary phase facilitated by the prior knowledge of geometrical parameters such as position of earthquakes, stations and stationary points at which seismometers must be placed.

Snieder (2004) showed that the requirements for the equipartition of energy equally in all directions, in order to retrieve the Green’s function using passive imaging, can be approximated to the requirement that scattered waves propagate on average isotropically near receivers. In other words, this means that given a pair of receivers, the main contributions to the Green´s function come from regions of space lying in the prolongation connecting the two receivers as can be appreciated in Figure 1.10

Tonegawa *et al.* (2010) used stationary phase arguments to retrieve Green´s functions estimates including direct P and S waves propagating between earthquakes at depths of 300-500 km below the Bonin Islands. Results from the work of Tonegawa *et al.* (2010) show that it is important to stack interferometric contributions around the stationary phase location.

Likewise, the size of the stationary phase region is important because it is related to the number of geophones that must be used. The rightmost plot in Figure 1.10 shows in grey the stationary phase region: geophones within this grey area will then be used for interferometric calculation. In the case of the Altiplano, when a sub-set of geophones are within the stationary phase region they need to be checked for functionality (Figure 1.3) and signal record quality apart from other factors before using them for interferometry.

Regarding other factors to consider, Tonegawa *et al.* (2010) suggested taking the source mechanism into account. Additional findings in the work of Tonegawa *et al.* (2010) concern the signal to noise relation versus the magnitude of the events: while the magnitude of the events has to be kept as small as possible in order to consider the earthquake as a point source, the larger the magnitude the better the signal to noise ratio will be. So, there must be a compromise between these two factors.

In the case of the Altiplano data, the recordings made by the geophones were noisy due to the weather conditions which affected the functioning of geophones and the complexity of the geology of the zone (for example, the attenuation of the S wave as demonstrated by Wölbern *et al.* 2009 makes the signal to noise ratio lower by deteriorating the S signal and allowing noise to be recorded). Nevertheless, events were chosen in such a way that they had the minimum magnitude possible, yet kept a good signal to noise relation at the same time.

In section 1.6, a detailed discussion of the Snieder (2004) approximation was given. Equation 1.6 demonstrates that the correlation of waves recorded at two receivers is equal to the Green´s function of the scattered waves propagating along those receivers. As explained in chapter 1, correlation of the wavefields will be performed using equation 1.7 and 1.8.

In this chapter, points such as the extent of the stationary phase region at the surface, the influence of the frequency content of the signal, the location of the earthquakes and their influence in the subsequent interferometric calculations will be investigated for the Altiplano.

2.3 Data used

The earthquakes used in this chapter were chosen from the catalogue of the International Seismological Centre (http://www.isc.ac.uk/). Events were chosen in time periods such that most of the geophones were operating. Also, factors such as the magnitude of the earthquakes were taken into account. This has to be kept to the minimum magnitude possible. If not, the spatial extent becomes a problem as the source cannot be considered to be a point source at the source-to-receiver distances considered here, as explained by Spudich and Bostwick (1987).

However, if the event is too small in magnitude the quality of the signal in comparison with the background noise will be low, which in turn affects the interferometry calculations. After experimentation with several earthquakes, it was considered that the best value for earthquake magnitude has to be between 4.4 and 5.4.

After being selected, events were windowed (meaning a time window of 300s was selected in which the earthquake of interest was contained) and correct earthquake source times were assigned (this is the zero time for the event, and all geophones in the survey, for this event, have the correct relative arrival times) to the header using SAC software from IRIS (Incorporated Research Institutions for Seismology).

Location was a further factor taken into account and the events considered in this research were all located beneath the Moho and close to the subducting slab. The idea was to have the best arrangement of earthquakes such that when they were converted into virtual geophones by seismic interferometry it would be possible to achieve the best “illumination” (meaning that their location is of interest in retrieving information like velocities of the areas considered). This was realised by selecting earthquakes that were located near to the respective zones of interest like for example the subduction slab, or the zone of partial melting (Wölbern *et al.*, 2009).

During the period of time in which geophones were deployed, earthquakes whose depths were more than 100 km are presented in Figure 2.1, in which around 400 events are represented with magnitudes ranging between 4.0 and 8.0 and with depths with values varying between 100 km and 500 km.

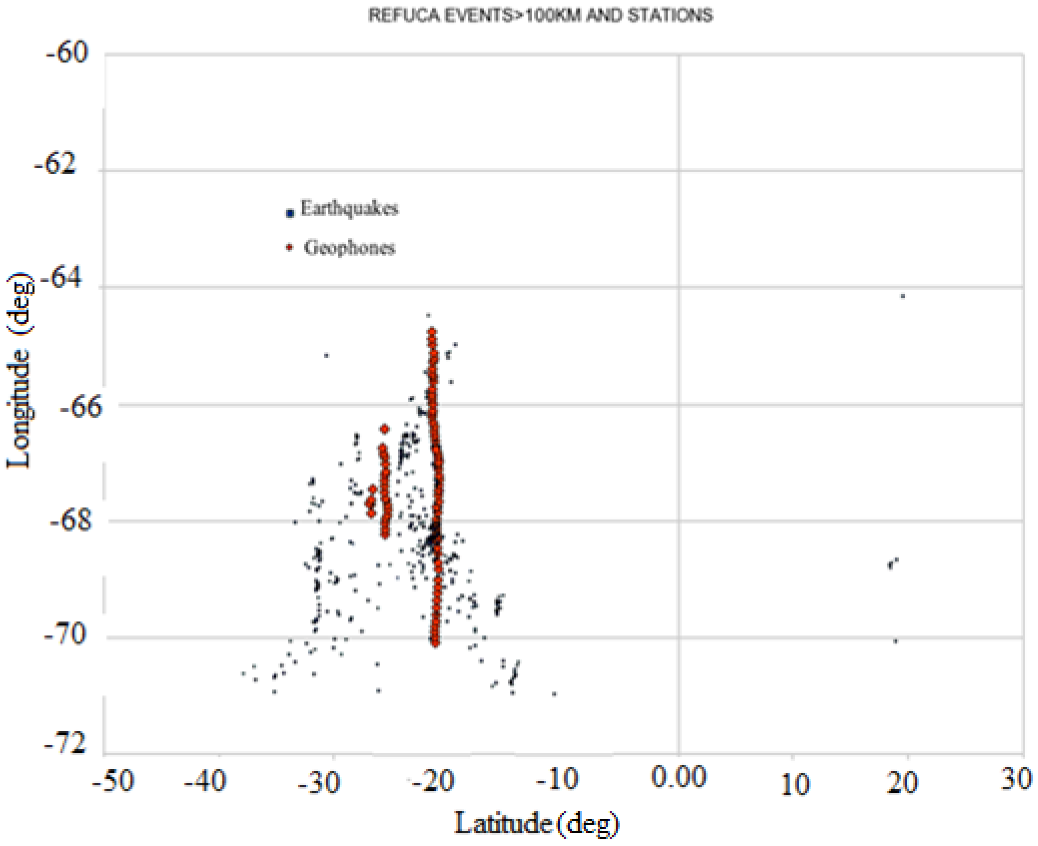

Figure 2.1 Complete set of earthquakes whose depths are more than 100 km. More than 400 events are displayed. The final subsets of earthquakes used are summarised in Table 2.1.

The final twenty-nine (29) events selected are shown in Table 2.1. All of them were situated below the Moho, with depths varying between 100 km and 500 km and with magnitudes varying between 4.4 and 5.4.

dd/mm/yy:hh:mm:ss	Lat. (°)	Lon. (°)	Depth (km)	Mag	Type	Catalog	Region
26/05/2002 09:19:23	-20.0019	-68.6439	136.00	5.3	ML	ISCCD	ARG
26/08/2002 13:53:08	-21.2519	-68.3129	110.40	5.1	ML	ISCCD	CHI
29/08/2002 02:28:22	-20.4959	-68.2759	131.00	5.2	MW	ISCCD	CHI
25/10/2002 11:48:59	-20.9069	-68.2279	109.20	5.2	MB	ISCCD	CHI
12/11/2002 13:06:40	-20.1178	-68.7134	114.00	5.3	MB	ISCCD	ARG
18/11/2002 22:38:33	-21.1709	-67.0859	196.60	5.2	MB	ISCCD	ARG
19/11/2002 12:56:43	-20.9798	-67.3592	186.00	5.2	MB	ISCCD	CHI
23/11/2002 13:33:31	-21.6009	-70.0169	262.20	5.0	ML	ISCCD	ARG
29/11/2002 17:54:10	-20.3259	-68.6001	100.00	5.3	MB	ISCCD	CHI
13/12/2002 19:25:42	-21.9899	-68.9799	123.50	5.0	MB1	ISCCD	PER
14/12/2002 01:18:00	-20.8079	-66.732	257.70	5.2	MB	ISCCD	CHI
20/12/2002 08:30:00	-20.9599	-67.9419	131.70	5.2	MB	ISCCD	CHI
30/12/2002 07:28:37	-21.1999	-67.2999	199.00	5.2	MW	MHDF	CHI
05/01/2003 09:25:55	-21.537	-68.289	126.10	5.1	MB	ISCCD	ARG
07/01/2003 17:27:12	-21.233	-68.673	111.10	5.2	MD	ISCCD	ARG
07/01/2003 17:40:38	-20.263	-68.694	124.90	5.3	MB	ISCCD	PER
09/01/2003 01:45:01	-20.991	-68.022	131.90	5.2	MB	ISCCD	PER
14/02/2003 03:46:02	-21.1889	-67.7049	156.80	5.2	MW	ISCCD	CHI
13/07/2003 07:25:51	-21.3669	-68.0501	128.20	5.1	MB	ISCCD	ARG
27/07/2003 11:41:27	-20.0499	-65.1899	350.60	5.3	ML	ISCCD	CHI
29/07/2003 14:02:51	-21.6999	-68.3599	149.30	5.0	MB	ISCCD	ARG
05/08/2003 09:04:44	-21.9739	-65.8831	214.20	5.0	ML	ISCCD	ARG
09/08/2003 10:25:56	-21.2219	-67.8329	196.40	5.2	MB	ISCCD	CHI
17/09/2003 21:34:52	-20.9419	-68.3919	152.00	5.2	MB	ISCCD	CHI
03/10/2003 11:54:09	-21.8897	-68.3102	121.80	5.0	MS	ISCCD	CHI
23/05/2003 00:50:13	-21.182	-66.6349	223.3	5.2	ML	ISCCD	ARG
12/12/2003 06:57:47	-21.3499	-68.4899	139.30	5.1	ML	ISCCD	CHI
27/12/2003 10:21:36	-20.5029	-68.9039	117.10	5.2	MB	ISCCD	PER
13/01/2004 21:54:24	-21.7589	-64.474	532.30	5.0	MB	ISCCD	ARG

Table 2.1 List of all events used for inter-source interferometry in this research.

Location of events in Table 2.1 was taken from the international seismologic catalogue (ISC). Usual velocity models used for this purpose are the IASP91 and the AK135, both of which are 1D velocity models. The major drawback of 1D velocity models is that they do not account for lateral velocity variations and in complex areas with strong Moho topography the application is limited (Hunsen *et al.*, 2003).

Thurber (1992) gives a classic example of an artefact introduced when using a 1D velocity model which consists of a lateral shift in the location of an earthquake due to an unmodelled lateral velocity contrast across a fault. In general, there are several sources of errors when locating an earthquake. For example, Husen and Hardebeck (2010) classify uncertainties in earthquake locations as measurement errors of seismic arrival times, modelling of calculated travel times and the nonlinearity of the earthquake location problem.

As explained by Husen and Hardebeck in general, the location uncertainty of events in a global catalogue such as the ISC, is of the order of 10 km horizontally and 25 km vertically, meaning that arrival time errors will be of the order of 3s, which needs to be accounted for when comparing arrival times between interferometry and ray tracing.

In order for the reader to obtain an understanding of the spatial distribution of the geometrical variables involved in this research, Figures 2.2, 2.3 and 2.4 present different 2D projections of the 3D geometry, in which the subducting slab, the chosen earthquakes and the geophones at the surface are shown.

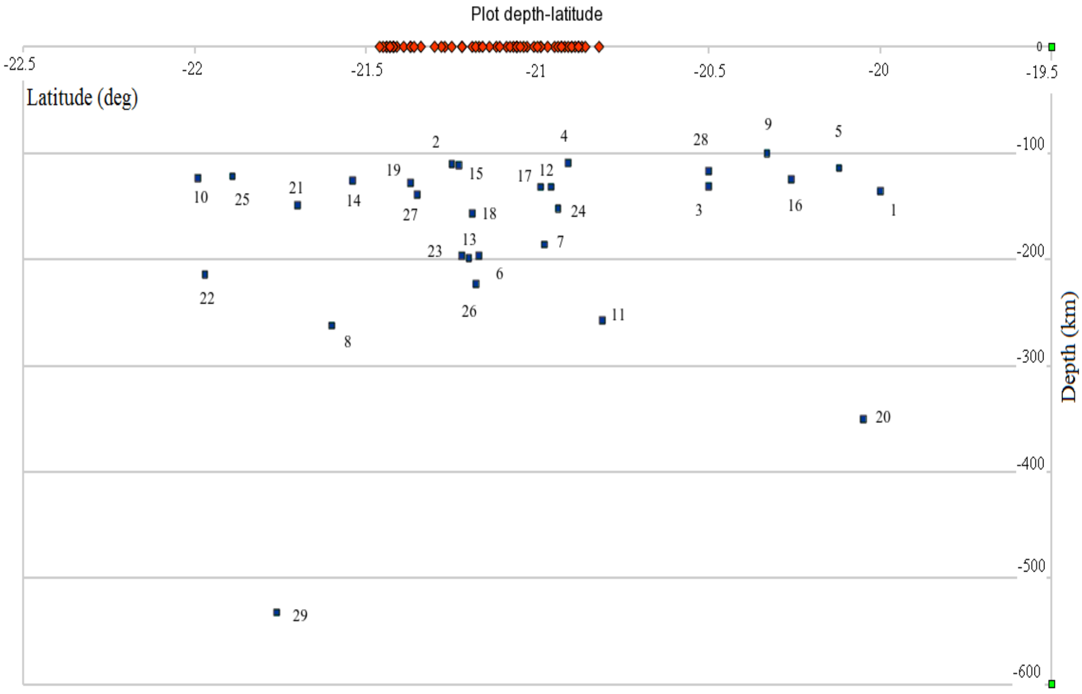

Figure 2.2 A projection plot, in 2D, of the 3D arrangements of earthquakes and geophones used in this research, showing depth versus latitude.

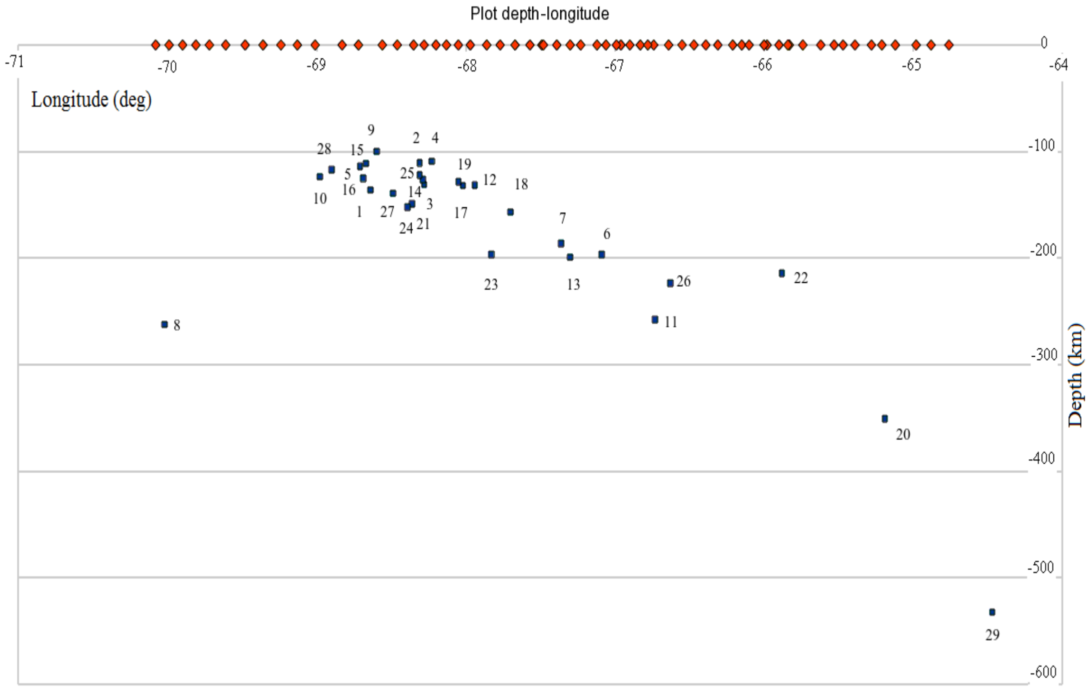

Figure 2.3 A projection plot, in 2D, of the 3D arrangements of the earthquakes and geophones used in this research, showing depth versus longitude.

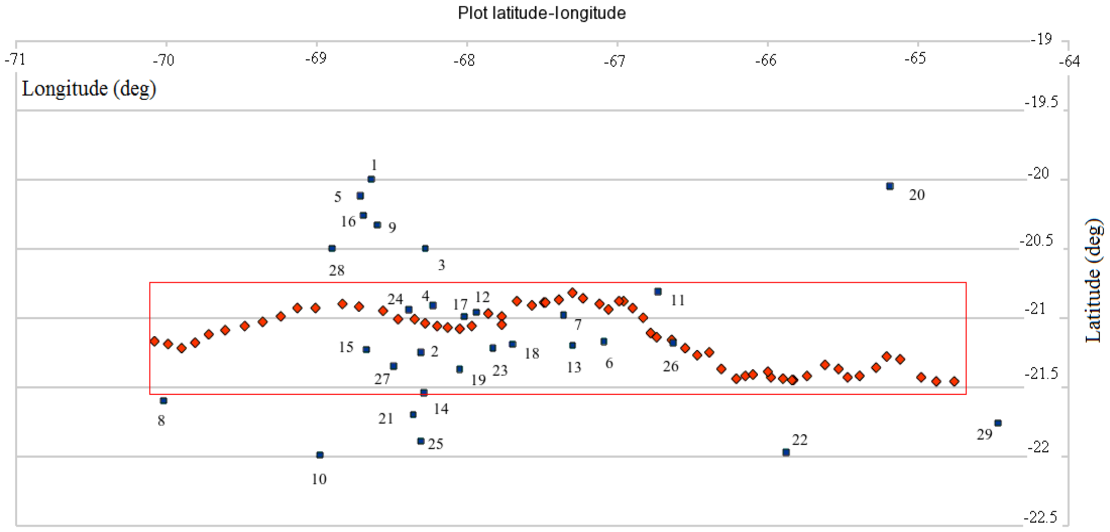

Figure 2.4 A projection plot, in 2D, of the 3D arrangements of earthquakes and geophones used in this research, showing latitude versus longitude. Red rectangle shows that the north profile (RF) is not a perfect right line.

2.4 Method

Data used in this research for cross-correlation purposes has been windowed, i.e. only a small portion (window -5, 15 s around the picked time) of the arrival has been preserved, for P arrivals only, and to suppress edge effects on the wavelets a hamming taper of 0.05 s width has been applied. This implies that the results obtained contained no effects relating to long-range coda waves.

Figure 2.5 shows the steps taken to select the part of the signal that will be used in the different cases for interferometric calculations: a) shows the raw data; in b) an arrival is picked - in this case a P arrival. Picking of arrivals was undertaken automatically and verified by visual inspection quality controls. Only in zones where arrivals were not clear was picking undertaken by hand; c) once the arrival was picked we could define the length of the window to be used. Again, the length of the window used can be chosen automatically. For every case several tests were conducted in order to choose the ideal length, e.g. in the case of a P coda wave, the ideal length resulted in 10s; d) shows the application of a taper filter, in order to smooth out changes at the end of the signal that has been cut. The parameters of the taper were chosen such that only the final part of the coda was affected. This was done in order to keep signal with the least modifications possible; finally, e) shows a zoom of the signal to be used after all manipulation and filtering.

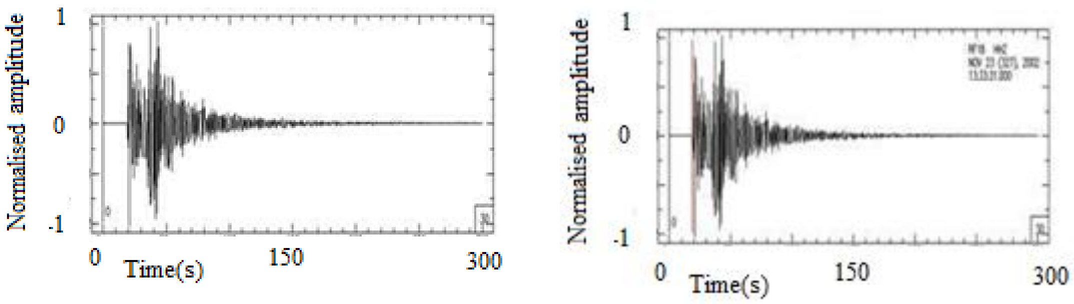

a) Raw data

b) Pick of an arrival, in this case a P arrival

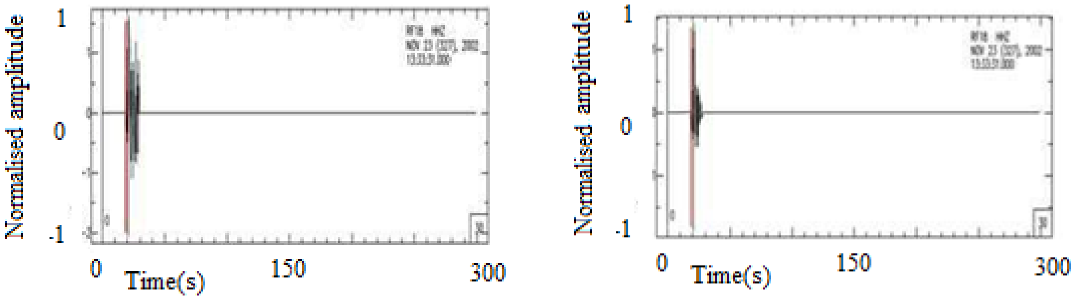

c) Cutting off the signal

d) Application of a taper filter

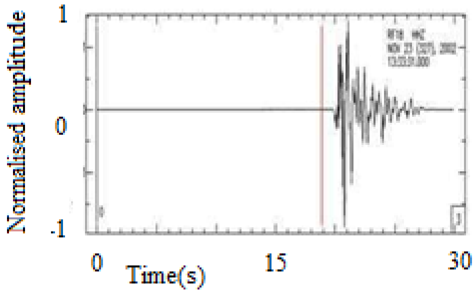

e) Zoom of signal in d

Figure 2.5 Steps taken to isolate coda waves. Processing steps include picking P or S arrivals, isolating coda P or S and the application of a taper filter in order to smooth the tail of the signal.

This time window technique has been used previously in other research works that were based on inter-receiver interferometry (Bakulin and Calvert, 2006; Bakulin *et al.*, 2007, 2008; Van Der Neut and Bakulin 2009). Also, a weighting process was assigned to the summation of the cross-correlation functions, with the more important contribution originating from the geophones situated along the extension of the lines connecting the two earthquakes with the geophones at the surface, and slowly decreasing towards both extremes of that line, as can be seen in Figure 2.6.

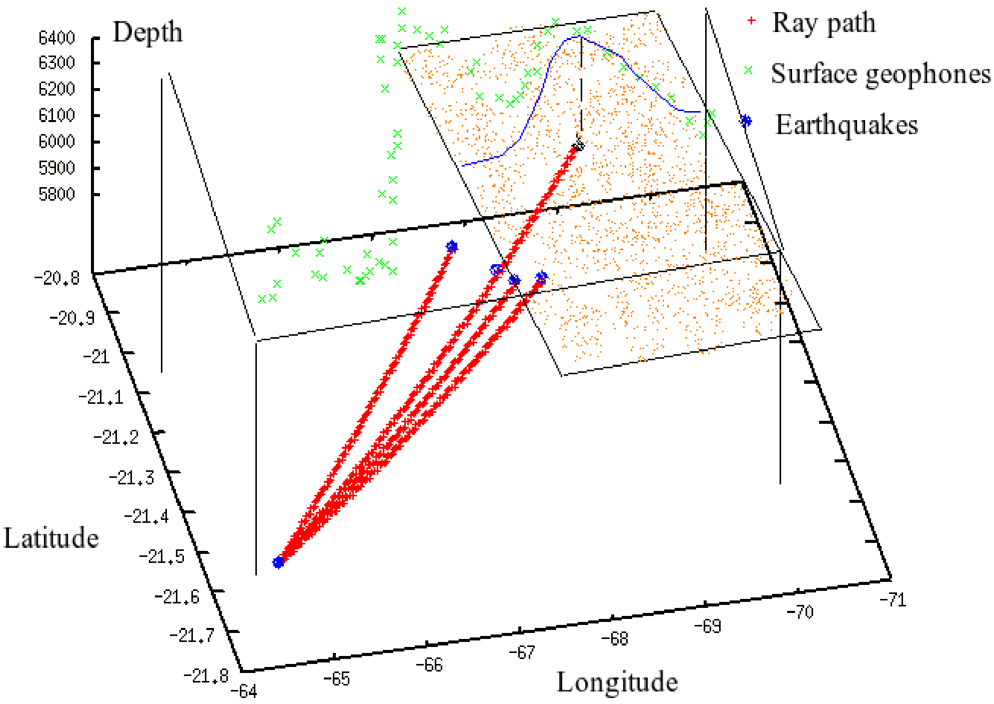

Figure 2.6 The geometrical configuration showing in a schematic way the weighting procedure, based on the stations closest to the prolongation of the ray path between the two given sources. Weighting is such that: it reaches a maximum in the centre of the ray path and decreases slowly to 0 at the edges of the Fresnel zone. In this diagram red lines represent the ray tracing path calculated by the ray tracing software from Grumberg *et al.* (2004), lines are calculated in discrete time intervals, so they may look as low resolution in the figure. The brown colour plane represents the surface of the earth. The depth scale represents the radius of the earth with 6400 km representing the surface of the earth (this is the format used by the ray tracing software). The box is drawn in order to facilitate to the reader the 3D visualisation of the geometrical configuration. Blue dots represent actual earthquakes and, finally, the blue line is the schematic representation of the influence of the geophones (weighted summed) at the surface when the cross-correlations are summed in order to calculate the inter-source Green´s functions.

The procedure of choosing a pair of earthquakes within the range of possibilities was based on their location as the idea was to examine the subducting slab. So, position is the parameter that gave the initial clue for consideration. Then, the other point taken into account in order to select a couple of given earthquakes was the prolongation of the ray path that joined them to the array of receivers on the surface (see Figure 2.6). If extrapolation of that path laid in the square shown in Figure 2.4, the earthquakes were picked for study, in an analogous way the earthquakes were chosen in the work of Tonegawa *et al.* (2010)

As an example of this extrapolation procedure, in Figure 2.7 the extrapolated results for a given couple of earthquakes are shown. In this figure, extrapolation was carried out to a point in the surface that lay within the allowed rectangular area of this figure. For ease of visualisation, only one of the many possible ray paths has been extrapolated.

In principle, any pair of sources can be used to retrieve body waves travelling between those pair of sources. As this chapter analysed 29 events, the number of possible pairs is too big to account for all of them. In this chapter, a representative example of pairs will be presented by fixing two earthquakes (08 and 11) and calculating the possible pairs to the rest of events. That means this chapter presents about 25 possible pairs of sources. Events 08 and 11 were chosen because they are deeper than the other earthquakes. The idea is to have waves travelling from below and illuminating the structures of interest when reaching the shallower sources, and at the same time, to have geophones at the surface within the stationary phase region of each pair of sources.

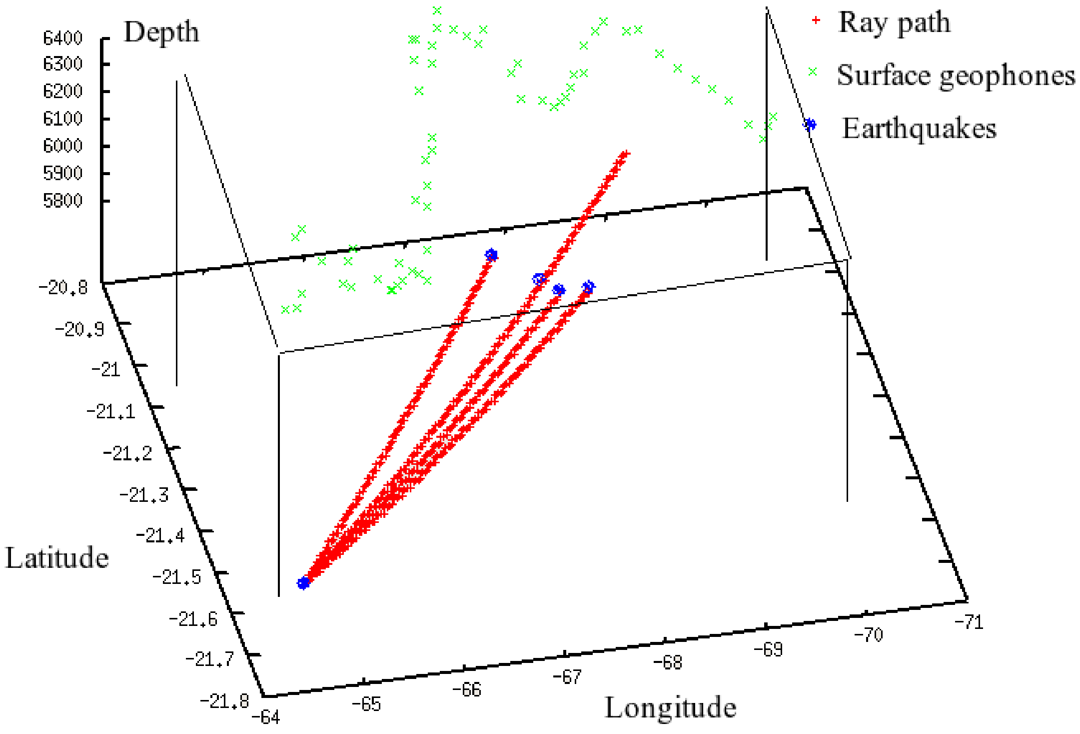

Figure 2.7 Example of extrapolation of an inter-earthquake ray path. For this case, only one path has been extrapolated. In blue, the different events pairs are depicted. In red is the ray path, as calculated using the ray-tracing package of Grumberg *et al.* (2004).

2.4.1 Ray tracing software used

The ray tracing code used in this research for calculation of the Fresnel zones was based on the IASP91 velocity model. The IASP91 model is a parameterised velocity model of global seismic properties for an average earth of radius 6371 km. The IASP91 velocity model is considered to be a standard representation of the Earth’s structure by the international association of seismology and physics of the Earth interior (IASPEI). The IASP91 velocity model is represented in Figure 2.8.

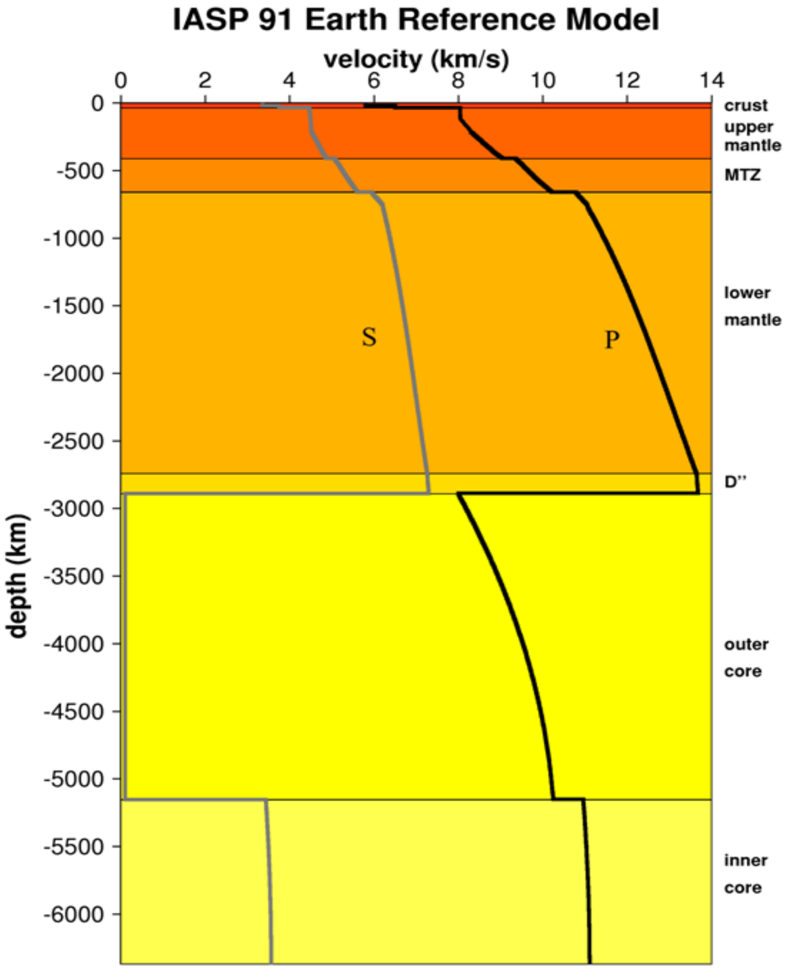

Figure 2.8 The IASP91 velocity model. Taken and adapted from http://commons.wikimedia.org/wiki/File:IASP91.png

The ray-tracing algorithm was developed by Grumberg *et al.* (2004) and based on the Snell-Descartes law in spherical geometry. This ray tracing code was chosen for the current research based on its portability, ease of installation, documentation and ability to represent different wave phases (as explained by the IASPEI standard seismic phase list, for example, PP, PS, SS, etc). The ray tracing code allows the user to choose the phase to be traced, as well as the coordinates of sources and receivers.

In order to calculate the theoretical arrival times, the 2D modelling subroutine "FDMOD2" from SU software was used together with the 2D velocity model from Heit (2005) show in Figure 2.20. The aforementioned velocity model was digitised and put in an appropriate format to be used by the SU routines. The digitised model is shown in Figure 2.9.

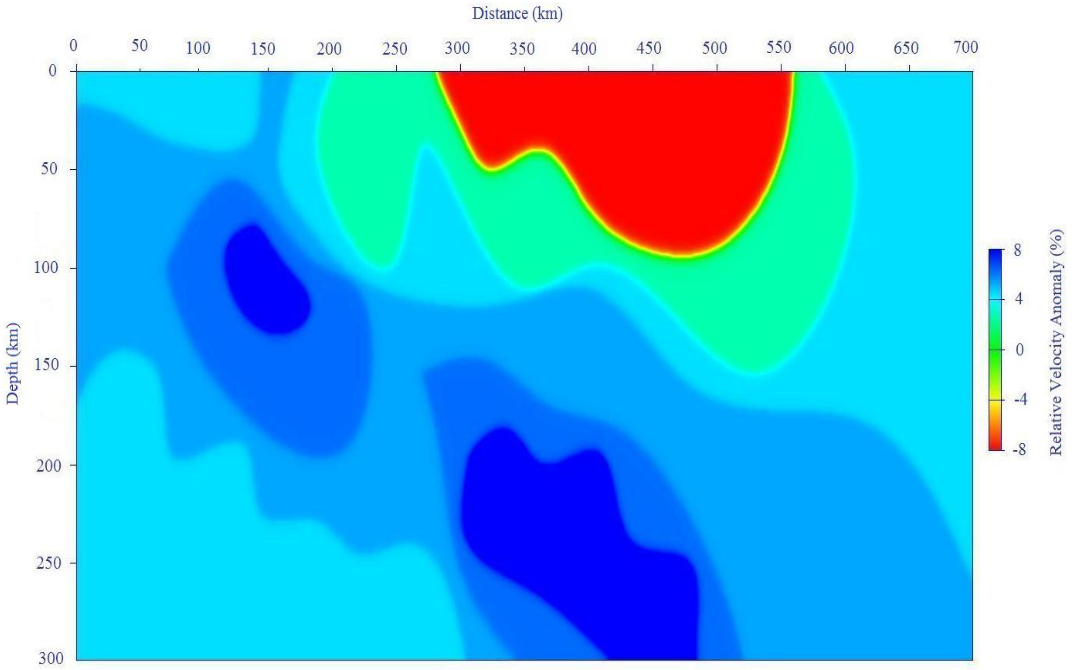

Figure 2.9 Digitised 2D velocity model used for 2D modelling with the routine FDMOD2

2.5 Results

In this section, only arrival times from Green´s functions are used for comparison with the synthetic data because the ray tracing code employed only calculates times and ray paths and also because the interferometric algorithm used does not account for attenuation.

As an example, in this section the cross-correlation functions that will be summed in order to calculate the inter-source Green´s functions are presented. Figures 2.10-2.13 show plots of the cross-correlation functions for events 08 and 11 to events 04, 12, 17 and 24, respectively.

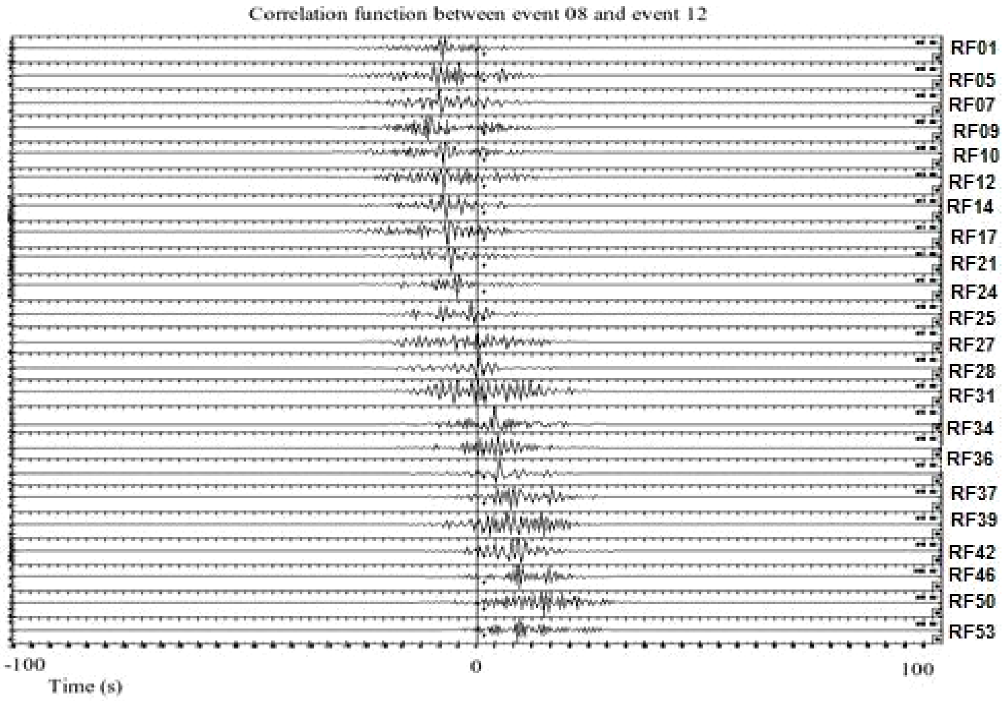

Figure 2.10 Cross-correlation functions between event 08 and event 12.On the vertical axis the cross-correlation for every pair of events considered.

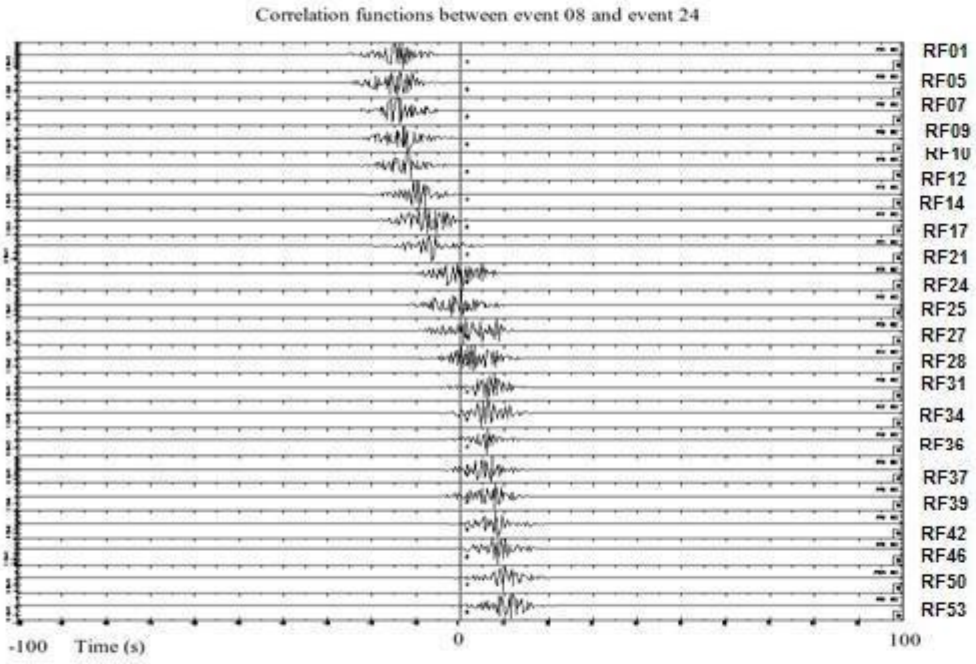

Figure 2.11 Cross-correlation functions between event 08 and event 24. On vertical axis the cross-correlation amplitude for every pair of events considered.

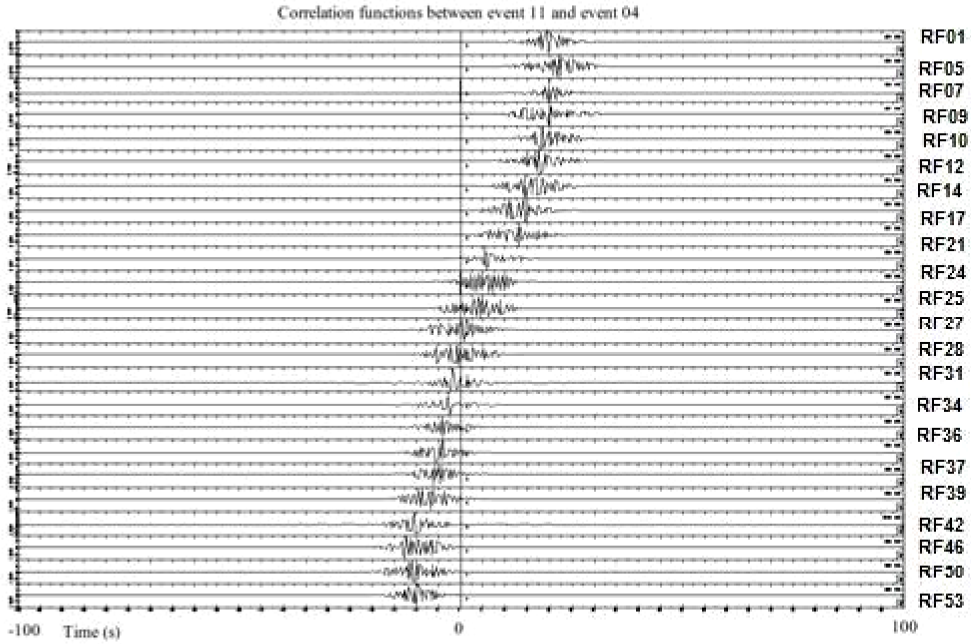

Figure 2.12 Cross-correlation functions between event 11 and event 04. On vertical axis the cross-correlation amplitude for every pair of events considered.

.

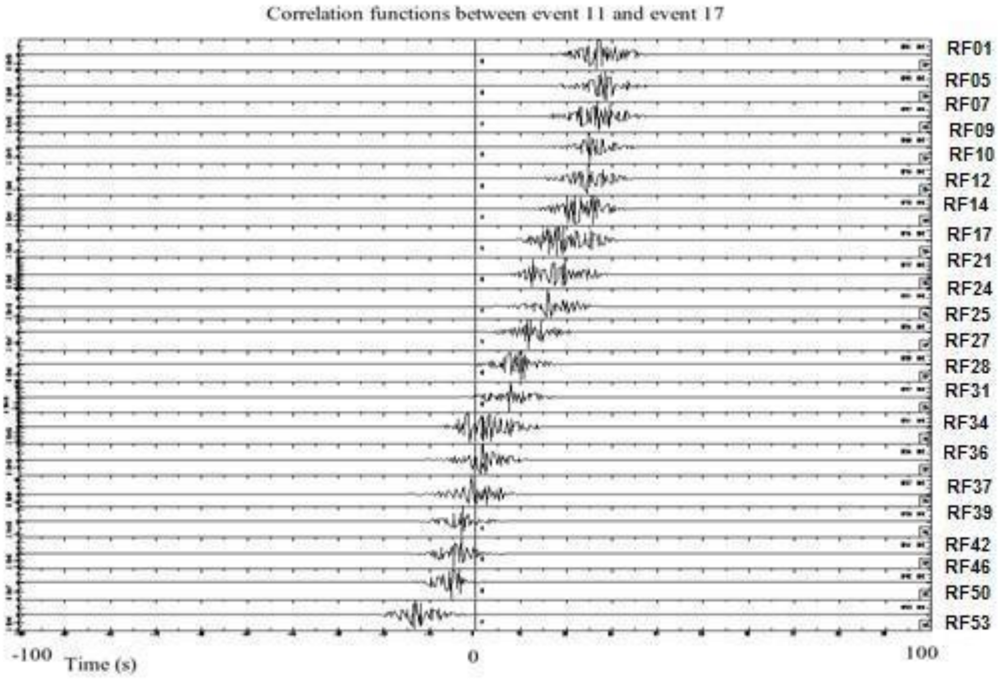

Figure 2.13 Cross-correlation functions between event 11 and event 17. On vertical axis the cross-correlation amplitude for every pair of events considered.

Figures 2.10 to 2.13 show that cross-correlation functions are well behaved functions, with no spikes or spurious events introduced by long range coda waves. In Figures 2.14 and 2.15, the inter-source Green´s functions obtained for the cases considered in this section are presented.

The following two cases will be considered: a) Inter-source Green´s functions between event 8 and the rest of events considered and b) Inter-source Green´s functions between event 11 and the rest of events considered. Additionally, and in order to assess the method, the predicted arrival times (calculated by the 2D ray tracing code) and the arrival times obtained by interferometry will be compared and plotted in those figures. Red boxes are drawn where the theoretical arrival times calculated from the 2D ray tracing are predicted and blue boxes will be drawn where arrivals calculated by interferometry are expected. In all boxes, single arrival times are centred in the middle of the box.

Referring back to Figures 2.2, 2.3 and 2.4, it can be noted that the different inter-source pairs considered in this chapter are located along the area considered (northern profile RF) so, in Figures 2.14, and 2.15, we have the possibility of comparing arrivals time in different zones along the northern profile. The analysis of the difference between the theoretical arrival time and the time obtained from interferometry proves that velocities are slow in the middle of the line and fast in the eastern part - this result is in agreement with the work of Wölbern *et al.* (2009).

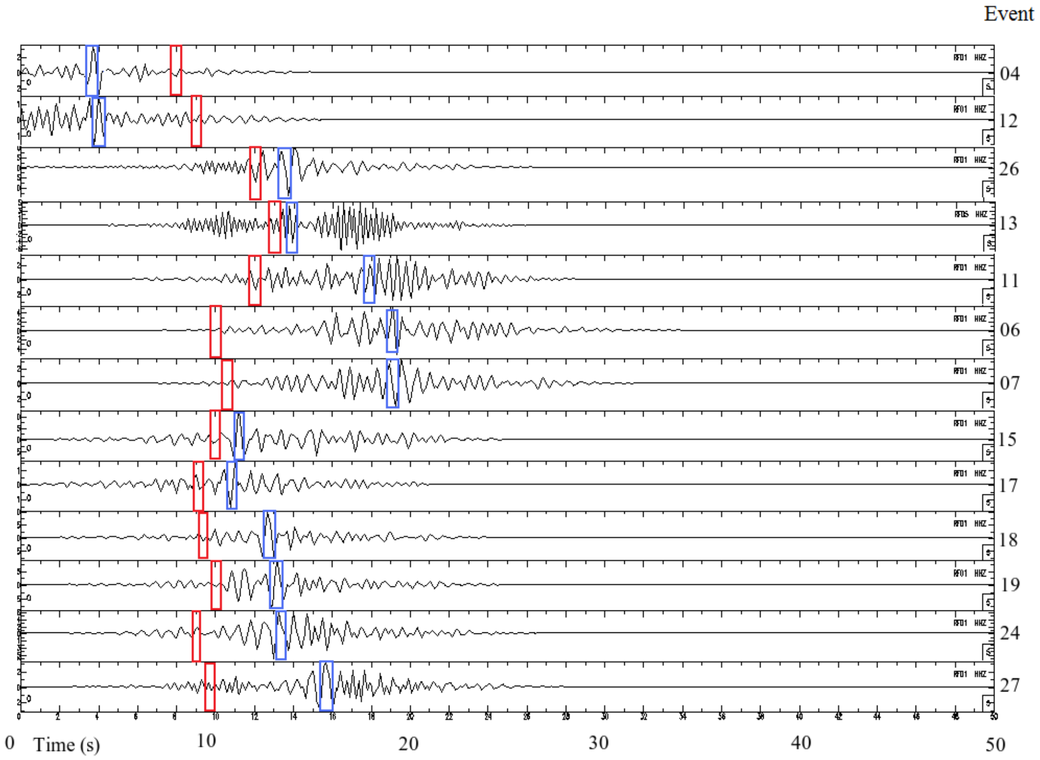

Figure 2.14 Inter-source Green's function estimates for event 08. The theoretical arrival times calculated using the 2D ray tracing package from SU are highlighted in red. Expected arrival times calculated from interferometry are highlighted in blue.

Figure 2.14 shows that some of the arrival times calculated using interferometry were faster than the predicted time, while others were slower. In the next section, the implications of this difference will be discussed.

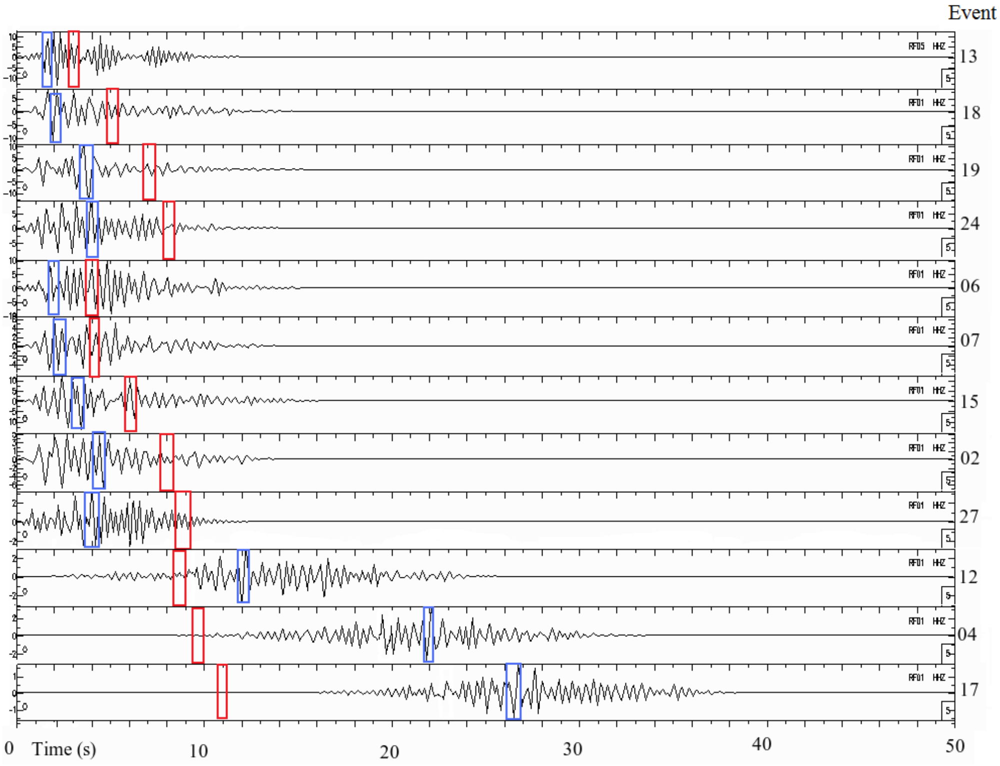

Figure 2.15 Inter-source Green's function estimates for event 11. The theoretical arrival times calculated using the 2D ray tracing package from SU are highlighted in red. Expected arrival times calculated from interferometry are highlighted in blue.

Figure 2.14 gives information regarding the velocity structure of the subduction slab, to see why refer back to Figure 2.3 where it can be seen that earthquake 8 is situated at a depth between 200 and300 km, which is below the other earthquakes considered here. Therefore, inter-source waves extracted will travel through the structure of the subducting slab, revealing velocity features of interest. Also, in this figure, it is clear that the pattern of earthquakes follows the structure of the subducting slab with more frequent earthquakes near the surface. The information extracted by the method of inter-source interferometry will provide useful material which will be discussed and analysed in the next section.

For the case in Figure 2.15, arrival times predicted by interferometry were earlier than the theoretical predicted times for the zone through which the ray was travelling. This result is in agreement with the high velocity body described by Heit (2005).

2.6 Discussion

Consider the first case from the results section (section 2.5) in which event 08 was chosen such that inter-source waves were calculated between event 08 and the rest of events shown in Figure 2.16. The results presented in this first case come from considering event 08 as the source and calculating the arrivals times to the rest of virtual receivers as show in Figure 2.16.

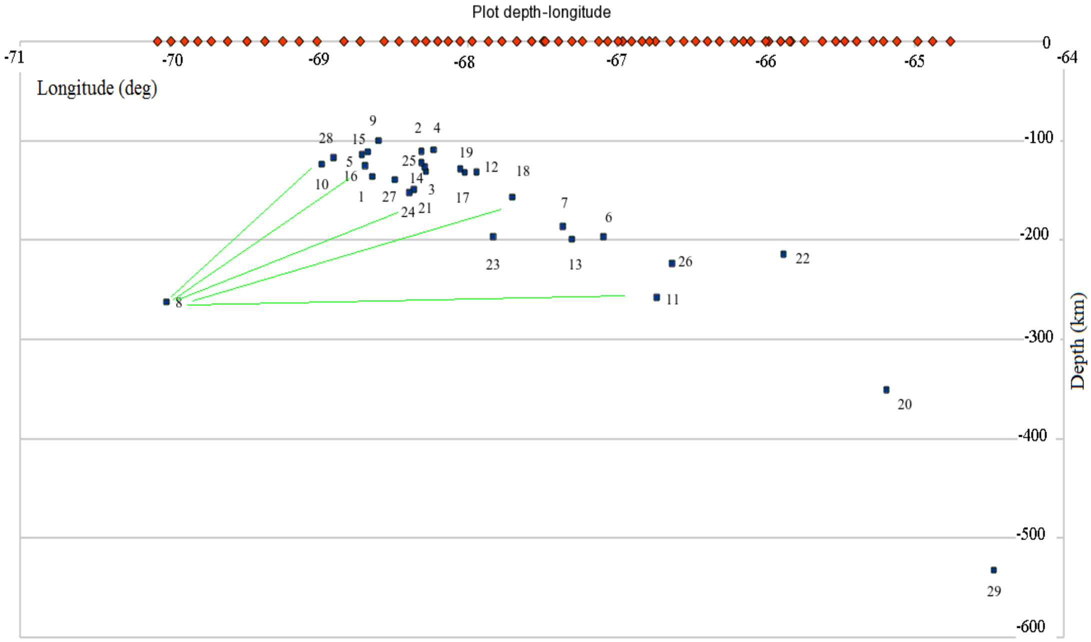

Figure 2.16 Event 08 is acting as a source, the rest of the sources as virtual sensors. Event 08 was chosen because of its relative position compared to the rest of the sources and because it can illuminate the other sources from one side below.

Figure 2.14 constitutes new information regarding the zone under consideration. It reveals that the velocity of the waves calculated from interferometry was faster near to events 12 and 4 because arrival times are earlier than the theoretical expected times (red squares). Events 2 and 4 were near 100 km in depth. This is at the frontier of the ALVZ (Altiplano low velocity zone) which indicates either that it may be the start of a high velocity zone, or that the ALVZ frontier is shallower than was originally thought. For events 6, 7 and 11, situated at a depth of around 200 km and in the middle of the RF line, the velocities were slower as can be appreciated from Figure 2.14 in which arrival times are later than the theoretical times predicted by the 2D ray tracing algorithm.

Now, consider Figure 2.15 from the results section. Again, the idea for this second example is to choose one earthquake whose position in relation to the rest of earthquakes makes the rays illuminate the different structures of interest. In Figure 2.17, the event 11 and the relative position of it compared to the position of the other earthquakes can be seen.

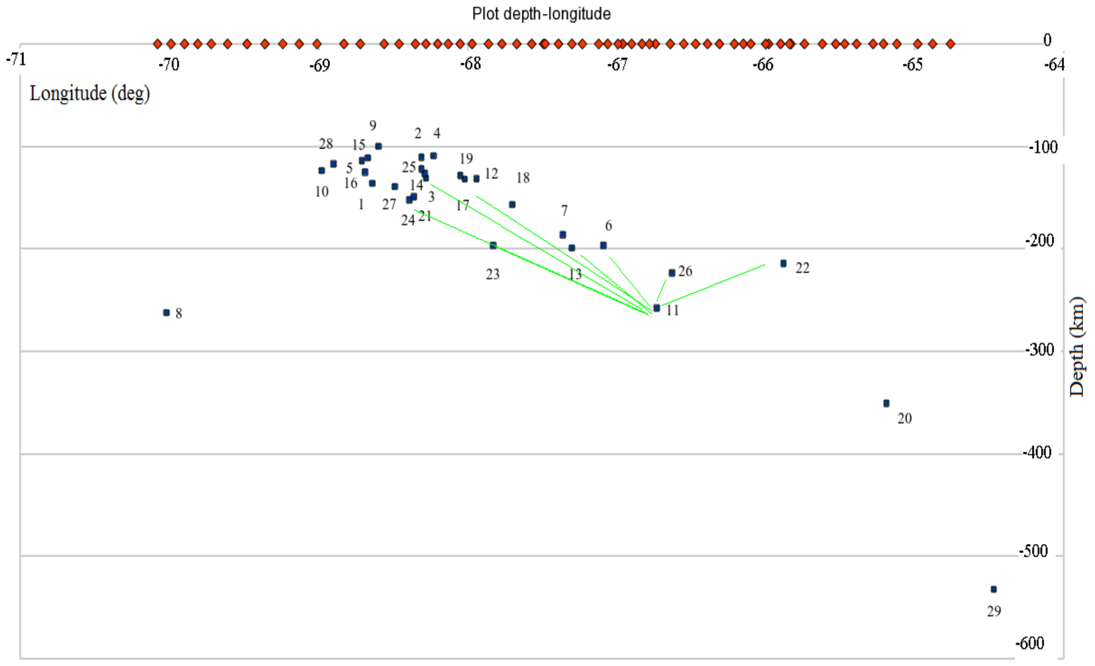

Figure 2.17 Event 11 is acting as a source, the rest of sources as virtual sensors. Event 11 was chosen because of its relative position compared to the rest of sources and because it can illuminate the other sources from one side below.

From both Figure 2.15 and Figure 2.18, it can be seen that Heit (2005) described a high velocity body for depth varying between 100-300 km for longitudes between 68° W and 66° W. In the case shown here, all virtual receivers have faster arrivals than those predicted from the 2D ray-tracing algorithm that uses the Heit (2005) velocity model. This fact can be interpreted as the zone of partial melting affecting the interferometric calculation.

In Figure 2.15, even though arrivals are dispersed it could be said that, in general, the difference between predicted and calculated time, on average, was around 4 seconds. As previous discussion mentions, velocity structure varies in a complex way depending on the depth considered. Those possible structures will affect the travel time and the trajectories followed by the rays. So, from previous results it is clear that it is a better idea to have the source under consideration near to the other sources that will act as virtual receivers in the case of complex structures, such as those studied here.

It is a good indication of the interferometry methodology that results from the work of Heit (2005) are replicated here. More specifically, in Figure 2.18 taken from the work of Heit (2005), it can be appreciated that for depths between 200 and 300 km, and for longitudes between 68° W and 66° W there is a high velocity zone. This high velocity zone, as was pointed out in the results section, is in agreement with results inferred from Figure 2.15, in which arrival times were faster than the ones calculated from use of the Heit (2005) velocity model. Results from seismic interferometry actually give a difference in velocity that is higher than that calculated by Heit (2005), indicating that the method is working at least in a qualitative way. Also, remember that the data used here is not the best possible because of problems involved in its acquisition. Essentially, what this difference in velocities indicates is that errors are introduced by the method, by the earthquake location methodology, and by the digitalisation of the velocity model.

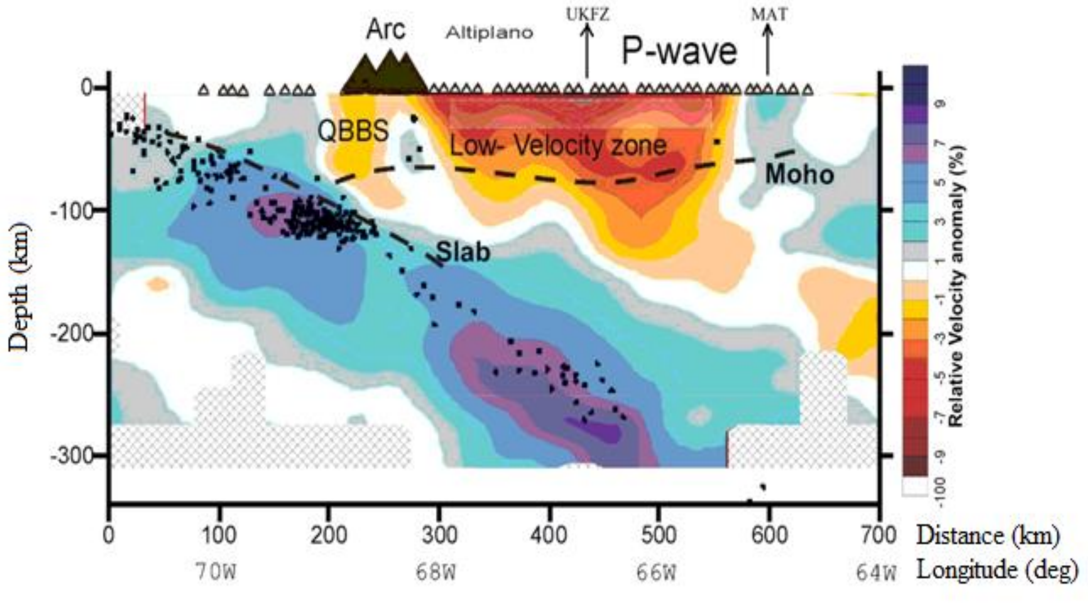

Figure 2.18 Taken and adapted from Heit (2005). P wave result of the receiver functions application. In the figure QBBS: Quebrada Blanca bright spot. UKFZ: Uyuni-kenayami Fault zone. MAT: main Andean Thrust. Low velocity zone which is the same ALVZ (Altiplano low velocity zone) mentioned in several research works of the Altiplano.

The time differences of arrivals obtained from seismic interferometry were strongly dependent on the path and the final destination of the waves travelling through the medium. Moreover, Figures 2.19 and 2.20, taken from the work of Heit (2005) and which represent plan views of the Altiplano zone, show the complexity of the area. From these figures, it can be appreciated that, depending on the depth, different configurations of velocities arise. For example, to the eastern part of the Altiplano and for a depth of 110 km, there is a low velocity zone, which progressively transforms into a high velocity zone at greater depths (see depths 170, 230 and 290 km respectively). The same example applies for the western region that goes from a high velocity zone into a low velocity zone in progressively deeper views.

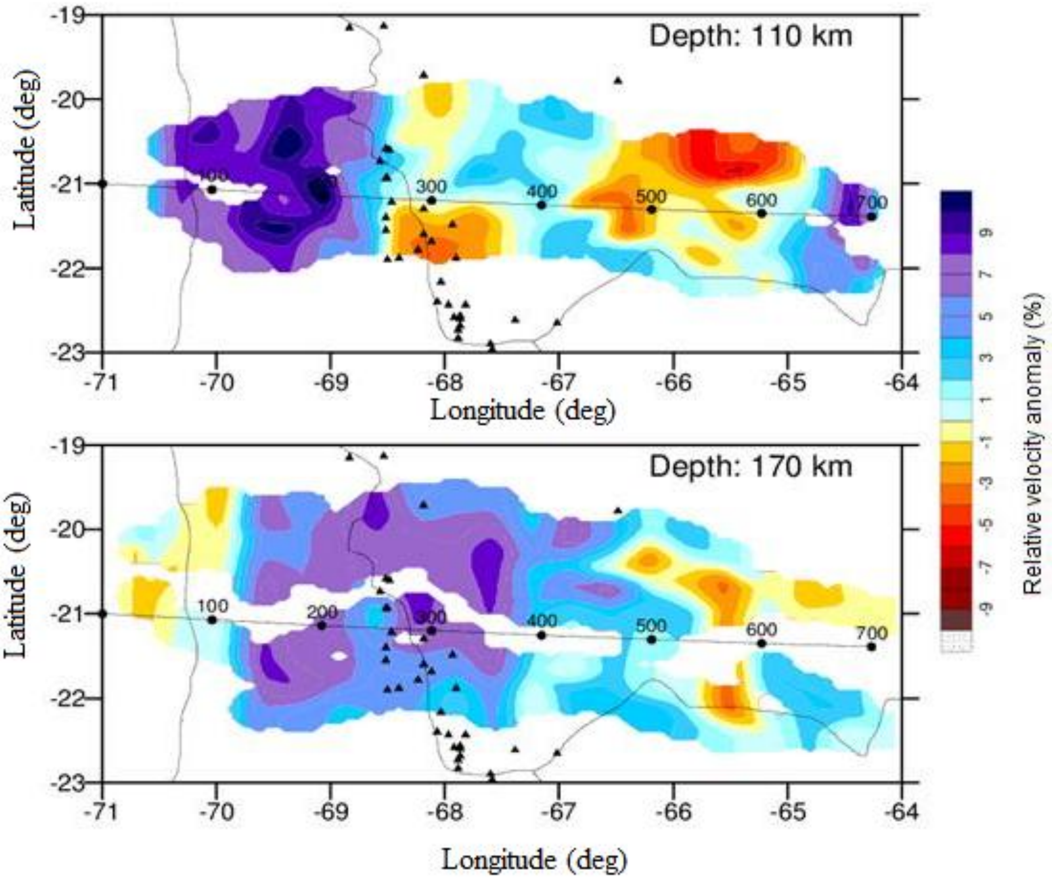

Figure 2.19 Taken and adapted from Heit (2005). Horizontal P wave velocity Altiplano 21°S. Real data inversion. Depths 110 km (top) and 170 km (bottom)

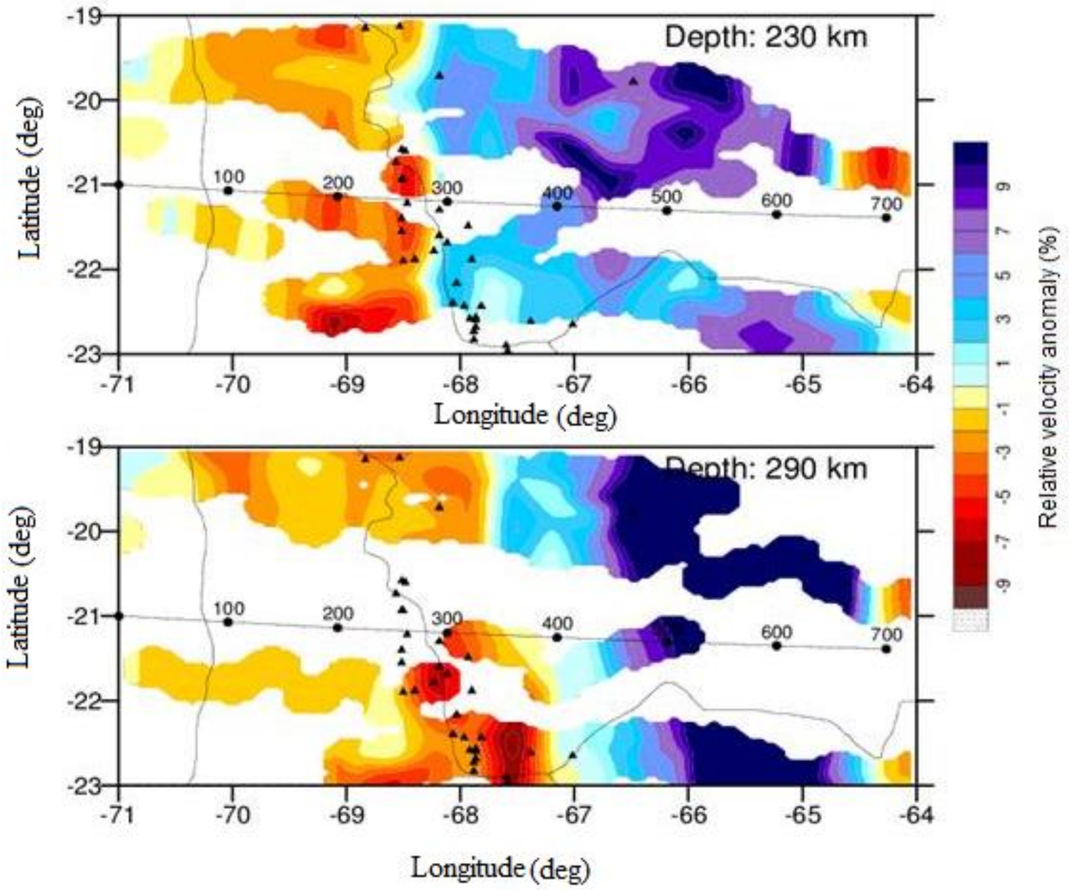

Figure 2.20. Taken and adapted from Heit (2005). Horizontal section P waves Altiplano 21° S. Real data inversion. Depths 230 km (top) and 290 km (bottom)

Comparing the new information given by the interferometric method with Figures 2.19 and 2.20, it can be expected that the ray path is affected by the complexity of the medium. In this case, waves travel through zones of high and low seismic velocities, which have an overall effect on the final result. So, in order to study a complex zone it is better that the separation between sources should be the minimum possible, in order to guarantee the accuracy of the interferometric calculations.

One important point to take into consideration is that not all couples of events were useful for retrieving waves travelling between earthquakes because the path considered could be such that it is not present in the original recorded information and can lead to the introduction of spurious signals. This is the reason why only events 08 and 11 were selected in order to look for waves travelling between these two sources to the rest of them. The reason for that was because these sources were deeper than the rest and also because the pairs formed by this configuration fulfilled the geometrical requirements of stationary phase explained in the methodology section.

Tonegawa *et al.* (2010) found that, in order to extract information about the travel time between two sources, it was necessary to take into account the size of the stationary phase region at the surface as well as the distribution of the sources. The size of the stationary phase region was affected by several factors, such as the type of waves considered (P or S). The size of stationary phase is also affected by the frequency content of the wave travelling in the medium.

For example, in order to define the geophones that will be used for seismic interferometry (that lies in the stationary zone) Tonegawa *et al.* (2010) take the area of stationary phase, at the surface, as the size of the first Fresnel zone, which in essence is defined as $\frac{1}{2f_0}$ where f_o is the dominant frequency of the propagating wave.

A schematic representation of the geometry of the Fresnel zone is presented in Figure 2.21. In this figure, T1 and T2 are the times taken by the P wave from events 01 and 02 to get to the geophones at the surface. The spatial size can be calculated by using the Fresnel zone criteria $\frac{1}{2f_0}$ with the time difference T2–T1. For example, for a dominant frequency of 1Hz the Fresnel zone is 0.5s meaning the time difference between event 01 and 02 has to be less than this.

For calculating the time difference between event 01 and 02 the ray tracing code of Grumberg *et al.* (2004) was used. This approximation of the Fresnel zone implies that five geophones centred at the stationary phase were used for interferometric calculations. To account for the low velocity zone near the surface, the number of geophones included is increased to two more at each side of the stationary phase.

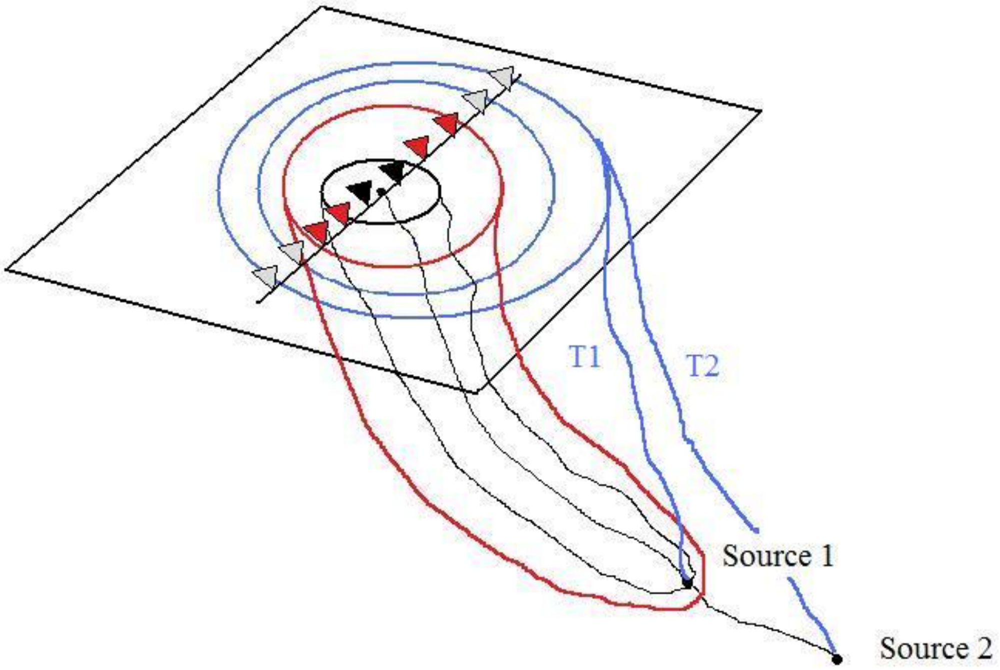

Figure 2.21 Schematic representation showing events 01 and 02, ray path travelling through the events and geophones at the surface. Red lines indicate the area of constructive interference that is equal to the first Fresnel zone given by $1/2f_0$.Black lines indicates the stationary phase zone where the time difference is << than $1/2f_0$. In practice, geophones coloured in black and red were used for interferometric calculations.

The dominant frequency, of course, will depend on the attenuation caused by the medium. For the Altiplano data, even though geophones recorded a range of frequencies from 0-100 Hz, useful frequencies were in the range 0-3.0 Hz. This range was also suggested by the work of Wölbern *et al.* (2009) based on geological characteristics such as the dominant frequency of the wavefield and to efficiently stack signals originating at dipping structures (Wölbern *et al.*, 2009).

As a final remark, an example of a typical record of an earthquake (Figure 2.22) with its first arrival picked and a taper applied will be presented. Also, a typical power spectrum is presented in Figure 2.23 but this time with no filter applied.

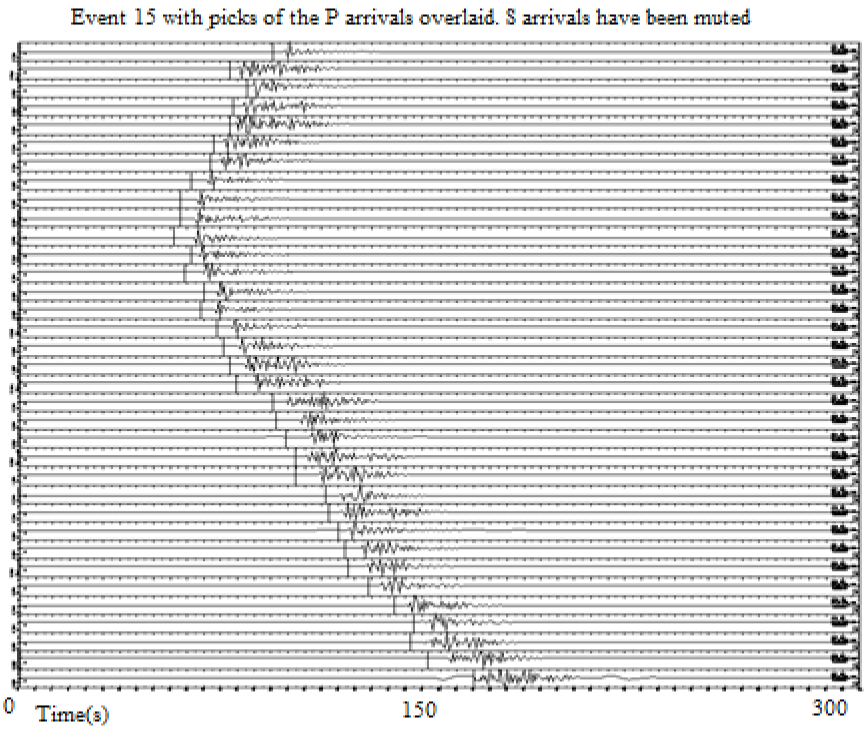

Figure 2.22 Event 15 with picks of the P arrivals overlaid. S arrivals have been muted and a taper applied in order to smooth endings.

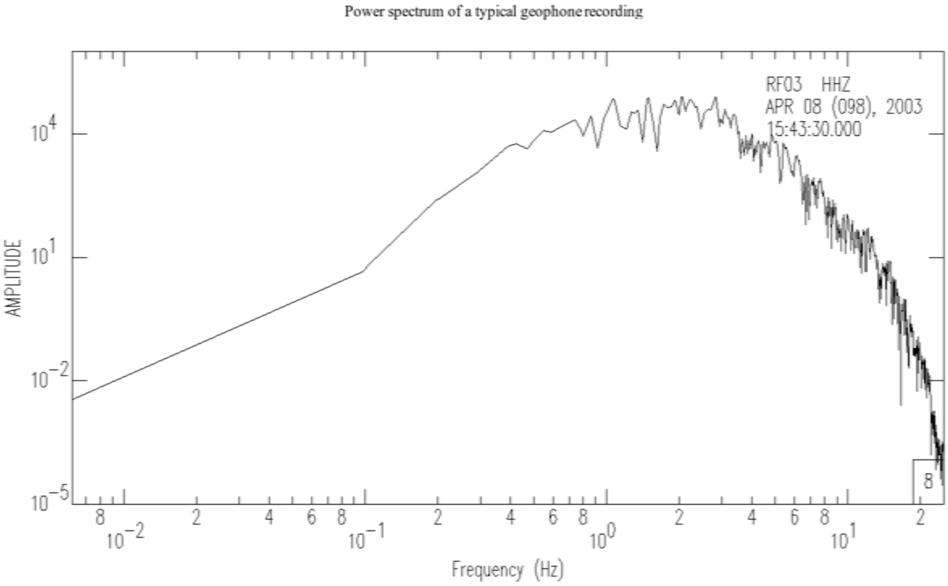

Figure 2.23 Typical power spectrums of an arbitrary event and a given geophone.

2.7 Conclusions

In this chapter, propagation of direct P waves between two sources has been derived using inter-source interferometry. As has been seen from this research, in order to better estimate the velocity structure in a complex area like that of the Altiplano, it is better practice to have events and virtual receivers situated as near as possible, to avoid distortions in the interferometric calculations.

An important factor, in order for the method to work, is the pre-processing of the data to be used. For example, in order to make the task of interpretation of the interferometric results easier, coda waves were cut and a taper filter applied as explained in this chapter. Equally important is the geometry of the sources of the ray paths followed by the waves between these sources, and of the geophones at the surface.

As was seen from the results in this chapter, the interferometric method presented in this research is in qualitative agreement with the velocity model obtained in the work of Heit (2005) which is a good direct practical indication that the method is valid and that it can be used to retrieve information from the medium. Nevertheless, interferometry does not always give good results as is the case for geophones 6, 7 and 11 in Figure 2.14 and for geophones 4 and 7 in Figure 2.15, potentially because there are more possible sources of errors (more parameters to be tuned).

As was discussed in section 2.3, expected errors in arrival times calculated by interferometry, created when locating earthquakes, is of the order of 3s. The ray tracing procedure will always have errors introduced by the algorithm used (for example, acoustic or elastic) and by the approximation of the velocity field to be modelled. Both methods are approximations and caution has to be taken when dealing with their results.

It is important to point out that there are a lot of variables (e.g., pre-processing of data, ray tracing of waves in order to choose receivers in the stationary phase region, events with small magnitude so they can be considered point sources but with enough energy to produce good results in the sense of signal to noise ratio, etc.) that have to be fine-tuned before this method is able to elicit useful results. Tuning all variables is not impossible but not always straightforward - it requires a time-consuming process of quality controls.

The above points confirm the idea that the method is only an approximation. Therefore, results have to be treated with caution and compared with result from other fields of the geosciences in order to confirm their validity.

Additional studies should take into account other phases, such as S arrivals as well as the exact influence of the source mechanism over the whole process of seismic interferometry.

As a conclusion, it can be said that the methodology requires the fine tuning of many variables, in which each variable produces its own approximation error and even though this methodology proved to work in the area, it is a better idea to use other seismic interferometry methodologies like coda waves or noise recordings which in this thesis prove to give better results as will be shown in the next chapters.

Chapter 3

BODY WAVE RETRIEVAL FROM SEISMIC CODA

3.1 Summary

While the reconstruction of surface waves from the correlation of random wavefields has been studied in detail, the reconstruction of body waves has not (Zhan, 2010). Resent work conducted on the Philippine Sea slab has developed a method for retrieving body waves using teleseismic earthquake waves. The objective of the present study is to apply that methodology to seismic data from the Altiplano plateau in the Andes region. Both areas share certain similarities, such as sharp velocity contrast around the top of the respective slabs, and strong heterogeneities. One important difference between the two regions is the fact that the presence of strong attenuation of S waves in the Andes region affects interferometric results in the sense that no information can be retrieved from coda S waves.

We show that inter-receiver Green’s functions are retrieved using P coda waves, as opposed to the situation in the Philippine Sea slab region (Tonegawa *et al.* 2009) where information was extracted from S coda waves only. Moveout of the retrieved waves is in agreement with theoretical moveouts predicted for previously estimated P and S wave velocities.

The present work also shows that attenuation, geological complexity and relative position of geophones, reference receiver (virtual source) and events used for calculating the cross-correlation functions, will have an impact upon which coda waves (P or S) are more suitable for body wave retrieval. Additional simulation with a simple model helps us to understand results coming from real data and gives insight into the need to distinguish cases where convolution, as the main operation of interferometry, is better than cross-correlation. The main conclusion is that a combined interferometric procedure incorporating cross-correlation and convolution is needed to describe the whole range of offset for the geometrical set-up.

3.2 Introduction

The retrieval of wavefields from noise and coda waves has been successful for surface waves in many studies. The usual method for retrieving surface waves is by reconstruction from ambient noise (Shapiro and Campillo, 2004) and from coda waves (Campillo and Paul, 2003). Campillo and Paul (2003) use diffuse waves, produced by distant sources, which are sufficient for retrieving direct waves between two points of observation. Other successful retrievals of surface waves were conducted by Shapiro *et al.* (2005) and by Sabra *et al.* (2005a) who made use of interferometrically constructed impulse responses to carry out tomographic velocity inversion.

Reconstructed surface waves have been used for crustal structure studies (Yao *et al.*, 2004; Shapiro *et al.*, 2005; Yang *et al.*, 2007; Bensen *et al.*, 2008; Lin *et al.*, 2008; Zheng *et al.*, 2008; Stehly *et al.*, 2009) to characterise seismic noise sources (Stehly *et al.*, 2006; Gerstoft *et al.*, 2008; Yang and Ritzwoller, 2008) and for seismic tomography studies (Sabra *et al.*, 2005b; Shapiro *et al.*, 2005).

Nevertheless, the retrieval of body waves by reconstruction from ambient noise and coda waves has proven to be more difficult than the retrieval of surface waves. The main reason for this is that theoretically a distribution of sources at depth is needed to retrieve body waves at the surface (Wapenaar, 2004, 2006c) and because surface waves generally obscure body waves due to the fact that surface waves are of an order of magnitude stronger than body waves.

The retrieval of body waves, by means of seismic interferometry, has its beginnings in the work of Roux *et al.* (2005) who demonstrated the presence of P-waves as well as Rayleigh waves in the noise correlation functions. Results obtained for arrival times compare favourably with theoretical body waves predictions. Mizayawa *et al.* (2008) also extracted downward propagating P and S waves produced by human activity in a borehole at Cold Lake, Alberta, Canada. Results from Mizayawa *et al.* (2008) work showed that P and S waves could be observed in the cross-correlations for both vertical and horizontal components.

Also, travel times were consistent with the velocity model coming from tomography. More recently, another successful study carried out by Tonegawa *et al.* (2009) shows, by means of the cross-correlation of teleseismic S coda waves, the detection of body waves including direct and reflected waves.

The objective of the present study is to assess the possibility of retrieving body waves using the methodology designed by Tonegawa *et al.* (2009), for data originally obtained during a passive experiment conducted by the GFZ. The experiment took place from March 2002 to January 2004 in the Andes region. As will be seen, the above correlational methodology is insufficient to work with all arrivals for the geometries considered here. It will be demonstrated that a new methodology that combines cross-correlation and convolution depending on the relative position of the earthquake geophones and reference receiver is needed in order to describe arrivals for long offsets.

This current study will make use of the data coming from the Altiplano and Puna plateaux. The Altiplano region is situated in the Andes, the world's largest continental mountain range (Giese *et al.* 1999. cited in Wölbern *et al.* 2009, p.296). Located on the western coast of South America, the Andes average length is about 7500 km, with a width varying from 200 km to 700 km and an average height of 4 km. The geography of the Altiplano and Puna plateaux is such that, to the west, both plateaux are confined by the active magmatic arc of the Western Cordillera. To the east, they are limited by a thin-layer fold and thrust belt of the Eastern Cordillera and the sub-Andean ranges. Towards the south, the Santa Barbara ranges and the Sierra Pampeanas are located on the eastern side of the Puna plateau.

Previous studies conducted in the region provide an idea of the complexity of the structure underneath the subsurface. In this respect, we know that a low-velocity layer in the crust, with its top boundary at about 15 km depth, has been detected on both plateaux (Yuan *et al.*, 2000; Wölbern *et al.*, 2009). Dipping interfaces cutting through the top of the low velocity crustal layer have also been detected (Wölbern *et al.*, 2009) and they are probably related to the presence of some major faults.

Detachment zones within the crust and velocity, and contrasts, possibly due to hot fluid accumulation, have also been conjectured (Heit, 2005). Therefore, strong heterogeneities exist in the region and together with the extreme topographic variations these affect the quality of the data that was collected, as well as the results arising from interferometry.

Hence, this study assesses what can be derived from a “difficult” data set. This chapter will introduce the reader to the details of data acquisition, the method used to perform the interferometric calculations and the results obtained. Additionally, it will explain the computer simulations conducted in order to give insight into the method used and results obtained. Finally, conclusions and recommendations will be given.

3.3 Method

As was mentioned in the introductory part, strong attenuation significantly affected the recorded data. Indeed, attenuation led to a complete lack of S wave energy (Wölbern *et al.*, 2009), as shown in Figure 3.1.

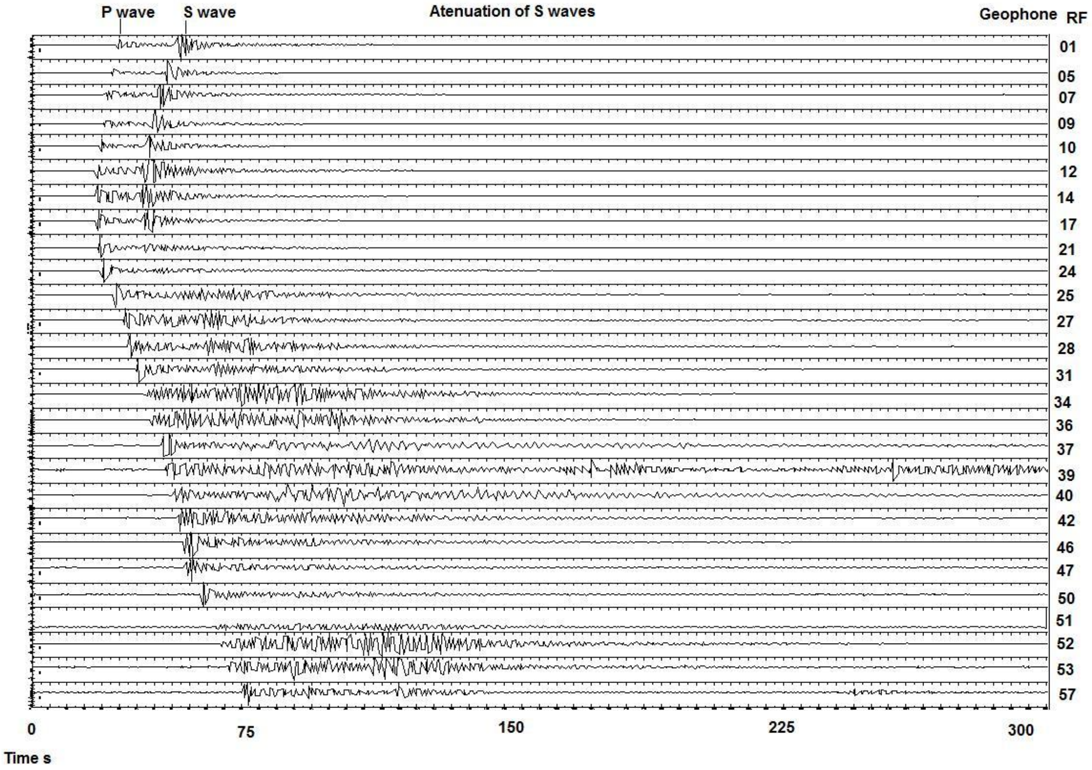

Figure 3.1 Attenuation of S wave for geophones situated in the northern profile RF (second arrivals). Attenuation is due to the zone of partial melted material.

Pre-processing steps taken included: elimination of bad records (due to GPS and/or noise problems), application of a filter (bandpass 0.2-3.0 Hz) to improve signal to noise ratio, and elimination of geophones that were inactive during the time interval of interest. In order to avoid contributions from surface waves, only deep events with epicentres close to the geophones were used. By implementing this restriction, it was almost assured that body waves dominated the recordings. As far as was possible, and to ensure equal partitioning of energy, various incident angles were chosen, in order to simulate more isotropic incidence of the wave energy. This is a requisite for retrieving wavefields without any ghost phases, as explained by Nakahara (2006).

The method used in this study is analogous to that implemented in the work of Tonegawa *et al.* (2009), which is based on the recovery of waves between two receivers by means of seismic interferometry. They (Tonegawa *et al.*, 2009) used only S coda waves to ensure that deterministic phases did not affect the interpretation procedures.

From the work of Tonegawa et al. (2009) it was unclear whether the cross-correlation functions of S coda waves were affected by deterministic phases isolated from the direct S waves. In this study, we keep these deterministic phases, as well as in a separate test suppressing them, in order to compare and make our own judgement regarding this issue.

This study tested the use of P wave and coda, S wave and coda, coda P wave only, coda S wave only, and complete seismograms, with all possible combinations of these various sets in order to calculate, by means of interferometry, the seismograms that would be obtained if the reference receiver had been a source.

Seismic events with a depth of more than 100 km were used to compute the cross-correlation functions (CCF), with a time length of 300 s and a frequency band of 0.2-3.0 Hz. The reason for choosing such a filter was based on the work of Wölbern *et al.* (2009) in which they chose these values for the northern profile, taking into consideration factors such as the limited frequency content caused by attenuation and by the high noise level present in the region.

Pre-processing steps applied to the signal, for interferometric calculations, are shown in Figure 2.5. Figure 3.2 depicts the geometrical set up for calculating the cross-correlation functions. First, a geophone was fixed as a reference point, such that events depicted in red in Figure 3.2 were symmetrically located around the fixed geophone. This ensured equipartitioning of energy. Then, for every earthquake, the cross-correlation function, between the fixed geophone and one geophone located at a distance d, was calculated. This operation was performed for all the possible geophone pairs. Finally for all earthquakes, all possible pairs with approximately equal inter-receiver distances were stacked. For this study, positive and negative relative distances were kept separate, so the plots showed in this work contain positive and negative distances and the location of the reference geophone is indicated by a red line. As was explained in the introductory part, equation 1.9 will be used for performing correlation operations and equation 1.10 will be used for stacking over all sources.

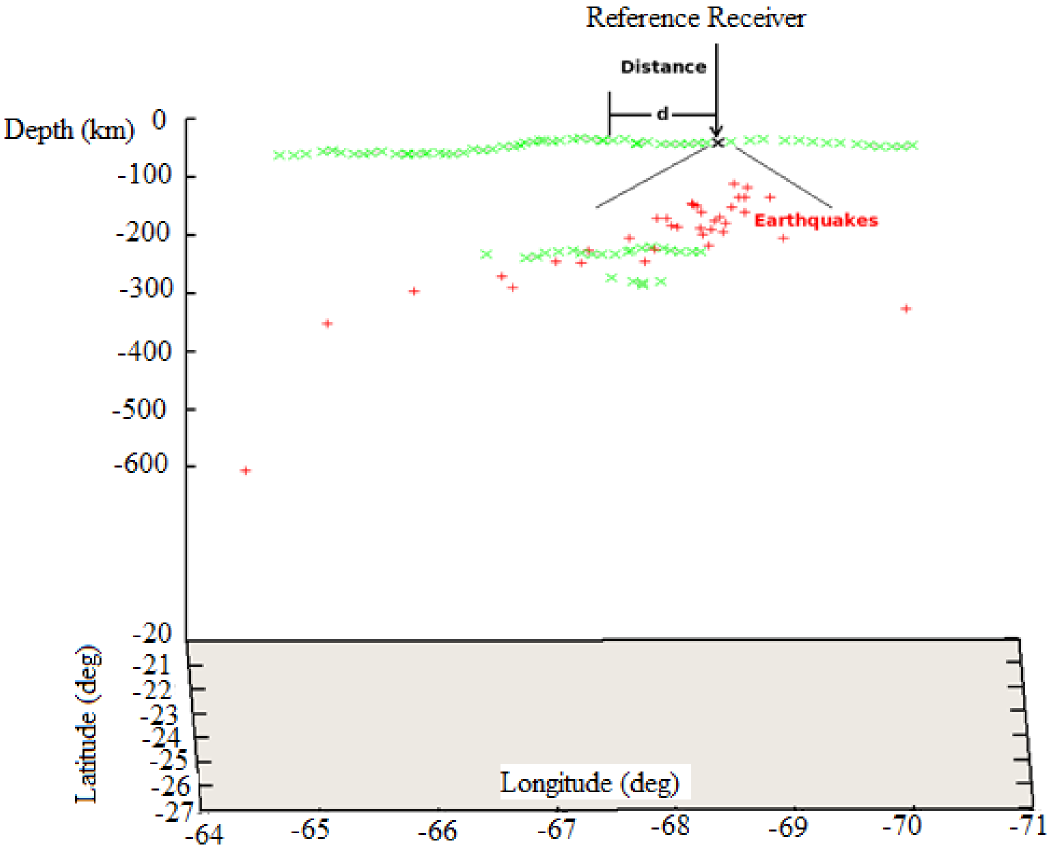

Figure 3.2 Geometrical set up. In black, the reference receiver. In red, the distribution of earthquakes used

3.4 Results

The cases studied in this section are summarised in Figure 3.3, but first consider application of the method outlined in section 3.3 in the case where the complete seismogram is used for both the reference receiver and the rest of the receivers. The result of such calculation is shown in Figure 3.4, in this figure the positions of the reference receiver is shown by the red line, relative offsets to the west and to the east of the reference receiver are shown on the vertical axis.

The horizontal axis displays time. In this plot, the acausal and causal part of the Green's function are plotted. In this figure, two parallel curves are clearly visible from the red line upwards in the plot and marked by the red arrows.

If we interpret the signals in Figure 3.4 as arrivals we can see that starting from the reference receiver (red line), arrivals tends to be delayed in negative time when offset increases upwards in the plot to around 200 km. Nevertheless, from this offset on the arrivals instead of increasing in delayed time they decrease when offset increases (inverse moveout). As will be demonstrated later on, this inverse moveout implies that cross-correlation by itself is not necessary the best operation to use for seismic interferometry.

Before going into the details of what is missing in the application of interferometry for this geometrical set-up, we analyse in more depth the meaning of the plot shown in Figure 3.4 and how the different components of our seismogram influence the construction of the plot.

With this objective in mind the analysis of the signal was separated in the following cases: A) reference receiver: complete seismogram; rest of receivers: complete seismogram. B) reference receiver: P wave and coda P; rest of receivers: P wave and coda P. C) reference receiver: coda P; rest of receivers: coda P. D) reference receiver: S wave and Coda S; rest of receivers: S wave and coda S. E) reference receiver: coda S; rest of receivers: coda S. F) reference receiver: P wave; rest of receivers: P wave and coda P. G) reference receiver: P wave, rest of receivers; coda P. H) reference receiver: S wave; rest of receivers: S wave. I) reference receiver: P wave and S wave; rest of receivers: P wave and S wave. J) reference receiver: S wave; rest of receivers: P wave. K) reference receiver: P wave; rest of receivers: S wave.

Figure 3.3 shows cases (A) through (K) in a schematic manner. The objective of this sub-division is to try to understand the influence of the deterministic phases, such as P and S waves and the influence of the coda P and/or S on the final result when using the complete seismogram (Figure 3.4).

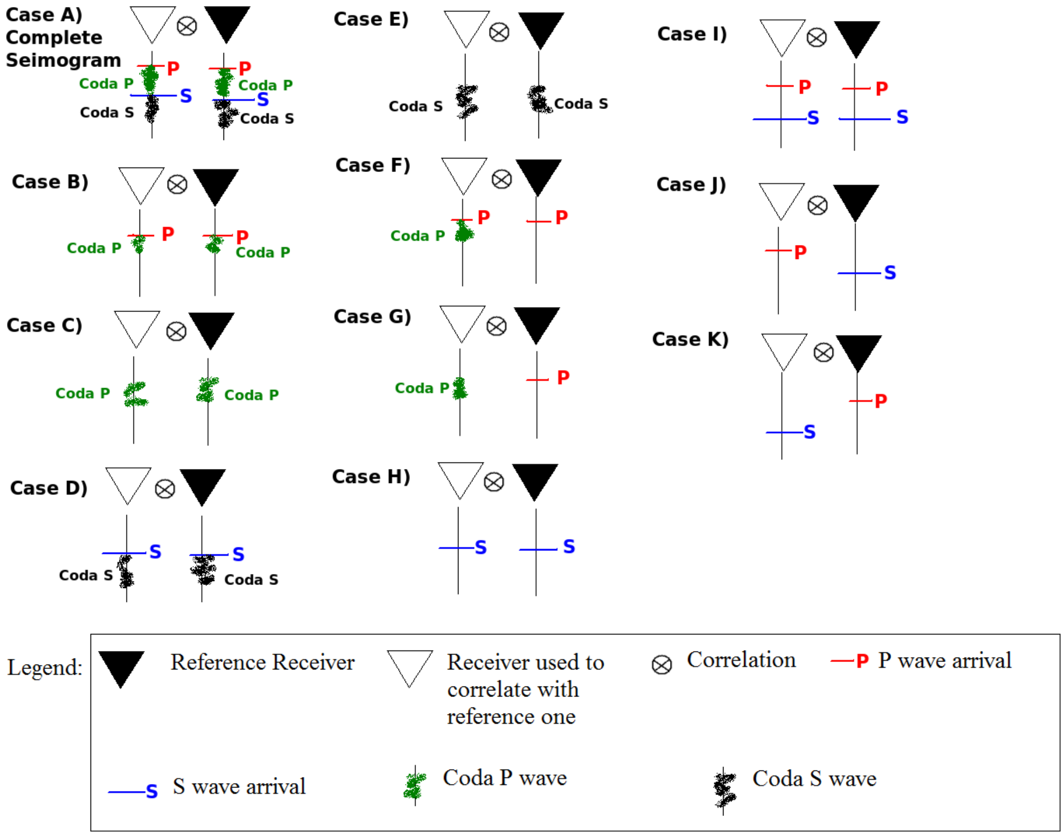

Figure 3.3 Schematic diagram of all cases studied. The reference receiver is represented by an inverted black triangle. White inverted triangle represents the rest of the receivers. The circle with an inner cross symbol represents the mathematical operation applied (correlation and/or convolution).

Scenario A: Reference receiver: complete seismogram; rest of receivers: complete seismogram.

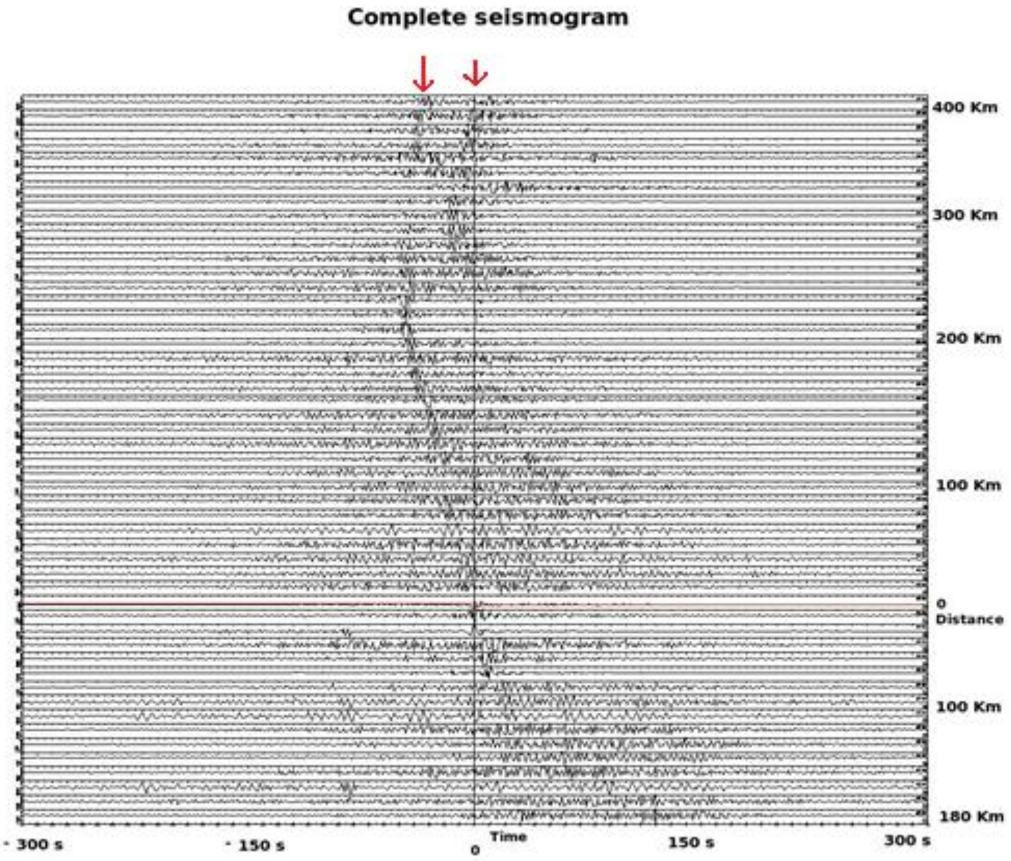

Figure 3.4 Result of interferometric calculations taking the complete seismogram for both the reference receiver and the rest of the receivers.

This case used the complete seismogram from all receivers. From the graph, it can be appreciated that two parallel lines are present in the plot. These comprise the cross-correlation of deterministic phases.

Here results for scenarios C, D, E and I will be presented and discussed because they summarise the principal characteristic and results for this section; the remainder of the scenarios will be depicted in appendix A. In order to improve visualisation in all plots, envelope functions of the seismograms obtained from the interferometric calculations were calculated.

For the purpose of visualisation, envelope functions have been coloured in red and black. In so doing, a threshold has been selected, such that its value is half the maximum amplitude of the window. If the signal was bigger than this threshold the amplitude was coloured in red, otherwise it was black. This ensures that all coherent and large events are highlighted.

Figure 3.35 summarises and presents the separated interpreted cases. So, the original result (Figure 3.4) can be understood as the superposition of all cases already detailed in scenarios (A) through (K).

Note that some amplitudes will dominate others, but the decomposition into possible combinations of waves gave an insight into where and how every factor in the seismogram affected the interferometric final output. Please note that, for offsets greater than 200 km, the slopes of the curves tend to bend and present inverse moveout. This will be explained by means of simple modelling in section 3.5.

As previously explained, the red line in Figure 3.4 represents the reference receiver. The vertical axis represents the distance on both sides of the 2D line where the reference receiver lies. The horizontal axis represents time (causal and acausal part of the cross-correlation).

Scenario C: Reference receiver: coda P; rest of receivers: coda P.

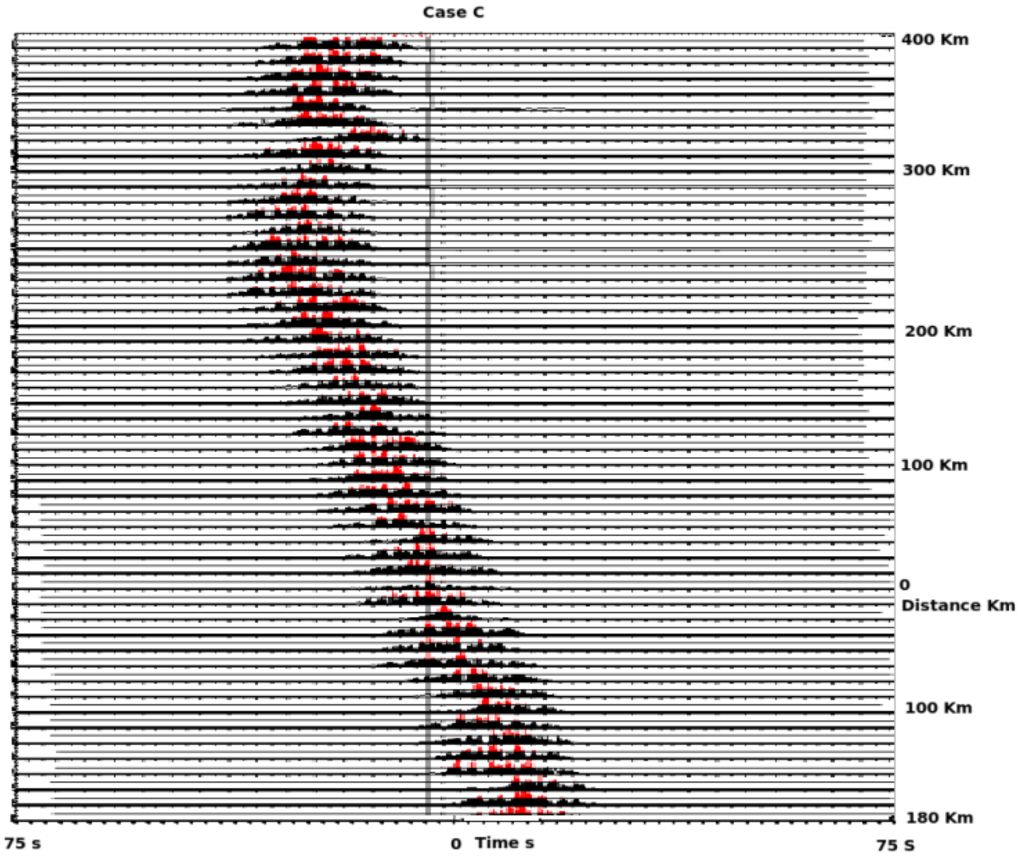

Figure 3.5 Scenario C. Result of taking coda P only for both the reference receiver as well as the rest of the receivers.

In this case (Scenario C), a clear but weak signal has been retrieved. This was an important result because, in this case, all deterministic phases had been removed and the retrieved wave has been obtained using only the coda part of the P arrival. This is an interesting result, because is the first time the coda wave is used in the Altiplano in order to retrieve body waves.

This is the equivalent of retrieving waves between receivers making use of seismic noise. These waves are useful in the sense that they give us information regarding the velocity of the waves travelling through the medium of interest.

Scenario D: Reference receiver: S wave and Coda S; rest of receivers: S wave and coda S.

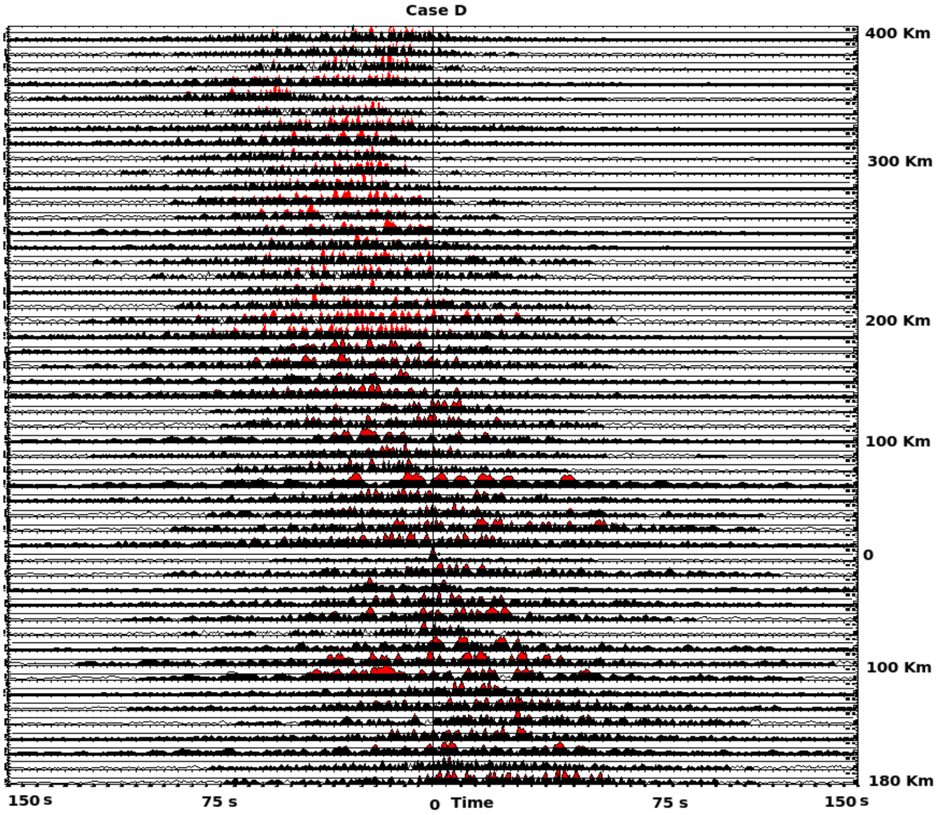

Figure 3.6 Scenario D. Result of taking S wave and coda S for both the reference receiver as well as the rest of the receivers.

In this case, no recognisable signal was retrieved, despite the fact that the S wave (a deterministic phase) and coda was taken to construct this graph. This can be explained by S wave attenuation caused perhaps by a melted material zone in the area (Wölbern *et al.*, 2009).

Scenario E: Reference receiver: coda S; rest of receivers: coda S

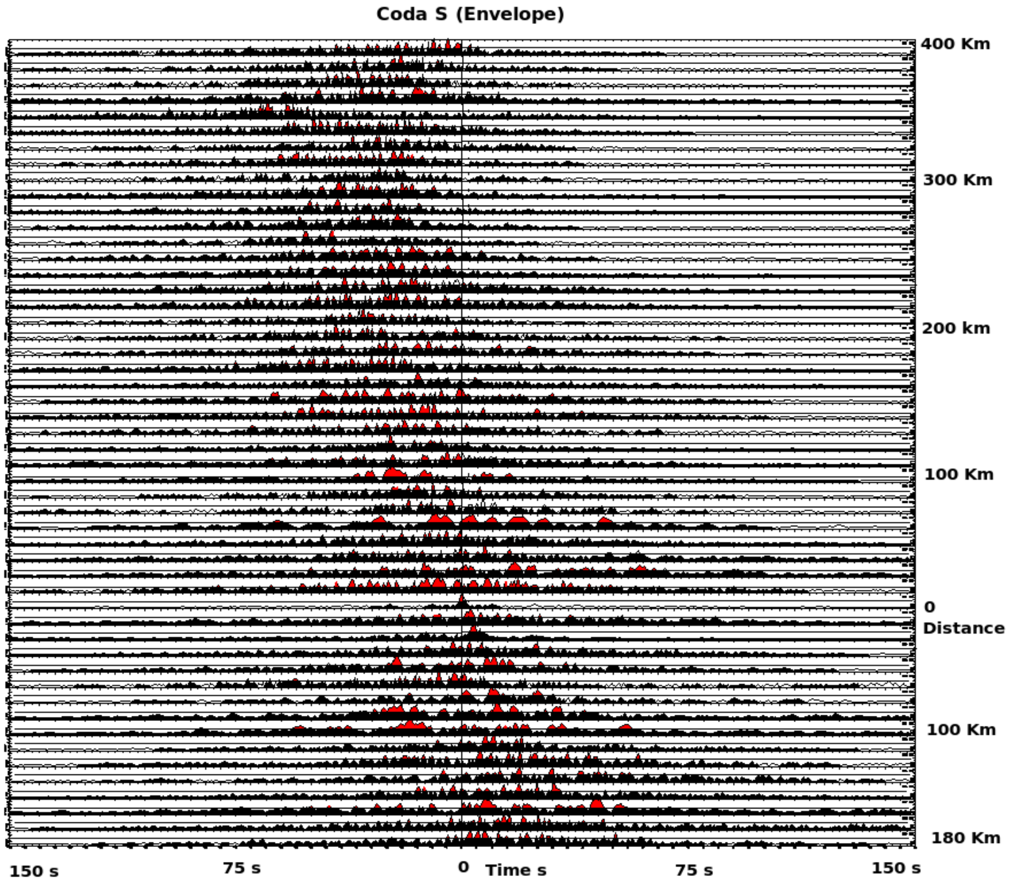

Figure 3.7 Scenario E. Result of taking S coda for both the reference receiver as well as the rest of the receivers.

Figure 3.7 shows the result of taking only coda S waves into consideration. As illustrated by this graph, it can be concluded that no signal is present. This can be linked to the fact that there was a complete lack of S waves in the data due to attenuation. This result is in contrast with those from the work of Tonegawa *et al.* (2009), in which they retrieved direct and reflected waves from coda S waves.

For the Andes region, the zone of melted material makes S waves likely to attenuate. Therefore, no information has been extracted from coda S. This result was a clear indication of the fact that regional features have to be taken into account when interpreting or carrying out interferometric calculations.

Scenario I: Reference receiver: P and S wave; rest of receivers: P and S wave.

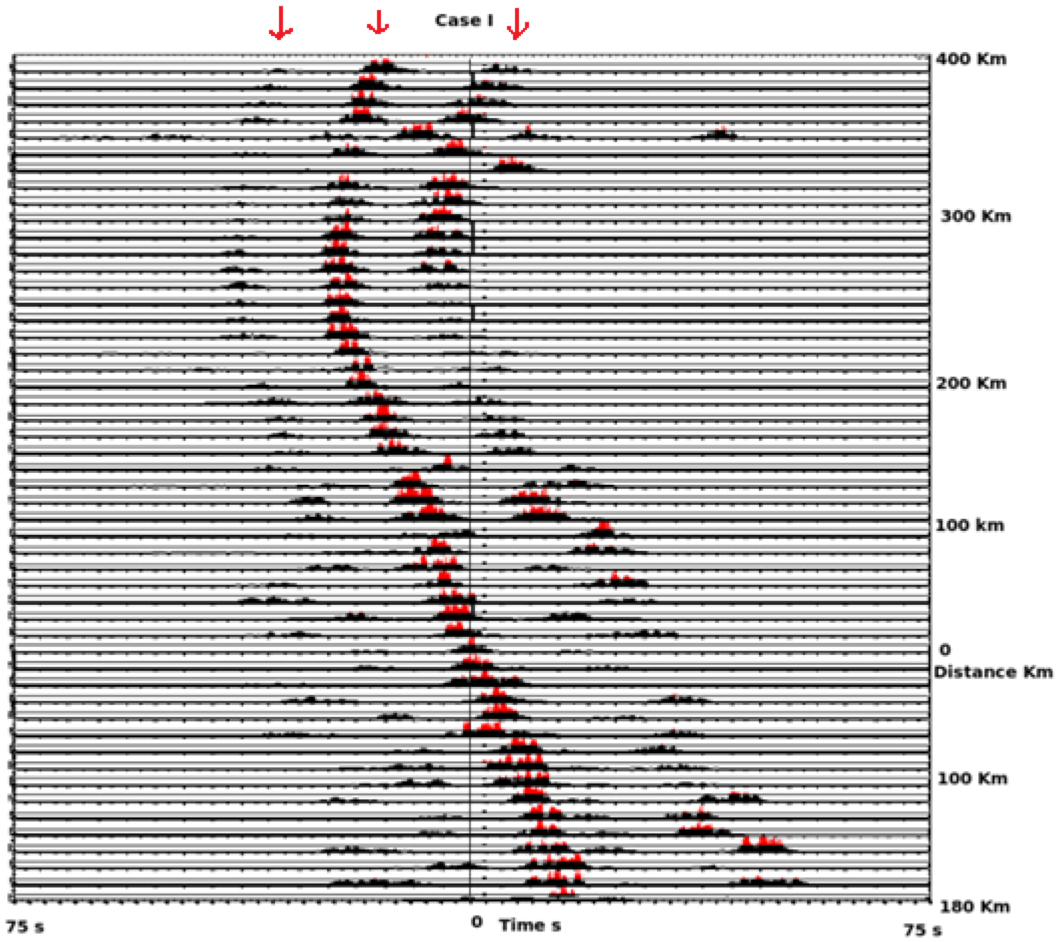

Figure 3.8 Scenario I in which and for the purpose of interferometric calculation, the reference receiver consisted of P and S arrivals while the rest of the receivers consisted of P and S arrivals as well.

In this case, we can appreciate three waves corresponding to the cross-correlation of S and P wave with the receiver with the corresponding S and P of the reference receiver. One of these expected waves has small amplitude compared to the order of magnitude of the other ones, so it is not possible to visualise all wave data together.

In summary, the most important result concerning this current study is that “retrieved body wave” is observed in the p coda; implying that the deterministic phases are not responsible for this result.

3.5 Synthetic tests

3.5.1 Objective

The objective of these tests is to use a known subsurface model for the distribution of geophones and earthquakes to create synthetic data. Data arising from this simulation will be processed following the same procedure outlined in section 3.3. Then, simulations will be compared to the above real data to aid their interpretation. Finally, a procedure that combines cross-correlation and convolution will be used on the synthetic data in order to show that reverse moveout can be removed if this combined procedure is used.

3.5.2 Program used

The program used for computer simulations was based on the algorithm developed by Wang (1999), with subsurface velocities from the tomographic results from the work of Heit (2005), which in turn were based on the 1D Earth model AK-135 (Kennet *et al.*, 1995). The modeller is a program for the calculation of synthetic seismograms based on a 1D layered half space earth model. It allows the user to choose parameters such as source depth, distance between sources, receiver depth, distance between receivers and the Green's function to be calculated e.g. explosion, strike slip and dip-slip sources. Also, the 1D velocity model used by the program can be modified. In this case, the original program consisted of 68 velocity layers with depths varying between 0 and 3000 km. Table 3.1 shows the velocity of the layers down to the depth of interest for the simulations.

No	Depth [km]	Vp [km/s]	Vs [km/s]	Ro [g/cm3]	qp	qs
1	0.00	5.80	3.36	2.72	1340.00	600.00
2	20.00	5.80	3.36	2.72	1340.00	600.00
3	25.00	6.50	3.75	2.92	1340.00	600.00
4	30.00	6.50	3.75	2.92	1340.00	600.00
5	35.00	8.04	4.47	3.31	1340.00	600.00
6	77.50	8.04	4.48	3.35	1340.00	600.00
7	120.00	8.05	4.50	3.37	1340.00	600.00
8	165.00	8.17	4.51	3.40	250.00	100.00
9	210.00	8.30	4.52	3.43	250.00	100.00
10	240.00	8.30	4.52	3.43	360.00	150.00
11	260.00	8.48	4.61	3.45	360.00	150.00
12	310.00	8.67	4.70	3.49	360.00	150.00

Table 3.1 Parameters of the simulation (layer number, depth, velocity of the P wave, velocity of the S wave, density and q factors for P and S waves) based on the AK-135 velocity model and tomographic results from the work of Heit (2005).

In order to be as representative as possible of real-life, a subset of 51 stations were used, with a separation distance between them of 10 km. Typical seismograms, with a source depth of 1 km, 10 km and 100 km, are shown in Figures 3.9, 3.10 and 3.11, respectively. Figures 3.9 and 3.10 are dominated by surface waves. This is the reason for the linear moveout in the set of seismogram. Figure 3.11 shows the synthetic seismogram when the source depth is 100 km. In this case, body waves dominated the simulation and the expected hyperbolic behaviour was observed.

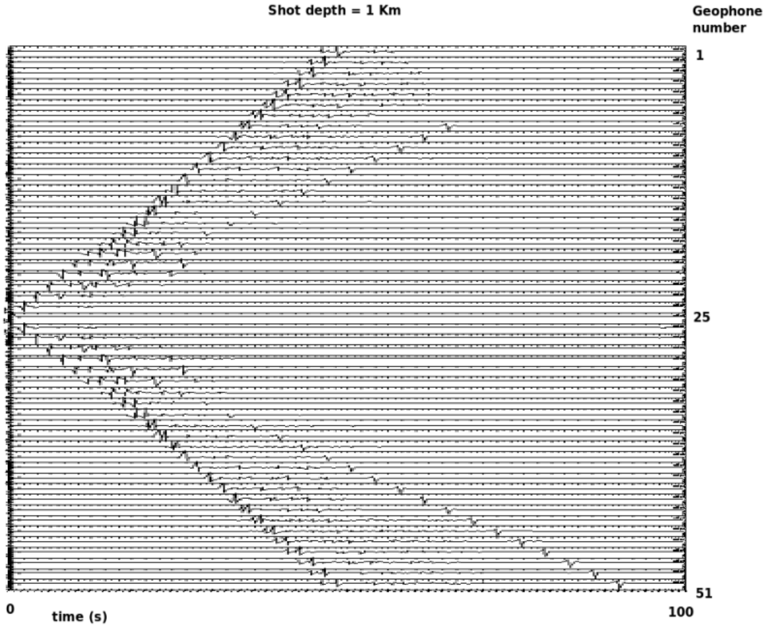

Figure 3.9 Synthetic seismogram for a source depth of 1 km. Surface waves dominate the simulation.

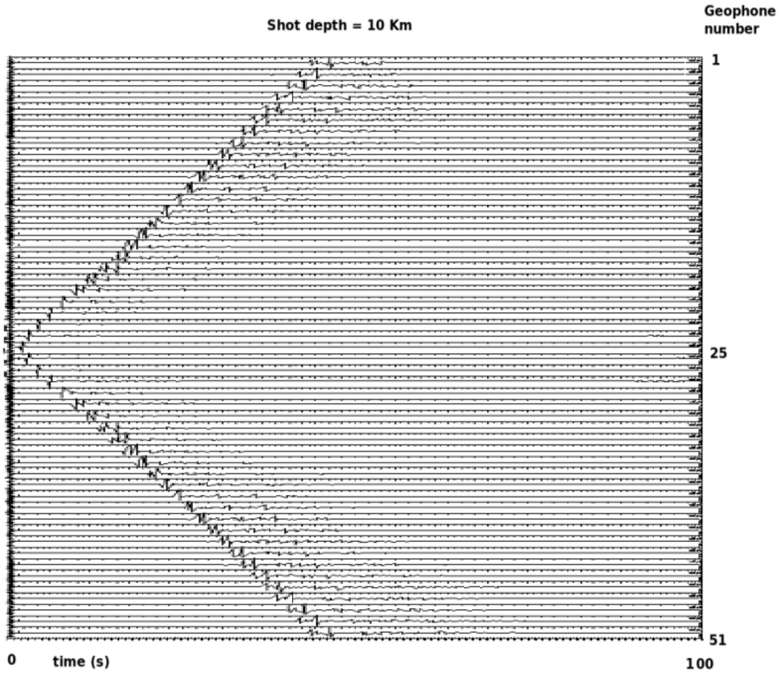

Figure 3.10 Synthetic seismogram for a source depth of 10 km. Still surface waves have an important contribution to the simulation results.

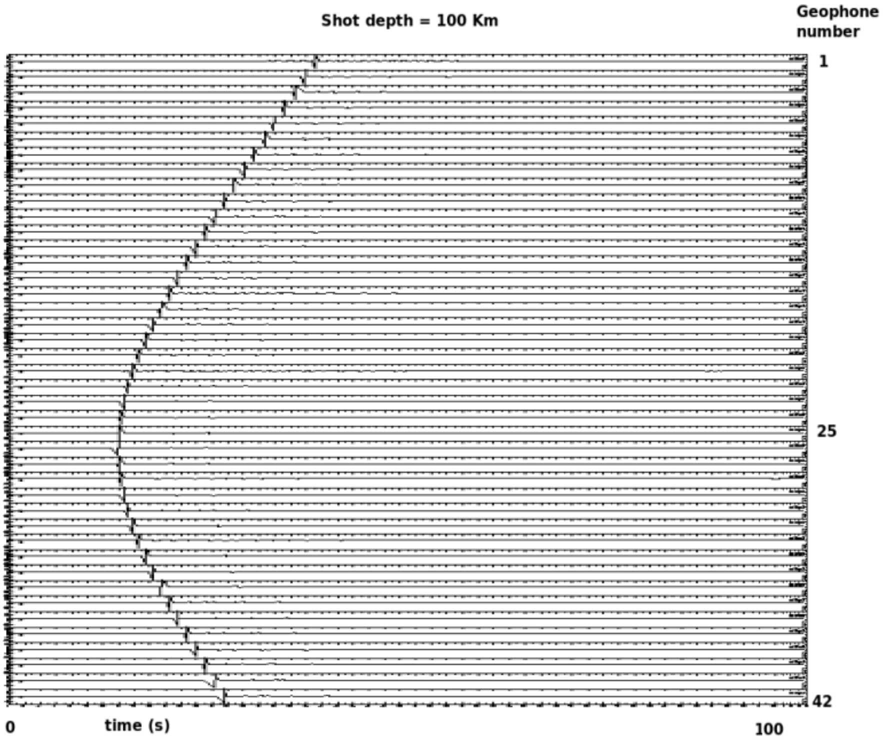

Figure 3.11 Synthetic seismogram for a depth source depth of 100 km. In this case, body waves dominated the simulations.

3.5.3 Method

The method used to process the synthetic seismograms was the same as that used for real data, and outlined in section 3.3, i.e., for every earthquake, the cross-correlation function between the fixed geophone (the reference geophone) and one geophone located at a distance d, was calculated. This operation was repeated for all possible geophone pairs. Finally, for all earthquakes, all possible pairs with approximately equal inter-receiver distances were stacked. Interestingly, results were similar to those found for the real data.

3.5.4 Results of the synthetic tests

In order to better understand the resulting trend of the Green´s function retrieved by interferometry and shown in Figure 3.4, a set of computer simulation consisting of three sets of tests were run.

The first set of simulations consists of four events and four cases in which the reference receiver is varied in position. The objective is to investigate the effect of varying the position of the reference receiver in relation to the cluster of events and also to investigate the effect of the length of the line of receivers.

The second set of simulations is divided into two cases: a) a second set of simulations using convolution and cross-correlation which is essentially a replication of the simulation of the first set but in this case using a combined procedure of convolution and cross-correlation that will depend on the relative position of the three variables: geophones, reference receiver and earthquakes. b) Same case as a) but with an increasing number of earthquakes. In this experiment, the intention is to check how the number of earthquakes used has an impact on the final results.

The third set of simulations is where the earthquakes not only vary in number but also in position. From this simulation, we will see that the incompleteness of the distribution of earthquakes does have an impact on the interferometric results.

-First set of simulations-

The first set consisted of applying cross-correlation to four events with depths of 100, 150, 180 and 200 km respectively.

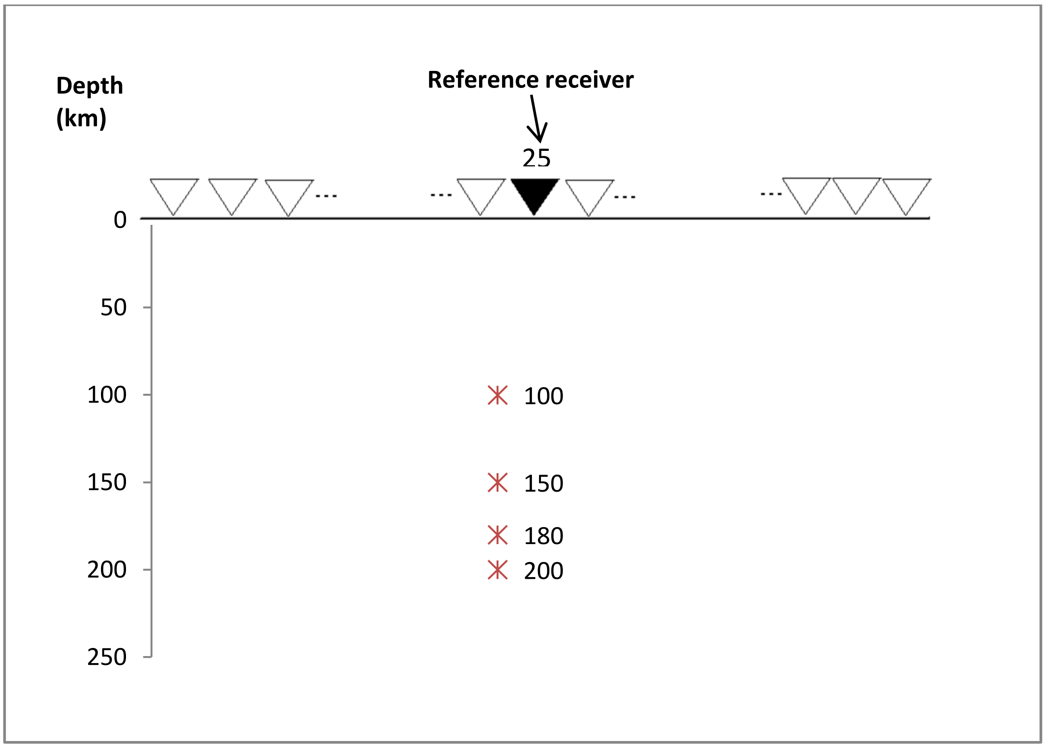

Figure 3.12 First set of simulations, case 1. Earthquakes and virtual source (reference receiver) are located in the middle of the line.

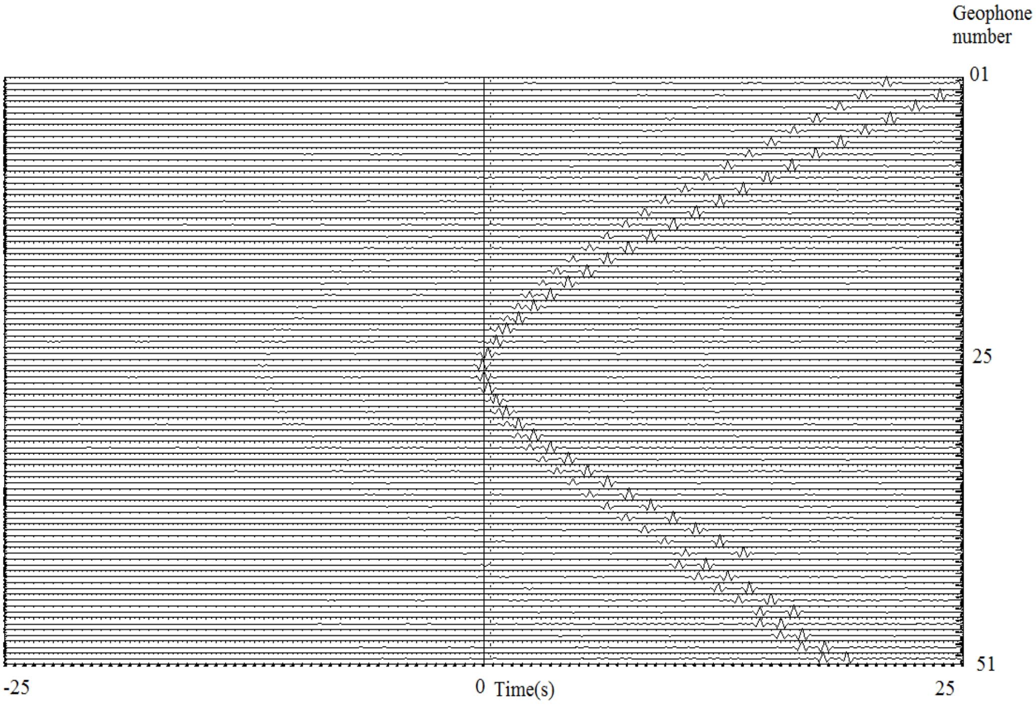

Figure 3.13 Result for first set of simulations, case 1 as shown in Figure 3.12.

In this case, all the events were located below geophone 25, just about the middle of Figure 3.13. Note that in this curve we can appreciate how the travel time for waves increases as the offset increases. This means that waves produced by earthquakes travel in both directions of the 2D line.

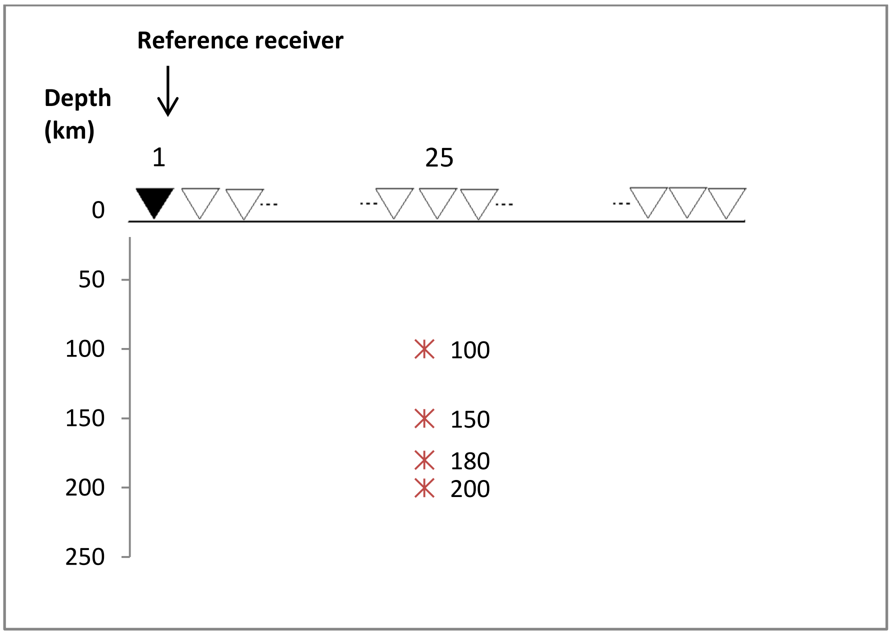

Figure 3.14 First set of simulations, case 2. Earthquakes in the middle and reference receiver at one extreme of the line.

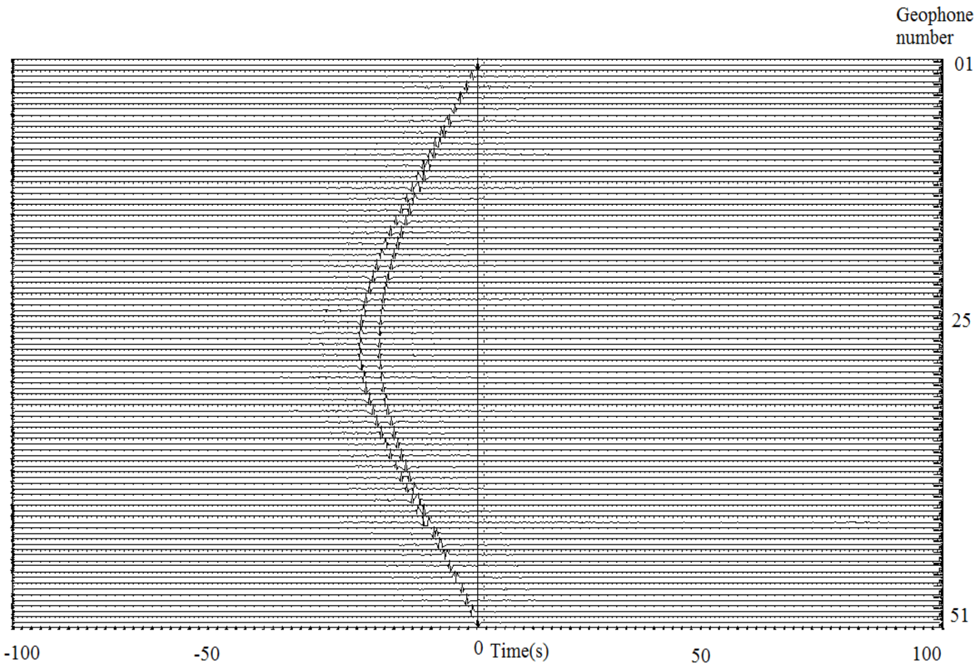

Figure 3.15 Result for the first set of simulations, case 2, where the geometrical configuration is shown in Figure 3.14.

In Figures 3.14 and 3.15 the reference receiver is situated at one extreme of the array. Events are again situated in the middle of the line (i.e. the location of geophone 25).

From the graph we can see the acausal part of the Green’s function. For this, the travel time increases as offset increases. For receivers situated beyond geophone 25 there is an inverse moveout, and for geophone 51 the graph indicates that for near zero time and an offset of around 500 km, there is energy arriving.

As will be shown, this apparently anomalous energy, arriving at zero time for long offsets, is due to the fact of using cross-correlation instead of convolution for receivers beyond geophone 25.

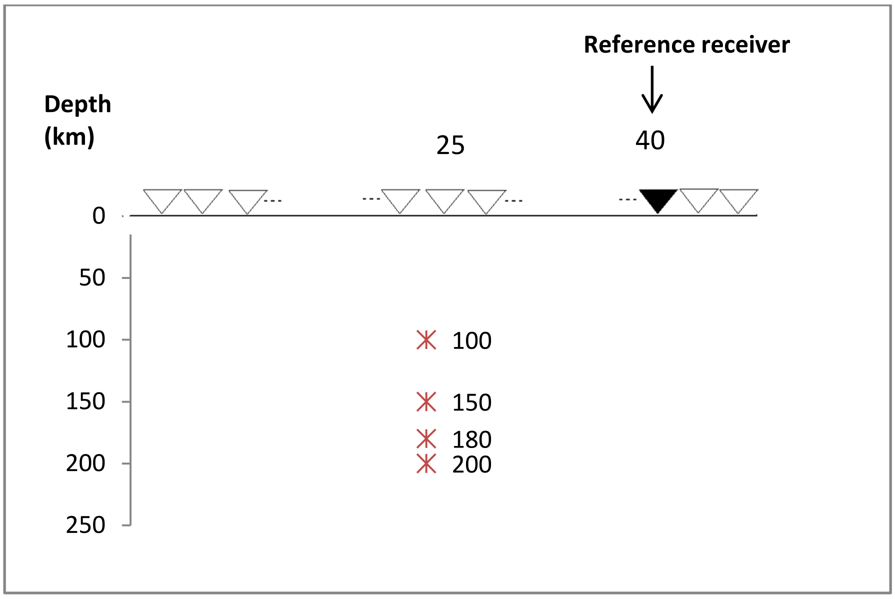

Figure 3.16 First set of simulations, case 3. Earthquakes in the middle. Reference receiver in an arbitrary point.

From the previous argument it is known that cross-correlation will work for geophones located on the same side of the reference receiver and whose energy sources are inside the boundary formed by the events. In this case, we consider geophones 26 to 51. In these situations it can be observed (Figure 3.17) that the causal and acausal sections of the Green’s function are retrieved and there is a zero crossing of geophone 40 (the reference receiver), as is expected. Please note that retrieval of the causal or acausal section for the present research will depend on how cross-correlation terms are defined i.e. the order in which terms are cross-correlated.

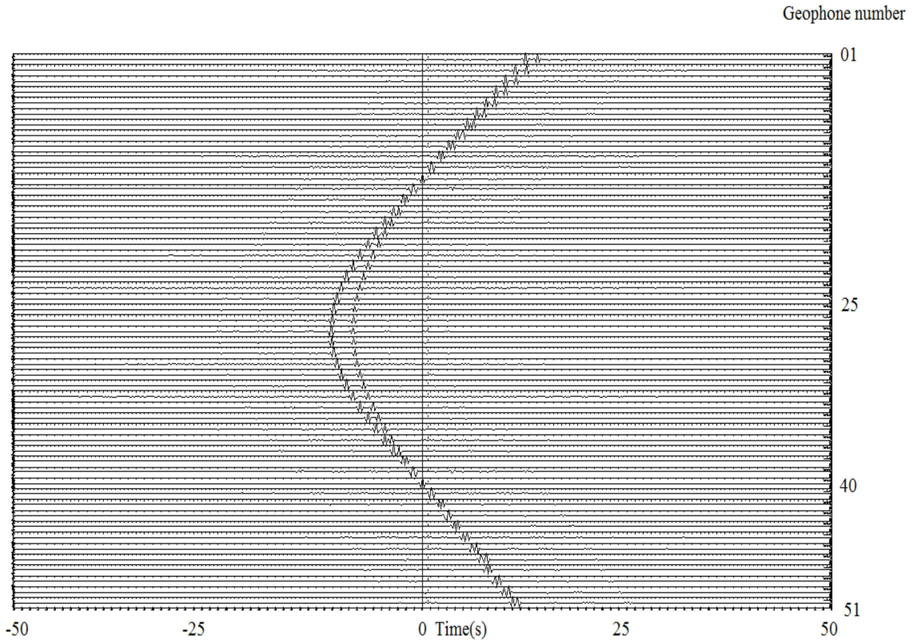

Figure 3.17 Results of the first set of simulation, case 3. Geometrical configuration depicted and explained in Figure 3.16.

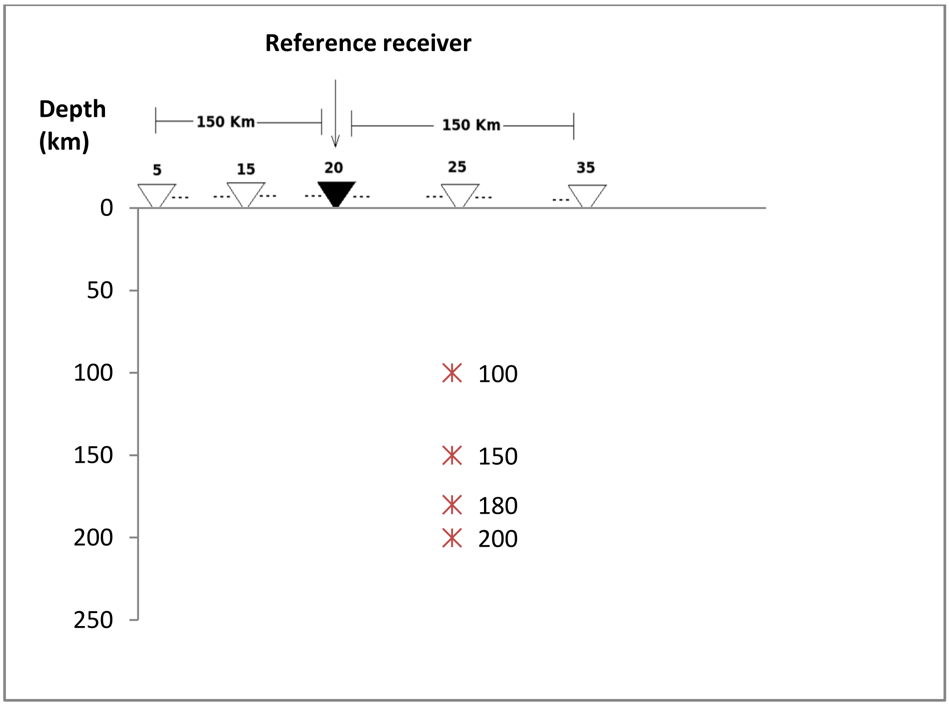

Figure 3.18 First set of simulations, case 4. Earthquakes are not located in the middle and the reference receiver takes an arbitrary position as depicted.

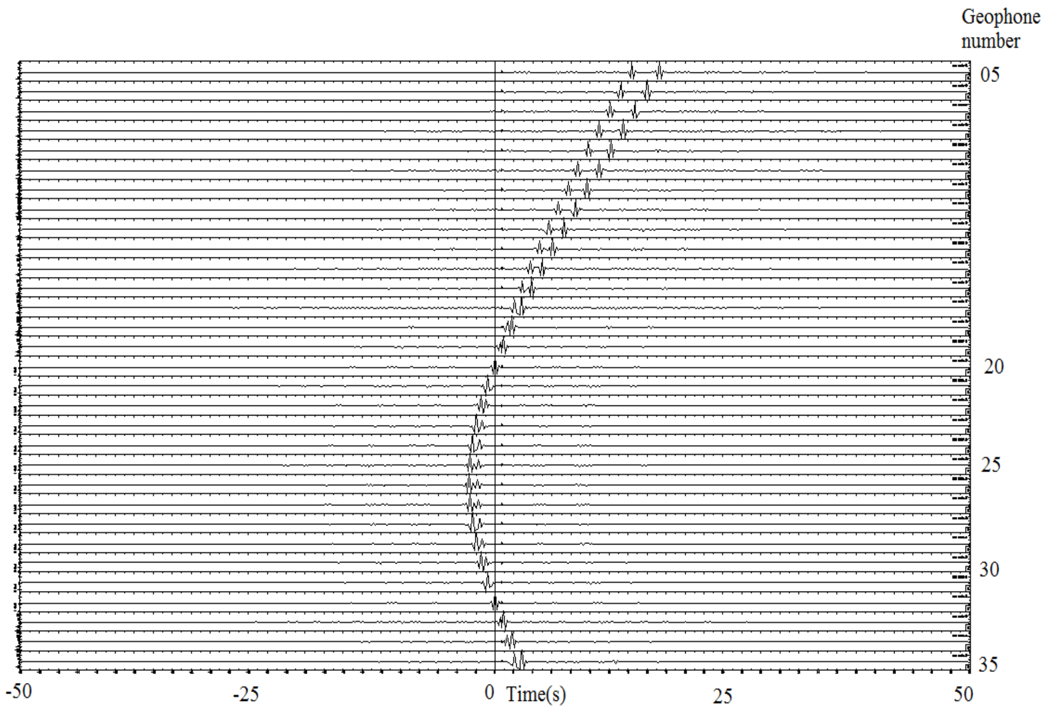

Figure 3.19 Result of the first set of simulations, case 4 as explained in Figure 3.18

In this case, the array length was shortened; choosing only geophones 5 to 35. The intention was to investigate whether geophones at large offsets would impact on the interferometric results obtained up to this point.

As the reference receiver was situated between geophones 5 to 25, only this part of the figure was analysed: the causal part was located from receivers 5 to 20, receiver 20 exhibits zero crossing, and from this point to geophone 25 there is the acausal part. Observed behaviour is as expected, because time of the arrivals increases with offset.

-Second set of simulations-

The second subset of tests consisted of two separated data sets. The first was a repetition of the first set of tests but, in this case, using cross-correlation and convolution.

-Second set of simulation case a)-

Using cross-correlation and convolution: for the cases of the first set of simulations

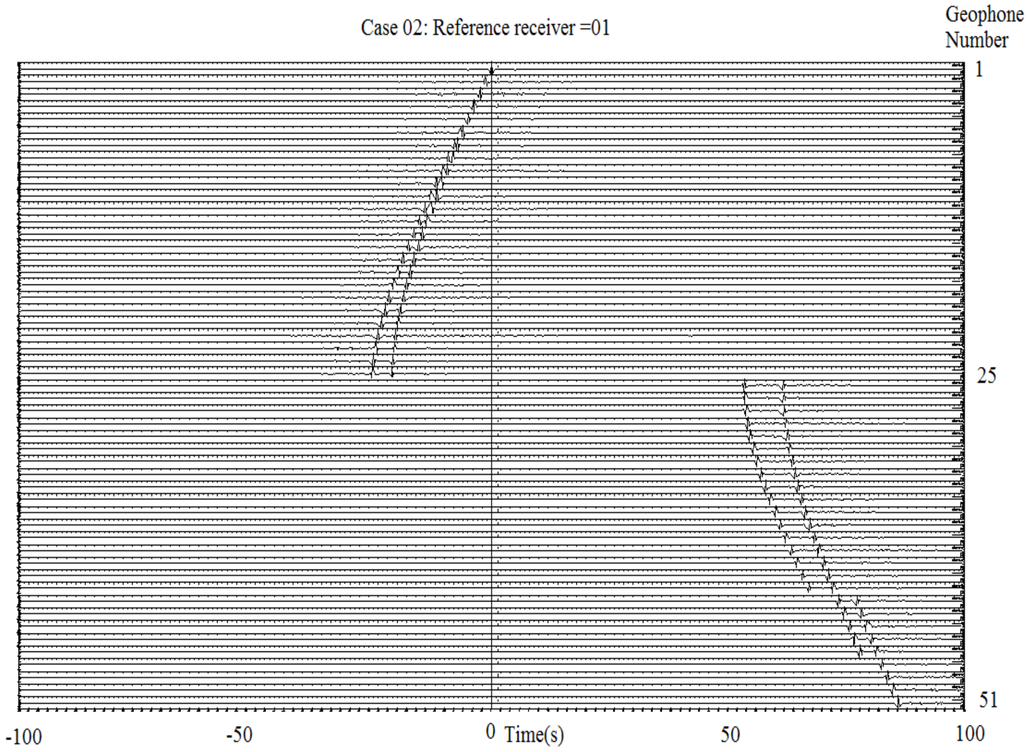

Figure 3.20 Result of second set of simulations, first sub-set, case 2. Geometrical configuration is presented in Figure 3.14 where earthquakes are located in the middle of the line and the virtual source (reference receiver) is located at one extreme of the line.

The repetition of case 2, where convolution was used instead of cross-correlation for geophones 26 to 51, as shown in Figure 3.20 suggests that inverse moveout is removed and as offset increases the time of arrival increases - as expected. Also, Figure 3.20 would suggest that a “jump” occurs near geophone 25. This is related to event coverage, meaning that the lack of sources reaching the surface is the cause for such a jump. As will be seen later in this section, when the simulation is run with sources near the surface such “jump” is removed.

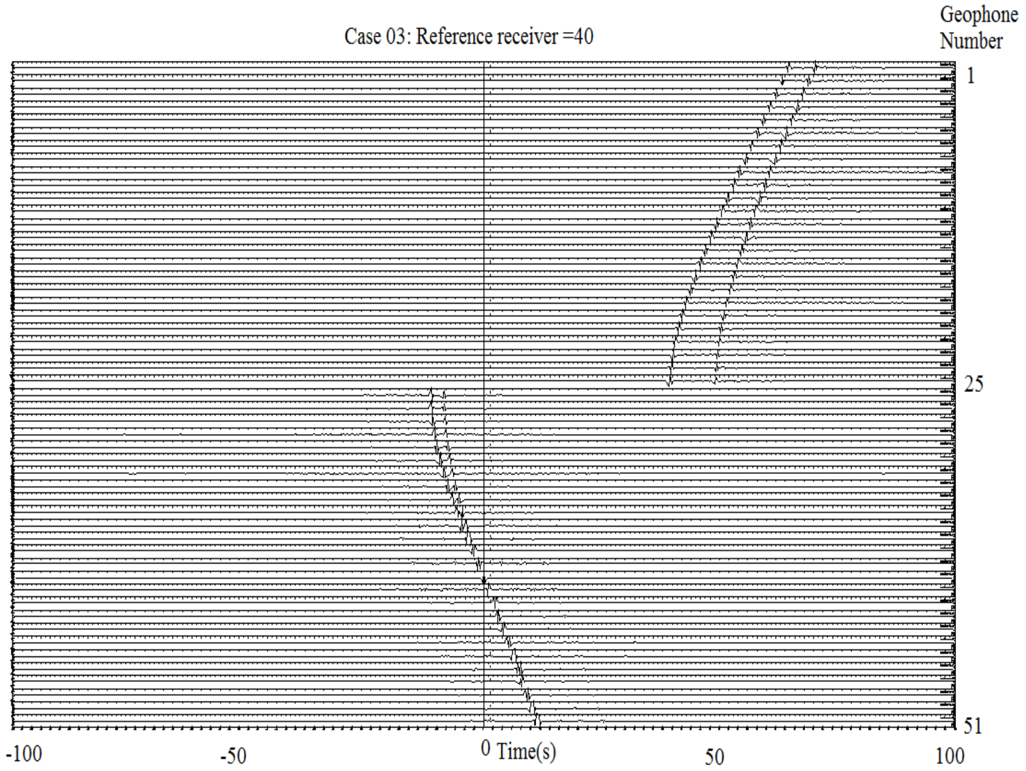

Figure 3.21 Result of second set of simulations, first sub-set, case 3. Geometrical configuration is represented in Figure 3.16 where earthquakes are situated in the middle of the line and the reference receiver (virtual source) in a general position that in this case is in geophone 40.

In the case shown in Figure 3.21, using convolution for geophones 1 to 25, the ambiguity of the inverse moveout and arrivals for long offsets near zero time were removed.

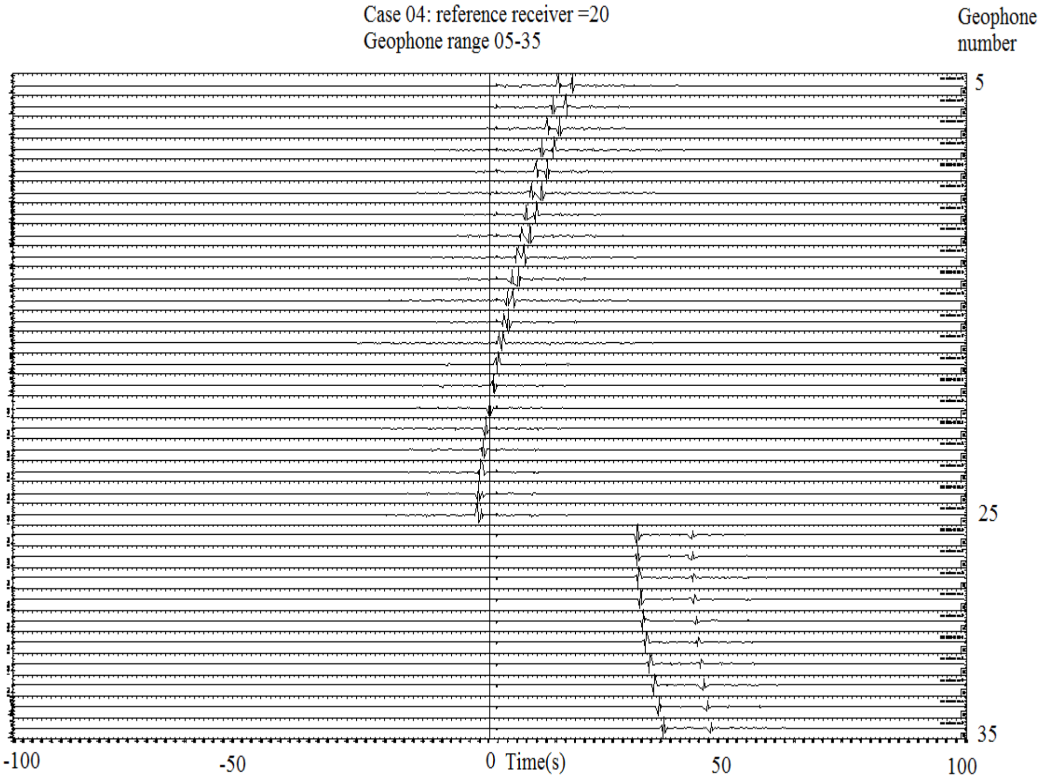

Figure 3.22 Result of second set of simulations, first sub-set, case 4. Geometrical configuration is presented in Figure 3.18. Earthquakes are not situated in the middle of the line but the reference receiver (virtual source) is.

By using deconvolution for geophones 25 to 35, the ambiguity of inverse moveout was removed and arrivals for long offsets placed at near zero time.

-Second sub set of simulation case b)-

Same as case a) but with increasing number of earthquakes

In the second sub-set, the total number of events used was incremented by taking events every 10 km, from a distance of 100 km to a distance of 200 km. For these cases we used cross-correlation and convolution, as appropriate.

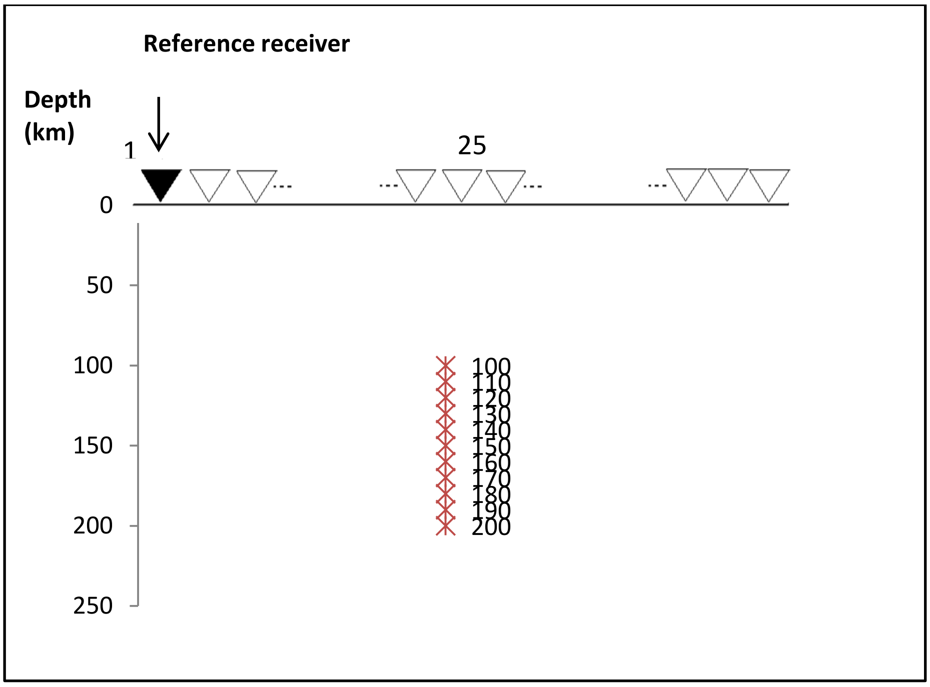

Figure 3.23 Second set of simulations, second sub-set, case 2. In this case, more earthquakes are present compared to the previous simulations. Depths vary between 100 and 200 km and the reference receiver is situated at one extreme of the line.

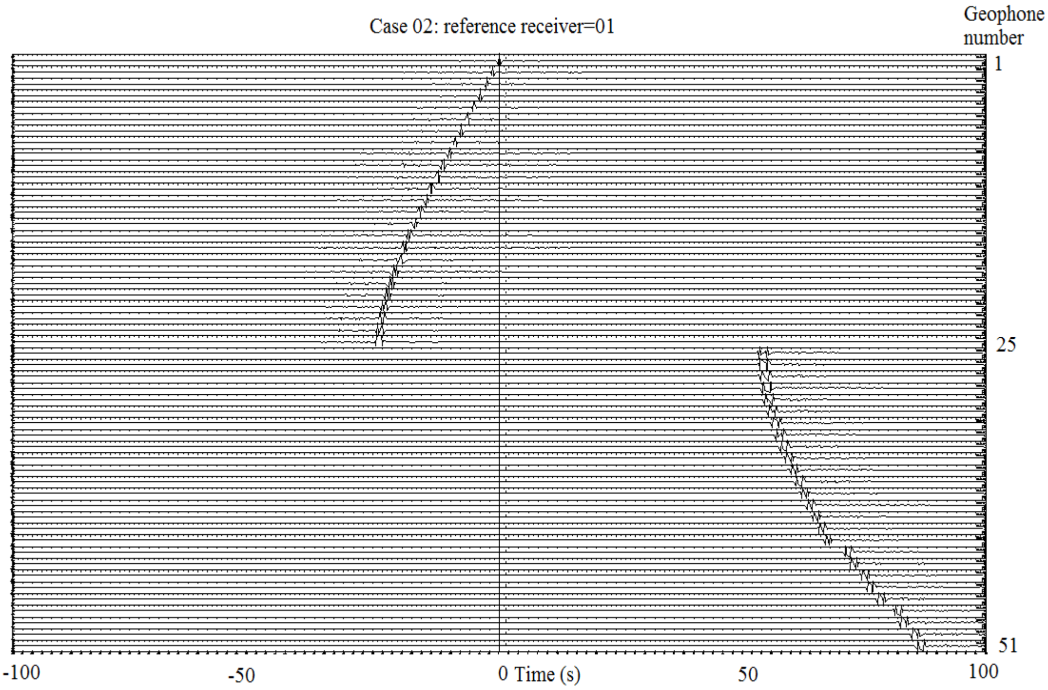

Figure 3.24 Result for second set of simulations, second subset, case 2. The geometrical configuration is presented in Figure 3.23. The combined process of convolution-cross-correlation was applied.

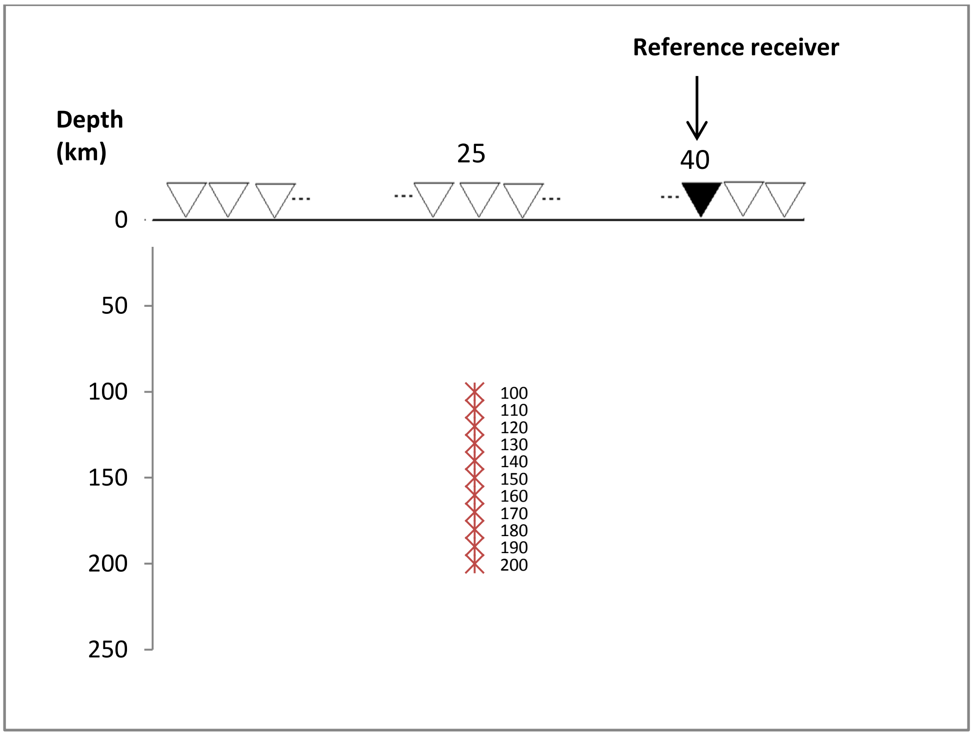

Figure 3.25 Second set of simulations, second sub-set, case 3. In this case, we have more earthquakes than in previous simulations with a range of depth varying between 100 and 200 km. Reference receiver (virtual source) is at geophone 40.

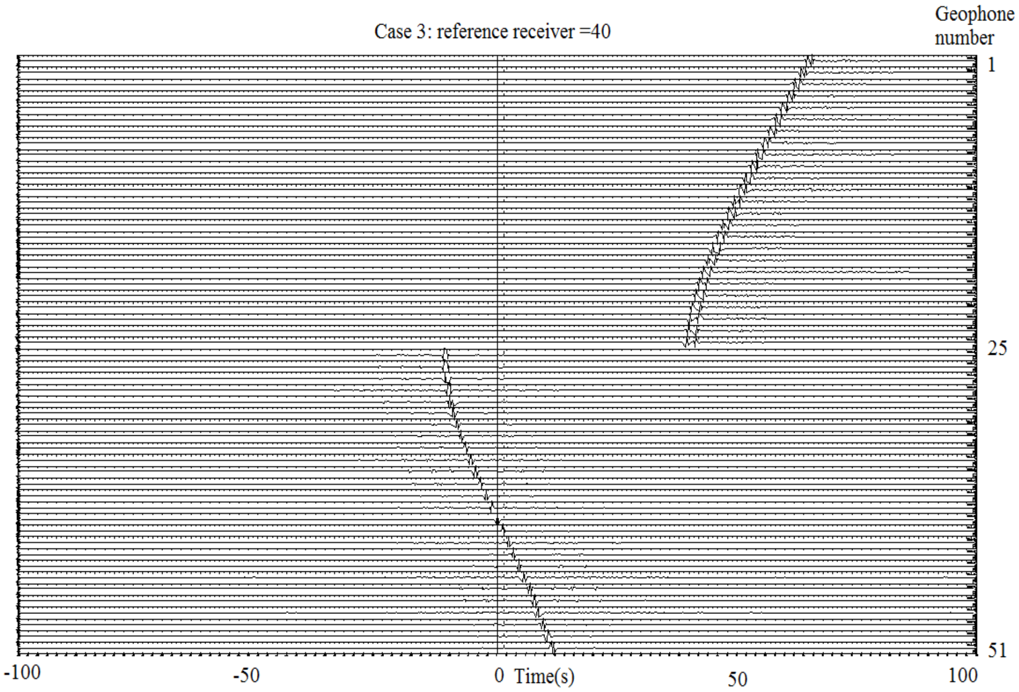

Figure 3.26 Result for second set of simulations, second sub-set, case 3. Geometrical configuration is shown in Figure 3.25.

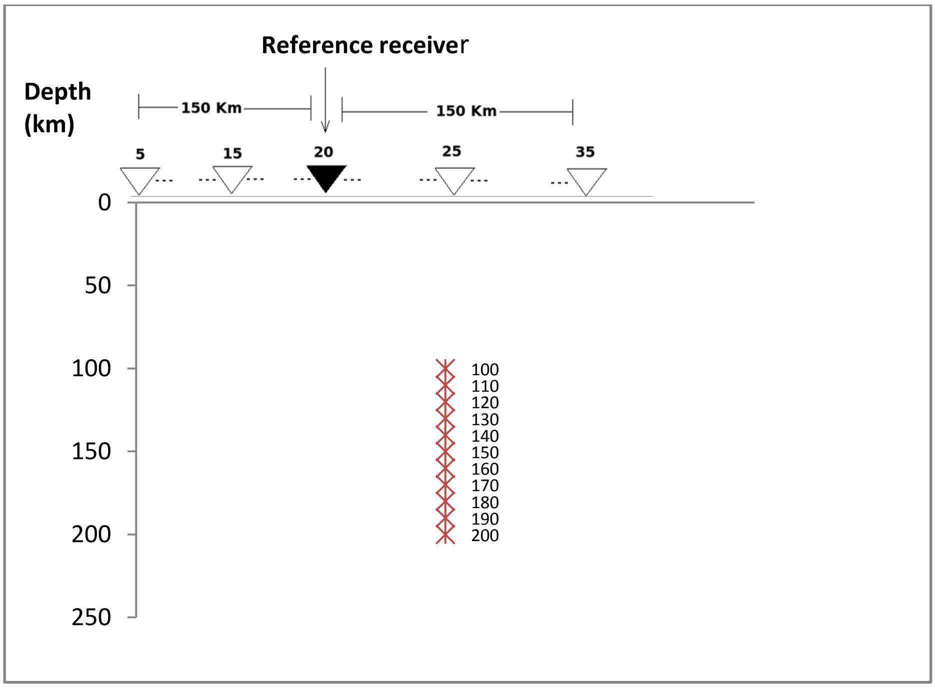

Figure 3.27 Second set of simulations, second sub-set, case 4. The range of depth for earthquakes is 100-200 km. Earthquakes are not centred but the virtual source (reference receiver) is.

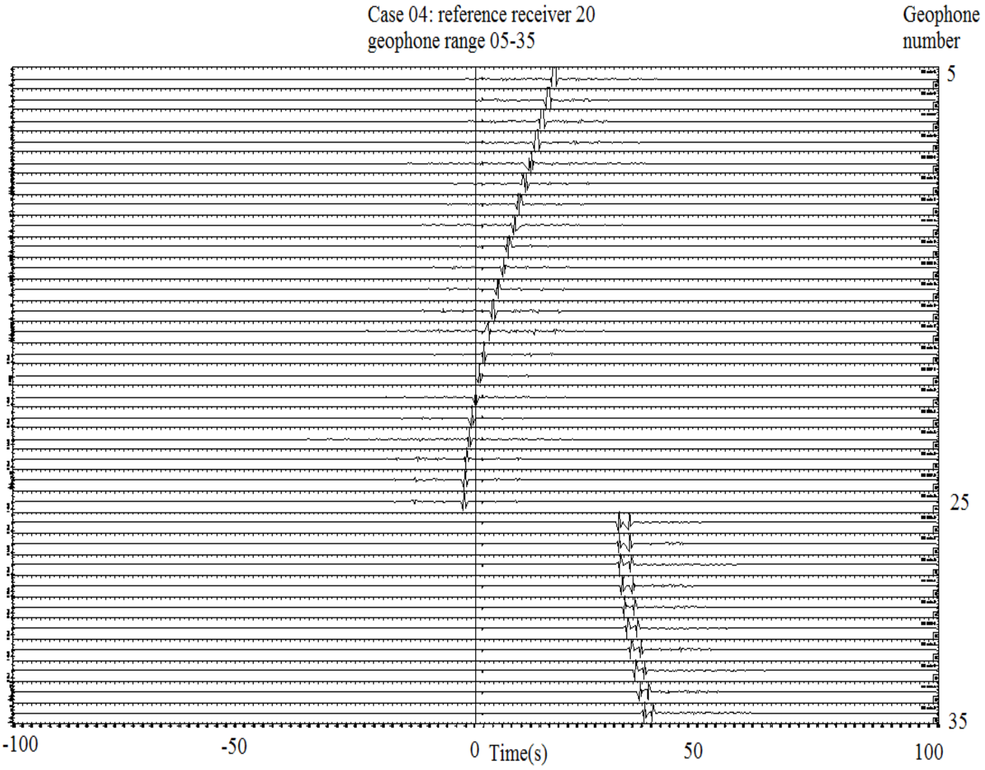

Figure 3.28 Result for second set of simulations, second subset, case 4. Geometrical configuration can be appreciated in Figure 3.27

In the case of the Figures 3.24, 3.26 and 3.28 a more coherent arrival can be observed, compared with the arrivals in Figures 3.20, 3.21 and 3.22. This is due to the fact that more events have been taken into account which has eliminated the effects of poor sampling on the source boundary produced by considering only 4 events, as was the case in the first set of simulations.

-Third set of simulations-

The third set of tests consisted of applying cross-correlation or convolution to events whose depth varies between 0 and 200 km every 10 km

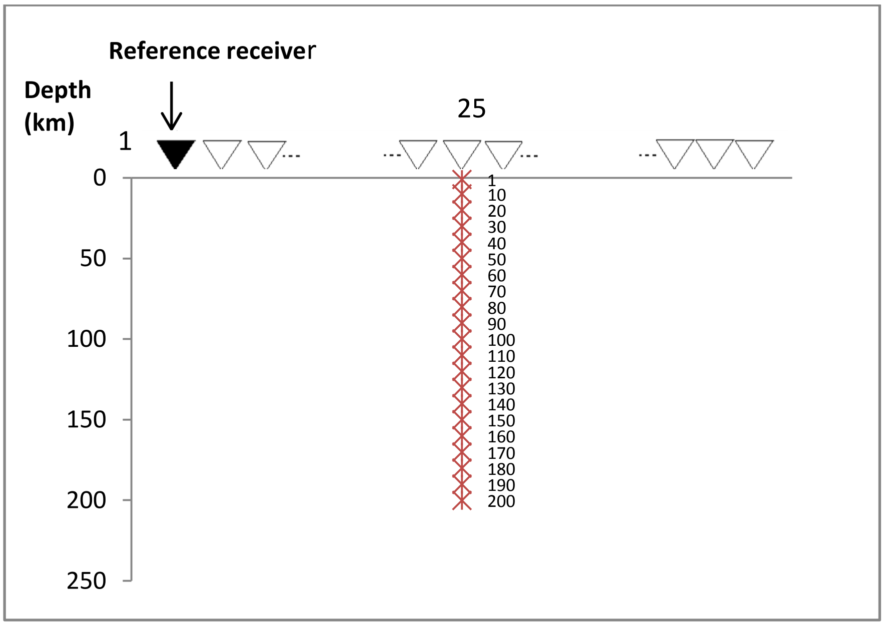

Figure 3.29 Third set of simulations, case 2. A new element present here is that earthquakes reach the surface as shown here.

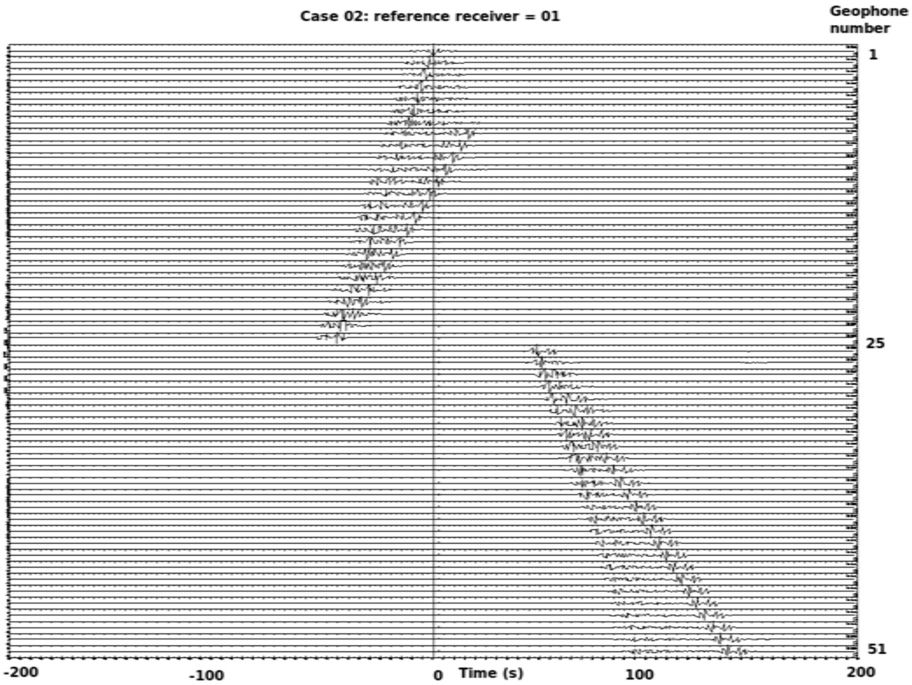

Figure 3.30 Result for third set of simulations, case 2. Geometrical configuration is shown in Figure 3.29.

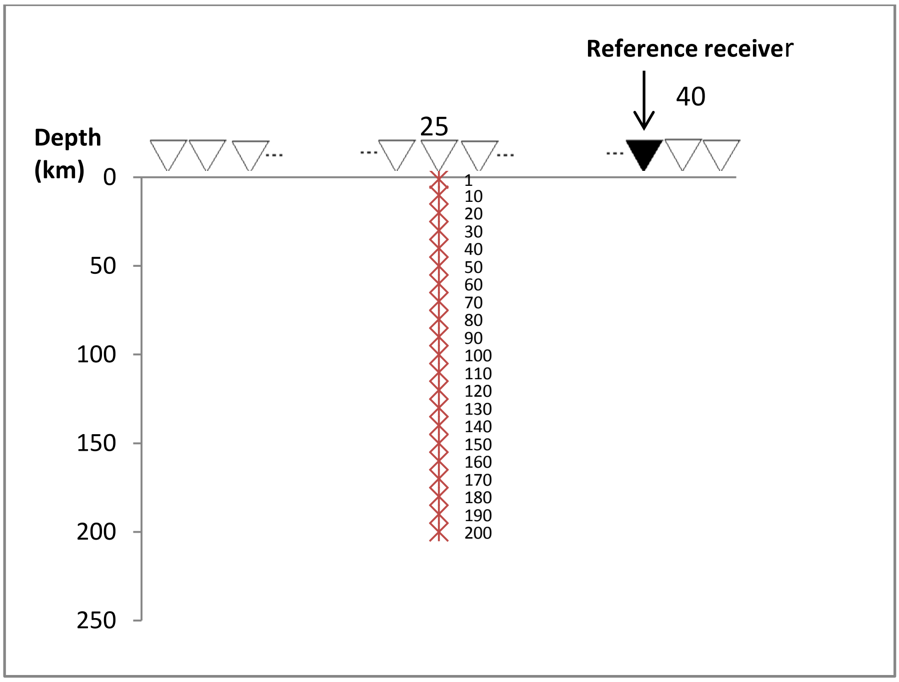

Figure 3.31 Third set of simulations, case 3. In this case, earthquakes reach the surface. Earthquakes are situated in the middle of the line and the reference receiver is set in geophone position 40.

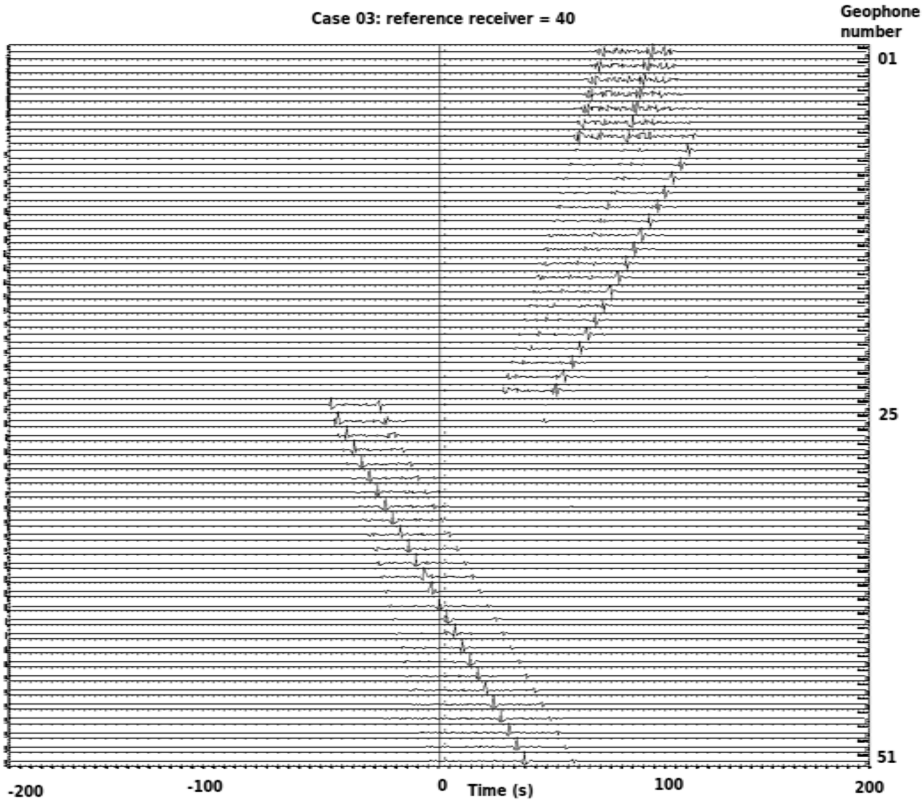

Figure 3.32 Result for third set of simulations, case 3 whose geometrical configuration is shown in Figure 3.31

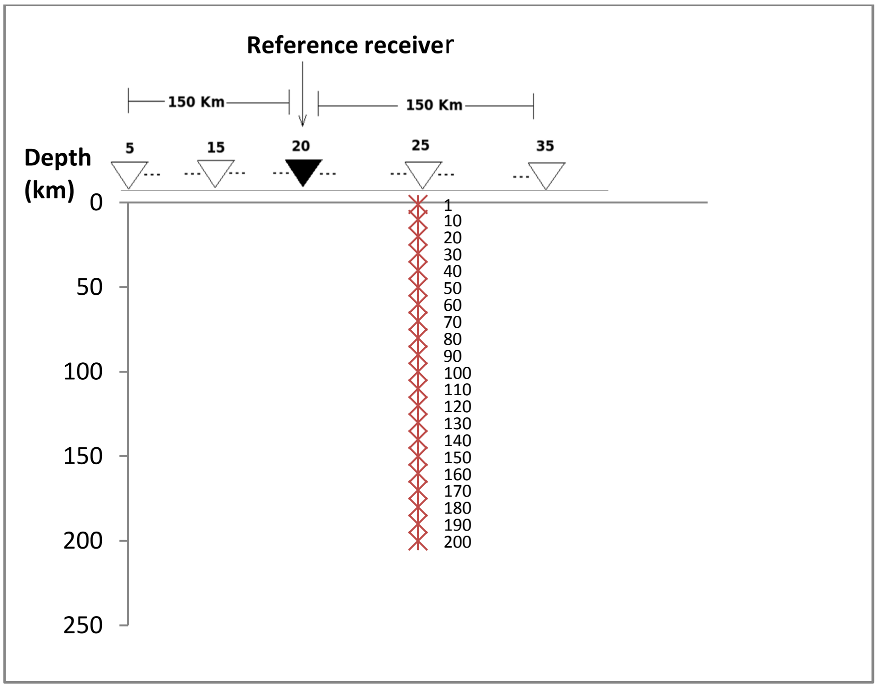

Figure 3.33 Third set of simulations, case 4. Earthquakes reach the surface and are not situated in the middle of the line. The reference receiver is, for this case, in the centre.

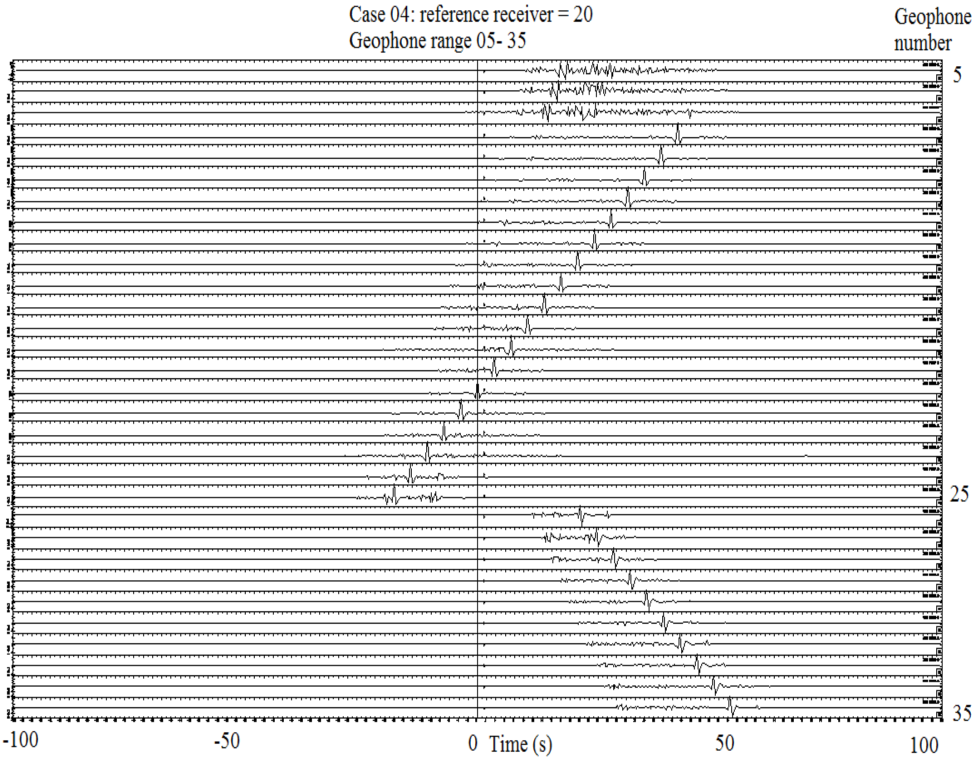

Figure 3.34 Result for third set of simulations, case 4 whose geometrical configuration is shown in Figure 3.33.

In this case, two important factors had to be taken into account. The first was that the modelling code produced surface waves when the depth of the receiver was close to the surface. Therefore, Figures 3.30, 3.32 and 3.34 show straight lines - which are different from the previous figures.

The second factor to be considered was that, in this case, events reached the surface and varied in depth with a dense sampling of 10 km. A comparison of Figures 3.24, 3.26 and 3.28 with previous cases revealed that the “jump” produced by geophone 25 was equal in magnitude on both sides of the causal and acausal part of the Green’s function.

From these simulations it can be concluded that the “jump” difference was as a result of a lack of sources reaching the surface. This can be because of the additional illumination that produces the sources close to the surface. It must be remembered that the jump is produced where sources are located. This could imply that to retrieve body waves in a correct way one needs a distribution of sources that reach the surface and this is true for surface waves as shown by Halliday and Curtis (2008).

3.5.5 Discussion of the synthetic tests

The results of all simulations can be summarised by discussing how the variation of each parameter influences the final interferometric result. If the reference receiver lies in the same position as the “centre of mass” of the cloud of events the retrieved wave travels towards each side of the reference receiver and no inverse moveout is present (as in Figure 3.13). This case is the simplest possible and is not repeated in the rest of the simulations.

In the case where the reference receiver lays at one end of the line the retrieved wave travels in one direction along the array, as in Figures 3.15, 3.23 and 3.29. The more general case in which the reference receiver lies at an arbitrary position within the array will result in waves travelling on both sides of the array but waves travelling beyond the “centre of mass” of the clusters of events will be affected in their moveouts and need to be corrected using convolution instead of cross-correlation (Figures 3.17, 3.19, 3.20, 3.21, 3.22, 3.24, 3.26, 3.28, 3.30, 3.32 and 3.34).

In relation to the effect of introducing the combined methodology of convolution and cross-correlation the result is that the methodology allows the resolution of the problem of inverse moveout as can be appreciated in the second set of simulations, as well as to compensate for the jump observed by considering the transition from adding phases to subtracting phases that naturally rises from the geometrical setup of geophones and earthquakes.

Another factor to take into account is the number of earthquakes or events used to perform the calculations. Apparently, increasing the number of earthquakes has no effect on the final “behaviour” of the waves retrieved as can be seen by comparing the first set of simulations with the other sets of simulations.

Finally, varying the position of earthquakes is important because the “centre of mass” of the cluster of events mark an important point where cross-correlation has to be abandoned and replaced by convolution. Also, illumination has to be taken into account i.e. if events do not reach the surface there will be missing information in the retrieved Green’s functions as shown in Figures 3.20, 3.21, 3.22, 3.24, 3.26 and 3.28. This is because it is expected that the intensity of the “jump” on either side of the retrieved waves would be the same in value (continuity of the curve) on either side where the “centre of mass” of the events is situated. We know that this problem is an illumination one because when events reach the surface such problems are less pronounced (remember that for these set of synthetic tests we started with a depth of 1 km) and additionally, in this case surface waves dominate as show in Figures 3.30, 3.32 and 3.34.

Halliday and Curtis (2008) demonstrated the importance of subsurface source distributions for the correct retrieval of surface waves. Forghani and Snieder (2010) concluded that possible problems encountered when extracting Green's functions must be caused by imperfection in the source distribution. In this chapter, it was demonstrated that a distribution of sources reaching the surface is necessary when correctly describing the interferometric results of the proposed method of combined convolution-cross-correlation. Also, it demonstrated that relative positions of sources at depth, geophones at the surface and virtual source position have to be taken into account at the same time when applying the proposed mixed method.

3.6. Discussion

From previous studies (Yuan *et al.*, 2000; Heit, 2005; Wölbern *et al.*, 2009) and from results presented in this current work, it can be confirmed that the area of study presents strong heterogeneities near the top of the slab and a low velocity anomaly in the upper crust, as well as a high velocity body between 100 km and 150 km depth.

This complexity translates into a data set that was difficult to analyse. Moreover, interpretation of deterministic phases other than S and P arrivals could be difficult and, in fact, led to misinterpretation of phases. For interferometric purposes, if the intention is to suppress these deterministic phases, there is a risk of also suppressing useful signals.

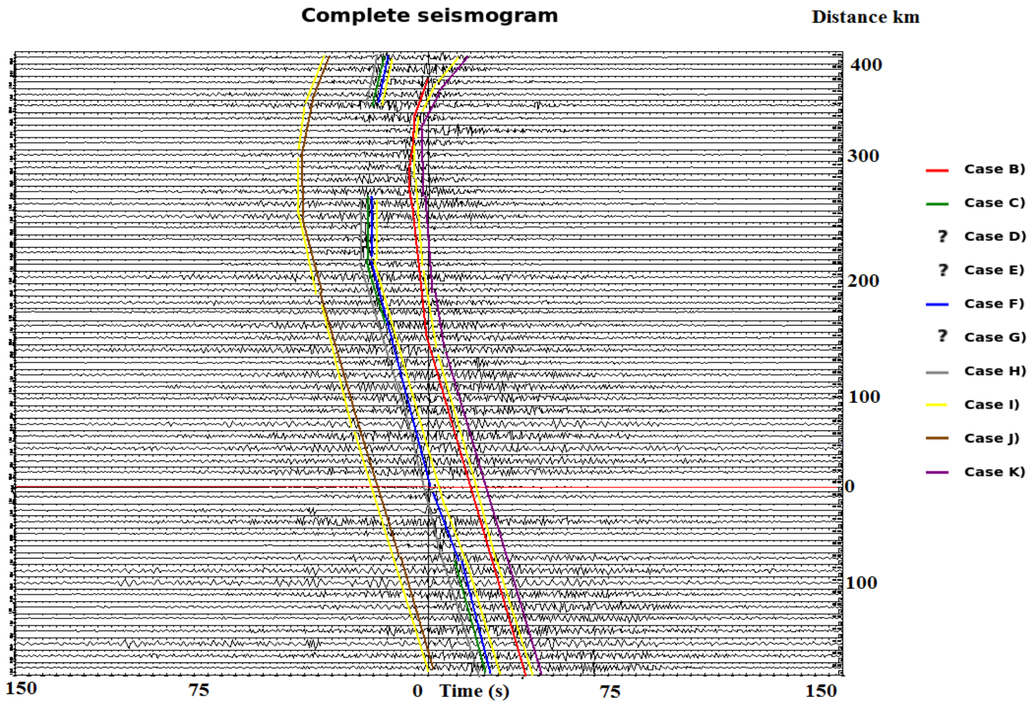

Figure 3.35 Interpretation of the different cases studied. Interpretation for every case has been drawn with different colours. Different cases may superimpose but were shown slightly separated for display purposes. The ? Sign in the figure key means that no information was interpreted from the curves displayed.

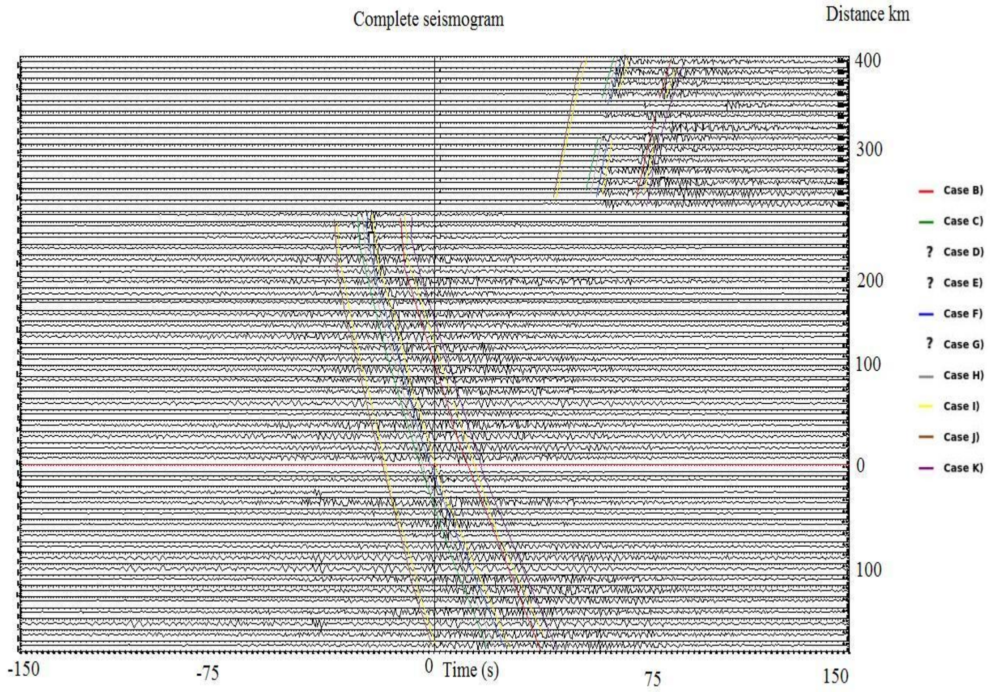

Figure 3.36 Application of the methodology to real data. Interpretation for every case has been drawn with different colours. Different cases may superimpose but were shown slightly separated for display purposes. The ? Sign in the figure key means that no information was interpreted from the curves displayed.

The application of the methodology to real data shows features expected from the results and conclusions drawn from the simulations. Please note, for example, that inverse moveout has been removed and that an asymmetrical jump is present, which can be explained by the fact that earthquakes chosen for this study where deeper than 100 km.

In this study it has been shown that coda P has relevant information about waves travelling between receivers, as opposed to the work of Tonegawa *et al.* (2009) where S coda waves were used to retrieve information about travelling waves between receivers. It is important to point out that this is not the first time coda P has been used for retrieving body waves travelling between receivers.

In fact, Abe *et al.* (2007) used coda P waves to apply interferometric seismic imaging [a procedure first introduced by Schuster *et al.* (2004)] to a dense-array experiment conducted at the Northern Fossa Magna basin, central Japan. From the work of Abe *et al.* (2007) it was not clear whether all direct P, S and reflected waves could be retrieved by cross-correlation of the waves recorded at two receivers. Also, another disadvantage of the work by Abe *et al.* (2007) was the introduction of spurious reflectors due to the interferometric procedures that can lead to migration artifacts.

Figure 3.4 can now be interpreted based on all the tests made so far. The decomposition into cases conducted in section 4 helped with the interpretation of Figure 3.4 in the sense that we can now describe the contribution of all possible terms to the final plot. In Figure 3.35, all the different cases have been shaded with different colours and maintained in their original positions. It is important to mention that different cases have different amplitudes; therefore they contribute differently to the final result.

The inverse moveout already mentioned in section 3.5 can now be explained as a product of the relative position between reference receiver, real earthquake and geophone. Of course, we have a wide distribution of earthquakes in the real data and not a vertical line of events like that of the numerical simulations. Nevertheless, if a "centre of mass" is defined for the whole cluster of earthquakes, the position of that "centre of mass" can be considered approximately as our boundary where cross-correlation has to be abandoned for convolution. This fact of changing cross-correlation to convolution clearly compensates for the inverse moveouts shown in Figure 3.4 as was seen from the application of the new methodology of combined correlation and convolution and depicted in Figure 3.36.

Results from simulations show that the distribution of sources will impact on the interferometric results. For example, if sources are close to the surface, then surface waves will dominate the results. Another point of influence is the "jump" present when cross-correlation passes over to convolution. As seen from the simulation, this jump is due to an incomplete distribution of sources.

Interpretation of the slopes of the curves depicted in Figure 3.35 shows that their values give information concerning the wave speed of P and S waves travelling through the medium. The velocity of these travelling waves compares well with the theoretical P and S velocity predictions for the area. This method has given information about the speed of P and S waves, travelling through the medium, which in this case were Vp= 9 km/s Vs= 5 km/s respectively. Also, along the whole range of offsets we can have information about the variation of the P and S velocities by looking into the plot in Figure 3.35.

3.7 Conclusions

It has been shown that cross-correlation of coda P waves can be used to detect body waves travelling between receivers. As demonstrated in this study, in the case of local events, deterministic phases and coda P are the only carriers of information from the interferometry point of view. This can be interpreted by taking into account the strong attenuation present in the area that plays the role of suppressing S waves and is highly likely to interfere with the interferometric results for coda S waves.

This result contrasts with that from Tonegawa *et al.* (2009) where they made use of coda S to detect direct and reflected body waves. Results from simulations can be extrapolated in order to explain results from real data. In the case of real data, events are dispersed in a cloud-like manner. Nevertheless, the bending observed for long offsets (like that shown in Figure 3.5) can be explained by the use of correlation instead of convolution as the main operation for interferometric calculations.

From this chapter, is it clear that a methodology combining cross-correlation and convolution is needed to describe correctly the geometrical set-up of our research from the point of view of seismic interferometry. Recommendations for broadening this study include a possible test to consider the events occurring alongside the low velocity zone studied in the work of Heit (2005), in order to check whether any additional information can be retrieved. Another factor to be taken into account is that the retrieval of body waves depends on the distance of separation between two stations and also on the incident angle of the scattered waves. Future studies should test parameters such as distance of separation, attenuation and source mechanism.

Additional recommendations include imaging and incorporating complex information concerning velocities and structure of the medium by making use of interferometric seismic imaging. Also, a detailed study of the spurious signals introduced by interferometry, and how to remove them using algorithms that correct for such bias, are required.

Chapter 4

RETRIEVAL OF SURFACE AND BODY WAVES BY REFLECTED WAVE ARRIVALS

4.1 Summary

The intention of this chapter is to determine whether or not it is possible, using passive seismic interferometry, to reconstruct body and surface waves between receiver pairs. This was achieved by making use of passive seismic recordings over a continuous six-month period. The methodology included suppression of the earthquake signature in order to ensure that the only contributions were from noise sources.

Six months of data were processed along two different profile lines located in the Altiplano and Puna plateaux, respectively. Seismic interferometry was applied such that the virtual source was located within each line making the geometry a 1D problem using ambient waves travelling along those lines.

Results are in agreement with previous knowledge of the geology of each zone. For the Altiplano plateau, a change in the velocity of the propagation of the waves due to a low velocity zone, and different velocities of propagation depending on the direction of propagation, were observed. For the Puna plateau, two different wave packets were observed: one of them was thought to be due to body waves reflected at the Moho or a refracted wave travelling along the subducting slab. Numerical simulations were used in order to better understand other observed signals which are thought to be an internal reflection of waves travelling between the surface and the Moho.

4.2 Introduction

This chapter considers waves travelling in the crust of the Altiplano, as well as possible reflections from the Moho. Therefore, we first review research already conducted in the area and how it has contributed to the knowledge and understanding of the subsurface.

Before embarking on a discussion of previous research work in the area, it is important to clarify some points regarding the geology and the projects carried out in the Altiplano. Figure 1.1 shows the principal geological structures present in the Altiplano region and also the location of the geophones deployed for the SEDA and BANJO projects.

The Altiplano is the most extensive area of high plateau on Earth outside of Tibet, with an average elevation of around 3,800 m. It is part of an area composed of five major sub-parallel morpho-structural units as can be appreciated in Figure 1.1: The Western Cordillera characterised by an active volcanic arc whose peaks reach an elevation of up to 6000 m; the Altiplano, the current area of study; the Eastern Cordillera, a mountain range characterised by folding and thrusting; the sub-Andean zone, an active thin-skinned series of mountainous foothills formed due to contractional tectonics; and the Chaco plain, a large morphological unit whose main characteristic is the lack of relief and long term stability, underlain by the Brazilian craton.

The BANJO and SEDA projects were passive source broadband seismic experiments conducted by the University of Arizona in conjunction with other organisations. The BANJO project took place between April 1994 and September 1995 and consisted of 16 stations deployed along an east-west transect at 19° S to 20° S. The SEDA project consisted of seven stations set in a north-south profile along the Altiplano deployed between April 1994 and June 1995, with a station spacing of 50 km and a total length of 300 km.

Another project of interest is the ANCORP 96 project. This project was a combined near-vertical wide angle reflection/refraction seismic project, conducted by the German institute GFZ, and whose aim was to provide an image of the subduction process of the NAZCA plate underneath South America, as well as to characterise the velocity field of the region.

From the BANJO and SEDA data, Beck *et al.* (1996) estimated the crustal thickness along an east-west line in the Andes at a latitude of 20° S and along a north-south line traversing the eastern edge of the Altiplano. They found variations in the Moho depth of around 40 km, with a maximum thickness varying between 70 and 74 km in the Western Cordillera and a variation between 32 and 38 km in the Chaco plain. In the central Altiplano, Beck *et al.* (1996) calculated crustal thickness to be between 60 and 65 km. Also utilising data arising from this work, Baumont *et al.* (2001) inverted travel times of Pn waves in order to characterise the Moho geometry along the Altiplano (20° S). This was different from previous work at that time in the sense that it used receiver function techniques. They found discrepancies beneath the Western Cordillera, where they estimated that the crust was 10 km thinner than previous models.

Using data from the ANCORP project, Giese *et al.* (1999) found that the crustal structure changed considerably from east to west. In the eastern part, the Moho discontinuity was easily identifiable. Nevertheless, the Moho was not recognisable in the Altiplano and in the Western Cordillera. Giese *et al.* (1999) interpreted this fact as the result of several processes that changed petrological and petrophysical properties of rocks in the crust. They also found a pronounced discontinuity at a depth of 70 km, and at the coast, the oceanic Moho is found at a depth of 40 km. Another interesting research project conducted with data from the ANCORP project was that of Haberland *et al.* (2003). They re-assessed data from local earthquakes and calculated 3D attenuation (Qp) tomographic images. Their findings supported the idea of partial melts in the middle and lower crust beneath the Altiplano.

Not necessarily all the research done in the Altiplano comes from data acquired by temporal deployment of geophones. Some important geological work has also been carried out. For example, Schmitz and Kley (1997) used geological cross-section balancing, and interpolation of seismic data to reach the conclusion that in the Eastern Cordillera, high seismic velocities exist between the upper and the middle crust with an underlying thick low velocity zone.

Allmendinger *et al.* (1997) suggested the presence of processes such as magmatic addition, lithospheric thinning, upper mantle hydration and tectonic underplating as an alternative to the commonly held interpretation of uplifting produced by crustal thickening which in turn is associated with horizontal shortening. Wodzicki (2000) reviewed quantitative paleoelevation estimates made for the central Andes and examined the sources and magnitudes of errors for each estimate and his analysis implies that the Altiplano-Puna plateau and the Eastern Cordillera have undergone a rapid uplifting process since the late Miocene with an uplifting rate of about 0.2-0.3 mm/yr.

Brasse *et al.* (2002) performed a long-period magnetotelluric study along two parallel profiles deployed at 19.5° S and 21° S, respectively. They found a dominant geoelectrical structure in the middle and deeper crust beneath the Altiplano. The boundaries of this electrical body are in agreement with a seismic reflection profile (the ANCORP project). They also concluded, based on data from other studies as well as their own, that this body was most probably formed by granitic partial melts.

Other research conducted in the area has been based on the interpretation of data from different fixed geophones or temporal projects with a small number of stations. For example, Vdovin *et al.* (1999) presented a study of the dispersion characteristics of surface waves propagating across South America and the surroundings oceans. They presented group-velocity maps of Rayleigh and Love waves and identified many known geological and tectonic structures in the group-velocity map - such as sedimentary basins, continental roots, thermal anomalies and variations in the crustal thickness, especially for the Altiplano.

Chinn *et al.* (2007) classified and analysed shear waves in the frequency range of 0.5-2.0 Hz. Their observations confirmed that lateral variation of the Sn propagation velocity occurred. They also confirmed the complexity of the area where, in some parts, no propagation of Sn waves was observed while in others they were seen to propagate efficiently. This last fact has previously been associated with the possibility that the Sn phase was refracted along the descending plate instead of travelling mainly through the over-riding mantle wedge.

An interesting piece of research, carried out with data coming from several temporary arrays belonging to different partners (Deutsche Forschungsgemeinshaft, US PASSCAL project, the Andes seismology group), was that of Yuan *et al.* (2002) who analysed P to S converted waves at the Moho, along with multiple waves reflected between the earth surface and the Moho, in order to estimate the Moho depth and the value of Vp/Vs. As a result of the study, they found that the Moho depth varied from about 35 km in the fore arc region to around 70 km beneath the Altiplano plateau. The Moho depth was estimated to be around 30 km in the Chaco plain. They also found that the Moho was deeper in the Altiplano than in the Puna plateau.

Zandt *et al.* (2003) used data from seven PASSCAL broadband seismic stations to delineate the lateral extension of what was thought to be a magma body (i.e. the partially melted zone). They found that crust above the partial melted body was characterised by symmetry of tilted axis and hexagonal geometry. They also postulated that anisotropy was due to aligned fluid-filled cracks produced by a normal fault which was related to the high elevations of the Altiplano plateau.

Lastly, the REFUCA project represents data from the area with the highest resolution so far. The data used in this thesis comes from that project, but other important interpretations and results have already been derived from it. For example, Heit *et al.* (2008) presented the results for the Altiplano northern profile (21° S) using tomographic inversion for P wave velocity anomalies. They found high-velocities on the west of the profile - indicating cold material from the fore-arc and a low velocity anomaly between the fore-arc and the volcanic arc relative to the presence of fluids. A strong low velocity anomaly was seen across the entire Altiplano plateau and between the inter-Andean and sub-Andean regions and a strong high velocity anomaly - which was thought to be caused by the Brazilian shield.

Wölbern *et al.* (2009) found similar structures for both plateaux, with some local differences. Similarities found were associated with a low velocity layer at a depth of 15 km, possibly indicating an area of partially molten material. Also, on both plateaux they found dipping interfaces cutting through the top of the low velocity layers; which is in agreement with the fault system known for the region.

Differences found between the plateaux were that for the Altiplano the thickness of the low velocity layer was about 20 km, the average thickness of the crust was 70 km and the zones of partial melting were well delimited. For the Puna plateau on the other hand there was no clear thickness of the low velocity layer, the average thickness of the crust was 60 km, and it was impossible to delineate the zones of partial melting due to the limited lateral extent of the deployment of receivers.

The intention of this chapter is to explore the methods of Zhan *et al.* (2010) applied to the Altiplano and Puna plateaux. Zhan *et al.* (2010) showed that it was possible to obtain body waves, under specific conditions, from the Moho reflections. Their argument and methodology were based on the work of Mori and Helmberger (1996) where they found that large amplitude SMS phases (S waves reflected from the Mohorovicic discontinuity) were caused when a simple structure was present which in turn, allowed large Moho reflections. On the contrary, when the geology is more complex, the seismic energy is partitioned into a more complicated set of seismic phases, giving amplitude-diminished Moho reflections as a result.

Even though Zhan *et al.* (2010) retrieved body waves for very simple Moho structures and the Altiplano and Puna plateaux geologies are very complex, there are still important questions to be researched. In this chapter, we will address the following research questions in the context of the work of Zhan *et al.* (2010): is it possible to retrieve body waves from Moho reflections as Zhan *et al.* (2010) did but for the Altiplano and Puna plateaux notwithstanding the fact than Moho geology is more complex that in the case presented by Zhan *et al.* (2010)? What is the influence of the strong and weak signals obtained in some parts of the Altiplano and Puna plateaux (Wölbern *et al.*, 2009) in relation to body wave retrieval using interferometry? What other factors, apart from geological complexity of the Moho, influences the retrieval of surface or body wave in the Altiplano and Puna plateaux?

4.3 Data used and processing methodology

As shown in Figures 4.1 and 4.2, the deployment of receivers consisted of two parallel lines, labelled as the northern line (RF) and the southern line (PC), where the acronyms RF and PC denotes the network code to identify geophones of the REFUCA project belonging to the northern and southern profiles respectively. The northern profile, located in the Altiplano plateau, included a total of 59 seismological stations that were deployed from March 2002 to January 2004. The northern profile had a total length of 600 km and station spacing about 10 km.

The southern profile, located in the Puna plateau, consisted of 19 seismological stations, deployed from July 2002 to January 2004. The southern profile had a total longitude of 200 km and a station spacing of 10 km.

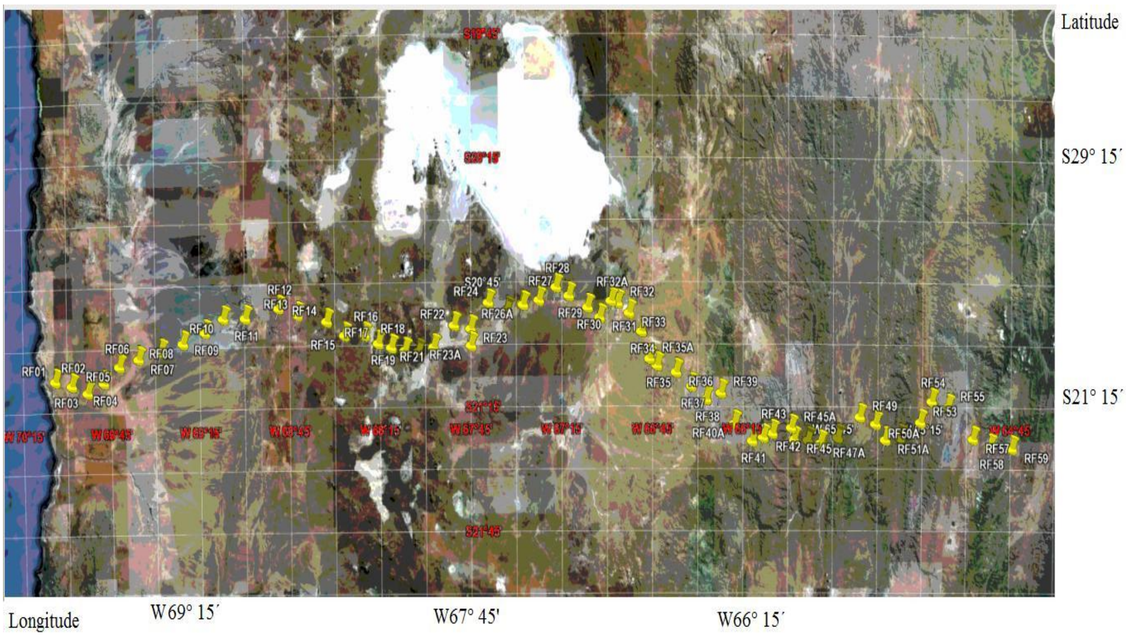

Figure 4.1 A closer look into the deployment of receivers for the northern line.

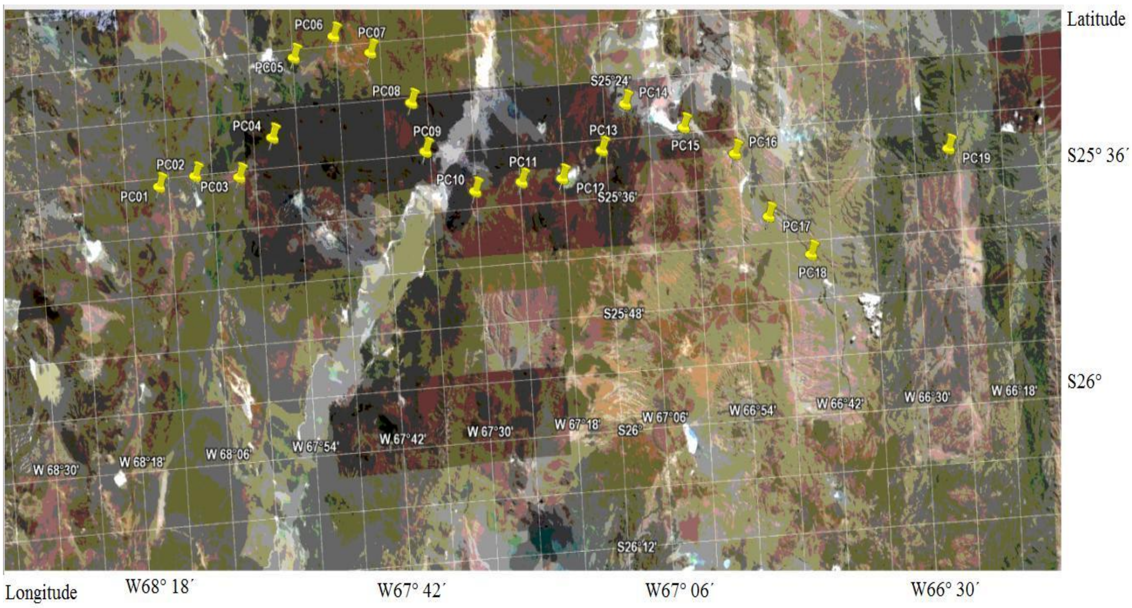

Figure 4.2 A closer look into the deployment of receivers for the southern line

Continuous recordings of six months of data, between March 2003 and August 2003, were downloaded in segments of one day. Then, these segments were processed following the methodology introduced by Bensen *et al.* (2007), which has proven to be effective in suppressing the earthquake signature.

A critical point to take into account regarding this research is the functioning of the geophones during the acquisition time period. Figures 4.3 and 4.4 show the operation of the geophones for the selected six-month period, for northern and southern lines respectively. An additional important factor in the case of the southern profile is the short distance of the line compare to that of the northern profile that limits the lateral resolution of structures of interest.

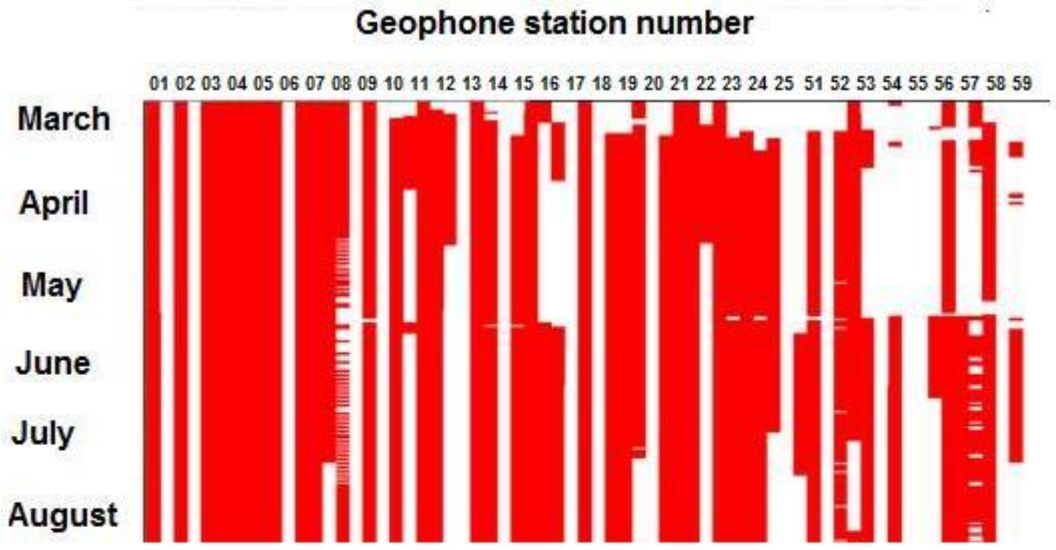

Figure 4.3 Periods when each of the geophones in the northern line were operational in the selected six-month period are shown by red blocks.

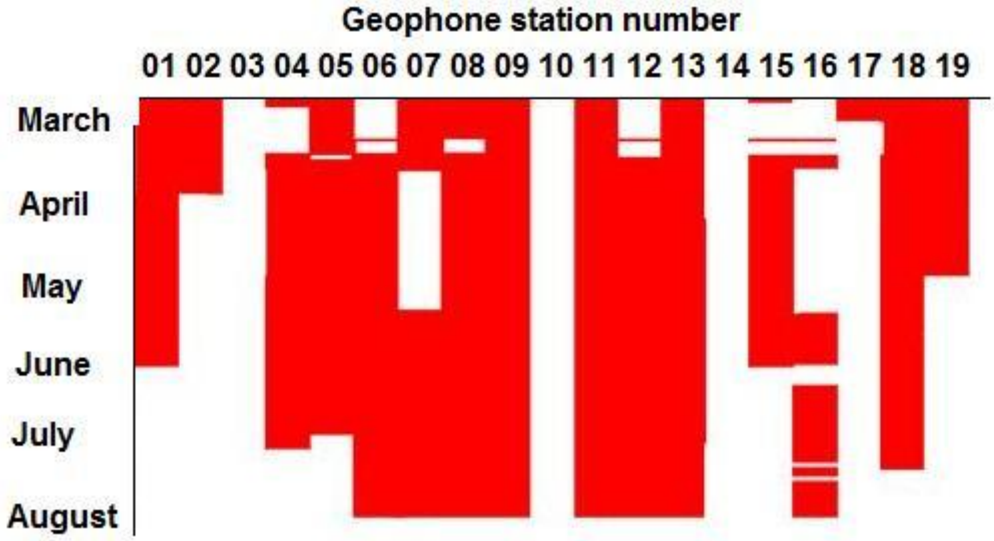

Figure 4.4 Periods when each of the geophones in the southern line were operational in the selected six-month period are shown by red blocks.

Another influential factor was that of the quality of the data for both lines. Even though a geophone could have been in operation during the period of time of interest this was not a guarantee of the quality of the data obtained. Regarding this point, visual quality controls were performed in order to guarantee the good quality of the data, before the application of the interferometric procedure.

The procedure used to process the data is analogous to that proposed by Bensen *et al.* (2007). In this part of the research, continuous recordings, from March 2003 to August 2003, of one day long each were downloaded from the GFZ servers.

Following this downloading process, records were resampled at 8 ms. The mean, linear trend and glitches were removed. Then, the processed seismograms were filtered by a bandpass filter between 0.04 to 1.0 Hz. Following that and in order to remove the effect of the earthquakes, envelope functions were calculated.

The smooth versions of the inverse of these envelope functions were used to weight the corresponding filtered seismograms between 0.04 and 1.0 Hz. Then, cross-correlations were computed over day segments and the daily correlations were then stacked. All the cross-correlations were normalised by their maximum amplitude, in order to prevent anomalous data from contaminating results, and also to avoid residual effects of earthquakes. Finally, to make the robust frequency ranges in the results more visible, a bandpass filter was applied.

As was mentioned in chapter 1, the principal mathematical operation is correlation by the use of equations 1.11 and 1.12. In this chapter, main figures will be depicted, explained and discussed. Additional supporting figures will be shown in appendix B.

4.4 Results

In this section, main figures will be shown and the remainder of the figures are attached in appendix B. Results of the application of seismic interferometry on the Altiplano (21°S) and Puna (25.5°S) profile lines are presented. For both lines, the resulting Green’s function will be shown according to month, and then the final results for the six months of processing will be presented. As will be made clear from this chapter, the quality of the data for the Puna plateau was inferior to that of the Altiplano.

For the Altiplano, the virtual source position was varied between geophones RF12, RF14, RF17 and RF19. The reason for doing that was to compare the interferometric Green’s functions along the receiver line. Unfortunately, for the Puna plateau the virtual source position was kept the same, at PC09, due to malfunctioning of the other receivers along the line, and also due to the limited number of geophones available that worked properly for the period of time considered in this chapter.

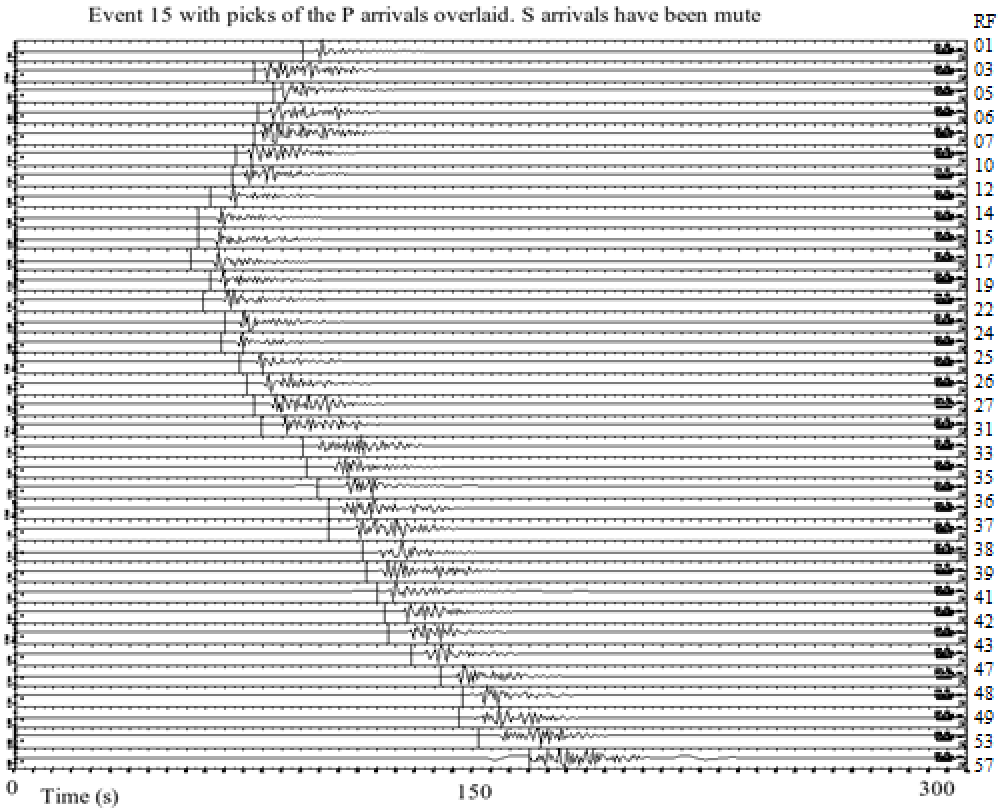

Figure 4.5 Seismogram for event 15 (see chapter 2)

Figure 4.5 shows a typical earthquake record with a magnitude of 5.2 and a depth of 111.10 km (for more details and location, see chapter 2, event 15) that is shown here in order to make a qualitative comparison between this record and the retrieved waves obtained in this chapter. This qualitative comparison will tell us whether the synthetic seismograms reproduce the moveout characteristics of the real recordings.

4.4.1 Altiplano plateau (21°S)

Month of March 2003

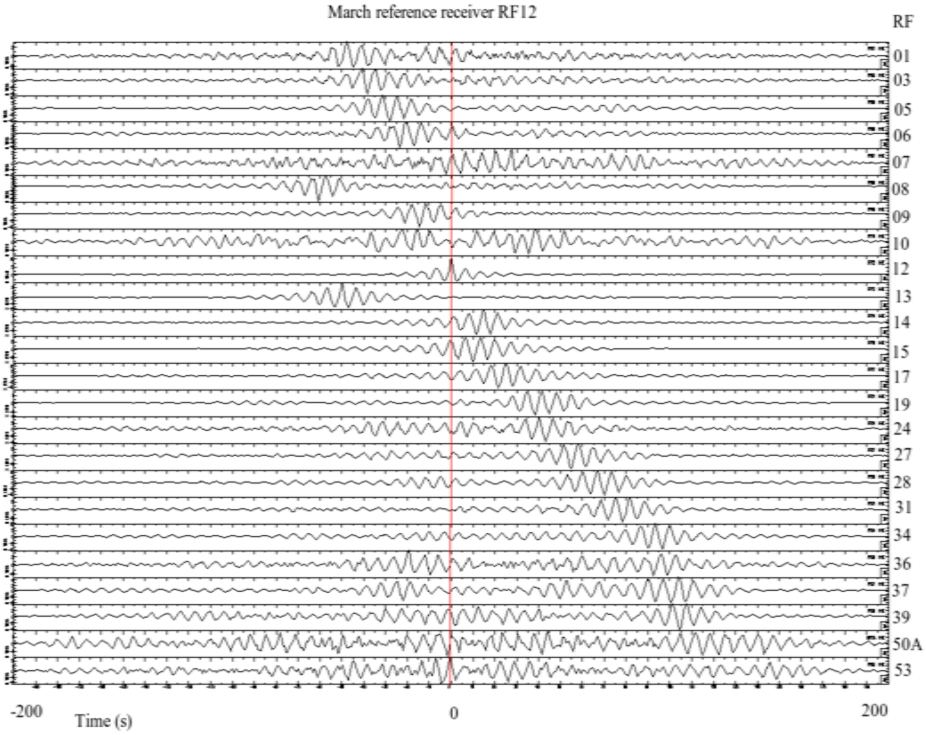

Figure 4.6 Estimated Green's function's for the month of March. Virtual source location at RF12.

For this figure, the following characteristic features can be seen:

- Two different slopes for each side of the array.
- The noise of the retrieved Green´s function is bigger from geophone 36 onwards, and also near geophone 12.
- The dispersion of the wave packet seems to be big, this will be analysed in the next section.

4.4.2 Puna plateau (25.5°S)

Month of March 2003

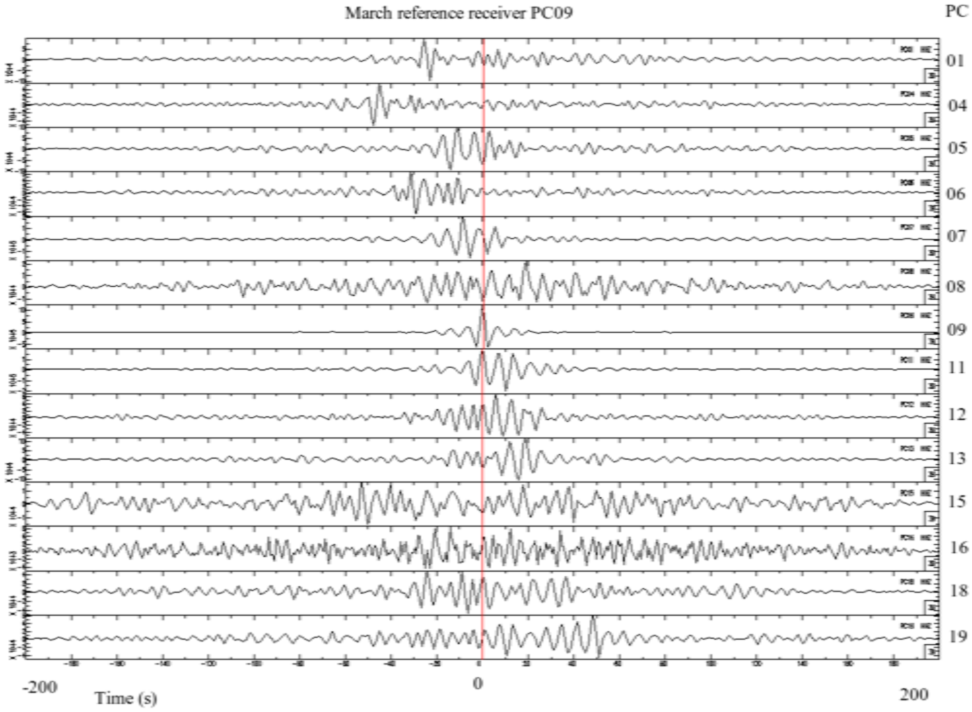

Figure 4.7 Green´s Function for the month of March. Virtual source location at PC09

For the Puna plateau month of March, the following characteristic features can be seen:

- Two different slopes for the same side of the array.
- The noise is incremented from geophone 15.
- Dispersion looks smaller than in the Altiplano case.

Turning now to the complementary figures depicted in appendix B.

As can be observed from Figures B.1, B.2 and B.3 there was a clear wave packet travelling along both sides of the line. Apart from this clear signal, and for positive times, there was a partially-coherent signal, starting from geophone 34 and running between 0 and 100 s until the end of the line.

In the month of April, the range of offsets used was longer, essentially because they were available as other stations became operational. It can be appreciated from figures B.4, B.5, B.6 and B.7 that at the end of the line the retrieved signal vanished, and also that the slope of the curve changed near geophone 33. Again, a weak signal was present (not as coherent as in the previous month) for positive times between 0 and 100 s and for long offsets.

Figures B.12, B.13, B.14 and B.15 show essentially the same characteristics as the previous figures for the months of March, April and May: i.e. noisy behaviour at the end of the line (western part), and a trend towards a change of slope in the middle of the line, as well as a weak signal at positive times between 0 and 100 s and for long offsets.

The results from July presented a somewhat curious feature, in that the maximum offset at which the wave arrivals were observed was clearly dependent on the location of the virtual source. As can be seen from Figures B.16, and B.17, where the signal become noisy at the end of the line, and in Figures B.18, and B.19, where the signal is still noisy but a little clearer than for the case when the virtual source was located at RF12 and RF14, respectively.

In the month of August, changes in the slopes of the waves retrieved were more obvious (see Figures B.20, B.21 and B.22 near receiver 42). Curiously, August was the month where seismic activity was stronger - as can be appreciated from figure 5.23 in chapter 6.

In the case of the Puna plateau, the quality of data was not as good as that for the Altiplano. Moreover, it can be seen from Figure B.1 to B.27 that, for the months of June, July and August, the dispersion of the data was more obvious than for other months. Also note that, due to limitation in the offset of the line, the features such as the change in the slope of the curve for long offsets observed for the case of the northern profile (RF) could not be observed here.

Figures B.28 to B.31 show all the features observed (i.e. changes in the slope near the centre of the line, a weak signal for times between 0 to 100 s and long offsets) in the graphs by months shown previously as was expected. Nevertheless, they appear to be a little noisier in some cases. For example, see Figure B.29 (reference receiver at RF14) where it can be seen that the retrieved signal for offsets beyond geophone 36 are difficult to appreciate. Nevertheless, the same situation is not seen in graphs B.28, B.30 and B.31. This can be interpreted as the dependence on the position of the reference receiver in relation to the correct reconstruction of the Green’s function.

4.5 Discussion

4.5.1 General remarks

Figures B.28, B.29, B.30, B.31 and B.32 depict the stack of correlations over six months of data and look a little bit noisier than those of the separated months. This is due to the fact that, in some months, the quality of the retrieved signal was better than in others. Usually, the quality of the signal is expected to improve as more data is included in the final stack. Nevertheless, the intermittent functioning of the geophones in this current project makes the summation process noisier in some cases. This fact is an indication that it is important to take arrays that are functioning in a discontinuous way in time into account before stacking.

Another factor equally important is the position of the virtual source. The Altiplano is a complex area with strong variations of geological features that depend on the position (of a geophone, for example) within the area. An example of such influence is the zone of partial melting, situated in the middle of the northern profile (line RF) which affects the propagation of S waves as was seen in Figure 3.1 of this thesis.

Changes in the noise production mechanism are an important issue to take into account. Consider Figures B.1 to B.27. It can be observed that depending on the month, the sum of the Green’s functions retrieved gives a better quality results than others. This is an indication that not only the position of the virtual source is important (as was mentioned when showing the results from Figure B.29) but also on how the noise is produced. In fact, these temporal observed variations of the Green´s functions can be explained by the non-stationarity of the arriving phases.

For example, De Stefano and Clemente (2006) showed that slight non-stationarity of wave phases can cause slow changes in the amplitude of the correlation functions. Changshen and Zhongliang (2009) found that the properties of the noise correlation functions depend on two factors: the underlying mechanism (diffuse wavefield or uncorrelated noise) and the time length of the recording. Tanimoto *et al.* (2006) also found that the variation of the noise correlation function is linked to seasonal variations in the relative excitation of higher modes compared to dominant fundamental-mode Rayleigh waves.

This point is clear from the results presented for the Puna plateau. Dispersion was strongest in the months of June, July and August making the final wave packet (Figure B.32) look more dispersed, even despite the fact that for the months of March, April and May the wave packet was more compact. Curiously, for the months of June, July and August, the seismic activity was more intense - as can be appreciated in Figure 5.23 of Chapter 6.

4.5.2 Body and surface wave retrieval

The intention of this section is to demonstrate with a couple of examples how the calculation of the velocities of the retrieved curves was completed. In the first example, the graph from March 2003 will be used in the calculations for line RF. In a second example, results for line PC will be shown, using the month of March 2003. This month was chosen because of the clarity of the signal and also because two different wave packets were observed, with one of them probably being a refraction travelling through the subducting slab and the other a reflection.

An analogous situation is when a seismic survey is shot and the different slopes of the first arrivals, in the shot records, are present. This change in the slopes of the shots records means refraction. In the case of this piece of research, the assumption is that the same refraction behaviour is present here as well. Nevertheless, care has to be taken interpreting the results because of the uncertainty in the data (intermittent functioning of receivers, quality of data) by that it means that changes can be due to a change in the surface wave group velocity along the line.

In Figures 4.8 and 4.9, the methodology by which the trend (slopes of the curves or velocity of the retrieved waves) is found is the following: For every Green´s function retrieved the envelope function is calculated, this defines a wave packet. The trend is found by connecting the middle of the wave packet (shown in blue) of all Green´s functions. The dispersion of the wave packet defines the error in calculating the velocity of the retrieved waves (depicted by the two red lines around the blue one).

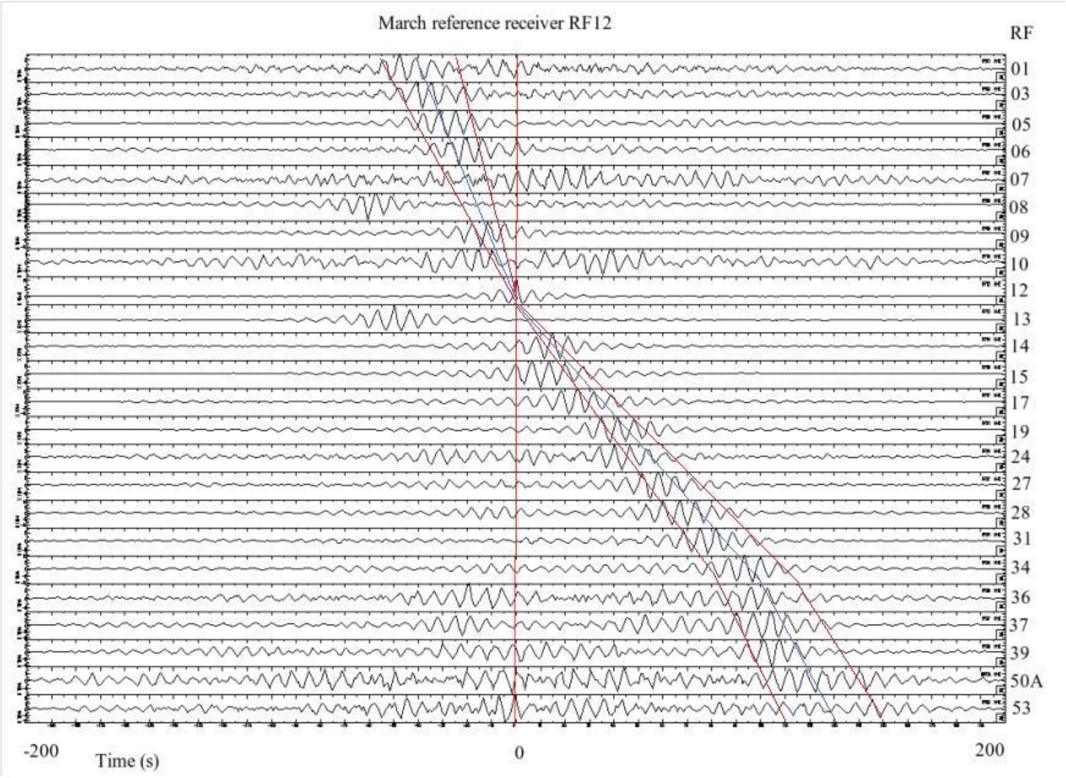

Figure 4.8 Waves retrieved for the month of March, northern profile. Virtual receiver at RF12. Data used in this section for velocity calculations were taken from this figure. The trend is found by connecting the middle of the wave packet (shown in blue) of all Green´s functions. The dispersion of the wave packet defines the error in calculating the velocity of the retrieved waves (depicted by the two red lines around the blue one).

Example 1: waves retrieved for northern profile (RF)

As can be appreciated from Figure 4.8, the virtual source location is in position RF12 and, from there, two waves packets could be seen travelling in opposite directions along the RF line. Here, velocities of these two travel packets were measured using the slope of the graph. It was clear that three different slopes were present; one between the start of the line (RF01) up to the virtual source location (RF12) and the other from the location of the virtual source (RF12) up to the geophone (RF34), and the third from RF34 up to the end of the line (RF53) . For all slopes, the velocities are such that:

One side of the northern (RF) line. (eastern part)

Case month of March, reference receiver at RF12.

Geophone position (Latitude, Longitude)	Travel time (s)	Inter-receiver distance (km)	Group velocity (km/s)
RF12(-20.89591;-6882790) RF28(-20.82134;-6729743)	73.68 ± 10.53	159.2 ±1.0	2.16 ± 0.31

Other side of the northern (RF) line. (western part)

Case month of March, reference receiver at RF12.

Geophone position (Latitude, Longitude)	Travel time (s)	Inter-receiver distance (km)	Group velocity (km/s)
RF12(-20.89591;-6882790) RF01(-21.17283;-7008462)	42.11 ± 16.84	134 ±1.0	3.18 ± 1.27

Other side of the northern (RF) line. (western part)

Case month of March, third slope.

Geophone position (Latitude, Longitude)	Travel time (s)	Inter-receiver distance (km)	Group velocity (km/s)
RF34(-20.99935;-6682792) RF53(-21.36119;-6527616)	25.26 ± 21.05	165.8 ±1.0	6.56 ± 5.47

In all cases, the distance between receivers was calculated with a Java script developed by Chris Veneers which uses the Haversine formula (equation 1.17) and can be accessed at the following web page: http://www.movable-type.co.uk/scripts/latlng.html. Errors were calculated by the standard procedure of error propagation in measurements.

The calculation indicated that the western part of the line presented a region of faster velocity than that of the eastern part, in both cases velocity results can be associated with surface waves values. This fact and the calculated velocity magnitude are in agreement with the works of Schmitz and Kley (1997) and Vdovin *et al.* (1999).

Note that dispersion of the wave packet is an important factor in the order of magnitude of the uncertainty errors. In fact, the bigger the distance from the reference receiver the bigger the magnitude of the error as can be seen from the third slope calculation.

Example 2: waves retrieved for the southern profile (PC)

As can be seen from Figure 4.9, the virtual source location is at PC09. From there, two wave packets were travelling in opposite directions along the PC line. This is new from the previous example in that, in the eastern part, two waves packets can be seen travelling with different velocities and interpreted in Figure 4.9. Slopes A (at a first glance it may look like PC04 is an erroneous result and we have to take another slope but also PC06 lies in the same slope) and B represents the two wave packets interpreted, respectively. For both slopes, velocities are such that:

For the interpreted blue line: (eastern part)

Geophone position (Latitude, Longitude)	Travel time (s)	Inter-receiver distance (km)	Group velocity (km/s)
PC09(-25.51648;-6761888) PC01(-25.53569;-68.23110)	26.37 ± 6.5	61.47 ± 1.0	2.33 ± 0.60

For the green line: (eastern part)

Geophone position (Latitude, Longitude)	Travel time (s)	Inter-receiver distance (km)	Group velocity (km/s)
PC09(-25.51648;-6761888) PC01(-25.53569;-68.23110)	42.55 ± 8.79	47 ± 1.0	1.12 ± 0.25

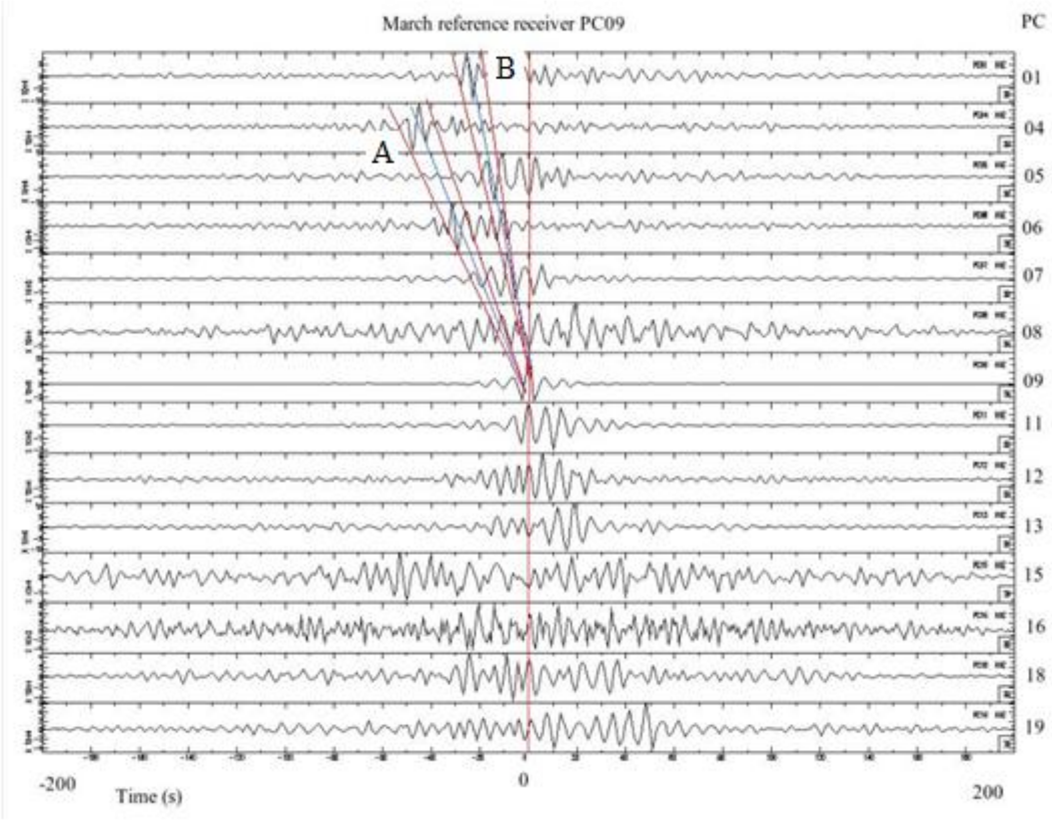

Figure 4.9 Month of March 2003; the interpretation of two different travelling waves. The trend is found by connecting the middle of the wave packet (shown in blue) of all Green´s function. The dispersion of the wave packet defines the error in calculating the velocity of the retrieved waves (depicted by the two red lines around the blue one).

A combination of Rayleigh and Love waves is not possible here because for the Altiplano the velocity difference between Rayleigh and Love waves is not bigger than 10% as pointed out by Vdovin *et al.* (1999), and here the difference between the two wave velocities almost doubled. However, the two waves packets observed could be the result of waves being reflected in the Moho and back to the receiver, or they could be the result of waves refracting along or reflecting from the subducting slab. Nevertheless, note that the information obtained using current data is not enough and interpretation based on surface and body waves is more likely to be correct rather than interpretation based on reflection and refraction in the Moho. This uncertainty is an indication that a thorough analysis based on better data is needed.

Velocities encountered in this section were within the range of velocities encountered in chapter 1 (Table 1.2). Nevertheless, the velocities given in Table 1.2 were calculated using a different approach within the seismic interferometry theory; i.e. that of turning sources into virtual receivers. In this chapter, geophones were turned into virtual sources. Also, the data used were different. In chapter 1, earthquakes were used to perform the corresponding calculations. In this piece of research, earthquakes were suppressed, in order to keep only the noisy part of the recordings. In summary, the fact that, in both approaches, the results of the calculated velocities were similar gives an indication of the robustness of the application of seismic interferometry for this particular area of study.

4.5.3 Further discussion

Apparently, it was possible to retrieve body waves in this study, as can be seen from Figure 4.9. In the case of Figure B.25, the third slope can be interpreted as a refracted wave travelling along the Moho. The analogous situation is the change of slope, for long offsets, in a shot record from a seismic survey, which is interpreted as a refraction arrival. In the case of Figure 4.9, aside from some important drawbacks, such as the size of the line and the quality of data, two clearly distinct signals were retrieved.

The velocity of both signals differs by almost a factor of two, even though they were assumed to be travelling in the same medium. Another important point is that the second wave packet observed (slope B Figure 4.9) is unlikely to be a wave travelling in a different direction to the array, as argued by Zhan *et al.* (2010). In the current case, the main source of noise was the Pacific Ocean which is perpendicular to the southern profile (PC). So it could be concluded that, in Figure 4.9, there were two different wave packets retrieved. Nevertheless, this could be the result of a refraction of the original wave packet of the wave travelling through a zone of high velocity (a high velocity layer of depth) in the easterly part, as pointed out by Schmitz and Kley (1997).

In relation to the strong and weak signals observed along the Altiplano, the findings of Giese *et al.* (1999) are in agreement with the results found here. To be more specific: the signal from the eastern part was clearer than that from the western part of the Altiplano.

In relation to how interferometry can contribute to existing studying, it could be said that interferometry is useful for validation, confirmation, and in data interpretation. Also, it is a different technique and can be used to re-assess previous knowledge. Additionally, it could be said that the results presented here showed consistent behaviour when the virtual source was moving along the line of receivers.

Also, it was observed that, when the position of the reference receiver was varied, while keeping the same period of time, the waves that were retrieved changed in clarity and resolution; indicating that the position of the virtual source within the line is an important factor and acts as a focus for the waves that can be retrieved in a certain period of time.

In relation to the other factors that influence the retrieval of surface or body waves, this piece of research dealt with the geometry of partial melts. Partial melts can act as lenses, in the sense they affect the trajectory of the waves (Wölbern *et al.*, 2009). Also, they prevent S waves from travelling through the partially molten medium. Additional factors affecting the retrieval of surface or body waves are lateral velocity variations (Chin *et al.*, 2007) that can lead to biases in the interpretation of results, and the different behaviours (from efficient travelling to no travelling at all) of S waves as predicted by Chin *et al.* (2007).

The factors already mentioned that affect the retrieval of body waves are related to the geometry of the Moho and the area of study. Additional factors include the distribution of noise sources, as explained by Wapenaar (2004, 2006c), the difference of the magnitude between surface and body waves, as described by Zhu and Helmberger (1996) and surface waves precursors that mask the body waves, as explained by Zhan *et al.* (2010).

Mori and Helmberger (1996) clarify that in order to obtain large amplitude reflections produced at the Moho, it is important that the Moho has a simple geometrical structure. This statement was confirmed in the work of Zhan *et al.* (2010) when they retrieved body waves from Moho reflected waves using seismic noise. In the Altiplano case, and based in the data obtained and analysed, surface waves dominated the majority of cases.

Nevertheless, in the case of the Puna plateau, body waves were retrieved as was seen from Figure 4.9 (evidence is not conclusive and the most probable wave retrieved are surface waves) implying that the condition of Moho having a simple geometrical structure is necessary in order to retrieve body waves.

4.6 Conclusions

As was seen in this chapter, for the northern profile (RF, 21°S), surface waves were retrieved by interferometry. Several previously known features were also observed in the results - such as a change of velocity near the centre of the line due to the “Altiplano low velocity zone” (ALVZ). Also, a difference was observed in the velocity of the propagation of the retrieved waves between the eastern and the western parts; this is consistent with the observations made by other researchers.

For the case of the Puna plateau, southern profile (PC, 25,5°S), the situation was different. Due to the small offset range, when compared to the northern profile (RF) the observations made for the southern profile were not apparent here. Nevertheless, two waves packets were observed whose velocity difference indicated the possibility of surface and body waves being retrieved and not Rayleigh and Love waves - because such a difference is not consistent with the expected differences for Love and Rayleigh waves for this zone as explained by Vdovin *et al.* (1999).

Recommendations for broadening this study should focus on how the offset range is related to the retrieval of surface or body waves because the geology on both plateaux is very similar. Also, the possibility of waves travelling and refracting along the subducting slab has yet to be investigated.

Additional recommendations include research into the influence of the geometry of the Moho in the retrieval of body waves. As pointed out by Zhan *et al.* (2010), retrieval of body waves can be achieved under specific conditions mentioned in their research. But, what happens with the low velocity zone in the Altiplano? Can this zone act as a wave guide, trapping most of the body wave energy? Also, can the subducting slab act in the same way, trapping body wave energy? Is that the explanation for the body wave observed in this chapter?

Chapter 5

SURFACE WAVE SOURCE-RECEIVER INTERFEROMETRY

5.1 Summary

The intention of this chapter is to present the results of applying a relatively new kind of interferometry, known as source-receiver interferometry, to surface waves in the Altiplano. Source-receiver interferometry was first introduced by Curtis (2009) and Curtis and Halliday (2010). The method transforms real sources or real receivers into virtual sources or virtual receivers, as opposed to conventional forms of interferometry which transforms real receivers into virtual sources and real sources into virtual receivers. Source-receiver interferometry can be equally thought of as transforming a real-source real-receiver pair to a virtual-receiver virtual-source pair.

This new form of interferometry is worth applying because it allows the calculation of the source-receiver record between two points x1 and x2, without having to take a direct measurement. This is useful in cases where geophones are found to be operating irregularly during a survey, so new information can be added as if it was recorded. This could represent the possibility of infilling periods of time during which no signals were recorded by geophones in a survey. Additionally, virtual recordings can be compared to real ones to check their quality. Curtis *et al.* (2012) also showed that the virtual recordings contain information about the phase of the earthquake source that is not available in the real recordings.

The source-receiver interferometry procedure is a second-order interferometric method - that is to say, two steps of interferometry are applied to the data. In this work, these two steps could be either cross-correlation or convolution, and for that reason, the tests conducted in this chapter evaluated the quality of the data and results for the two steps of interferometric calculation involved.

Also, this chapter will assess two independent methodologies, one being the use of events recorded by geophones (i.e., active earthquake sources) in order to perform the interferometric calculations. The other uses passive recordings made by the geophones deployed in this project. In order to do the latter, a methodology introduced by Bensen *et al.* (2007), which suppresses earthquake signatures, was followed. Both methodologies showed consistent results when compared with those from other fields of geosciences. Nevertheless, for the second step of interferometry, the methodology using active sources show better quality than those of passive recordings.

5.2 Introduction

Common use of seismic interferometry makes use of correlation, convolution or deconvolution to calculate the Green's function between a pair of receivers as though one of them acts as a source. Procedures for calculating such a response between the two geophones use either background noise source (Campillo and Paul, 2003; Wapenaar and Fokema, 2006a; Draganov *et al.*, 2006; Bensen *et al.*, 2007, 2008; Yang *et al.*, 2008; Yang and Ritzwoller, 2008; Zheng *et al.*, 2008) or active sources (Bakulin and Calvert, 2006; Slob *et al.*, 2007; Lu *et al.*, 2008; King *et al.*, 2011). Other advances (Hong and Menke, 2006, Curtis *et al.*, 2009; Tonegawa *et al.*, 2010) make use of reciprocity to calculate the Green's function between two sources.

This chapter is concerned with the application of a combined and new methodology, first introduced by Curtis (2009) that turns real-source, real-receiver pairs into virtual-receiver virtual-source pairs, respectively. The aggregated value of applying this kind of interferometry is because it allows calculating the source-receiver record between two points x1 and x2, without having to take a direct measurement. This is useful in the case of the Altiplano where geophones were found to be operating irregularly during the survey, so new information can be added as it was recorded, this could represent the possibility of infilling periods of time during which no signals were recorded by geophones in a survey. Additionally, virtual recordings can be compared to those that are real.

In the Andes case, the geometrical distribution of sources and receivers fulfils the geometrical requirements as originally explained by Curtis (2009), and later updated by Curtis and Halliday (2010) which presents a methodology to provide Green's functions on source-to-receiver paths. This method is based on three representation theorems corresponding to three possible canonical geometries (see Figures 1.9 and 1.10).

In fact, in the Andes case, two parallel lines of receivers were deployed and earthquakes occurred during the deployment period. Some earthquakes are "surrounded" by the two indicated lines, as can be seen in Figure 5.1. The reason to apply this new theory of source-receiver interferometry to the Andes data was that it allows adding new source-receiver paths to the existing survey and testing the effectiveness of source-receiver seismic interferometry on real data.

This current piece of research investigated whether it was possible to add this new information as it was recorded. More specifically, it was investigated whether, by using geophones in the southern profile (PC), it was possible to fill in missing recordings in the northern profile (RF). Moreover, the idea was to compare these virtual recordings with the real ones, to look for similarities and differences. If successful, this could make it possible to infill the periods of time during which no signal was recorded by the geophones.

The results of this chapter are divided in two main parts. The first part shows results using active sources. The second shows results using noise recordings. Before showing the results of interferometry in part 1, a subsection is presented to the reader depicting some typical seismograms.

The intention of this part of the chapter is to familiarise the reader with the typical patterns encountered when an arbitrary earthquake is recorded by all the geophones in the RF profile line. This will give the reader insight into the characteristic patterns of recordings which are later shown to be reproduced by the interferometric calculations. Also, this section shows that anisotropy in the velocity field, as found in the results section, was consistent with previous studies in the area, and also with real recordings of geophones in the line RF. Additionally, in this first part, the second pass of interferometry was applied in order to obtain the final Green´s functions that will be compared to the real recordings.

The second part consists of interferometry using noise sources and shows the results of applying the method developed by Bensen *et al.* (2007), in which earthquake signatures are removed from recordings. This section begins by showing some examples of how the Green's function varies by day (over one month), and by month (within the entire period of recording) revealing possible changes in source mechanism.

In this second part some qualitative comparisons are made between interferometric results and real recordings on geophones that lie as close as possible to the corresponding virtual source. Of principal importance in this second section is the Green's function for the first step of interferometry because it reproduces the recording pattern, observed for real sources, along the RF profile line. As will be seen, the quality of the data in the second step of interferometry was not as good as that from the active sources.

Finally, some arguments based on the travel time demonstrate that there is consistency between the arrival time of the calculated Green's functions and of the real recordings. Also, power spectra made on both real and calculated seismograms provide insight into the difference in frequency content between real recordings and those coming from passive interferometry.

5.3 Data used

A group of nine earthquakes was selected in order to perform the interferometric calculation. Pre-processing steps included synchronisation of the origin time, filtering and windowing of the event of interest. Also, a group of 20 additional earthquakes were chosen in order to make qualitative comparisons between their first arrival times and those from interferometric calculations.

Choosing events for this part of the study was not as straightforward as it may appear. Even though a substantial number of earthquakes were available, not all of them were suitable for performing interferometry. For example, the magnitude had to be taken into account for reasons of signal to noise quality. Also, depth was an important factor in considering the type of wave recorded by geophones. In this case, depths were required to be less than approximately 100 km, in order to ensure that mainly surface wave energy was recorded.

Quality of data is another important factor and is related to the functioning of the geophones. In the current case, this was very problematic, as can be seen in Figure 1.3, chapter 1. This implied that synchronisation between earthquakes and periods of proper functioning of geophones have to occur for an event to be chosen. Another additional factor is the relative location of events and geophones. This is important especially when considering interferometry using the stationary phase approximation. Also, source-receiver interferometry has its own specific geometrical requirements.

As is clear, there are several parameters that need to be tuned in order to have the correct geometrical set up and the approximate data ready to perform an interferometric calculation. All this implies a time-consuming procedure, and quality controls that in practice were carried out by automatic scripts and by visual or manual routines.

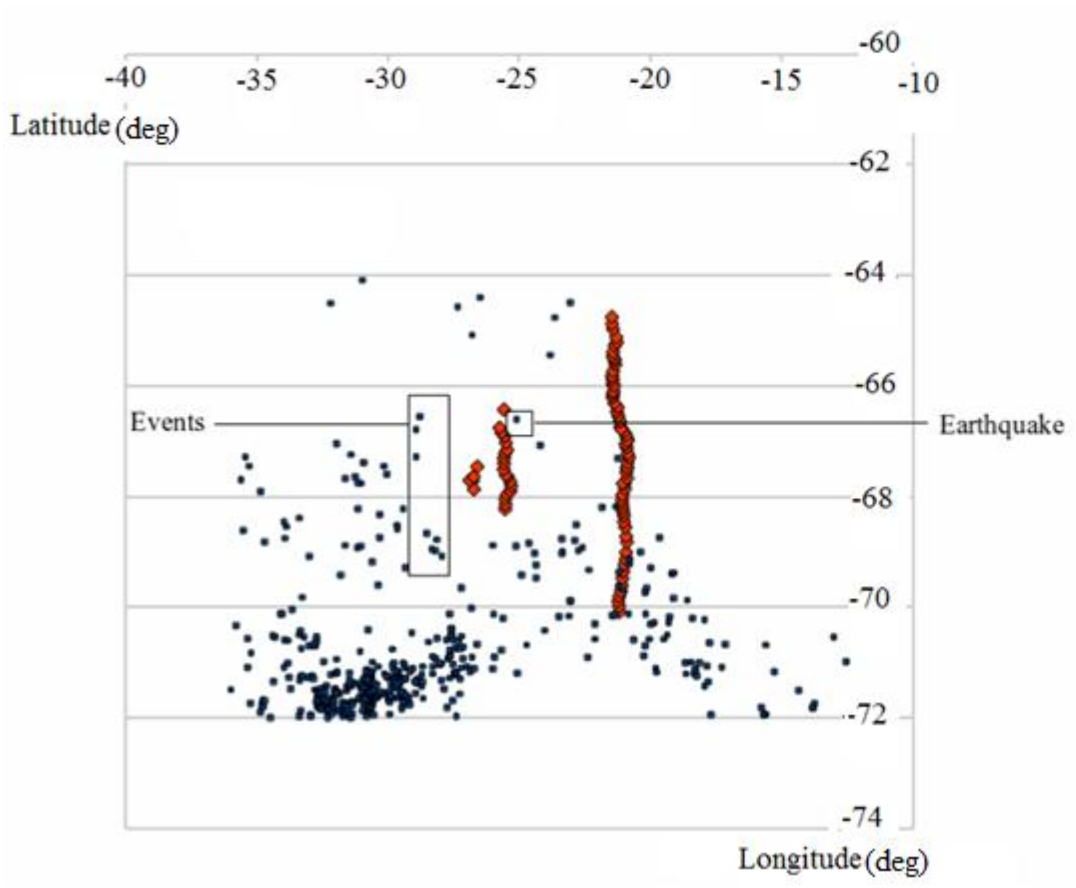

Figure 5.1 Geometrical configuration used to apply interferometry to active sources. In this figure, events refer to earthquakes used for interferometric calculations. The earthquake shown is used for comparison between real data and interferometry results.

In the case of passive noise sources, continuous recordings between March 2003 and August 2003 were downloaded in segments of one day for a period of six months. Then, the one-day segments were processed following the methodology introduced by Bensen *et al.* (2007).

As explained by Weaver and Lobkis (2005), the diffusive noise source field and the cross-correlation of signals between geophones will converge to the complete Green´s function - meaning that all reflection, scattering and propagation modes will be present. In this piece of research it was assumed that a random field was being used.

The geophones functioned intermittently during the period of acquisition. This resulted in the choice to analyse a particular sub-period of six months out of the whole period of almost two years in which the geophones used for this piece of research were deployed. Also, a significant number of geophones were not functioning during the whole project, as can be seen in Figure1.3 chapter 1.

This resulted in information “voids” along the profile line. Another critical point is that of the quality of the data recorded. Even though a geophone could have been in operation during the period of time of interest this was not a guarantee of the quality of the data. Regarding this point, visual quality control checks were carried out in order to ensure good quality of the recordings before they were analysed.

5.4 Method

As was seen and explained in chapter 1, the method used in this chapter is based on the application of source-receiver interferometry by means of equations 1.9, 1.10 and 1.16. For the geometrical configuration of earthquakes and geophones considered in this chapter, the two steps of interferometry were performed by cross-correlation, due to the relative position of sources and receivers shown in Figures 5.2 and 5.3. This means we are using the same principle of two steps of interferometry but instead of convolution and the cross-correlation we are using two steps of interferometry by cross-correlation.

Figure 5.2 shows the first step of interferometry in which a summation process is performed over sources that lie within the stationary phase region in order to calculate the Green’s functions between PC06 and RF stations. Then, Figure 5.3 shows the second step of interferometry described by equation 6.1 in which using Green’s functions from the first step of interferometry, the recording in RF of the earthquake, and by summing over all stations it is possible to get the Green’s function between PC06 and the earthquake.

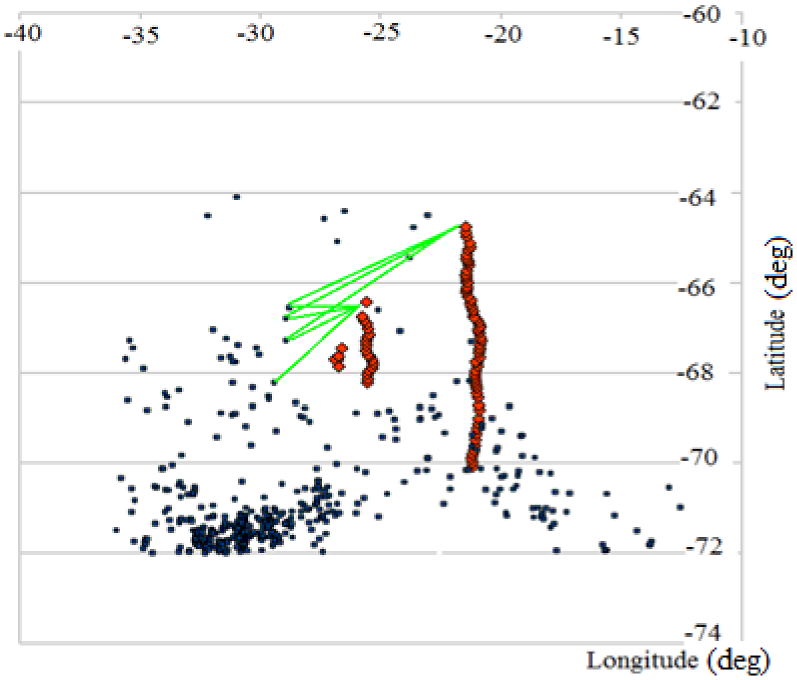

Figure 5.2 First step of interferometry. By summing over sources that lie in the stationary phase zone the Green's functions between PC06 and RF stations have been calculated.

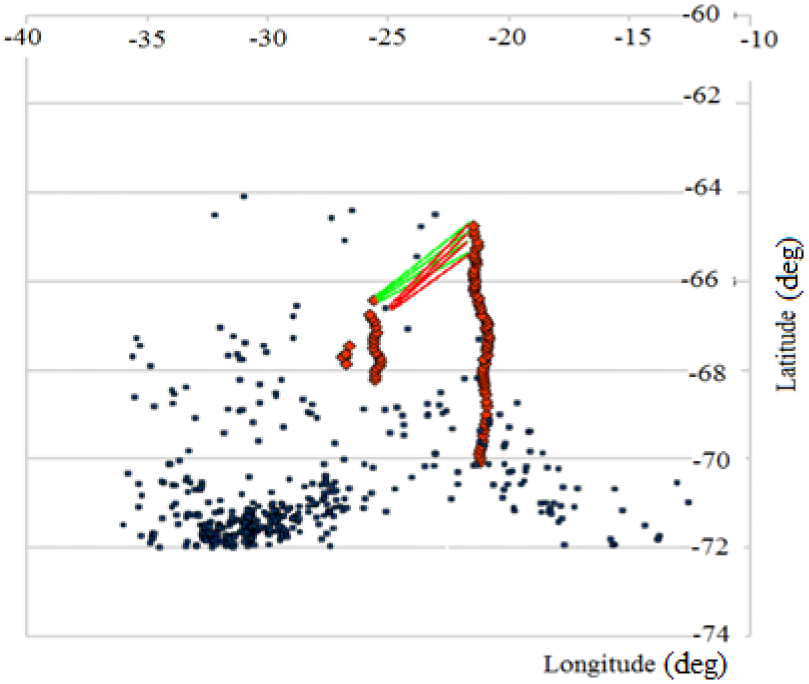

Figure 5.3 Second step of interferometry. Using Green's functions from the first step of interferometry and the recording in RF of the earthquake. Summing over all stations it is possible to get the Green's function between PC06 and the earthquake.

Following source-receiver interferometry, results will be presented for active sources where nine earthquakes were used (case 1) and passive noise recordings during a period of six months (case 2).

1) Case 1: active sources

In the case of using active sources (earthquakes), summations of the cross-correlation functions to obtain the respective Green´s functions of each step of interferometry were performed over the geophones and/or sources that lay in the inter-source path of the stationary phase region. Also, similarly to the manner undertaken in chapter 3, the geophone recordings were muted by picking P and coda P and then applying a taper filter in order to make the cross-correlation easier to analyse.

2) Case 2: passive noise recordings

The case of passive recording differs from that of active sources in that no summation over sources or receivers is needed, because it is assumed that the correlated responses are a superposition of uncorrelated sources acting simultaneously. In the case of using noise, the methodology of processing consisted of the following steps:

1. - Resample to 8 ms in order to make the files smaller and therefore reduce the computational time. Remove mean, trend and glitches.

2. - Seismograms were bandpass filtered between 0.04 Hz and 1.0 Hz.

3. - To remove the effect of earthquakes:

    3a. - Envelope functions are calculated.

    3b. - The smooth version of the inverse envelope functions were used to weight the corresponding filtered seismograms, resulting in a 1-bit seismogram.

4. - Cross-correlation of the geophone recordings were computed over the day segments and stacked.

5. - All the cross-correlations were normalised between -1 and 1 by dividing by the biggest amplitude. The aim of this is to avoid that erratic data and residual effects of

earthquakes contributes to the final results. Finally, a bandpass filter was applied to improve the image quality of the Green´s functions.

5.5 Results

Before showing the results from interferometry, it is important to be familiar with the typical earthquake recording pattern observed along the set of receivers. This will give the reader insight into the “behaviour” and characteristics of the surface waves recorded. That will be useful when comparing Green´s functions coming from interferometry with that of the real recordings.

5.5.1 Study of typical seismograms

Figures 5.5 to 5.7 present typical horizontal and vertical component recordings of the earthquake shown in Figure 5.4. These were made by geophones in the RF profile.

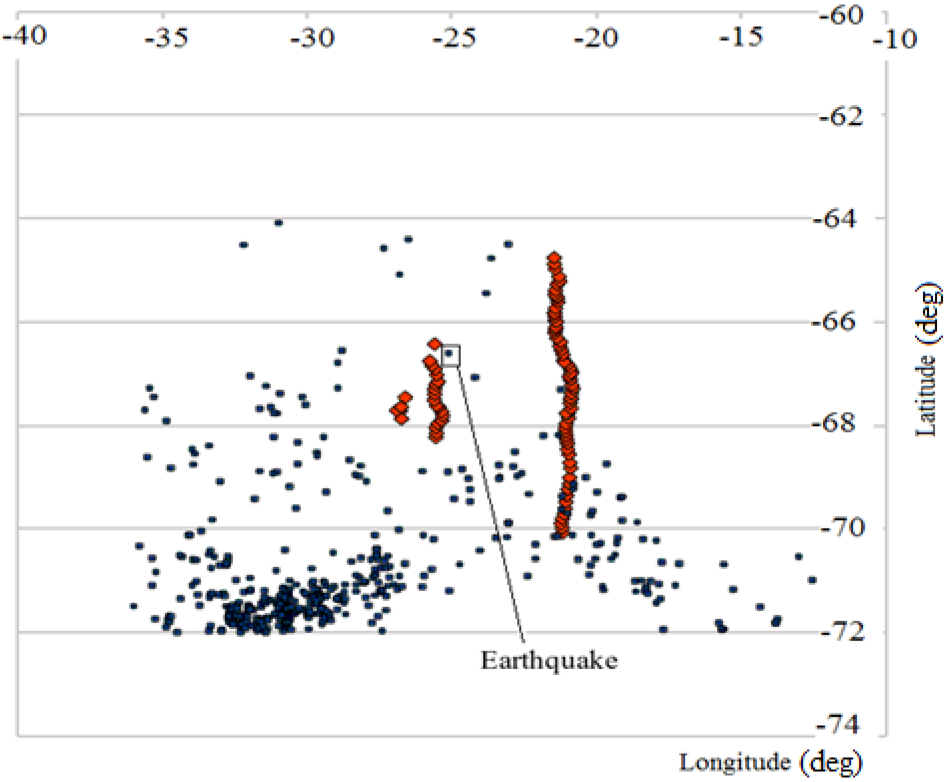

Figure 5.4 Earthquake used to show typical recordings patterns along the RF line

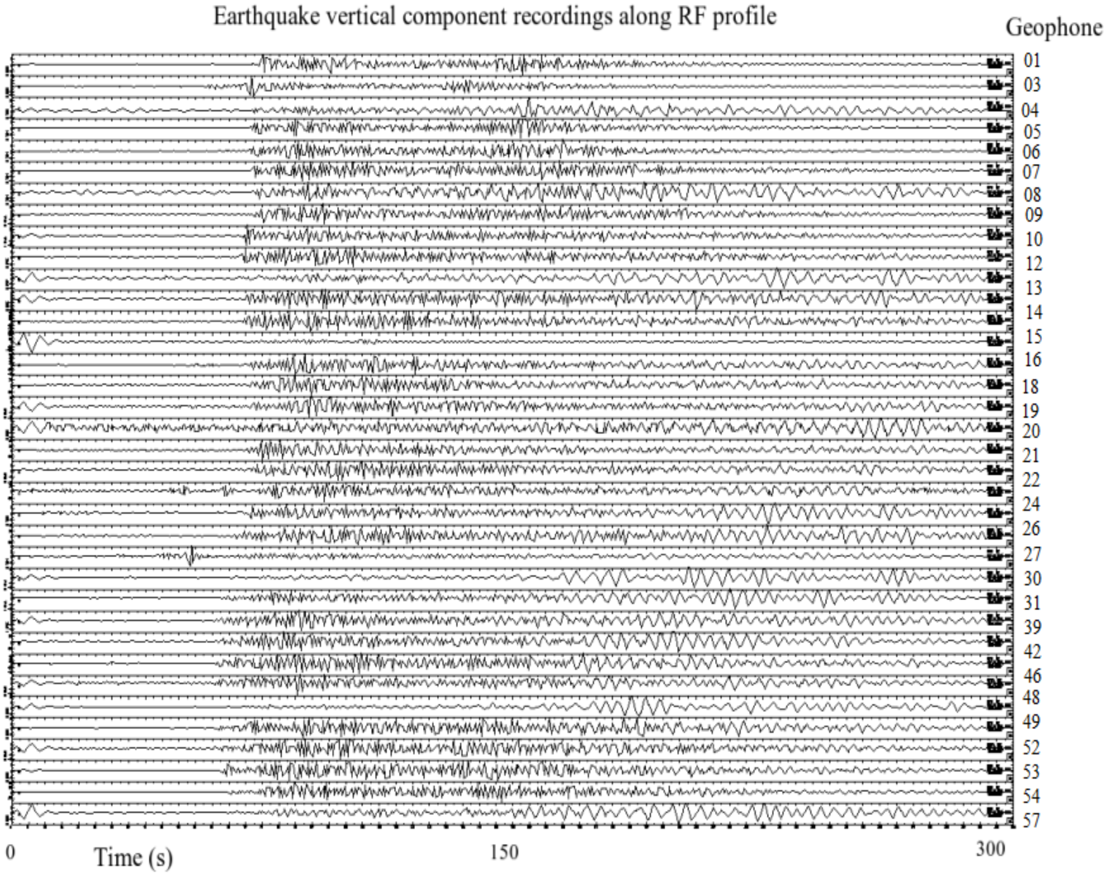

Figure 5.5 Vertical component recordings along the RF line of stations for the specific earthquake shown in Figure 5.4.

The three components (one vertical and two horizontals: east and north) of the earthquakes chosen for this study were downloaded in order to test source-receiver interferometry, not only in the vertical direction but also in the horizontal directions.

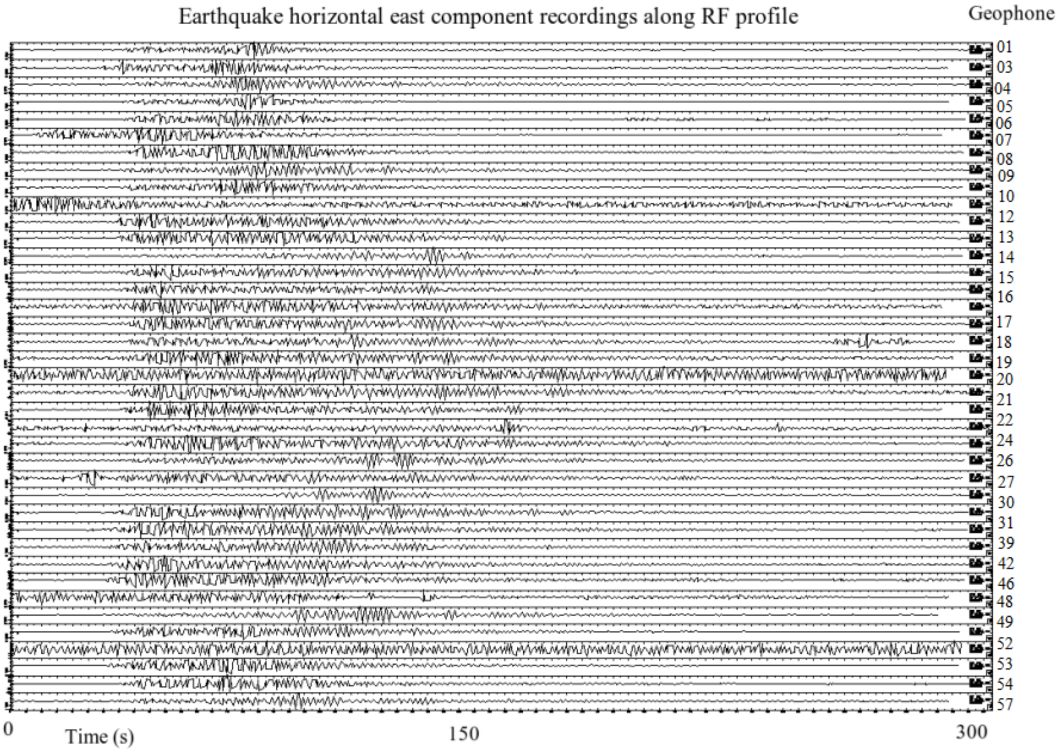

Figure 5.6 Earthquake horizontal east components along RF line of stations for the specific earthquake shown in Figure 5.4.

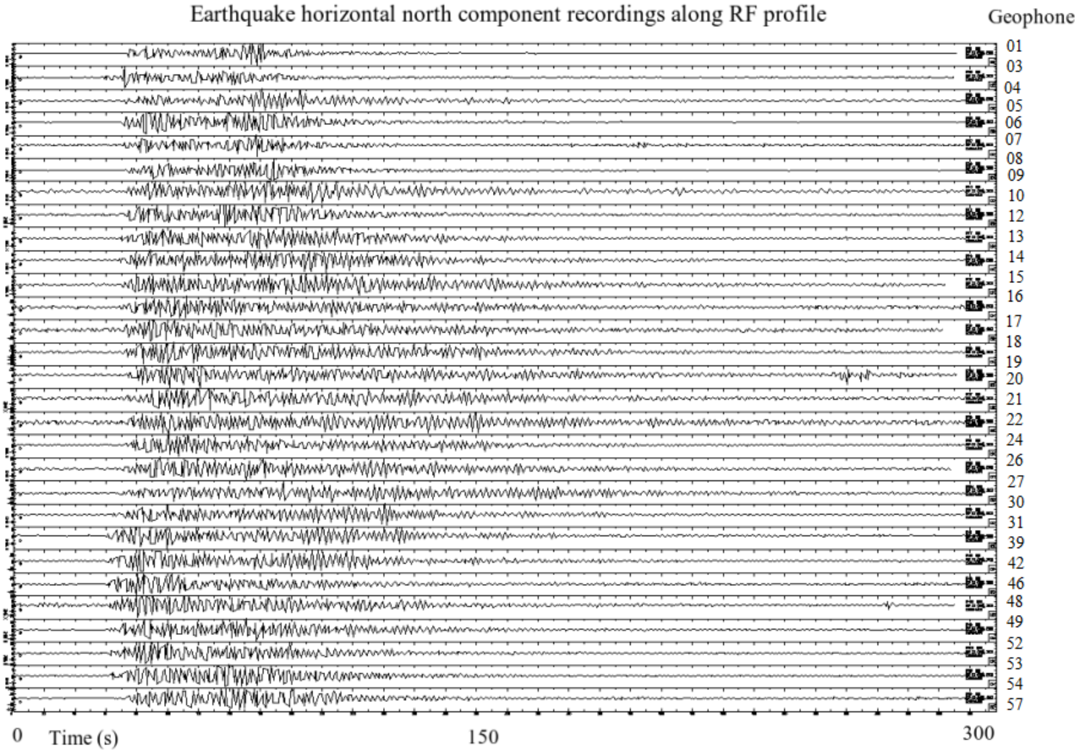

Figure 5.7 Earthquake horizontal north components along RF line of stations for the specific earthquake shown in Figure 5.4.

Additionally, over 20 events from different locations were analysed in order to check moveout, the quality of data, and to confirm what seemed to be a high velocity region. For simplicity, not all of the events have been presented in this section. Figures 5.9 to 5.11 show events 188 and 08 as examples of typical moveouts:

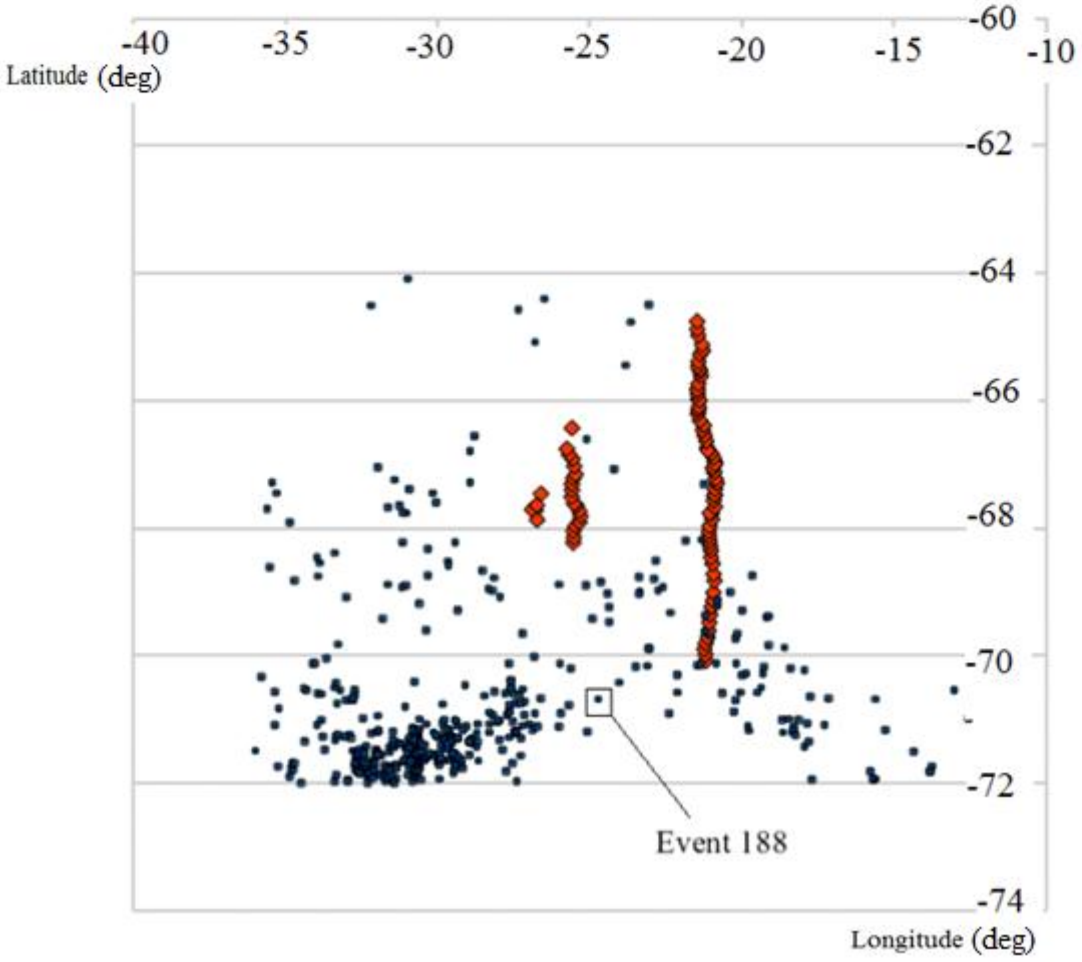

Figure 5.8 A subset of 20 events from the whole set of earthquakes were selected and analysed for further testing

As can be seen from Figure 5.8, a large number of earthquakes occurred during the time that the geophones were recording. Nevertheless, even from this selection only 20 events could be found that showed data that was useful for the current study. Principal problems faced were that only few stations were active, from those active stations some of them had bad records and for active stations with good recordings not all of them were suitable for analysis.

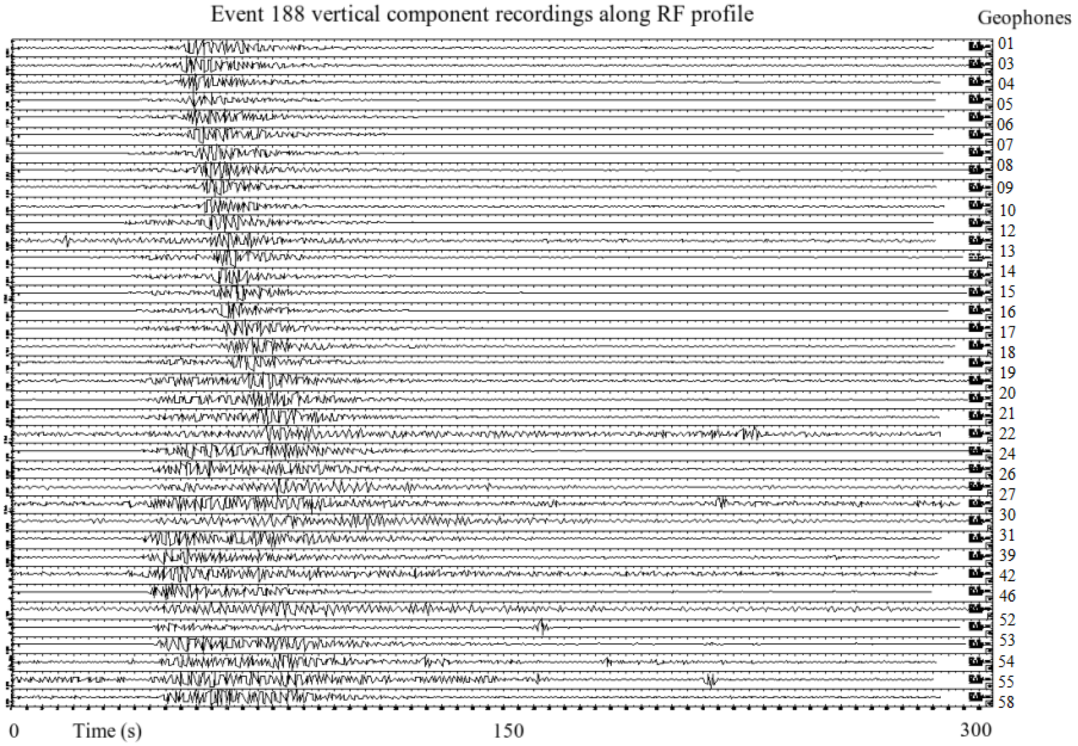

Figure 5.9 Event 188 vertical component recorded along the RF line of stations for the specific earthquake shown in Figure 5.8.

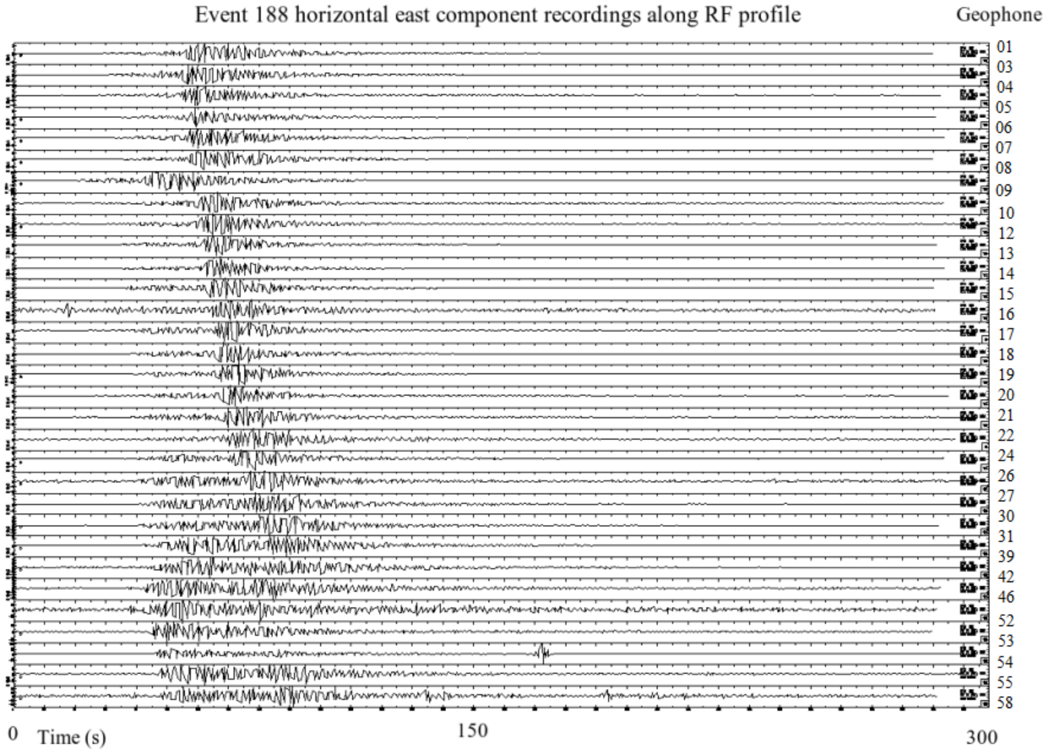

Figure 5.10 Event 188 horizontal east component recorded along the RF line of stations for the specific earthquake shown in Figure 5.8.

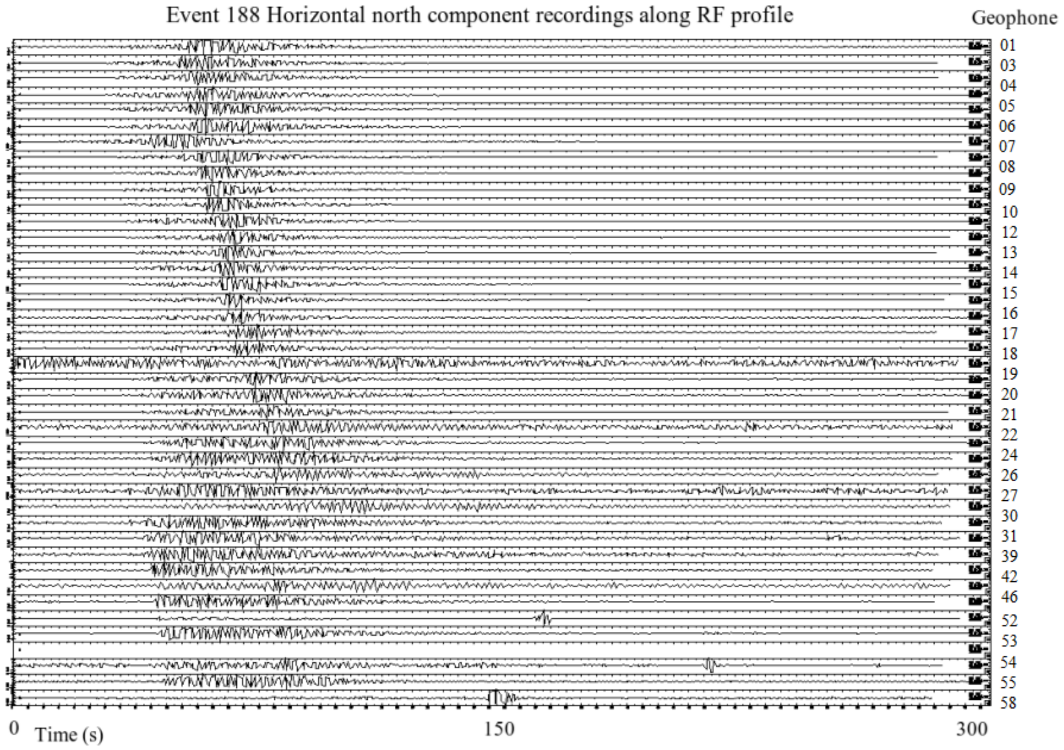

Figure 5.11 Event 188 horizontal north component recorded along the RF line of stations for the specific earthquake shown in Figure 5.8.

From Figures 5.9, 5.10 and 5.11, and taking into account the location of earthquake 188, it was clear from the three components shown that waves travelling along the RF profile line traverse a region of different velocities, one fast and one slow. It was expected that surface waves will arrive first for geophones located close to the earthquake (in this case, near the end of the line or bottom geophones in all the figures).

In this case, first arrivals were almost comparable to arrivals at the beginning of the line (upper geophones in all figures) indicating that a zone of low velocity should be present. In other words, there is a low velocity zone near the shore. This result is consistent with findings from different works, such as Trampert and Woodhouse (1996) and Vdovin *et al.* (1999).

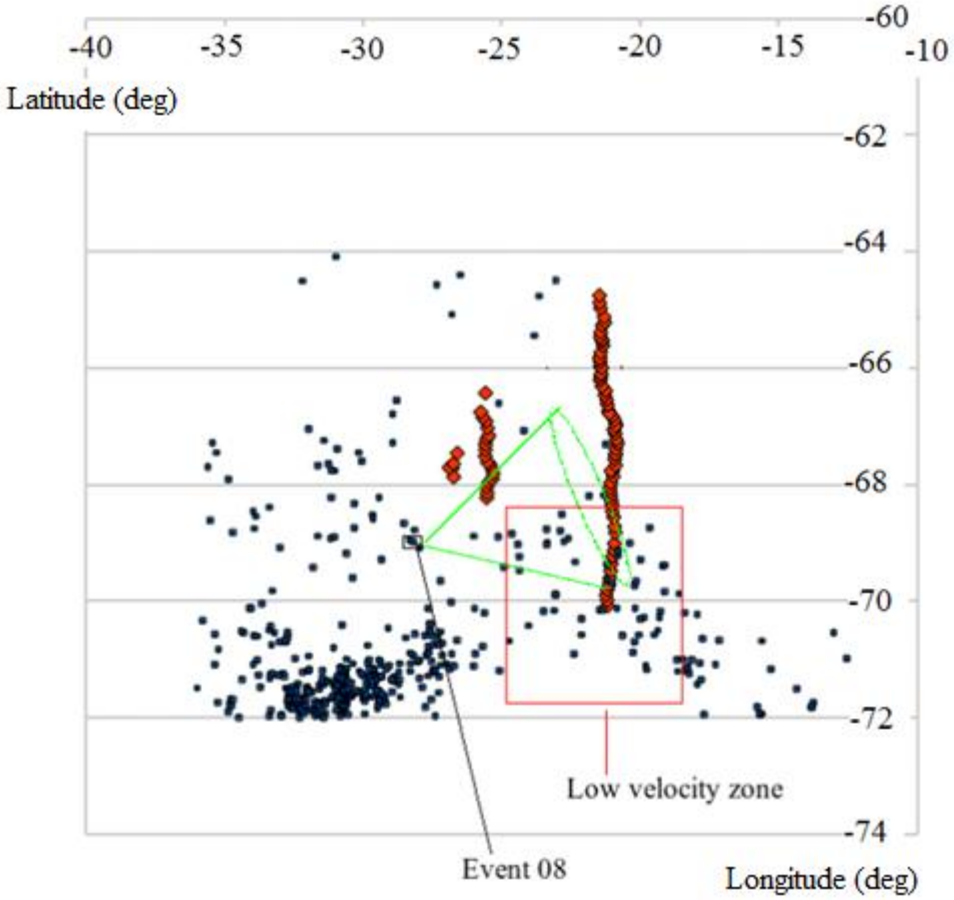

Figure 5.12 Earthquakes and low velocity zone. As interpreted from several events

Figure 5.12 depicts a low velocity zone that is consistent with the finding of Mauchline (2010) and also with the low-velocity anomalies found in the works of Trampert and Woodhouse (1996) and Vdovin *et al.* (1999) concerning the dispersion characteristics of surface waves propagating across South America and the surrounding oceans.

The next three graphs will show the recordings of the geophones along the northern line (RF) for event 08. These graphs are presented here as a second example of the typical recordings patterns encountered when recording surface waves along the RF line.

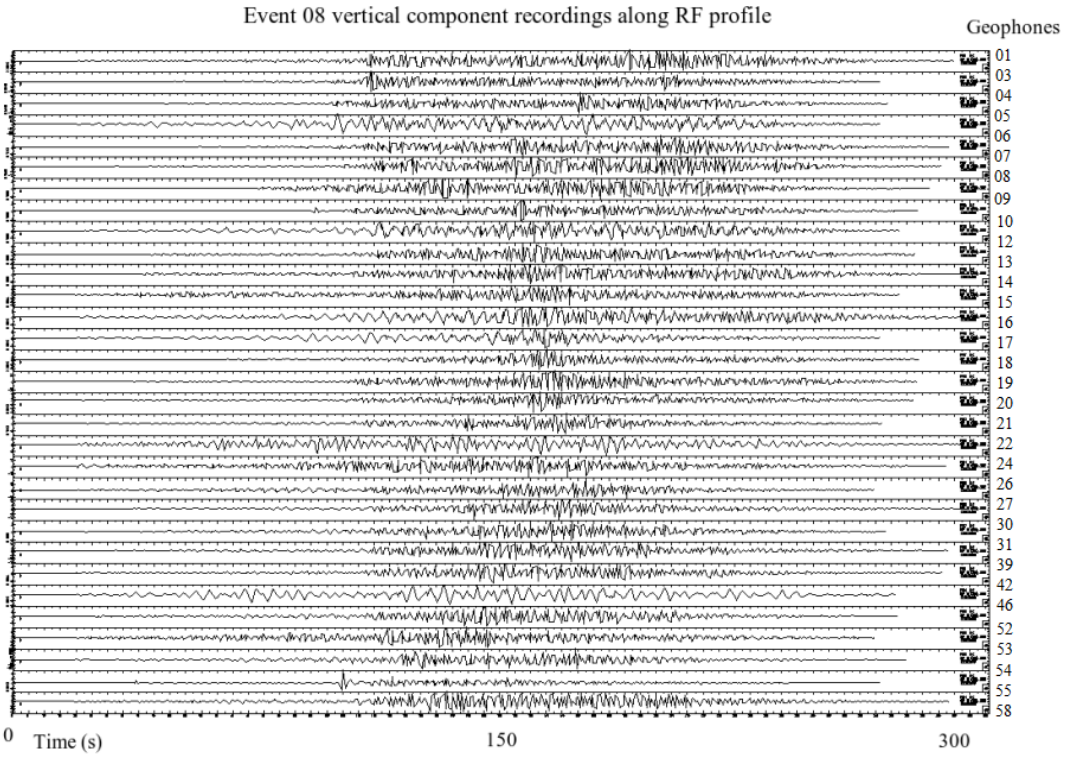

Figure 5.13 Recordings of the geophones along the northern profile (RF) for event 08. In this figure, vertical components of geophone recording are depicted.

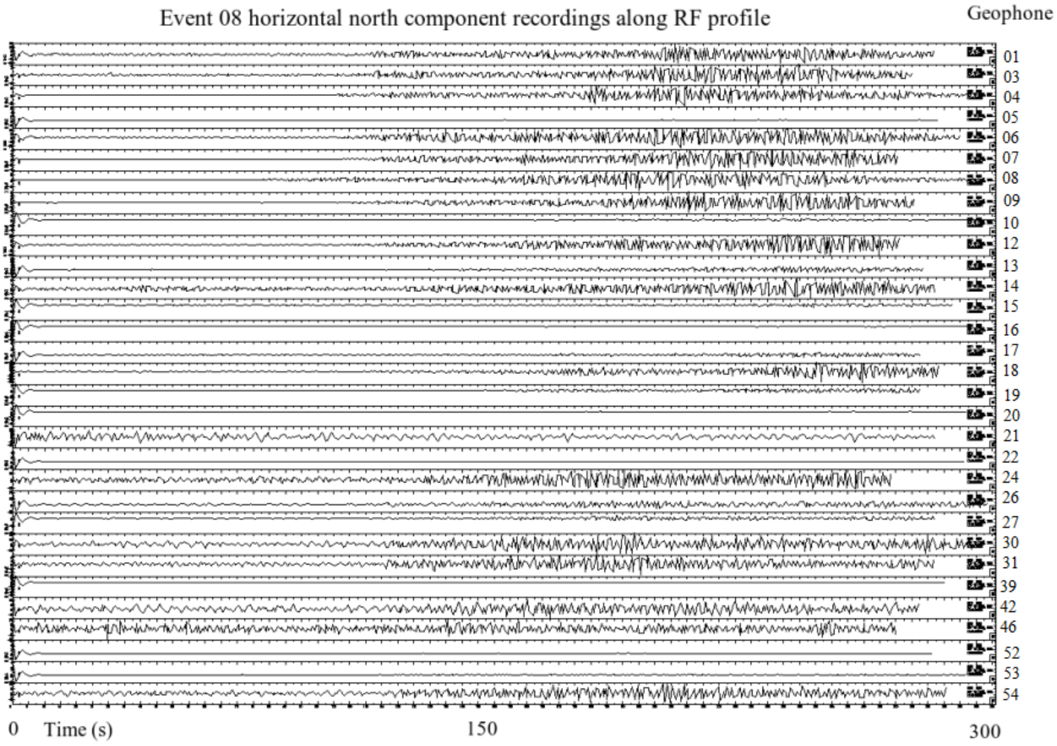

Figure 5.14 Recordings of the geophones along the northern profile (RF) for event 08. In this figure. horizontal north components of geophone recording are depicted.

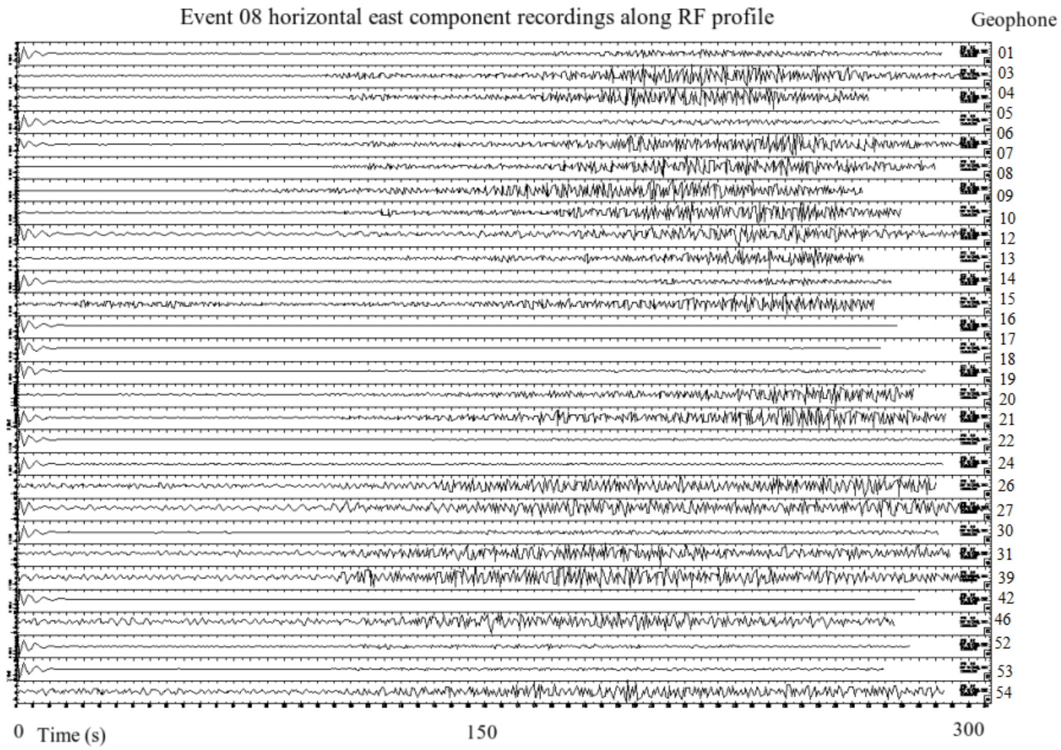

Figure 5.15 Recordings of the geophones along the northern profile (RF) for event 08. In this figure, horizontal east components of geophone recording are depicted

This concludes this section concerning typical recording patterns for line RF. The more important lesson learnt from this exercise is that surface waves will travel through regions where velocities are divided for zones of high and low velocities, so arrival times along the northern receiver line (RF) will differ from expected arrival times. In the next section, results from the interferometric calculation will be shown and analysed.

5.5.2 Seismograms obtained from interferometry

5.5.2.1 Case 1: use of active sources

Figure 5.16 shows the Green’s functions for the first step of interferometry calculated between geophone PC06 in profile PC and every geophone in line RF. The procedure followed in this part is the one described in section 1.6 of this thesis where equation 1.16 is used. Equation 1.16 in essence means interferometry by convolution, then interferometry by cross-correlation. In the current case, the two steps of interferometry were performed by cross-correlation due to the relative position of sources and receivers. For the purpose of simplicity and ease of visualisation, only P and coda P parts of the seismogram have been selected for performing interferometric calculations.

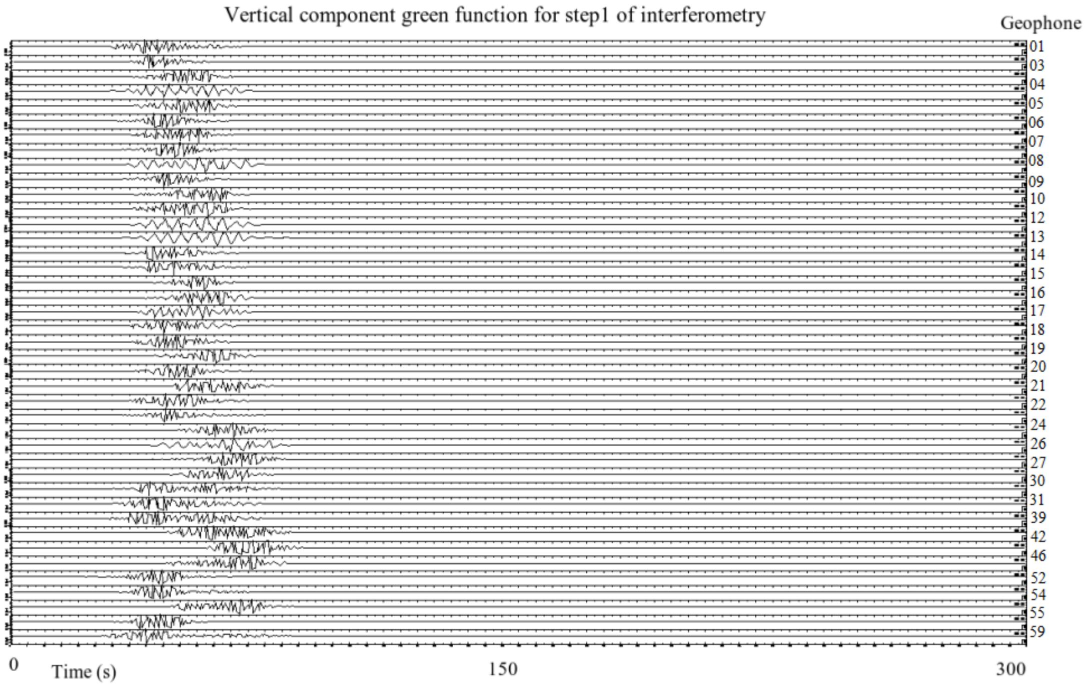

Figure 5.16 Green’s function vertical component for the first step of interferometry. These Green’s functions are in agreement in relation to the arrival time, with the real seismograms recorded along the RF profile.

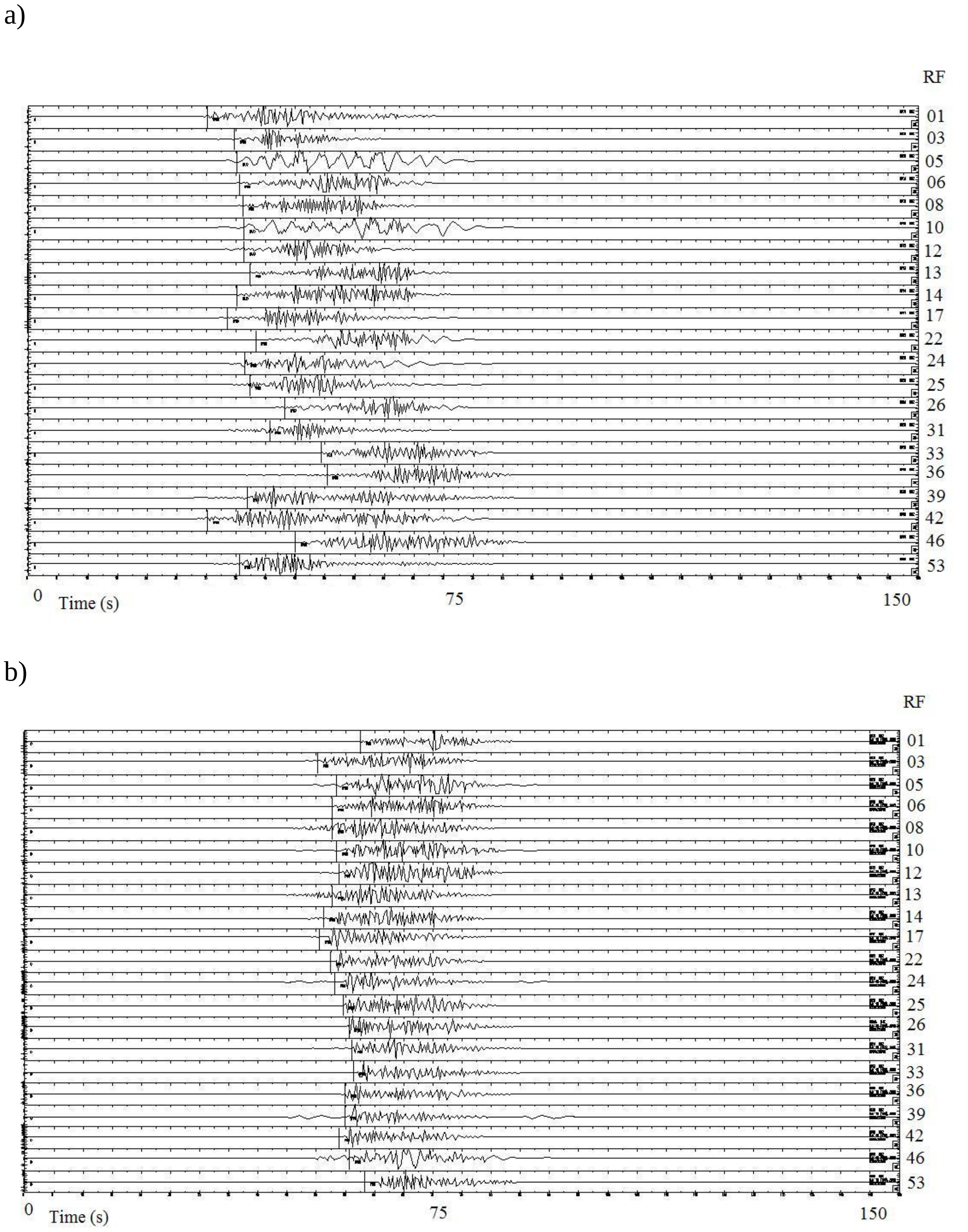

Figure 5.17 Comparison between seismograms obtained from interferometry a) and real recordings b). For the ease of visualisation only P and coda P have been kept in figures. Please note that apart from geophones 33 and 36 the first arrivals have similar trends in both cases.

The Green's functions retrieved have the same first arrivals time characteristics of real recordings in the sense that they have replicated the velocity features characteristic of the zone. As is already generally known, receivers at the beginning of the line were located near the shore, where there was a low velocity zone. This made the waves travel slower than those that travelled to the other end of the RF profile. Surface waves travelling, for example, from event 08 shown in Figure 5.14 will travel along different ray paths, so waves travelling from the same initial point will be affected differently for the far and near parts of the northern line. The result was that arrival times in both extremes of the line appeared to be the same for these two different sets of offsets. Results for the low velocity zone near the shore were consistent with those from previous studies of the zone by Vdovin *et al.* (1999), Ekstrom *et al.* (1997) and Trampert and Woodhouse (1996).

Figure 5.18 shows the result of applying a second step of interferometry defined in the method section.

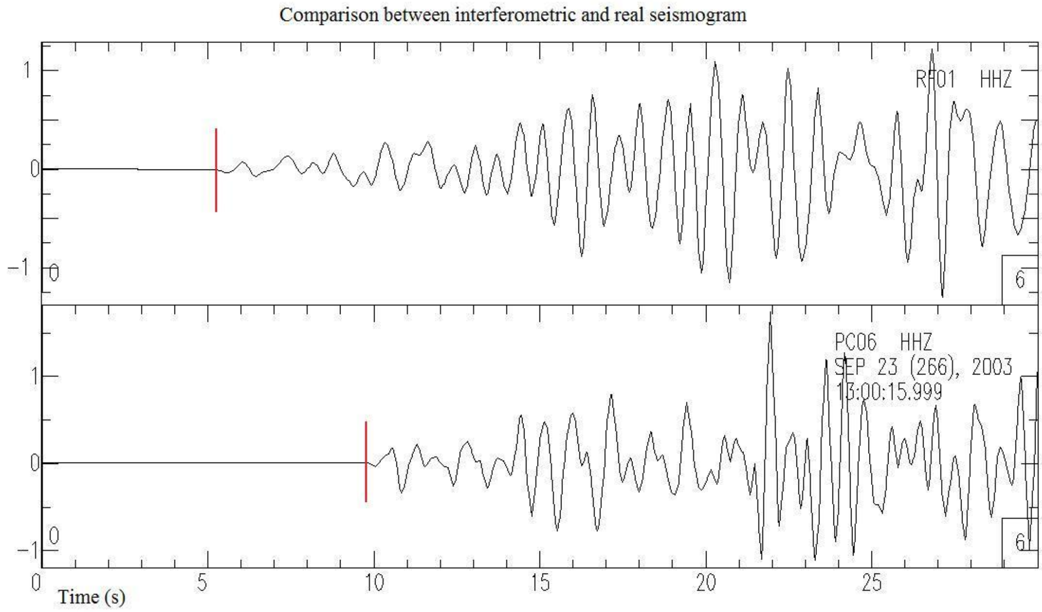

Figure 5.18 Comparison of the Green´s function between the earthquake shown in Figure 5.1 and geophone PC06 (above) and real recording (for same earthquake) made by geophone PC06 (below). In both figures, a bandpass filter of 0.2-3.0 Hz was applied.

In Figure 5.18 arrival times have been marked in red. As can be seen, there is a difference in arrival time (arrival time for the calculated green´s function is around 5s while arrival time for the geophone recording is around 10s), but the main features (pattern of peaks and troughs) of the waves were analogous. The main difference in time could be due to the fact that a second-order interferometry method was used. This meant that errors from the first step were propagated into the second. Also, there were factors, such as attenuation, that were mitigated by using normalisation.

Nevertheless, normalisation, especially if attenuation played an important role, does not always work. Another factor that could account for the difference between the two seismograms is the use of only a small number of events to make the calculation. Nevertheless, despite all of these setbacks, a good result was obtained from the first step of interferometry.

5.5.2.2 Case 2: Use of passive recordings

The following section shows how the Green´s functions calculated between geophone PC06 and every geophone in line RF vary by day, by month and the calculation using all six months of data. These final Green’s functions have been compared with the real recordings for earthquakes that occurred near geophone PC06.

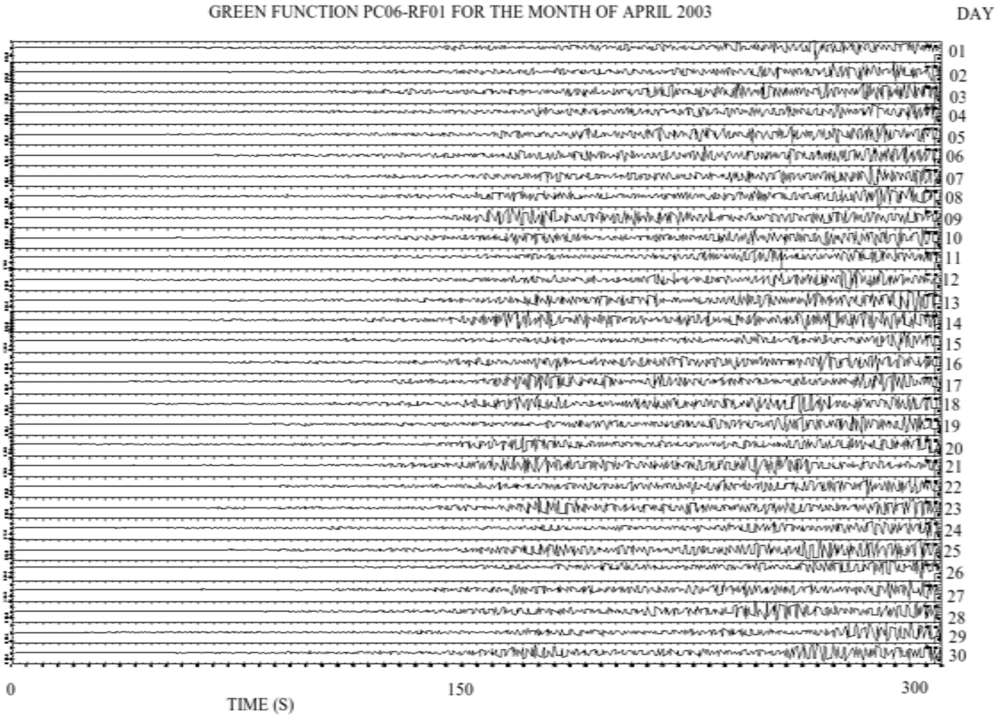

Figure 5.19 Green’s function between PC06 and RF01, each calculated using 1 day of data, for the month of April 2003.

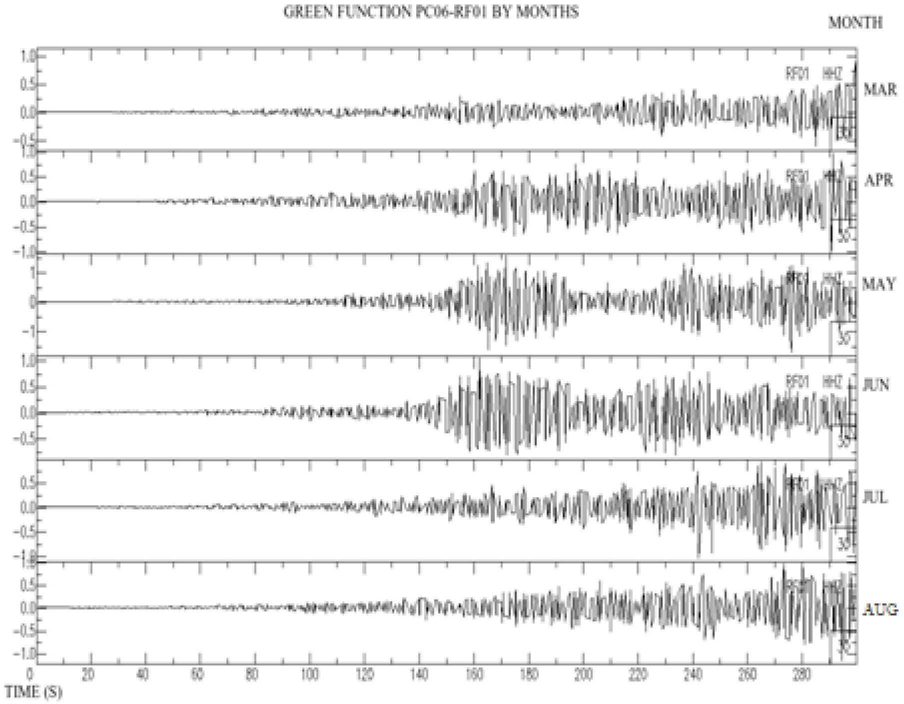

Figure 5.20 How the Green's function between PC06 and geophones RF01 varies every month in the six-month period.

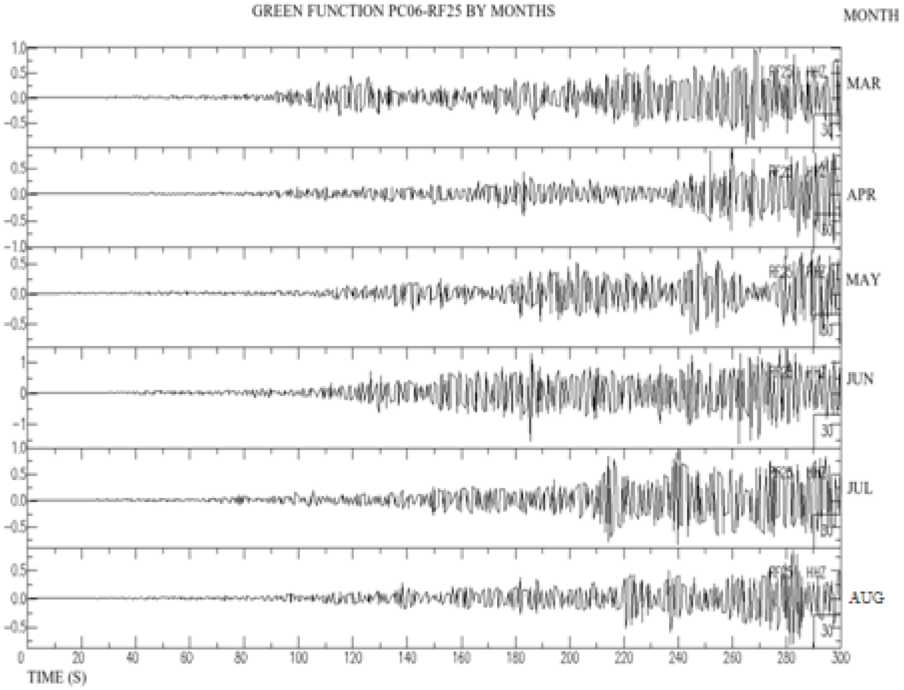

Figure 5.21 How the Green's function between PC06 and geophones RF25 varies every month in the six-month period.

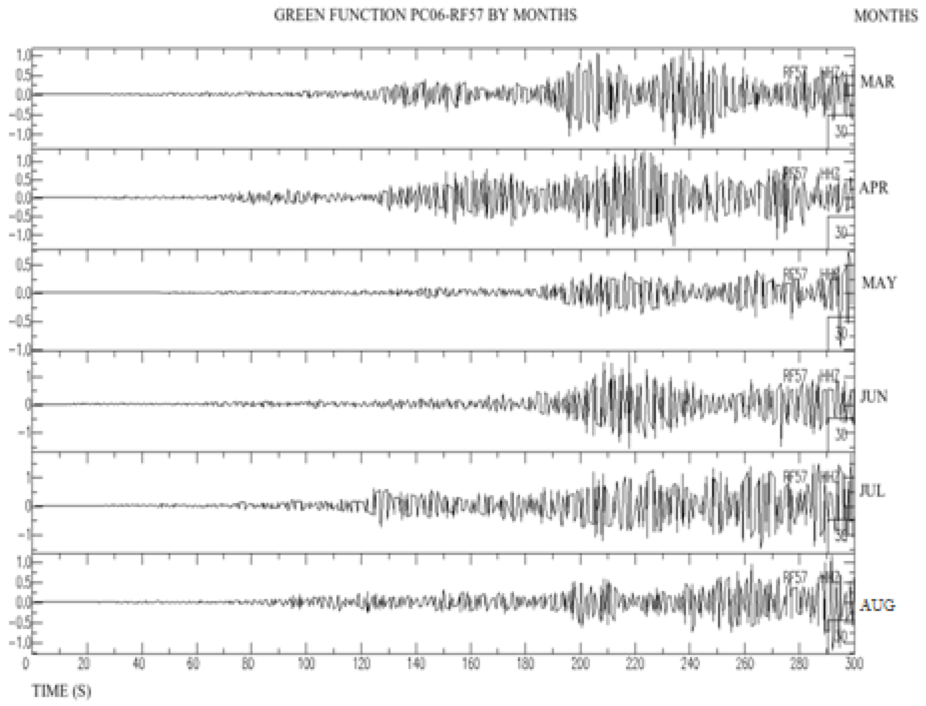

Figure 5.22 How the Green’s function between PC06 and geophones RF57 varies every month in the six-month period.

In Figures 5.20, 5.21 and 5.22 there is a small difference in arrival time, between corresponding features around 200s for the months of July and August. It is interesting to note that seismic activity in the area was more intense (earthquakes with a magnitude of more than 7.0) during this period of time, as can be seen in Figure 5.23 which shows the magnitude of the earthquakes taking place against days. As can be appreciated from Figure 5.23, three major earthquakes with a magnitude of more than 7.0 took place around the months of July-August 2003. This variation of the Green´s functions are in agreement with the work of Changshen and Zhongliang (2009) where the properties of the noise correlation functions depend on the underlying mechanism (diffuse wavefield or uncorrelated noise). Also, this is in agreement with the work of Tanimoto *et al.* (2006) where the variation of the noise correlation function is linked to seasonal variations in the relative excitation of higher modes compared to dominant fundamental-mode Rayleigh waves.

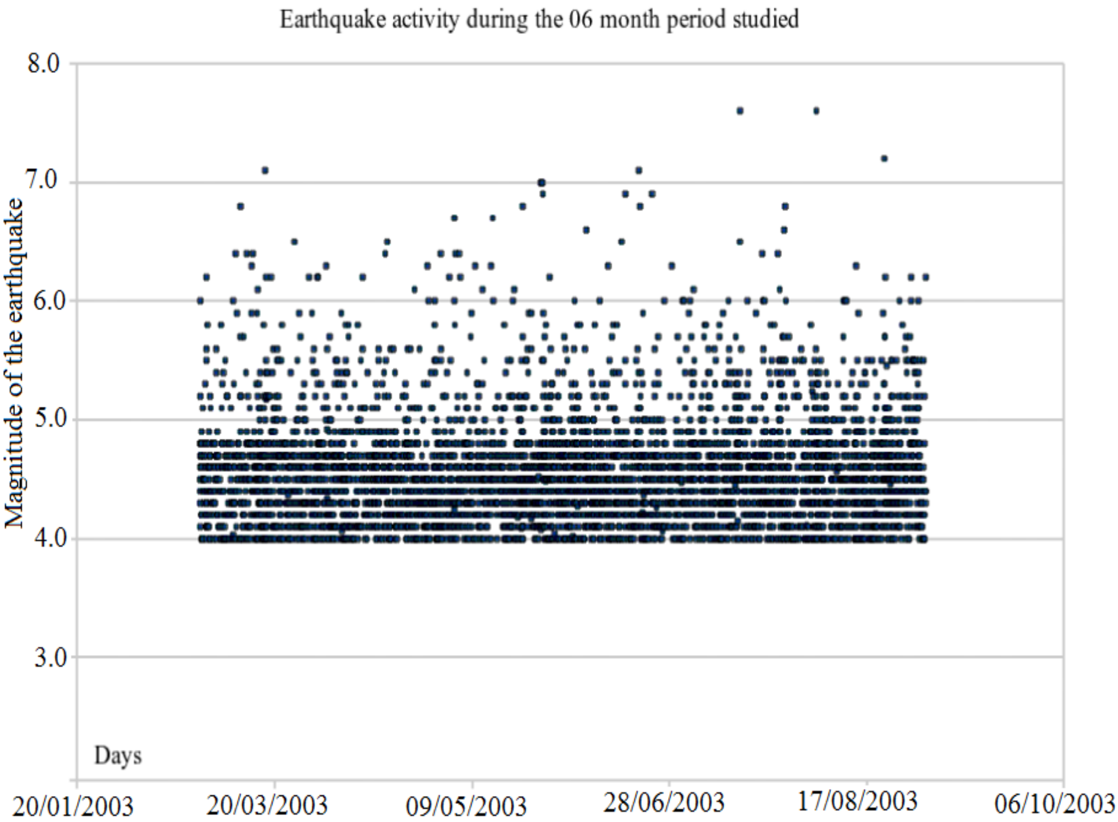

Figure 5.23 Plot showing the magnitude of earthquakes as a function of time for the six-month period considered in this study. Periods during which large earthquakes occurred can be related with changes in arrival times in the Green's functions.

The following figures show the final Green's functions between geophone PC06 and some receivers in line RF. In all plots, the upper figure is the calculated Green's function and in the bottom figure the real recordings from corresponding events (even though different in amplitude) are highlighted by arrows.

In all graphs presented in this section, comparisons between the calculated green's function and the corresponding real recordings were carried out by using earthquakes that were closest to the geophone PC06, as show in Figure 5.24.

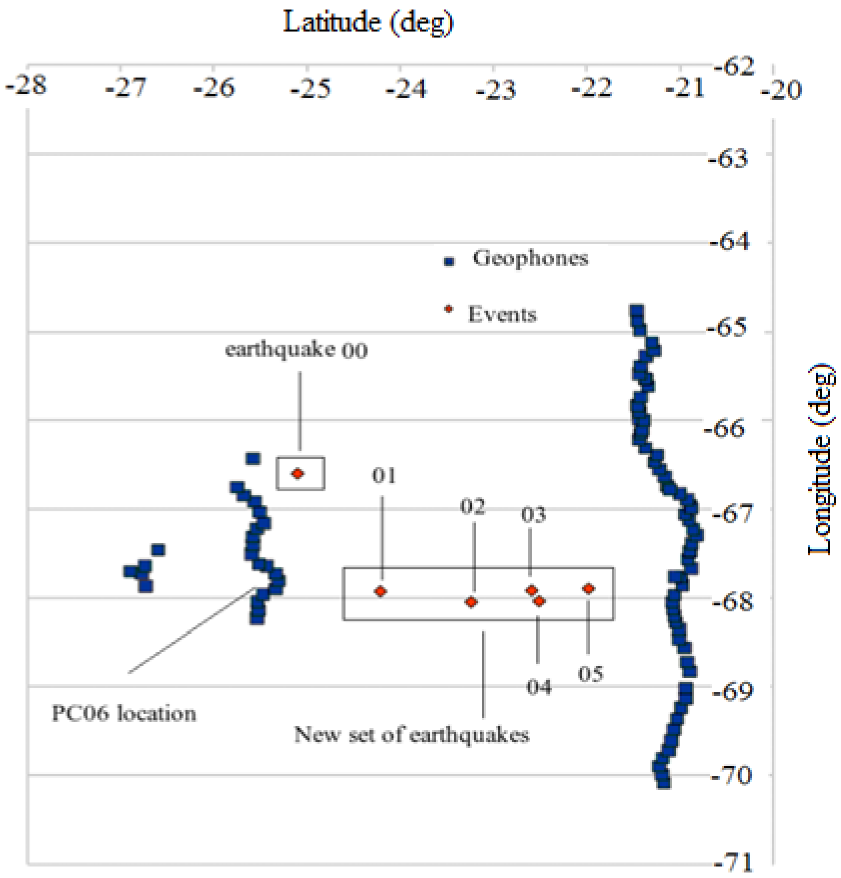

Figure 5.24 Geometrical configuration for the earthquakes considered.

Comparison for horizontal components (using earthquake 00)

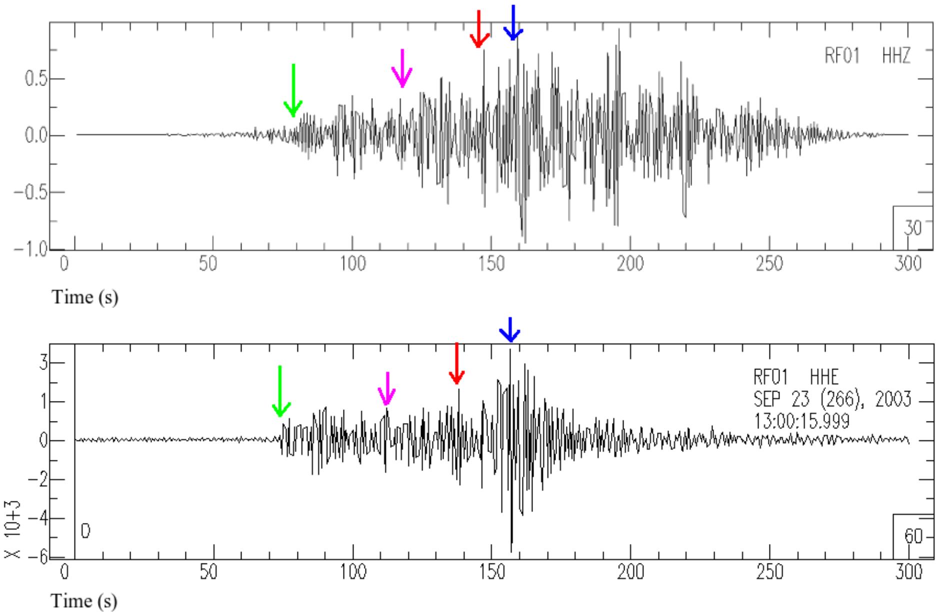

Figure 5.25. For geophone RF01 comparison between calculated Green´s function (above) and real seismogram (below) for the first step of interferometry for horizontal east component. Corresponding events has been highlighted by coloured arrows.

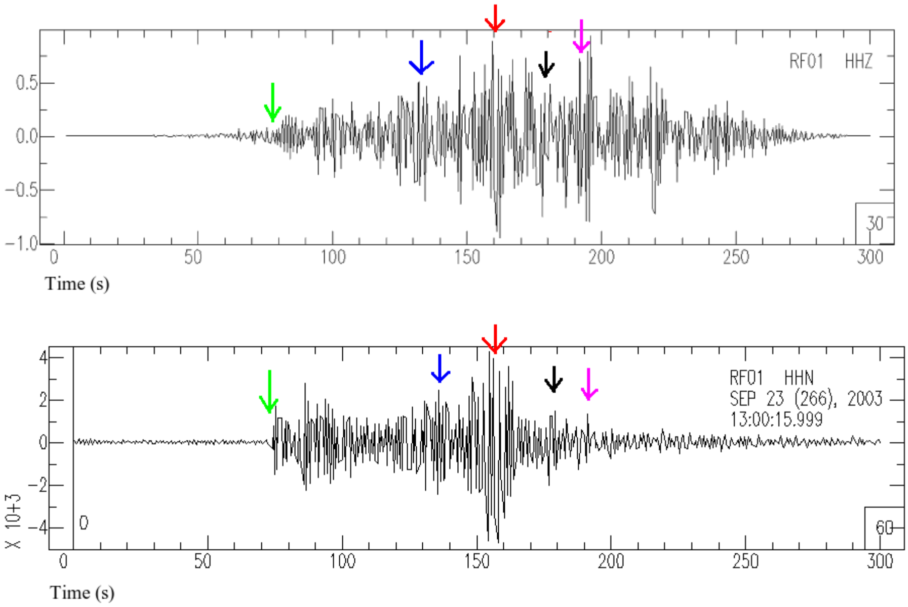

Figure 5.26.For geophone RF01, comparison between calculated Green´s function (above) and real seismogram (below) for the first step of interferometry for horizontal north component. Corresponding events has been highlighted by coloured arrows.

Comparison for vertical components (using earthquake 00)

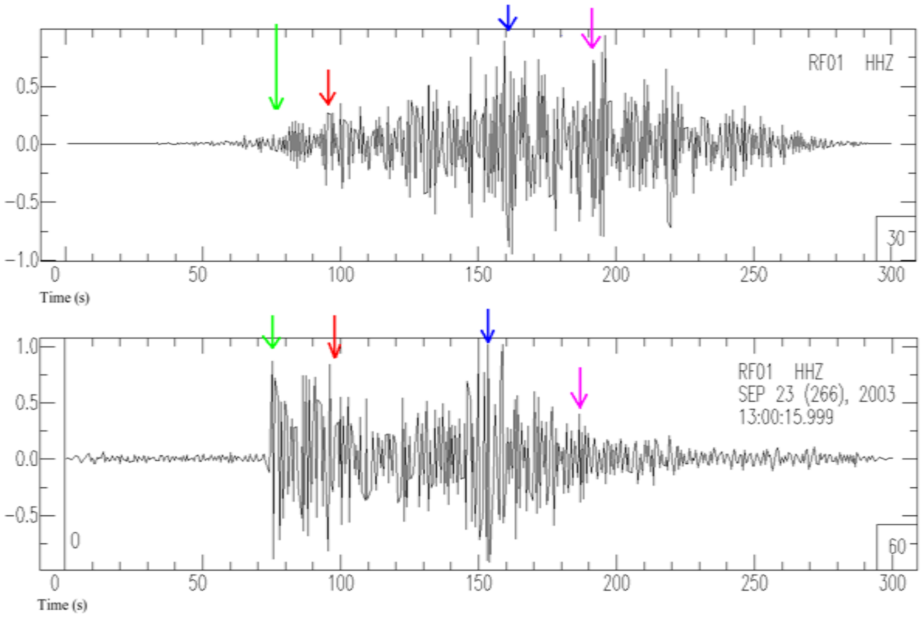

Figure 5.27. For geophone RF01, comparison between calculated Green´s function (above) and real seismogram (below) for the first step of interferometry for vertical component. Corresponding events has been highlighted by coloured arrows.

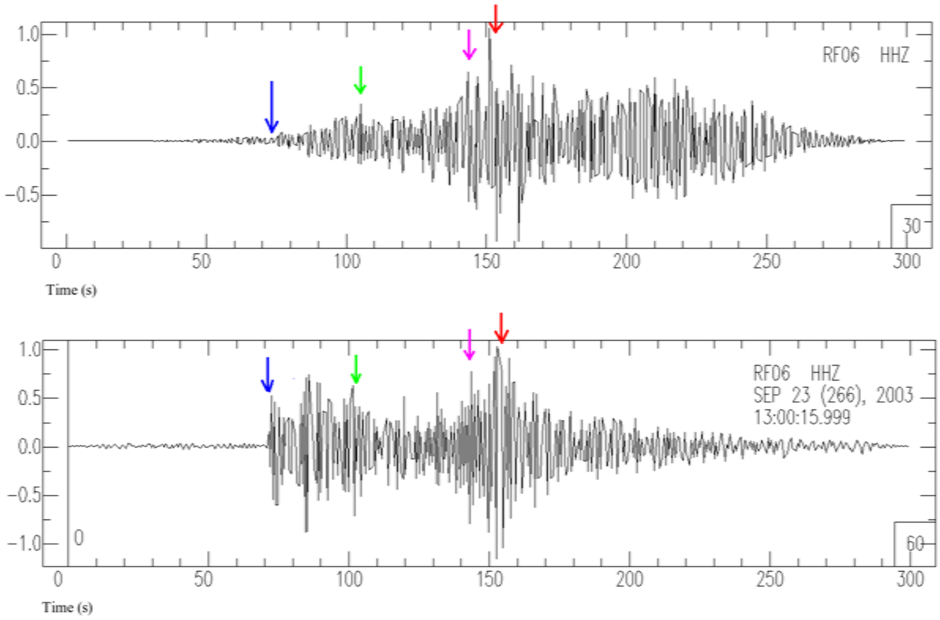

Figure 5.28. For Geophone RF06, comparison between calculated Green´s function (above) and real seismogram (below) for the first step of interferometry for vertical component. Corresponding events has been highlighted by coloured arrows.

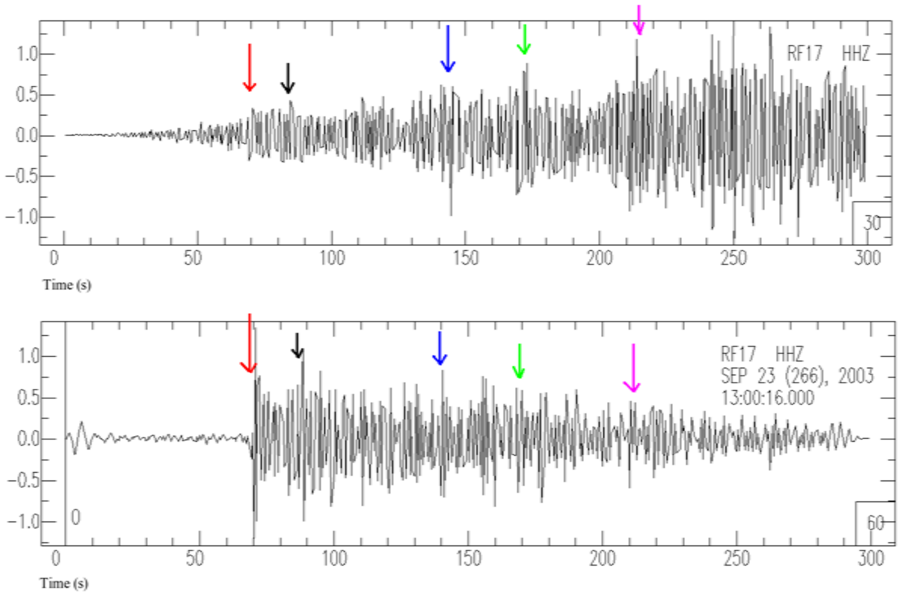

Figure 5.29. For geophone RF17, comparison between calculated Green´s function (above) and real seismogram (below) for the first step of interferometry for vertical component. Corresponding events has been highlighted by coloured arrows.

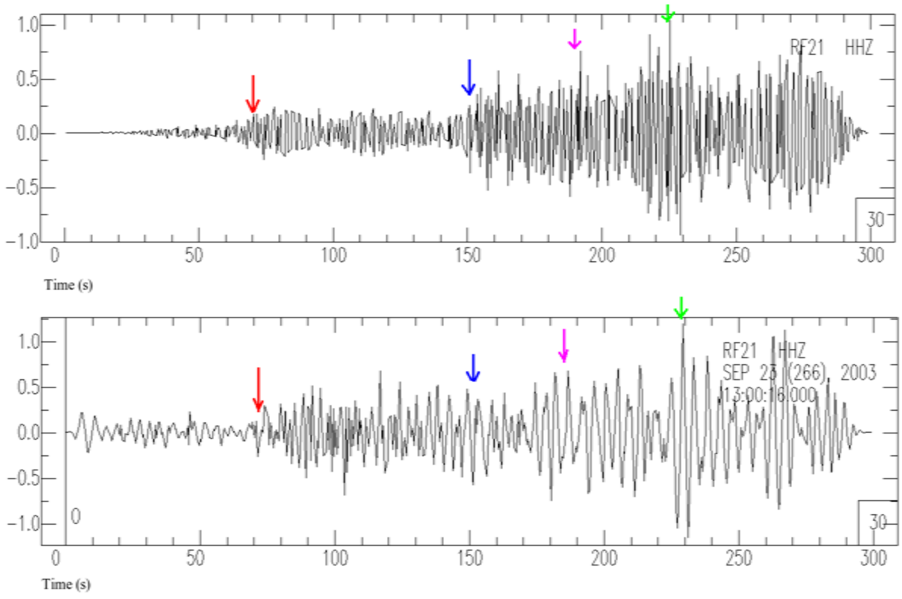

Figure 5.30. For geophone RF21, comparison between calculated Green´s function (above) and real seismogram (below) for the first step of interferometry for vertical component. Corresponding events has been highlighted by coloured arrows.

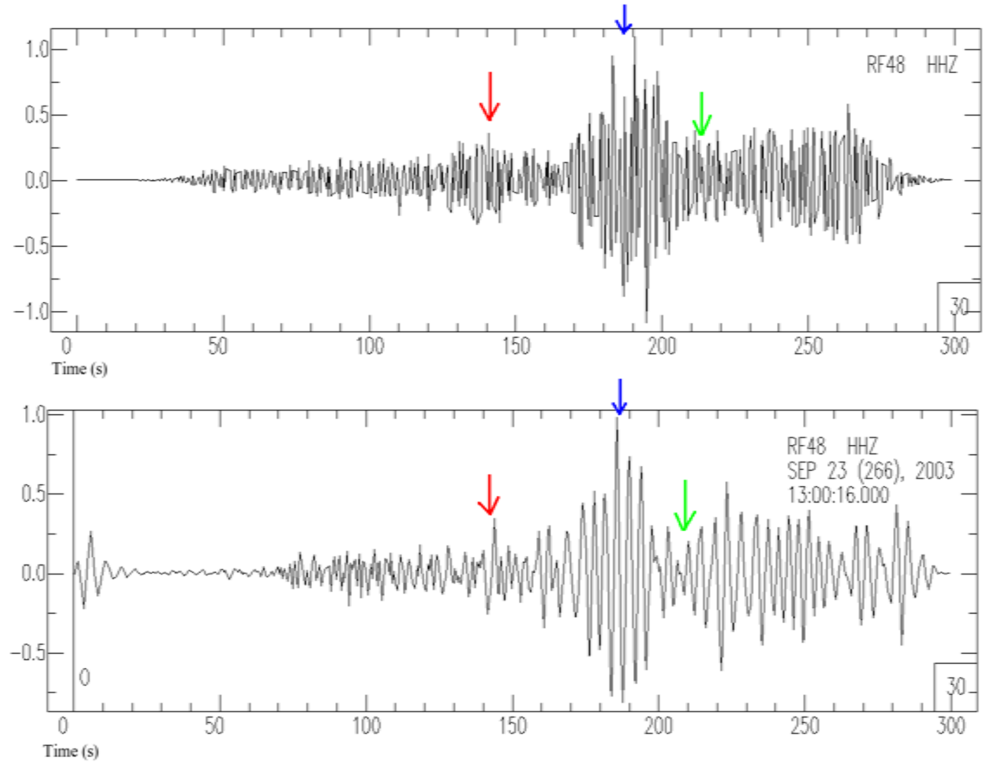

Figure 5.31. For geophone RF48, comparison between calculated Green´s function (above) and real seismogram (below) for the first step of interferometry for vertical component. Corresponding events has been highlighted by coloured arrows.

Additional tests to surface-wave interferometry results for case 2 (passive recordings)

Some additional tests were carried out in order to a) add some comparisons between real recordings and calculated Green’s functions, b) to demonstrate that the difference in distance between the real earthquake and geophone PC06 was consistent with the difference in arrival time between the real recordings and interferometric results, and c) to show the power spectrum of the real recordings when compared to that of the interferometric Green’s function.

The geometrical set up, showing the earthquakes that were used for making comparisons against the interferometric calculations is given in Figure 5.24. The main problem faced in this part of the research was that none of the earthquakes that occurred in the period of time the project was deployed lay in the same geometrical place as that of the geophones. This is an important restriction regarding the issue of comparison because it implies that only qualitative relationships can be made.

The remainder of the chapter will concentrate on showing comparisons that were made using earthquake 01 (see Figure 5.24) only because the rest of the earthquakes were too far away to make corresponding comparisons.

Figure 5.32 shows the whole set (for all geophones) of the calculated Green's functions versus real ones. As the first arrivals are weak, they have been highlighted (represented by vertical lines in these figures). Please note that the trend is analogous to the real case.

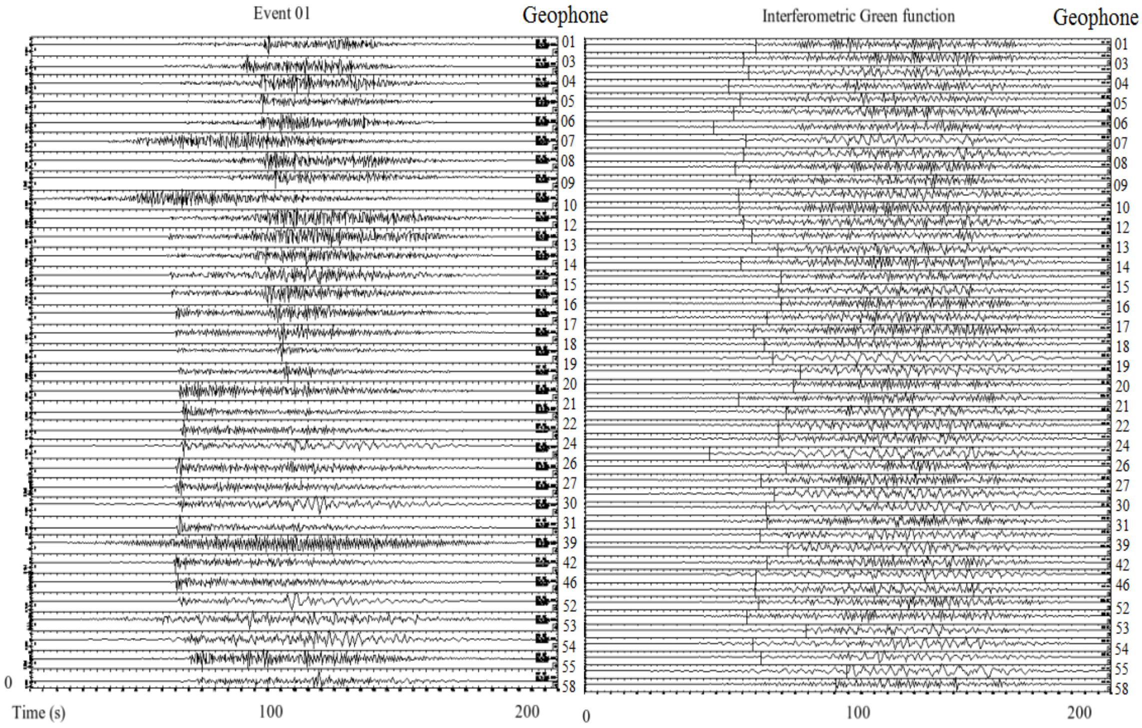

Figure 5.32 Comparison between real recording and calculated Green's functions for event 01.

The following figures show a comparison between the real recordings and the calculated Green's functions for the first step of interferometry, for geophones that were located in the extension of the path between geophone PC06 and earthquake 01.

These were: RF19, RF21, RF22, RF24 and RF25. The calculated Green´s functions are a bit noisy at the beginning of the signal making the task of picking the first arrivals difficult. The approach used here to pick first arrivals was to identify for each case the amplitude of the noise or minimum amplitude seen at the beginning of the signal, then where the amplitude of the signal doubled, a first arrival is picked. For example in Figure 5.33, the amplitude of the noise is 16.67 V/m and the first arrival is picked where amplitude become 33.33 V/m. In that way it is ensured that a first arrival is picked and not noise or a spurious signal.

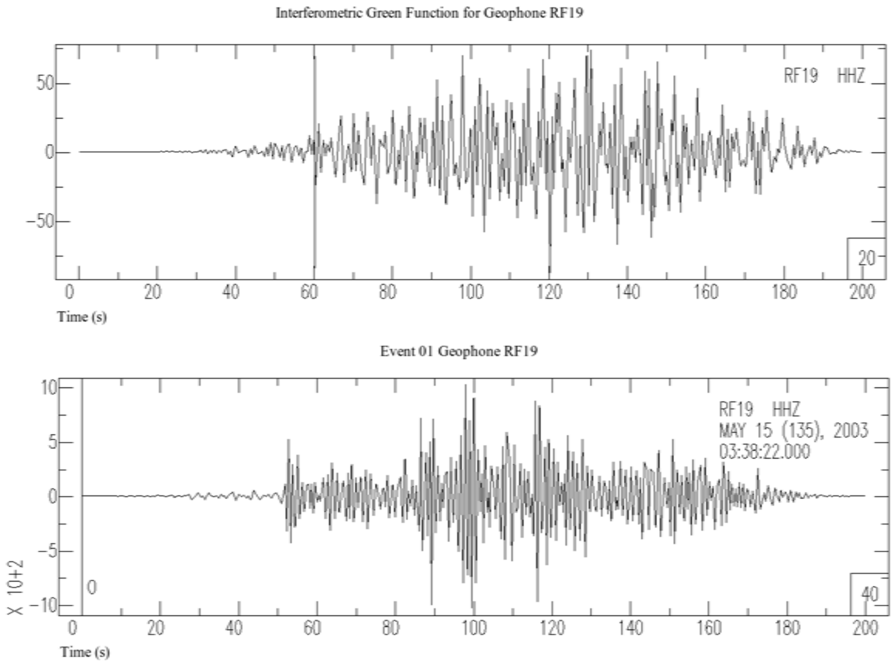

Interferometric Green Function for Geophone RF19

Event 01 Geophone RF19

Figure 5.33 Comparison between Green´s function (above) and real recording (below) for the first step of interferometry for geophone RF19.

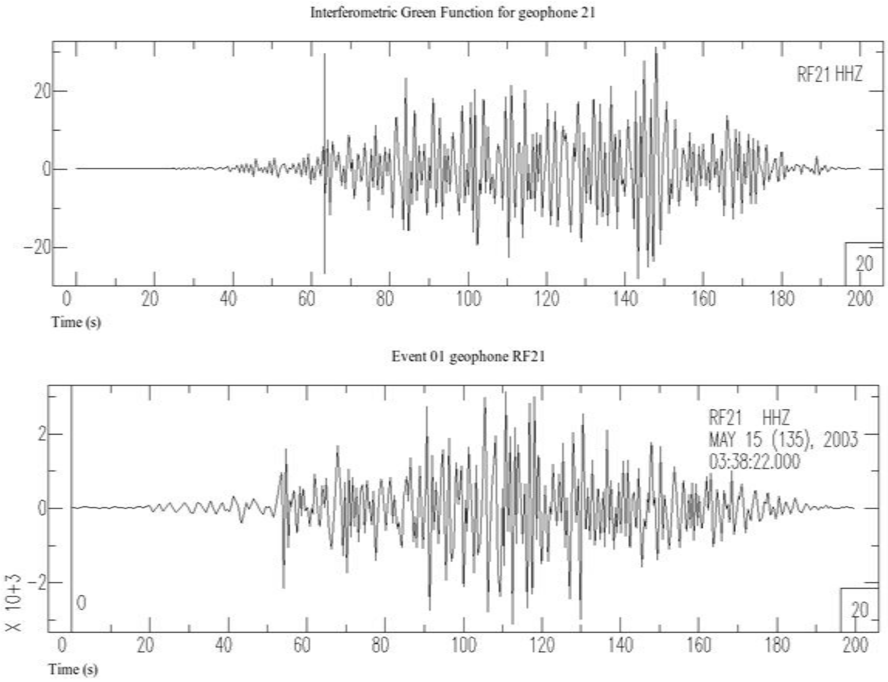
Interferometric Green Function for geophone 21

Event 01 geophone RF21

Figure 5.34 Comparison between Green’s function (above) and real recording (below) for the first step of interferometry for geophone RF21.

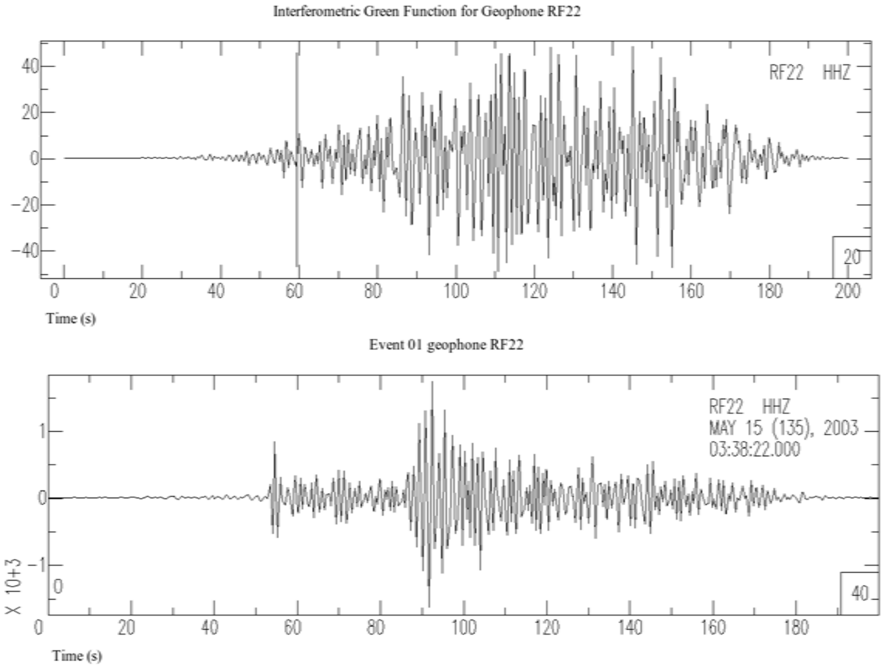
Interferometric Green Function for Geophone RF22

Event 01 geophone RF22

Figure 5.35 Comparison between Green’s function (above) and real recording (below) for the first step of interferometry for geophone RF22.

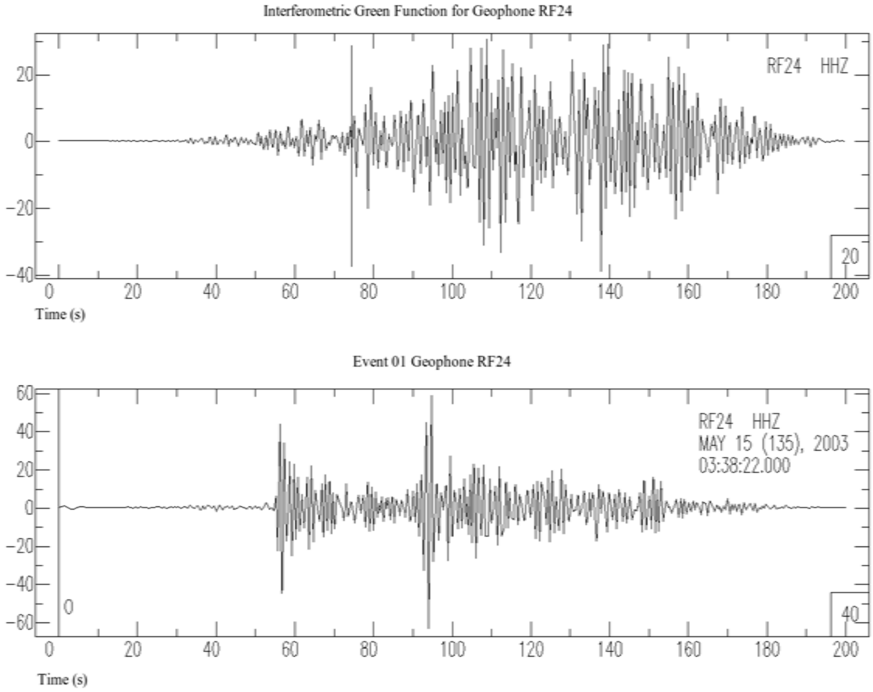

Figure 5.36 Comparison between Green’s function (above) and real recording (below) for the first step of interferometry for geophone RF24.

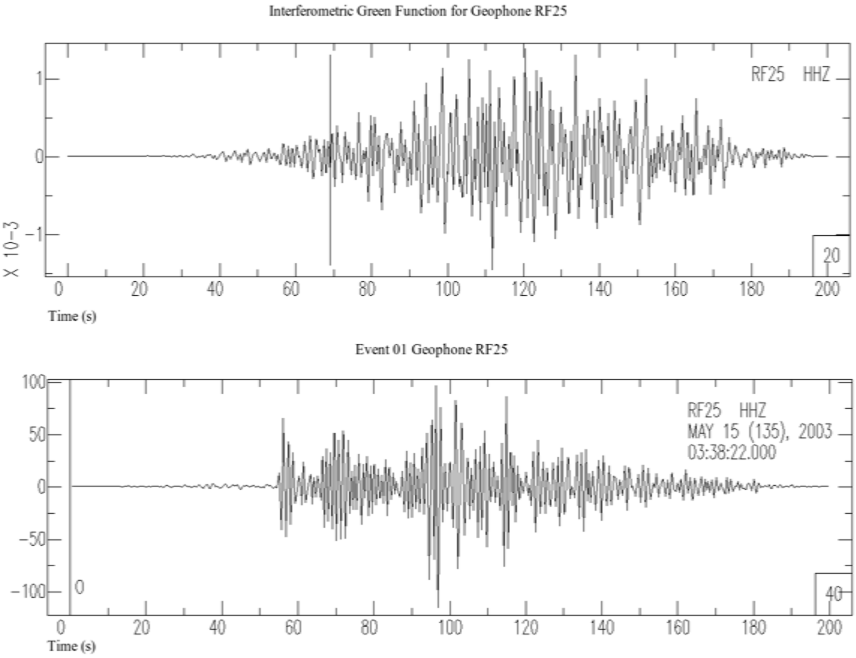

Figure 5.37 Comparison between Green’s function (above) and real recording (below) for the first step of interferometry for geophone RF25.

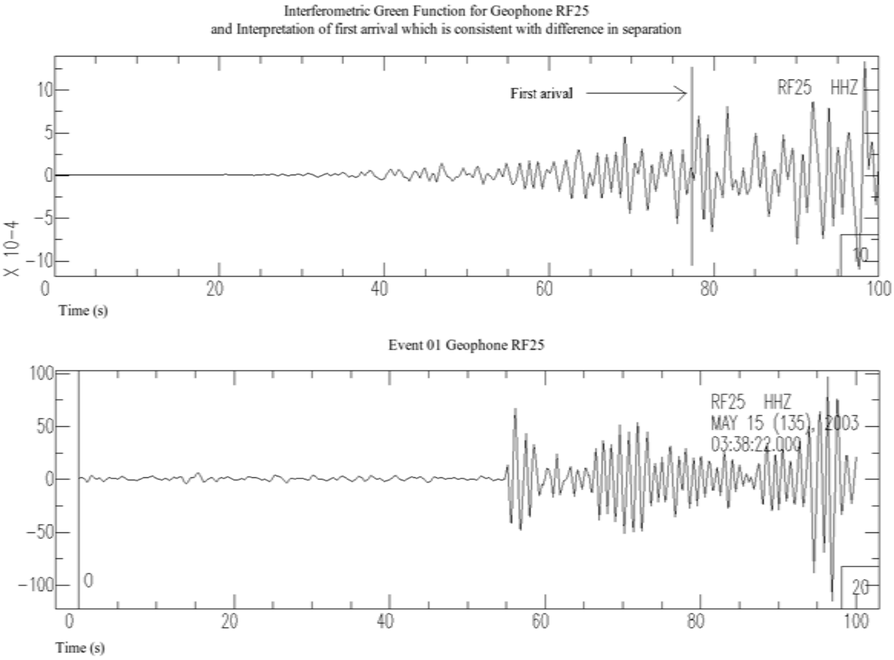

Figure 5.38 Interferometric Green's function (above) for the first step of interferometry and interpretation of first arrival of a real recording (below) is consistent with the difference in separation.

By using an example, it is possible to demonstrate that the difference in arrival time observed in Figure 5.38 is consistent with the difference in separation between geophone PC06 and the earthquake shown in Figure 5.38. Let see why with the following calculation:

If waves are assumed to travel through the great circle path between the considered points (position of RF25, PC06 and earthquake 01 in figure 6.34) of this geometrical configuration the distance can be calculated using the Java script developed by Chris Veness. (See chapter 1, equations 1.17 and 1.18)

The additional distance travelled by the waves in Figure 5.38 is the distance between the position of earthquake 01 and geophone PC06.

For earthquake 01: location = (-24.21; -67.93)
For PC06: location = (-25.30; -67.81)
Distance between earthquake 01 and PC06 = 121.8 km.

The velocity taken from the IAP91 velocity model is around 5 km/s so the theoretical difference in time is around 24s. This value is very close to that calculated from Figure 5.38. This is only an estimate of real value; nevertheless the numerical values are close. A problem in this calculation is the lack of an accurate velocity model, the anisotropic nature of the velocities present in the area, and the difficulty in interpreting the first arrivals due to the low quality signal-to-noise ratio.

Finally, a power spectrum plot is presented for both the original recording, filtered in the region of the frequency of 0.2-1.0 Hz, and the power spectrum of the Green's function that results from interferometry. The Green's function is also filtered in the region of the frequency of 0.2-1.0 Hz. This plot is important because it gives an indication of the frequencies that form part of the signals to be compared, and helps with understanding possible differences in the form of the seismograms. Figure 5.39 shows the power spectrum for event 01 geophone RF25 and the analogous plot calculated from the interferometry-calculated Green's function after application of a bandpass filter that tried to equalise the spectrum by using the spectral whitening module of the SAC program.

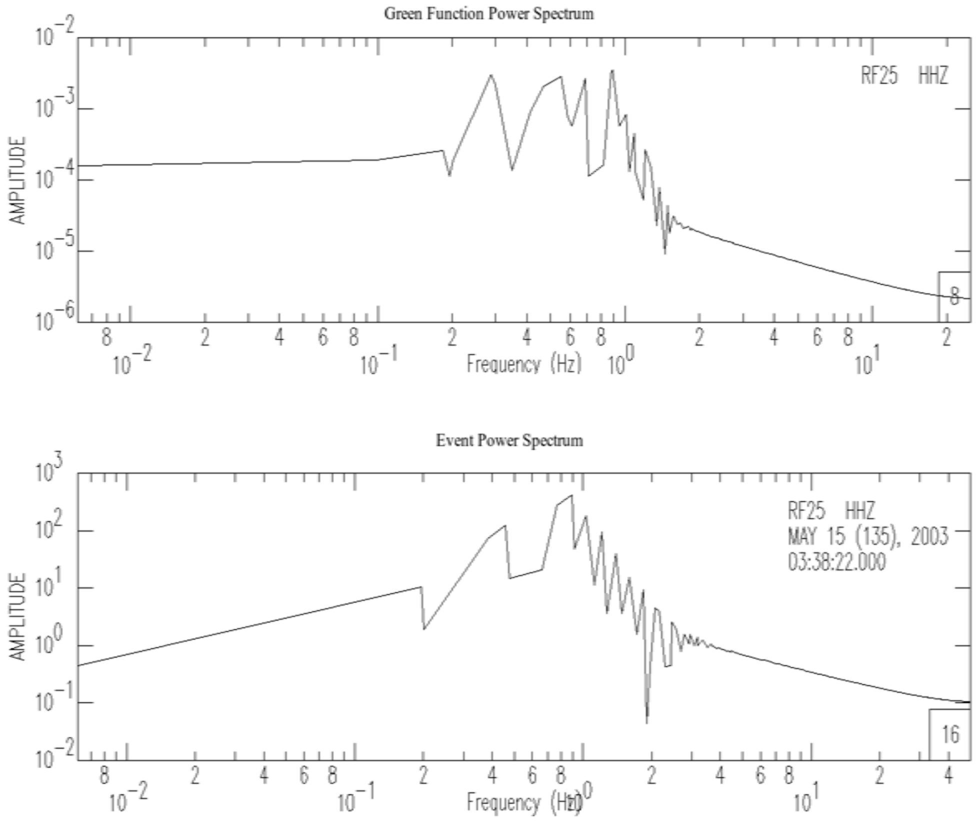

Figure 5.39 Comparison of power spectrum for event 01 geophone RF25.The power spectrum gives an indication of the frequencies that form part of the signals to be compared and explain possible differences in the form of the seismograms and Green´s functions.

5.6 Discussion

The importance of this piece of research lies in the fact that this is the first application of source-receiver interferometry theory over a real data set that has originated from an area of high geological complexity. This piece of research encountered several difficulties and drawbacks, for example, the fact that none of the earthquakes took place in the period of time that the project was deployed, and none lay close to the geophones, and this implied that only qualitative comparisons could be made.

Another problem to be faced was the anisotropic nature of the velocities present in the area and the difficulty in interpreting the first arrivals for the case of the Green’s functions, due to the quality of the signal in relation to noise played an important role.

- An additional important complication in the approximation derived by this research was that it was conducted in a complex area with proven attenuation of S waves (Wölbern *et al.*, 2009), due to zones of partial melted material, and most probably the changes in amplitude are due to loss of energy during propagation between each receiver pair. This meant that relative amplitudes were not recovered correctly, but corresponding arrivals could still be identified. Moreover, the cross-correlation approach that was used assumed that the medium is lossless, i.e. the method did not account for attenuation. This introduced the question of processing the data in order to compensate for such effects.

- The issue of attenuation has already been tackled by studies such as that of Snieder (2007), in which he stated that in an inhomogeneous attenuating medium one needs sources in the volume and the surface of integration for the Green’s function extraction. Another possibility in this current case was to work with convolutional interferometry because it is valid for media with losses due to the fact that such interferometry methods do not need time-reversal to perform calculations.

- Another point set against the current study is that of the frequency content of the Green’s function and that of the real recordings. Even though a filter was applied to make the frequency content in both signals the same, they will never be exactly equal because they came from different processes. This is besides the fact that even if a frequency could have been present, such a frequency could have been attenuated when compared to that of the real recording. Therefore, the power spectrum will not look the same (see Figure 5.39) and, as a consequence, the corresponding signal will also not look the same.

Despite all these difficulties and problems some good points and results were found that gave a beneficial indication of the suitability of the method for the current data. For example, in the case study of passive recordings, the first arrivals of the

Green’s functions were different in relative amplitude from those of the real recording. Nevertheless, the horizontal east components were more similar in relative amplitude than the vertical and the horizontal north ones. This could be an indication of the directional nature of the noise source (i.e. the Pacific Ocean in this case). Indeed, the eastern component of the reconstructed Green’s function showed a better match than other components when compared to the real recording. Again, this is consistent with the fact that the ocean is producing noise in a west-east direction.

Further favourable results are that, as shown in Figure 5.38, the difference in arrival time between the real recording and the calculated Green’s function is consistent with the difference in separation between geophone PC06 and the earthquake.

This current research also indicated that the variation of the Green´s function between two receivers in a given period of time was related to the source mechanism. In fact, temporal observed variations of the Green´s functions can be explained by the non-stationarity of the arriving phases. Slight non-stationarity of wave phases can cause slow changes in the amplitude of the correlation functions. (De Stefano and Clemente, 2006) Also, properties of the noise correlation functions depend on the underlying mechanism, to know diffuse wavefield or uncorrelated noise (Changshen and Zhongliang, 2009). Additionally, the variation of the noise correlation function is linked to seasonal variations in the relative excitation of higher modes compared to dominant fundamental-mode Rayleigh waves (Tanimoto *et al.,* 2006).

A distinct way of monitoring the area is by means of coda waves. This idea was first introduced by Poupinet *et al.* (1984) and latterly called coda wave interferometry by Snieder *et al.* (2002). The idea was to track small changes in the phase of the coda waves which are caused by velocity changes in the medium.

Unfortunately, this method needs a repeatable source before and after the change in the medium is produced, which was not possible in this instance because each earthquake is unique in characteristics such as depth, source mechanism, duration, magnitude, location, etc. This was therefore almost impossible to obtain in practice.

Finally, and in order to answer the question posed at the beginning of the chapter concerning the possibility of infilling missing records, it could be concluded that no direct replacement of records could be carried out, because the method only served to replicate data in a qualitatively way. Correction algorithms are needed in order to be more precise. Nevertheless, qualitative behaviours were indeed reproduced. This was a good indication of the validity of the method and is also useful information that can be used for other purposes, or to support another interferometric calculation.

5.7 Conclusions

This chapter has not only considered surface wave seismic interferometry, but also a new kind of seismic interferometry introduced by Curtis (2009): that of source-receiver interferometry. The chapter considered two main methodologies: using events and using noise records. As it was demonstrated, both methodologies showed good approximation to what could be expected for a single application of interferometry. Nevertheless, in the first step of interferometry, the noise procedure showed signs of being affected by attenuation, while the active source procedure did not.

Even though both methods seemed to produce coherent results when compared to real cases, results could only be compared in a qualitative way due to limitations such as good quality of data, and that none of the earthquakes lay in the same geometrical place as the geophones in line PC. Also, from both methodologies that were checked for the second step of interferometry mentioned and explained in section 5.4, the data was not clean enough in the case of noise sources.

One important factor to take into account for further studies is that of the relation between attenuation and scattering. In fact, in the case of noise sources, attenuation plays an important role in the sense that the signal retrieved cannot recover the same amplitude. Nevertheless, features in seismograms are analogous. This could be an indication of the limitation of the methodology presented here or it could indicate that a gain function has to be applied to the data before the interferometric calculations can be carried out.

As was confirmed during the work presented in this chapter, qualitative behaviour of a virtual geophone placed in the location of a real one will reproduce the expected response. Nevertheless, in order to add new information to fill in missing recordings, a correction algorithm that takes amplitudes into account is required.

Chapter 6

DISCUSSION AND CONCLUSION

6.1 General remarks

The purpose of this chapter is not to repeat the conclusions already outlined in each chapter but to present a unified view of the whole thesis, making appropriate conclusions, remarks and recommendations for future studies.

Seismic interferometry has proven to become an established methodology over recent years. At the same time, the Altiplano region is a zone of complex geology and geophysical characteristics as well as a zone of worldwide interest due to the controversy over its process of formation. Several research works have been conducted in the area, which allowed us to test new ideas with seismic interferometry and to compare the results from this research with previous studies. This was important because one of the aims of this project was to study to what extent the virtual receiver, obtained from interferometry, emulates the response of a real sensor placed at the same location of the virtual receiver.

The way to approach this was to apply the different established and new methodologies of seismic interferometry to the area making the task of interpreting different results from different methodologies simpler and, for the same area, comparing the efficacy of different methodologies such as:

- The stationary phase approximation with the novel concept of transforming a source into a virtual receiver.
- The coda wave approach together with a proposed methodology of convolution and cross-correlation.
- The passive recording technique together with a novel idea of retrieving body waves by means of reflected waves, and
- The implementation on real data of the novel technique of source-receiver interferometry.

Regarding the limitations of this research, it is imperative to point out the problems associated with the data. Due to the difficulty with access to the area and severe weather conditions, geophone stations operated in a discontinuous way during the survey time of the REFUCA project. This not only affected the availability of the data, but also the quality of recorded data. The main action taken to circumvent these problems was pre-processing of the data. Other factors affecting the quality of the data set were, for example, GPS timing problems and also the high noise content of the data coming from the functioning of the geophones which can lead to incorrect noise processing (for seismic interferometry seismic noise is desirable, but not electronic noise from geophones). Both cases were treated by rejecting the recording, in the case of the GPS problem, or by applying filtering and or rejection, in the case of noisy records.

One way to predict the success of the application of the interferometric technique in the first stages of this research was the execution of a pilot project that measured to what extent positive results could be obtained by the use of seismic interferometry. This pilot study was summarised in section 1.7 and, by the time it was performed, gave good, positive results in the sense that the novel technique of turning earthquakes into virtual receivers (Curtis *et al.*, 2009) was implemented for the first time in an area of high geologic complexity, and which showed a clear indication of direct surface wave arrivals and moveout, related to inter-source distance, at the considered receiver stations.

Also, interferometric results were shown to be compatible with previous velocity studies conducted in the area. Nevertheless, information concerning the source mechanism of the earthquakes considered and studied in this thesis was another drawback that this research had to manage. Even though the seismic information was as complete as possible in the seismic catalogues, source mechanisms were not always available for the earthquakes chosen for this research.

Another point that was problematic for this project was the velocity model needed for ray tracing in order to calculate travel times which were compared to travel times obtained from interferometry. This difficulty was relieved by making use of velocity models from previous research carried out in the area. Also, the previous velocity models were used to compare results from interferometry. Finally, common problems like storage and calculation capacities were solved, thanks to the resources of the University of Edinburgh.

6.2 Stationary phase approximation

Chapter 2 and the student pilot project showed that it is possible to retrieve body and surface waves using the stationary phase approximation. So, these two pieces of research achieved the first objective of this thesis, that of constructing an artificial or virtual sensor for any energy source that could then be used to detect surface and/or body waves. Nevertheless, results indicate that several factors have to be taken into account and results need to be analysed and compared to other methods in order to recognise possible bias introduced in the interferometric procedure.

For example, in chapter 2 the complexity of the medium and the strong and rapid velocity changes dictated a constraint on the separation of the sources (earthquakes of Table 2.1) that were used to calculate waves travelling between them. These sources had to be near each other in order to retrieve reliable information, indicating that in future research in complex media, separation distance between sources cannot be greater than the distance at which the velocity changes in a significant way.

Additionally, the student pilot project conducted at the beginning of this research programme brought attention to the importance of the quality of the data, the accessibility to it and the feasibility of the seismic interferometry method to the Altiplano area.

In relation to the second aim of this research, that of assessing as to what extent the virtual receiver, calculated by seismic interferometry, emulated the response of a real sensor placed at the same location, both chapter 2 and the student pilot project made that assessment by comparing velocity information obtained from interferometry with that from other methods such as tomography, and/or the receiver functions technique.

Results for body waves were consistent with pre-existing information, implying that velocity information retrieved by interferometry is reliable. A different result was obtained for body waves, (chapter 2) in which velocities inferred from seismic interferometry differ from those from tomography but reproduces qualitative behaviour of the velocity field (especially the low velocity zone).

6.3 P and S coda wave interferometry

Coda wave interferometry was tested in chapter 3. The new proposed methodology of combined correlation-convolution applied to coda P and coda S wave proved to be successful for retrieving body waves. Also, the calculated velocity of the retrieved waves agreed with the expected velocity for body wave in the Altiplano.

Additionally, new conclusions were drawn from the application of the methodology proposed in chapter 3 to the area, for example, coda S wave failed to produce a clear retrieved wave (Figure 3.7) result that is thought to be caused by the zone of partial melting material present in the Altiplano. So, as a concluding point, in this case it is suggested to use coda P instead of coda S.

Another important conclusion drawn from the results of this section is that of source distribution in depth. From the simulations run, it was concluded that if the correct Green’s function is to be estimated then earthquakes considered in this chapter for interferometry calculations, must reach the surface.

The combined methodology of cross-correlation and convolution proposed in this chapter help to describe the apparently contradictory behaviour of the retrieved waves (Figure 3.4, for example) such as the inverse moveout observed in the plots of the retrieved waves as well as the arrival time for long offsets. This combined methodology was derived by considering the relative geometrical relation between earthquakes located in the subsurface, geophones at the surface and virtual sources in the surface. These parameters together with the source distribution (as was seen from the simulations) are fundamental when defining the interferometric methodology to be used in this and in future studies.

6.4 Passive recordings

Since the pioneering work of Shapiro and Campillo (2004) the technique of seismic interferometry by the use of passive recordings has been demonstrated to be robust. In this research, the retrieval of surface waves was clear as seen from the results in chapter 4 by which the first aim of this research was accomplished. The surface velocities derived from interferometry using passive recordings agreed well with previous information about the velocities in the area, indicating that the method is valid and confirming that the waves retrieved were in fact surface waves. This contributed to the second aim of the research for which the comparison is between the velocities values obtained.

In relation to body waves retrieval, as was seen in chapter 4, for the Altiplano plateau there was no indication of body wave retrieval meanwhile for the Puna plateau the situation was different. Two wave packets were observed (Figure 4.9) whose velocity difference indicated the possibility of surface and body waves being retrieved and not Rayleigh and Love waves - because such a difference is not consistent with the expected differences for Love and Rayleigh waves for this zone as explained by Vdovin *et al.* (1999). The fact that body waves are not retrieved in the Altiplano plateau and are retrieved in the Puna plateau can be related to the fact of simpler geology of the Puna plateau (Heit, 2005). For example, there is no partially melted material zone. This implies that the methodology only works when the geometry of the Moho and the velocity structure above it is as simple as possible; a result that is in agreement with the conclusions derived from the work of Zhan *et al.* (2010). In this research some indications of body waves were obtained from results in the Puna plateau. As seen in this case, the velocity retrieved agreed well with the expected body wave velocity for the zone. Nevertheless, for the Altiplano plateau no positive results were found.

The results obtained for the Altiplano and Puna plateaux points to the fact that continuity of the Moho and the relative impedance contrast are important factors for successful body wave retrieval. For example, surface waves retrieved in chapter 4 section 4.4 showed strong and weak signals observed along the Altiplano, which are thought to be due to the continuity and impedance contrast of the Moho.

These results are in agreement with the results found in the work of Giese *et al.* (1999); to be more specific the signal from the eastern part was clearer than that from the western part of the Altiplano. Also, this research showed that the length of the line or profile of geophones located at the surface is a limiting factor when retrieving surface or body waves from seismic interferometry (Figures 4.8 and 4.9) in the sense that a profile with long offsets will give more information (such as for example refracted waves in Figure 4.8) of the media than a profile with short offsets. Finally, a suggestion for further research will be to take into account interferometry factors such as the impedance contrast and geometry of the subducting slab, because it could trap body waves that can be retrieved by the method.

6.5 Source-receiver interferometry

Source-receiver interferometry is a novel idea within seismic interferometry originally proposed by Curtis (2009). As this idea has only been tested, so far, on synthetic data and for data coming from New Zealand, this part of the research aimed at testing it on real data for the Altiplano region.

The source-receiver interferometry method was tested in this research by using two different approaches: deterministic sources and passive noise recordings. Both methodologies met the first aim of the research by demonstrating that surface waves could be retrieved by source-receiver interferometry. They do that by showing good approximation and coherent results when compared to real cases. The second aim of the research was to assess to what extent the calculated virtual receiver emulates the response of a real sensor placed in the same location as the virtual. In this research, this second aim was achieved by comparing the pattern structure of the retrieved Green's function and that of the corresponding real seismograms.

All of these comparisons show that surface waves were retrieved, implying the validity and usefulness of the method. Nevertheless, important conclusions and recommendations were draw from this research, such as for example, in the first step of interferometry, the passive recording method showed signs of being affected by attenuation, as did the active source method but in a lesser manner as was seen from the analysis of Figures 5.18 for the active case and Figures 5.25 to 5.31 for the passive case.

Another important conclusion is that results can only be compared in a qualitative way due to limitations such as quality of data and that more of the earthquakes do not lie in the same geometrical place as the geophones in line PC. Nevertheless, features such as the arrival times for every geophone along the northern profile in seismograms are analogous. This is an indication of the limitations of the methodology presented here.

Another drawback for the application of interferometry is attenuation. As was seen from sections 5.5.2.1 and 5.5.2.2, a gain or recovery function needs to be applied to the data before the interferometric calculations can be carried out. Another possibility for the attenuation case is to work with convolution interferometry because it is valid for media with losses due to the fact that such an interferometry method does not need inversion in time to perform calculations.

6.6 General recommendations

- The third aim of this research was to establish a methodology for retrieving surface and/or body waves in a complex area, such as the Altiplano, and to delineate advantages and disadvantages of the said methodology. As was seen from this thesis, every methodology has points in its favour and points against its application, and it is not straight forward to choose which methodology is the best to apply to a given case study.

- The general advice inferred from this research is that, when dealing with a new area, if the intention is to apply interferometry, the best practice is to start by conducting a pilot project in order to test all methodologies available and decide which one works best, then apply this methodology to the whole area and data set.

- As a concluding remark relating to the aims of the research, it can be said that they were, in general, achieved. Nevertheless, care has to be taken as to what extent these results are valid or applicable. The importance of this research is the information that may be retrieved from every technique, such as the velocity structure, and/or in the case of this research, characteristics of the zone of partial melting such as boundaries and its velocity field.

6.7 Future research

This research has made use of the most common techniques within seismic interferometry. Future research in the area should take into account recent developments such as that of interferometry by deconvolution which improves the quality of the retrieved Green’s function, or developments that take into account attenuating and moving media, or other facts such as diffusion, bending waves, elastodynamics and irregular illumination.

Some reference that has already taken such factors into account can be found in the work of Slob *et al.* (2007) and Halliday and Curtis (2009), where they considered interferometry by cross-convolution. Draganov *et al.* (2010) used an adaptive filter to deal with the problem of losses and at the same time estimate attenuation parameters. Additionally, interferometry by multidimensional deconvolution takes into account attenuating media, as explained by Schuster and Zhou (2006), and Wapenaar (2008a, 2008b).

Also, new algorithms within seismic interferometry have been proposed recently, like that of Curtis and Halliday (2010b) or that of Poliannikov (2011); both consisting of two consecutive applications of seismic interferometry, which opens a new range of possible results. Poliannikov (2011) demonstrated for a synthetic model that it is possible to image a subducting slab. Unfortunately, in this current research, the intermittent functioning of the receivers made the fold of coverage a problem and, as explained in the introduction section, this idea had to be abandoned. Future studies in the area should take into account this problem and apply such a procedure on real data.

One interesting possible direction of research is that of directional bias in passive noise and active source wavefields. Bias can be introduced in Green´s functions estimates when amplitudes of energies have directional variations. Correction algorithms have been proposed previously, for example, van der Neut and Bakulin (2009) proposed a method based on wavefield separation and Wappenaar *et al.* (2008b) proposed a correction method based on multidimensional deconvolution.

More recently Curtis and Halliday (2010) proposed a method that corrects for dimensional bias for interferometric estimates. In the Altiplano region, the main source of passive noise wavefields is the Pacific Ocean. This fact makes wavefields become stronger in one direction and an algorithm has to be developed in order to correct for this directional contribution. Future research will do that by defining a methodology analogous to that of Curtis and Halliday (2010). Even though this current research did not take this into account, future research projects could be focused on the detection and correction of possible interferometric errors caused by the directional nature of the illuminating wavefields.

Another possible research direction is that of the changes in the medium such as velocity field, measured by seismic interferometry. But the changes measured by interferometry can also come from a change in the illuminating wavefield, for example, a change in the swell of the ocean colliding against the shore. Such changes in the source mechanism leave the medium intact; nevertheless it can be measured by seismic interferometry. Future research should discriminate between these two kinds of changes.

.

.

BIBLIOGRAPHY

Abe, S., Kurashimo, E., Sato, H., Hirata, N., Iwasaki, T. and Kawamaka, T. (2007) 'Interferometric seismic imaging of crustal structure using scattered teleseismic waves', *Geophysical Research Letters,* 34(19), L19305.

Aki, K. and Richards, P. (1980) *Qualitative Seismology,* New York: W.H. Freeman.

Allmendinger, R., Jordan, T., Vay, S. and Isacks, B. (1997) 'The evolution of the Altiplano-Puna Plateau of the Central Andes', *Annual Review of Earth and Planetary Science,* 25, 139-174.

Bakulin, A. and Calvert, R. (2004) 'Virtual source: new method for imaging and 4D below complex overburden', in *SEG Annual Meeting,* Denver, Colorado, Society of Exploration Geophysicists, 2477-2480.

Bakulin, A., Mateeva, A., Metha, K., Jorgensen, P., Ferrandis, J., Herjold, S. and Lopez, J. (2007) 'Virtual source applications to imaging and reservoir monitoring', *The Leading Edge,* 26(6), 732-740.

Bakulin, A. and Calvert, R. (2006) 'The virtual source method: Theory and case study', *Geophysics,* 71(4), SI139-SI150.

Bakulin, A. and Calvert, R. (2008) 'Virtual Source Method: overview of history and development', in *SEG Annual Meeting,* Las Vegas, Nevada, Society of Exploration Geophysicists, 2726-2730.

Baumont, D., Paul, A., Zandt, G. and Beck, S. (2001) 'Inversion of the Pn travel times for lateral variations of Moho geometry beneath the Central Andes and comparison with the receiver functions', *Geophysical Research Letters,* 28(8), 1663-1666.

Beck, S., Zandt, G., Myers, S., Wallace, T., Silver, P. and Drake, L. (1996) 'Crustal thickness variations in the Central Andes', *Geology,* 24(5), 407-410.

Bensen, D., Ritzwoller, M. and Shapiro, N. (2008) 'Broadband ambient noise surface wave tomography across the United States', *Journal of Geophysical Research,* 113(B5), B05306.

Bensen, G., Ritzwoller, M., Barnien, M., Leveshin, A., Lin, F., Moschetti, M., Shapiro, N. and Yang, Y. (2007) 'Processing seismic ambient noise data to obtain reliable broad-band surface dispersion measurements', *Geophysical Journal International,* 169(3), 1239-1260.

Berkhout, A. and Verschuur, D. (1997) 'Estimation of multiple scattering by iterative inversion. Part I: Theoretical considerations', *Geophysics,* 62(5), 1586-1595.

Bostock, M. and Rondenay, S. (1999) 'Migration of scattered teleseismic body waves', *Geophysical Journal International,* 137(3), 732-742.

Brasse, H., Lezaeta, P., Rath, V., Schwalenberg, K., Soyer, W. and Haak, V. (2002) 'The Bolivian Altiplano conductivity anomaly', *Journal of Geophysical Research,* 107(85), 2096.

Callen, H. and Welton, T. (1951) 'Irreversibility and generalized noise', *Physical Review,* 83, 1231-1235.

Calvert, R., Bakulin, A. and Jones, T. (2004) 'Virtual sources, a new way to remove overburden problems', in *66th Annual Meeting.*, European Association of Geoscientists and Engineers, 234.

Campillo, M. and Paul, A. (2003) 'Long-range correlations in the diffuse seismic coda', *Science,* 299, 547-549.

Changsheng, J. and Zhongliang, W. (2009) 'Temporal variation of noise correlation function (NCF) in Beijing and surroundings: its relation with climate events implications', *Earthquake Science,* 22, 75-81.

Chinn, D., Isacks, B. and Barazangi, M. (2007) 'High-frequency seismic wave propagation in Western South America along the continental margin in the Nazca plate and across the Altiplano', *Geophysical Journal of the Royal Astronomical Society,* 60(2), 209-244.

Claerbout, J. (1968) 'Synthesis of a layered medium from its acoustic transmission response', *Geophysics,* 33(2), 264-269.

Cole, S. (1995) *Passive seismic and drill-bit experiments using 2-D arrays,* unpublished thesis Stanford University.

Curtis, A., Berh, Y., Entwisle, E., Galleti, E., Townsend, J. and Bannister, S. (2012) 'The benefit of hindsight in observational science: retrospective seismological observations', *Earth and Planetary Science Letters,* 345-348, 212-220.

Curtis, A., Gertoff, P., Sato, H., Snieder, R. and Wapenaar, K. (2006) 'Seismic Interferometry-turning noise into signal', *The Leading Edge,* 25(9), 1082-1092.

Curtis, A. and Halliday, D. (2010a) 'Directional balancing for seismic and general wavefield interferometry', *Geophysics,* 75, SA1-SA14.

Curtis, A. and Halliday, D. (2010b) 'Source-receiver wave field interferometry', *Physical Review E,* 81(4), 046601.

Curtis, A., Nicolson, H., Halliday, D., Trampert, J. and Baptie, B. (2009) 'Virtual seismometers in the subsurface of the earth from seismic interferometry', *Nature Geoscience,* 2, 700-704.

Daneshvar, M., Clay, C. and Savage, M. (1995) 'Passive seismic imaging using microearthquakes', *Geophysics,* 60(4), 1178-1186.

De Stefano, A. and Clemente, P. (2006) 'S.H.M. on historical heritage: robust methods to face large uncertainties, SAMCO final report. F11, Selected paper', available: http://www.SAMCO.org [accessed March 2013].

Derode, A., Larose, E., Campillo, M. and Fink, M. (2003a) 'How to estimate the Green's function of a heterogeneous medium between two passive sensors? Application to acoustic waves', *Applied Physics Letters,* 83(15), 3054-3056.

Derode, A., Larose, E., Tanter, J., de Rosny, A., Tourin, M., Campillo, M. and Fink, M. (2003b) 'Recovering the Green's function from field-field correlations in an open scattering medium (L)', *Journal of the Acoustical Society of America,* 113(6), 2973-2976.

Derode, A., Roux, P. and Fink, M. (1995) 'Robust acoustic time reversal with high-order multiple scattering', *Physical Review Letters,* 75, 4206.

Draganov, D., Campman, X., Thorbecke, J., Verdel, A. and Wapenaar, K. (2009) 'Reflection images from ambient seismic noise', *Geophysics,* 74(5), A63-A67.

Draganov, D., Ghose, R., Reingrok, E., Thorbeck, J. and Wapenaar, K. (2010) 'Seismic interferometry, intrinsic losses and Q-estimation', *Geophysical Prospecting,* 58, 361-376.

Draganov, D., Wapenaar, K., Mulder, W., Singer, J. and Verdel, A. (2007) 'Retrieval of reflections from seismic background-noise measurements', *Geophysical Research Letter,* 34(4), L04305.

Draganov, D., Wapenaar, K. and Thorbeck, J. (2003) 'Synthesis of the reflection response from the transmission response in the presence of white noise sources', in Engineers, E. A. o. G. a., ed. *65th Annual International Conference and Exhibition,* Stavanger, Norway, EAGE, 218.

Draganov, D., Wapenaar, K. and Thorbeck, J. (2006) 'Seismic interferometry: Reconstructing the Earth's reflection response', *Geophysics,* 71(4), SI61-SI70.

Duguid, C., Halliday, D. and Curtis, A. (2011) 'Source-receiver interferometry for seismic wavefield construction and ground-roll removal', *The Leading Edge,* 30(8), 838-843.

Duval, T., Jefferies, S., Harvey, J. and Pomerantz, M. (1993) 'Time-distance helioseismology', *Nature,* 362(6419), 430-432.

Ekström, G., Tromp, J. and Larson, E. (1997) 'Measurements and global models of surface wave propagation', *Journal of Geophysical Research*, 102(B4), 8137-8157.

Fink, M. (1997) 'Time reversed acoustic', *Physics Today,* 50(3), 34-40.

Fokkema, J. and van der Berg, P. (1993) *Seismic Applications of Acoustic Reciprocity,* Elsevier.

Forghani, F. and Snieder, R. (2010) 'Underestimation of body waves and feasibility of surface-wave reconstruction by seismic interferometry', *The Leading Edge,* 29(7), 790-794.

Gaiser, J., Vasconcelos, I. and Calderon, M. (2008) 'Elastic interferometry for OBC data: Theory and examples', in *78th Annual Meeting*, Las Vegas, Nevada, Society of Exploration Geophysicists, 1073-1077.

Gerstoft, P., Sabra, K., Roux, P., Kuperman, W. and Fehler, M. (2006) 'Green´s functions extraction and surface-wave tomography from microseismic in Southern California', *Geophysics*, 71(4), SI23-SI31.

Gerstoft, P., Shearer, P., Harmon, N. and Zhang, J. (2008) 'Global P, PP, and PKP wave microseismic observed from distant storms', *Geophysical Research Letters,* 35(23), L23306.

Giese, P., Schenber, E., Schilling, F., Schmitz, M. and Wigger, P. (1999) 'Crustal thickening processes in the Central Andes and the different natures of Moho-discontinuity', *Journal of South American Earth Sciences,* 12(2), 201-220.

Grunberg, M., Genaud, S. and Mangenet, C. (2004) 'Seismic Ray-Tracing and Earth Mesh Modelling on Various Parallel Architectures', *The Journal of Supercomputing*, 29(1), 27-44.

Haberland, C., Rietbrock, A., Schurr, B. and Brasse, H. (2003) 'Coincident anomalies of seismic attenuation and electrical resistivity beneath the Southern Bolivian Altiplano Plateau', *Geophysical Research Letters,* 30(18), SDE1-1.

Halliday, D. and Curtis, A. (2008) 'Seismic interferometry, surface waves and source distribution', *Geophysical Journal International*, 175(3), 1067-1087.

Halliday, D. and Curtis, A. (2009) 'Seismic interferometry of scattered surface waves in attenuative media', *Geophysical Journal International,* 178(1), 419-446.

Halliday, D. and Curtis, A. (2010) 'An interferometric theory of source-receiver scattering and imaging', *Geophysics*, 75(6), SA95-SA103.

Halliday, D., Curtis, A., Robertsson, J. and van Manen, J. (2007) 'Interferometric surface-wave isolation and removal', *Geophysics*, 72(5), A69-A73.

Heit, B. (2005) *Teleseismic tomographic images of the Central Andes at 21 and 25.5: an inside look at the Altiplano and Puna plateaus*, unpublished thesis Universität Berlin.

Heit, B., Koulakov, I., Asch, G., Yuan, X., Kind, R., Alcoser-Rodríguez, I., Tawackoli, S. and Wike, H. (2008) 'More constrains to determine the seismic structure beneath the Central Andes at 21° S using teleseismic tomography analysis', *Journal of South American Earth Sciences*, 25, 25-36.

Hong, T. and Menke, W. (2006) 'Tomographic investigation of the wear along de San Jacinto fault, Southern California', *Physics of the Earth and Planetary Interiors*, 155(3-4), 236-248.

Hunsen, S., Kissling, E., Deichmann, N., Wiener, S., Giardini, D. and Baer, M. (2003) 'Probabilistic earthquake location in complex three-dimensional velocity models: Application to Switzerland', *Journal of Geophysical Research*, 108(B2), 2077.

Husen, S. and Hardebeck, J. (2010) 'Earthquake location accuracy', available: http://www.corssa.org [accessed March 2013].

Kennet, B. and Engdahl, E. (1995) 'Constrains on seismic velocities in the earth from travel times', *Geophysical Journal International*, 22(1), 108-124.

King, S., Curtis, A. and Poole, T. (2011) 'Interferometric velocity analysis using physical and non-physical energy', *Geophysics*, 76(1), SA35-SA49.

Lin, F., Moschetti, M. and Ritzwoller, M. (2008) 'Surface wave tomography of the Western United States from ambient seismic noise: Rayleigh and Love wave phase velocity maps', *Geophysical Journal International*, 173(1), 281-289.

Lobkis, O. and Weaver, R. (2001) 'On the emerge of the Green´s function in the correlations of a diffuse field', *Journal of the Acoustical Society of America*, 110(6), 3011-3017.

Lobkis, O. and Weaver, R. (2003) 'Coda-wave interferometry in finite solids: Recovery of P-to-S conversion rates in an elastodynamic Billiard', *Physical Review Letters*, 90(25), 254302.

Lu, R., Willis, M., Campman, X., Ajo-Franklin, J. and Toksoz, M. (2008) 'Redatuming through a salt canopy and target oriented salt-flank imaging', *Geophysics*, 73(3), S63-S71.

Malcon, A., Scales, J. and van Tiggelen, B. (2004) 'Extracting the Green´s function from diffuse equipartitioned waves', *Physical Review E*, 70(1), 015601.

Mauchline, K. (2010) *Seismic wavefield interferometry across the Central Andes: estimating the surface wave Green´s function between an earthquake source and a virtual receiver*, unpublished Thesis. University of Edinburgh.

Mehta, K., Snieder, R. and Grazier, V. (2007) 'Extraction of the near-surface properties for a lossy layered medium using the propagation matrix', *Geophysical Journal International,* 169(1), 271-280.

Miyazawa, M., Snieder, R. and Venkateraman, A. (2008) 'Application of seismic interferometry to extract P-and S-wave propagation and observation of shear-wave splitting from noise data at Cold Lake, Alberta, Canada', *Geophysics,* 73(4), D35-D40.

Mori, J. and Helmberger, D. (1996) 'Large-amplitude Moho reflections (SmS) from Landers aftershocks, Southern California', *Bulletin of the Seismological Society of America,* 86(6), 1845-1852.

Nakahara, H. (2006) 'A systematic study of the theoretical relations between spatial correlation and Green´s function in one- two- and three-dimensional random scalar wavefield', *Geophysical Journal International,* 167(3), 1097-1105.

Nataf, C. and Richard, Y. (1996) '3SMAC: an a priori tomographic model of the upper mantle based on the geophysical modelling', *Physics of the Earth and Planetary interiors,* 95, 101-122.

Nishida, K., Kawakatsu, H. and Obara, K. (2008) 'Three-dimensional crustal S wave velocity structure in Japan using microseismic data recorded by Hi-net tilmeters', *Journal of Geophysical Research,* 113(B10), 10302.

Nowack, R., Dasgupta, S. and Schuster, T. (2003) 'Correlation migration of scattered teleseismic body waves with application to the 1993 Cascadia experiment', in *AGU Fall Meeting,* San Francisco, California, American Geophysical Union,

Nowack, R., Dasgupta, S., Schuster, T. and Sheng, J. (2006) 'Correlation migration using Gaussian beams of scattered teleseismic body waves', *Bulletin of the Seismological Society of America,* 96(1), 1-10.

Poliannikov, O. (2011) 'Retrieving reflections by source-receiver wavefield interferometry', *Geophysics,* 76(1), SA1-SA8.

Poupinet, G., Ellworth, W. and Frechet, J. (1984) 'Monitoring velocity variations in the crust using earthquakes doublets: An application to the Calaveras fault, California', *Journal of Geophysical Research,* 89(B7), 5719-5731.

Rayleigh, J. (1945) *The Theory of Sound,* New York: Dover Publications Inc.

Rickett, J. and Claerbout, J. (1999) 'Acoustic daylight imaging via spectral factorization: Helioseismology and reservoir monitoring', *The Leading Edge,* 18, 957-960.

Rickett, J. and Claerbout, J. (1996) *Passive seismic imaging applied to synthetic data: Technical report*.

Roux, P. and Fink, M. (2003) 'Green´s function estimation using secondary sources in a shallow water environment', *Journal of the Acoustic Society of America,* 113(3), 1406-1416.

Roux, P., Sabra, K., Gerstoft, P., Kuperman, W. and Fehler, M. (2005) 'P-waves from cross-correlation of seismic noise', *Geophysical Research Letters,* 32(19), L19303.

Sabra, K., Gerstoft, P., Roux, P., Kuperman, W. and Fehler, M. (2005a) 'Extracting time-domain Green´s function estimates from ambient seismic noise', *Geophysical Research Letters,* 32(3), L03310.

Sabra, K., Gerstoft, P., Roux, P., Kuperman, W. and Fehler, M. (2005b) 'Surface wave tomography from microseisms in Southern California', *Geophysical Research Letters,* 32(14), L14311.

Scherbaum, F. (1987a) 'Seismic imaging of the site response using micro earthquake recording. Part I. Method', *Bulletin of the Seismological Society of America,* 77(6), 1905-1923.

Scherbaum, F. (1987b) 'Seismic imaging of the site response using micro earthquake recording. Part II. Application to the Swabian Jura, southwest Germany, Seismic network', *Bulletin of the Seismological Society of America,* 77(6), 1924-1944.

Scherbaum, F. (1987c) 'Levinson inversion of earthquake geometry SH-transmission seismograms in the presence of noise', *Geophysical Prospecting,* 35(7), 787-802.

Schmitz, M. and Kley, J. (1997) 'The geometry of the Central Andean back arc crust: Join interpretation of cross-section balancing and seismic refraction data', *Journal of South American Earth Science,* 10(1), 99-100.

Schuster, G. (2001) 'Theory of daylight/interferometric imaging: Tutorial', in *63rd Meeting,* Utah, European Association of Geoscientists and Engineers,

Schuster, G. (2009) *Seismic Interferometry,* New York: Cambridge University Press.

Schuster, G., Yu, J., Sheng, J. and Rickett, J. (2004) 'Interferometric/daylight seismic imaging', *Geophysical Journal International,* 157(2), 832-852.

Schuster, G. and Zhou, M. (2006) 'A theoretical overview of model-based and correlation-based redatuming methods', *Geophysics,* 71, SI103-SI110.

Shapiro, N. and Campillo, M. (2004) 'Emergence of broadband Rayleigh waves from correlations of the ambient seismic noise', *Geophysical Research Letters,* 31(7), L07614.

Shapiro, N., Campillo, M., Stehly, L. and Ritzwoller, M. (2005a) 'High resolution surface-wave tomography from ambient seismic noise', *Science,* 307(5715), 1615-1618.

Shapiro, N., Campillo, M., Stehly, L. and Ritzwoller, M. (2005b) 'High-resolution surface wave tomography from ambient seismic noise', *Science,* 307, 1615-1617.

Slob, E., Draganov, D. and Wapenaar, K. (2007) 'Interferometric electromagnetic Green´s functions representations using propagation invariants', *Geophysical Journal International,* 169(1), 60-80.

Slob, E. and Wapenaar, K. (2007) 'Electromagnetic Green's function retrieved by cross-correlation and cross-convolution in media with losses', *Geophysical Research Letters,* 34(5), 5307.

Snieder, R. (2004) 'Extracting the Green´s function from the correlation of coda wave: A derivation based on stationary phase', *Physical Review E,* 69, 046610.

Snieder, R. (2007) 'Extracting the Green´s function of attenuating heterogeneous acoustic media from uncorrelated waves', *Journal of the Acoustical Society of America,* 121(5), 2637-2643.

Snieder, R., Gret, A., Douma, H. and Scales, J. (2002) 'Coda wave interferometry for estimating nonlinear behaviour in seismic velocity', *Science,* 295(5563), 2253-2255.

Snieder, R., Miyazawa, M., Slob, E., Vasconcelos, I. and Wapenaar, K. (2009) 'A comparison of strategies for seismic interferometry', *Surveys in Geophysics,* 30(4-5), 503-523.

Snieder, R. and Safak, E. (2006b) 'Extracting the building response using seismic interferometry: Theory and application to the Millikan Library in Pasadena, California', *Bulletin of the Seismological Society of America,* 96(2), 586-598.

Snieder, R. and Scales, J. (1998) 'Time-reserved imaging as a diagnostic of wave and particle chaos', *Physical Review E,* 58(5), 5668-5675.

Snieder, R., Sheiman, J. and Calvert, R. (2006a) 'Equivalence of the virtual-source method and wave-field deconvolution in seismic interferometry', *Physical Review E,* 73, 066620.

Snieder, R., Wapenaar, K. and Larner, K. (2006c) 'Spurious multiples in seismic interferometric imaging of primaries', *Geophysics,* 71(4), SI111-SI114.

Spudich, P. and Bostwick, T. (1987) 'Studies of the seismic coda using an earthquake cluster as a deeply buried seismograph array', *Journal of Geophysical Research,* 92(B10), 10526-10546.

Stehly, L., Campillo, M. and Shapiro, M. (2006) 'A study of the seismic noise from its long-range correlation properties', *Journal of Geophysical Research: Solid Earth,* 111(B10), B10306.

Stehly, L., Fry, B., Campillo, M., Shapiro, N., Guilbert, J., Boschi, L. and Giardini, D. (2009) 'Tomography of the Alpine region from observations of seismic ambient noise', *Geophysical Journal International,* 178(1), 338-350.

Tanimoto, T., Ishimaru, S. and Alvizuri, C. (2006) 'Seasonality in particle motion of microseisms', *Geophysical Journal International,* 166(1), 253-266.

Thurber, C. (1992) 'Hypocenter velocity structure coupling in local earthquake tomography', *Physics of the Earth and Planetary Interiors,* 75(1-3), 55-62.

Tonegawa, T. and Nishida, K. (2010) 'Inter-source body wave propagation derived from seismic interferometry', *Geophysical Journal International,* 183(2), 861-868.

Tonewaga, T., Nishida, K., Watanabe, T. and Shiomi, K. (2009) 'Seismic interferometry of teleseismic S-wave coda for retrieval of body waves: an application to the Philippine sea slab underneath the Japanese islands', *Geophysical Journal International,* 178(3), 1574-1586.

Trampert, J., Cara, M. and Frogneux, M. (1993) 'SH propagation matrix and Qs estimates from borehole- and surface- recorded earthquake data', *Geophysical Journal International,* 112(2), 290-299.

Trampert, J. and Woodhouse, J. (1996) 'High resolution global phase velocity distributions', *Geophysical Research Letters,* 23(1), 23-24.

van der Neut, J. and Bakulin, A. (2009) 'Estimating and correcting the amplitude radiation pattern of a virtual source', *Geophysics,* 74(2), SI27-SI36.

van Manen, D., Curtis, A. and Robertsson, J. (2006) 'Interferometric modeling of wave propagation in inhomogeneous elastic media using time reversal and reciprocity', *Geophysics,* 71(4), SI47-SI60.

van Manen, D., Robertsson, J. and Curtis, A. (2005) 'Modeling of wave propagation in inhomogeneous media', *Physical Review Letters,* 94(16), 164301.

van Manen, D., Robertsson, J. and Curtis, A. (2007) 'Exact wave field simulation for finite-volume scattering problems', *Journal of the Acoustical Society of America,* 122(4), EL115-EL212.

Vasconcelos, I. and Snieder, R. (2006) 'Interferometric imaging by deconvolution: Theory and numerical examples', in *76th Annual Meeting,* New Orleans, Louisiana, Society of Exploration Geophysics, 2416-2420.

Vasconcelos, I. and Snieder, R. (2007) 'Seismic interferometry by deconvolution: theory and examples', in *69th Annual International Conference and Exhibition,* European Association of Geoscientists and Engineers,

Vasconcelos, I. and Snieder, R. (2008a) 'Interferometry by deconvolution: part I - theory for acoustic waves and numerical examples', *Geophysics,* 73(3), S115-S128.

Vasconcelos, I. and Snieder, R. (2008b) 'Interferometry by deconvolution: part 2 - theory for elastic waves and application to drill-bit seismic imaging', *Geophysics,* 73(3), S129-S141.

Vdovin, O., Rial, J., Levshin, A. and Ritzwoller, M. (1999) 'Group-velocity tomography of South-American and the surrounding oceans', *Geophysical Journal International,* 136(2), 324-340.

Wang, R. (1999) 'A simple orthonormalization method for stable and efficient computation of Green's functions', *Bulletin of the Seismological Society of America,* 89(3), 733-741.

Wapenaar, K. (2003) 'Synthesis of an inhomogeneous medium from its acoustic transmission response', *Geophysics,* 68(5), 1756-1759.

Wapenaar, K. (2004) 'Retrieving the elastodynamic Green´s function of an arbitrary inhomogeneous medium by cross correlation', *Physical Review Letters,* 93(25), 254301.

Wapenaar, K. (2006c) 'Green´s function retrieval by cross-correlation in case of one-sided illumination', *Geophysical Review Letters,* 33(19), L19304.

Wapenaar, K. (2006d) 'Seismic interferometry for passive and exploration data: reconstruction of internal multiples', in *76th Annual International Meeting,* New Orleans, Louisiana, Society of Exploration Geophysicists, 2981-2985.

Wapenaar, K., Draganov, D. and Robertsson, J. (2006b) 'Introduction to the supplement on seismic interferometry', *Geophysics,* 71(4), S1-S14.

Wapenaar, K., Draganov, D., Thorbecke, J. and Fokkema, J. (2002) 'Theory of acoustic daylight imaging revisited', in Geophysicists, S. o. t. E., ed. *72th Annual International Meeting,* Salt Lake City, Utah, Society of Exploration Geophysicists, 2269-2272.

Wapenaar, K. and Fokkema, J. (2006a) 'Green's function representation for seismic interferometry', *Geophysics,* 71(4), S133-S146.

Wapenaar, K., Fokkema, J. and Snieder, R. (2005) 'Retrieving the Green´s function in an open system by cross-correlation: a comparison of approaches', *Journal of Acoustical Society of America,* 118(5), 2783-2786.

Wapenaar, K., Slob, E. and Snieder, R. (2006) 'Unified Green´s function retrieval by cross correlation', *Physical Review Letters,* 97(23), 234301

Wapenaar, K., Slob, E. and Snieder, R. (2008a) 'Seismic and electromagnetic controlled source interferometry in dissipative media', *Geophysical Prospecting,* 56, 419-434.

Wapenaar, K., Slob, E., Snieder, R. and Curtis, A. (2010a) 'Tutorial on seismic interferometry: part 1 Basic principles and applications', *Geophysics,* 75(5), 75A195-75A227.

Wapenaar, K., Slob, E., Snieder, R. and Curtis, A. (2010b) 'Tutorial on seismic interferometry: part 2 understanding theory and new advances', *Geophysics,* 75(5), 75A211-75A227.

Wapenaar, K., Van der Neut, J. and Ruigrok, E. (2008b) 'Passive seismic interferometry by multidimensional deconvolution', *Geophysics,* 73, A51-A56.

Wapenaar, K., Van der Neut, J., Ruigrok, E., Draganov, D., Slob, E. and Thorbecke, J. (2008) 'Seismic interferometry by cross-correlation or deconvolution?, in Inin *78th Annual Meeting,* Las Vegas, Nevada, Society of Exploration Geophysics , 2731-2736.

Weaver, R. and Lobkis, O. (2001) 'Ultrasonics without a source: Thermal fluctuation correlations at MHz frequencies', *Physical Review Letters,* 87(13), 134301.

Weaver, R. and Lobkis, O. (2002) 'On the emergence of the Green´s function in the correlation of a diffuse field: Pulse-echo using thermal phonons', *Ultrasonics,* 40(1-8), 435-439.

Weaver, R. and Lobkis, O. (2005) 'Fluctuations in diffuse field-field correlations and the emerge of Green´s function in open systems', *Journal of the Acoustical Society of America,* 117(6), 3432-3439.

Wodzicki, G. (2000) 'Uplift history of the Central and Northern Andes: a review', *Geological Society of America Bulletin,* 112(7), 1091-1105.

Wölbern, I., Heit, B., Yuan, X., Ash, G., Kind, R., Viramonte, J., Tawackoli, S. and Wilke, H. (2009) 'Receiver function images from the Moho and the slab beneath the Altiplano and Puna plateaux in the central Andes', *Geophysical Journal International,* 177(1), 296-308.

Yang, Y., Li, A. and Ritzwoller, M. (2008) 'Crustal and uppermost mantle structure in southern Africa revealed from ambient noise and teleseismic tomography', *Geophysical Journal International,* 174(1), 235-248.

Yang, Y. and Ritzwoller, M. (2008) 'Characteristics of ambient seismic noise as a source for surface wave tomography', *Geochemistry, Geophysics, Geosystems*, 9(2), Q02008.

Yang, Y., Ritzwoller, M., Levshin, A. and Shapiro, N. (2007) 'Ambient noise Rayleigh wave tomography across Europe', *Geophysical Journal International,* 168(1), 259-274.

Yao, H., Van Der Hilst, R. and De Hoop, M. (2006) 'Surface-wave array tomography in the SE Tibet from ambient noise and two-station analysis -I. Phase velocity maps', *Geophysical Journal International,* 166(2), 732-744.

Yuan, X., Sobolev, S. and Kind, R. (2002) 'Moho topography in the Central Andes and its dynamics implications', *Earth and Planetary Science Letters,* 199(3-4), 389-402.

Yuan, X., Sobolev, S., Kind, R., Oncken, O., Bock, G., Ash, G., Schurr, B., Graeber, F., Ruddoff, A., Hanka, W., Wylegalla, K., Tibi, R., Haberland, C., Rietbrock, A., Giese, P., Wigger, P., Rower, P., Zandt, G., Beck, S., Wallace, T., Pardo, M. and Compte, D. (2000) 'Subduction and collision processes in the Central Andes constrained by converted seismic phases', *Nature,* 408, 958-961.

Zandt, G., Leidig, M., Chmielowki, J., Baumont, D. and Yuan, X. (2003) 'Seismic detection and characterization of the Altiplano-Puna Magma body, Central Andes', *Pure and Applied Geophysics,* 160(3-4), 789-807.

Zhan, Z., Ni, S., Helmberger, D. and Clayton, R. (2010) 'Retrieval of Moho-reflected shear waves arrivals from ambient seismic noise', *Geophysical Journal International,* 182(1), 408-420.

Zheng, S., Sun, X., Song, X., Yang, Y. and Ritzwoller, M. (2008) 'Surface wave tomography of China from ambient seismic noise correlation', *Geochemistry, Geophysics, Geosystems,* 9(5), 05020.

Zhu, L. and Helmberger, D. (1996) 'Advancement in source estimation techniques using broadband regional seismograms', *Bulletin of the Seismological Society of America*, 86(5), 1634-1641.

Appendix A

Results from section 3.4

Scenario B: Reference receiver: P wave and coda P; rest of receivers: P wave and coda P.

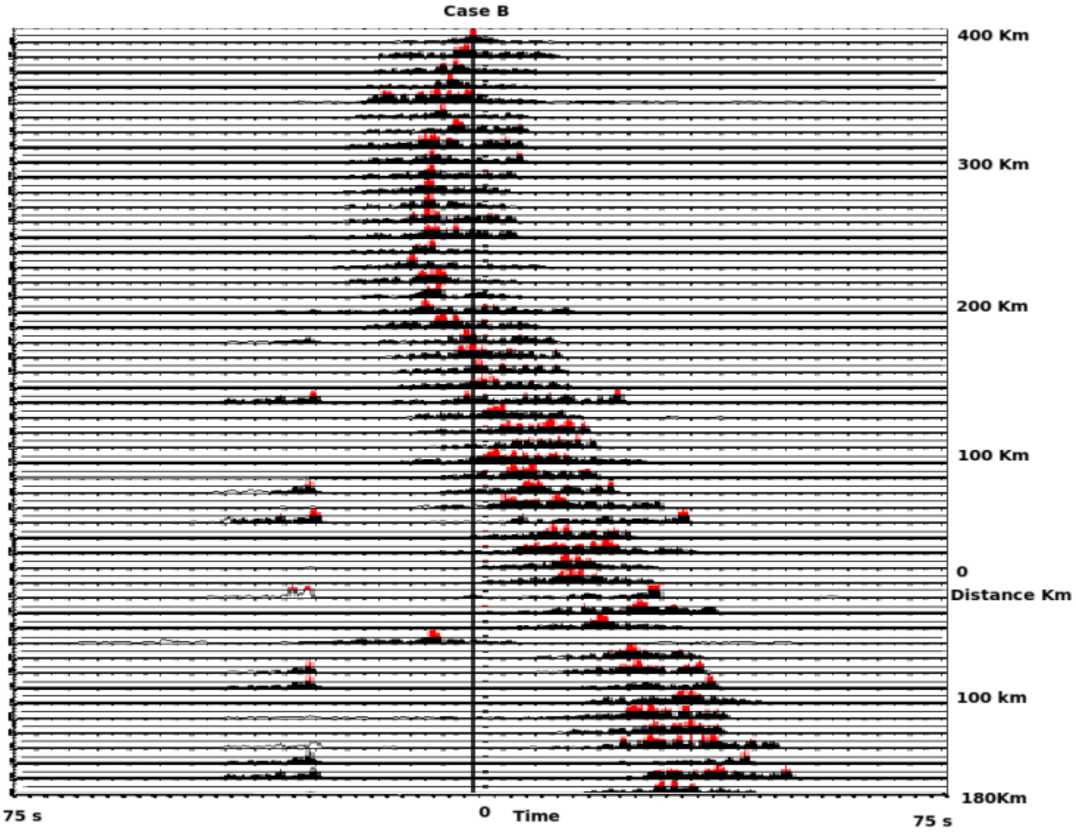

Figure A.1 Scenario B in which the P wave arrival and the P coda are used for both the reference receiver as well as the rest of the receivers.

Scenario F: Reference receiver: P wave; rest of receivers: P wave and coda P

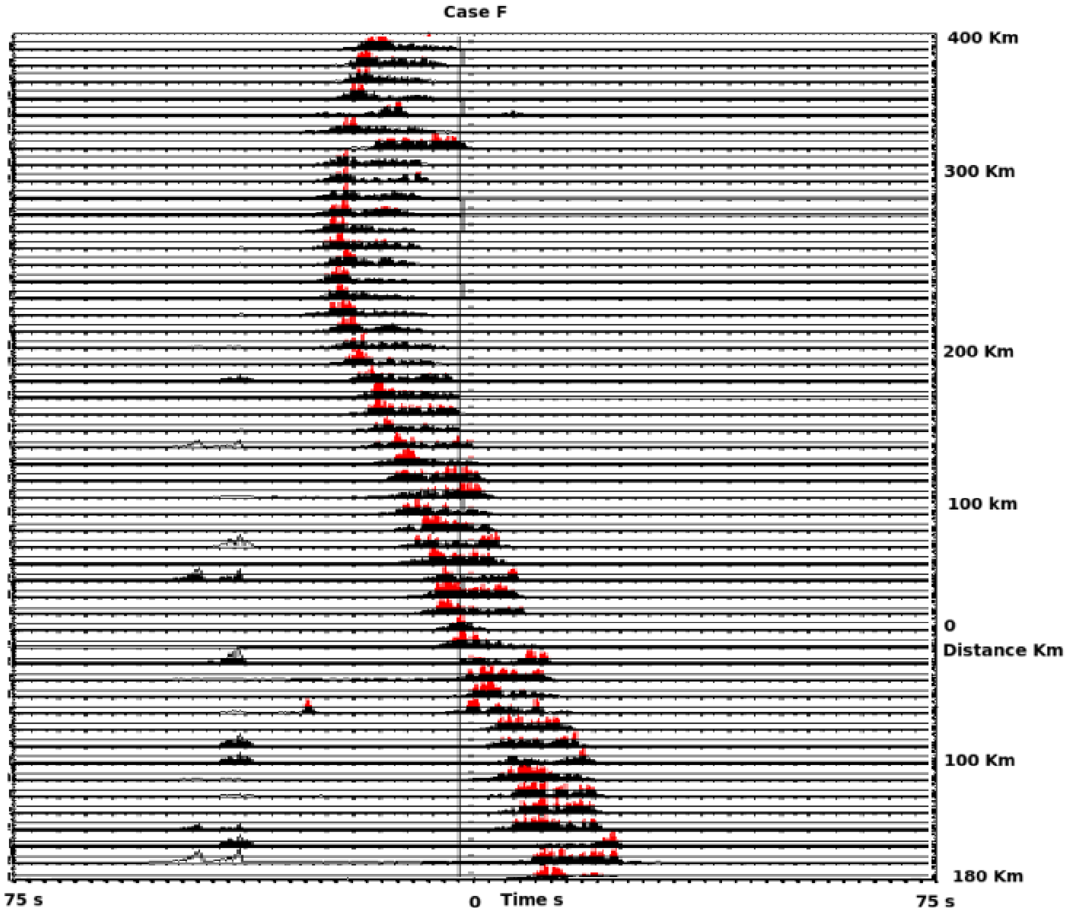

Figure A.2 Scenario F in which, for performing interferometric calculations, the reference receiver consisted of only P arrivals and the rest of the receivers P arrivals and coda P.

Scenario G: Reference receiver: P wave; rest of receivers: Coda P

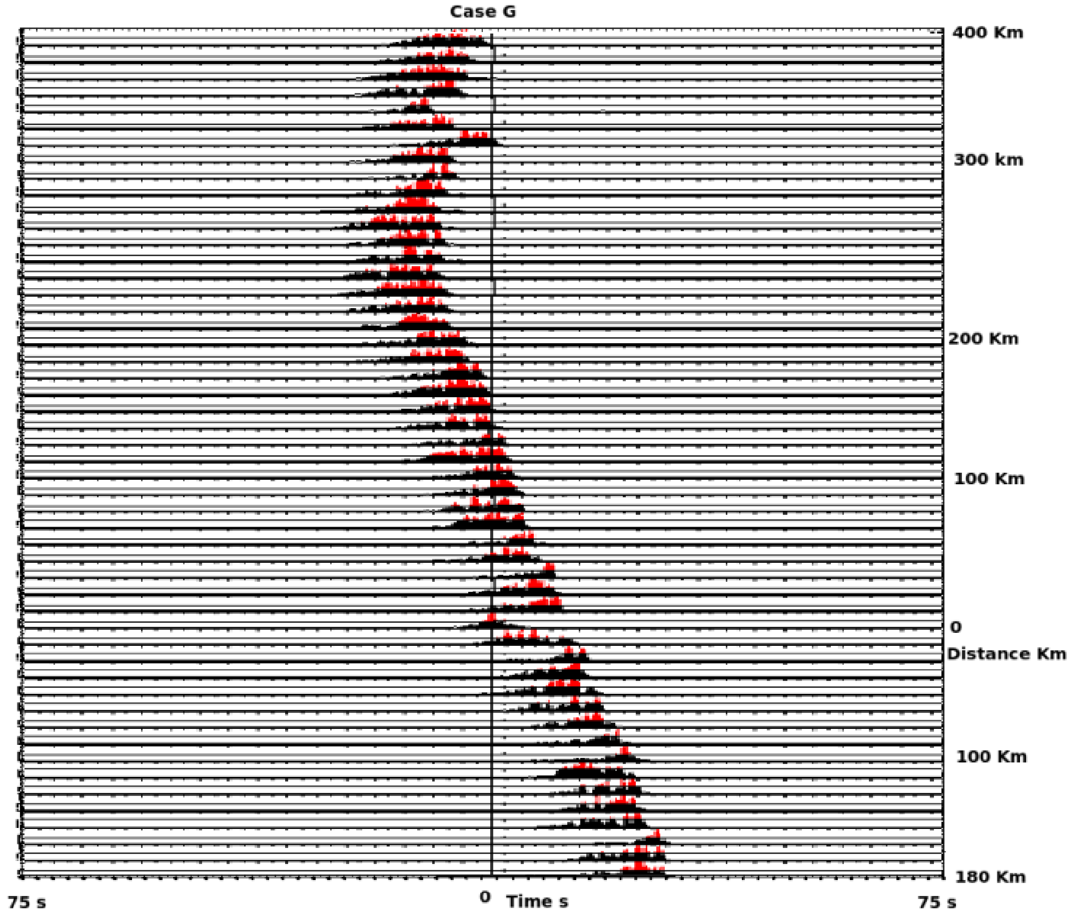

Figure A.3 Scenario G in which, for performing interferometric calculations, the reference receiver consisted of P arrivals and the rest of the receiver of coda P.

Scenario H: Reference receiver: S wave; rest of receivers: S wave

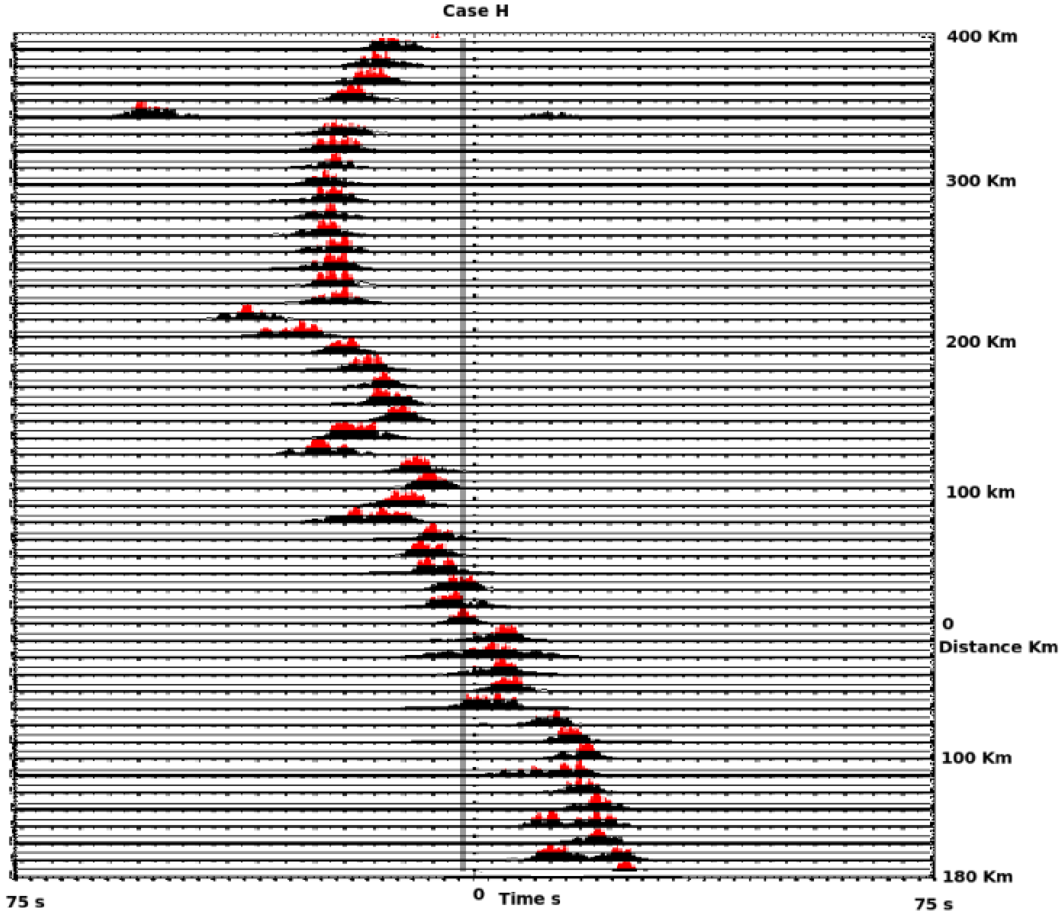

Figure A.4 Scenario H in which, for the purpose of interferometric calculation, the reference receiver consisted of S arrival and the rest of the receivers of S arrivals.

Scenario J: Reference receiver: S wave; rest of receivers: P wave

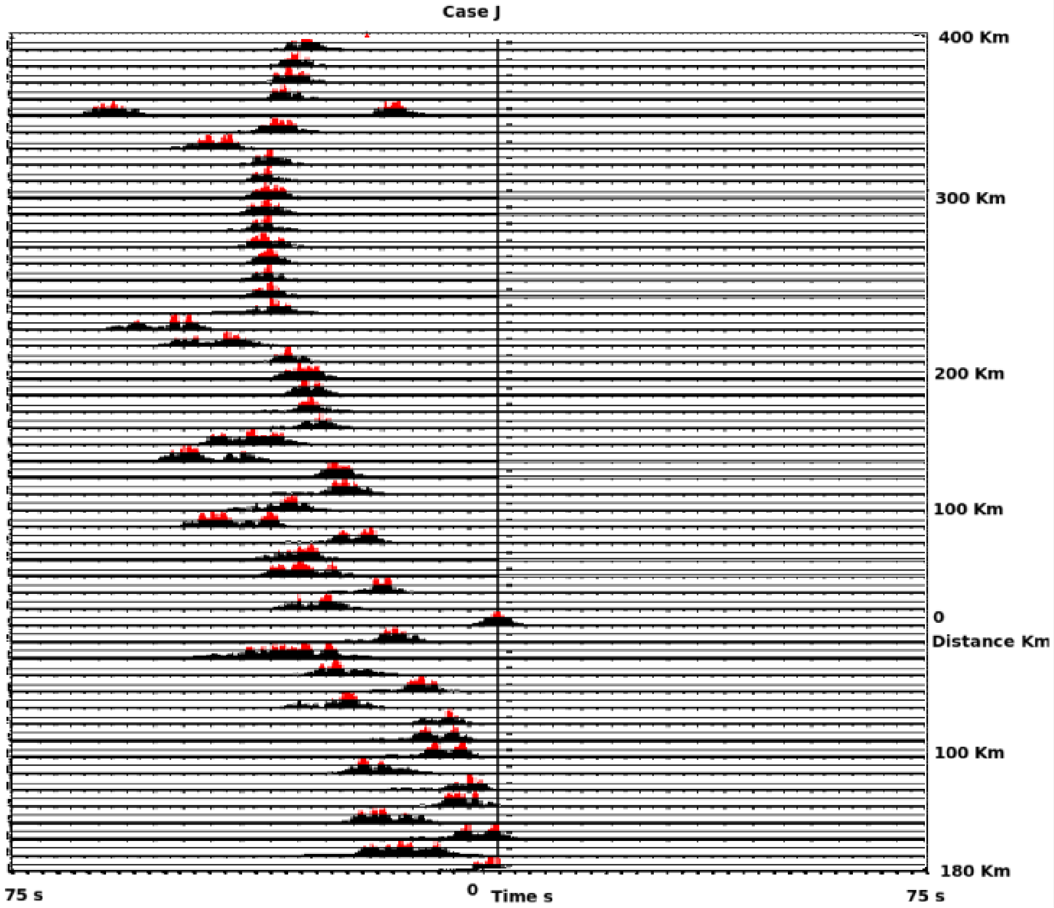

Figure A.5 Scenario J in which, for interferometric calculation, the reference receiver consisted of S arrival and the rest of the receivers consisted of P wave arrival.

Scenario K: Reference receiver: P wave; rest of receivers: S wave

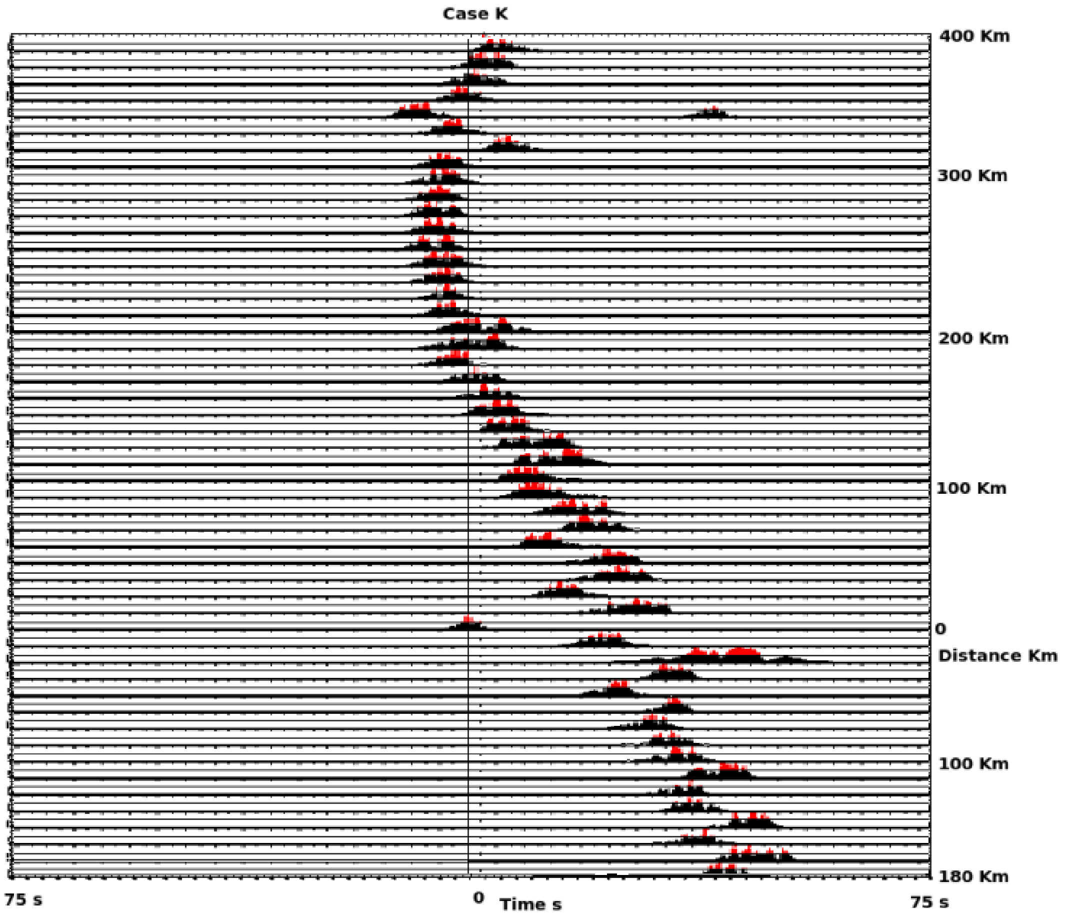

Figure A.6 Scenario K in which, for interferometry calculations, the reference receiver consisted of P wave arrival, the rest of the receivers consisted of S wave arrivals.

Appendix B

Results from section 4.4

Month of March 2003

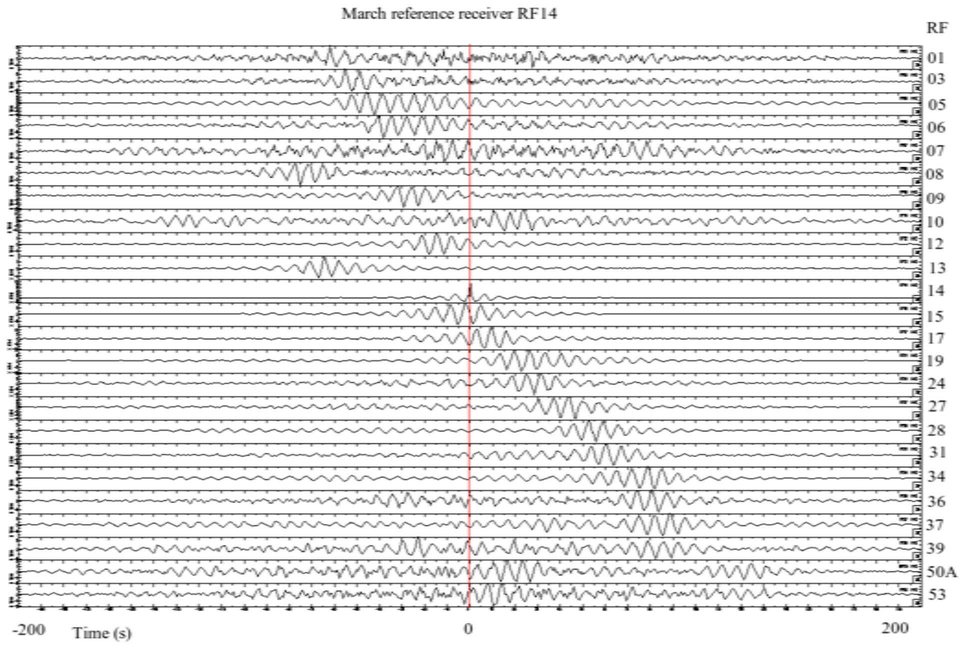

Figure B.1 Estimated Green’s function’s for the month of March. Virtual source location at RF14.

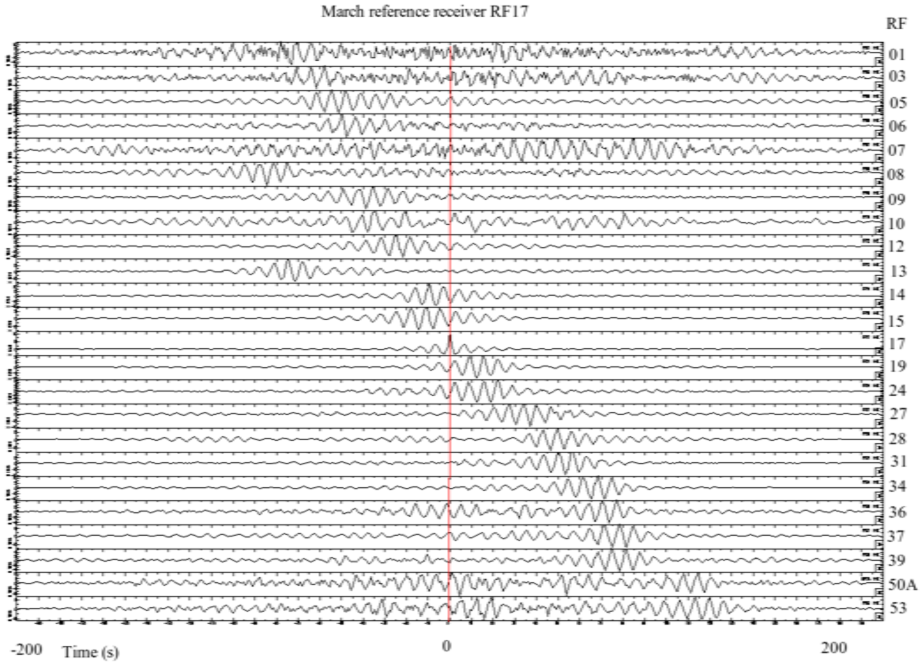

Figure B.2 Green’s function for the month of March. Virtual source location at RF17.

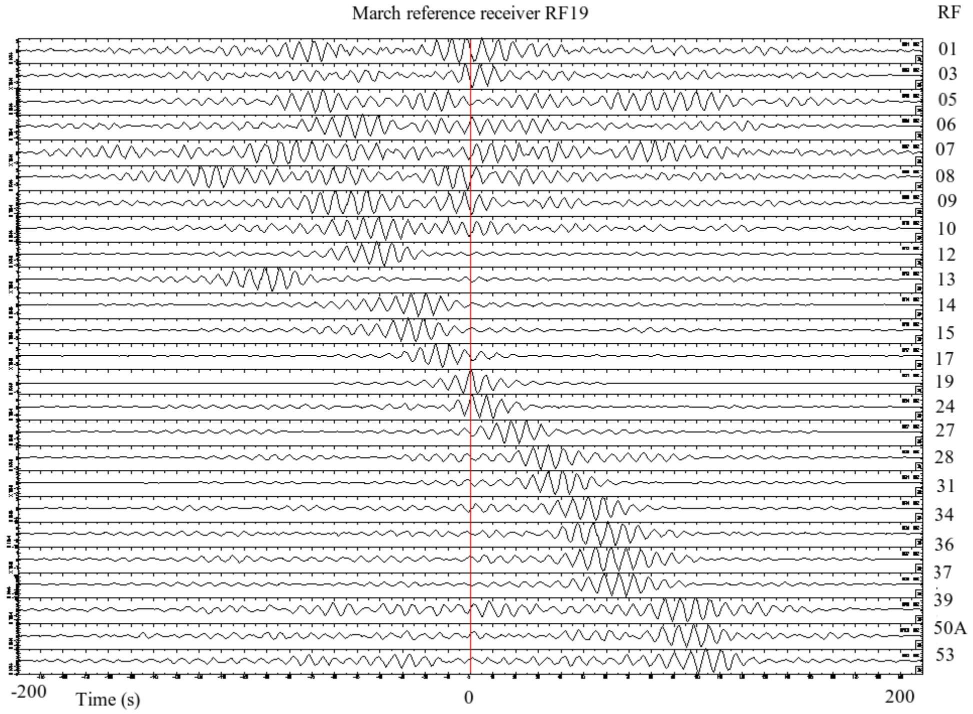

Figure B.3 Green’s function for the month of March. Virtual source location at RF19.

Month of April 2003

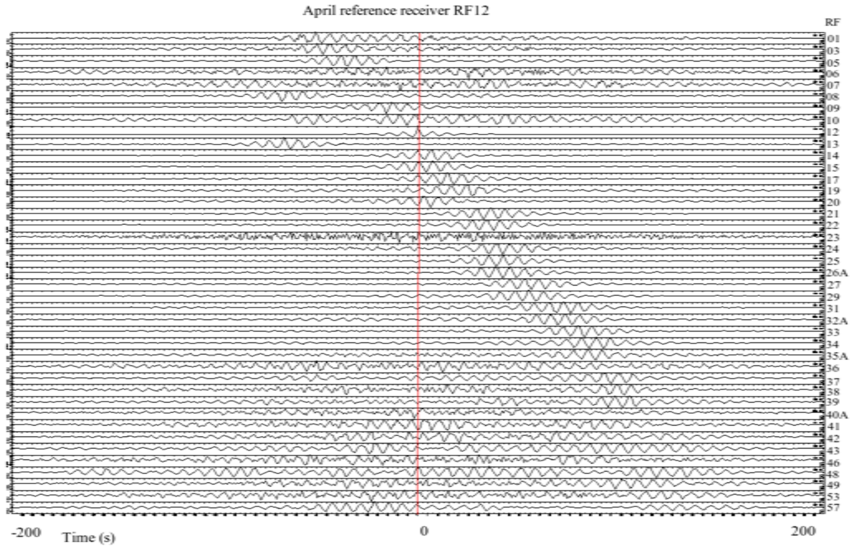

Figure B.4 Green’s function for the month of April. Virtual source location at RF12.

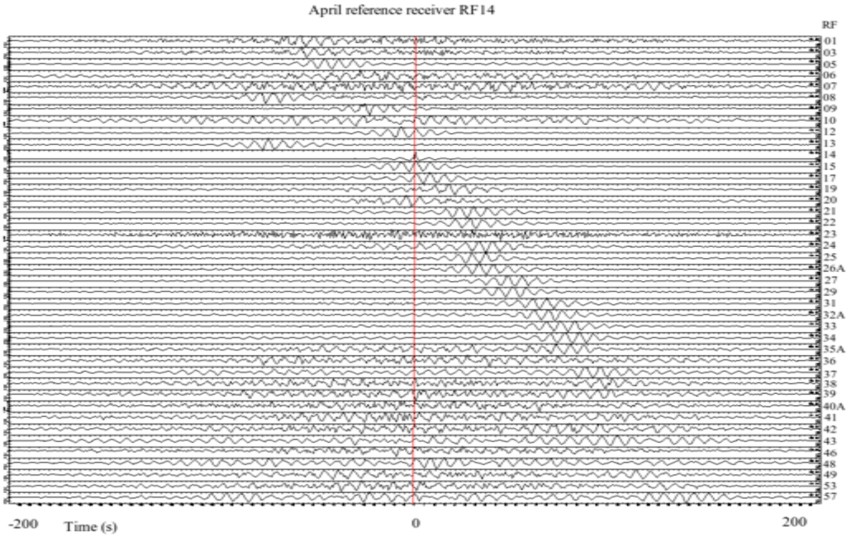

Figure B.5 Green’s function for the month of April. Virtual source location at RF14.

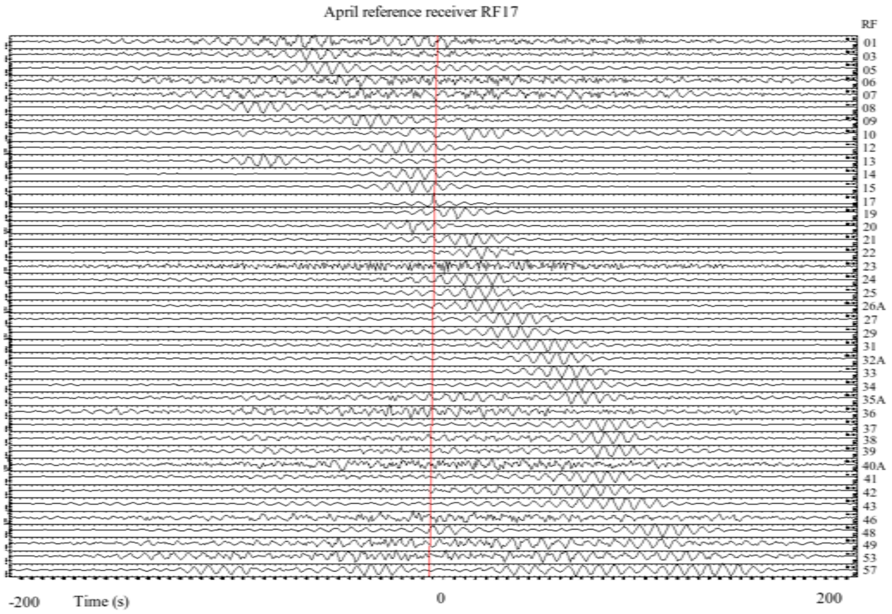

Figure B.6 Green’s function for the month of April. Virtual source location at RF17.

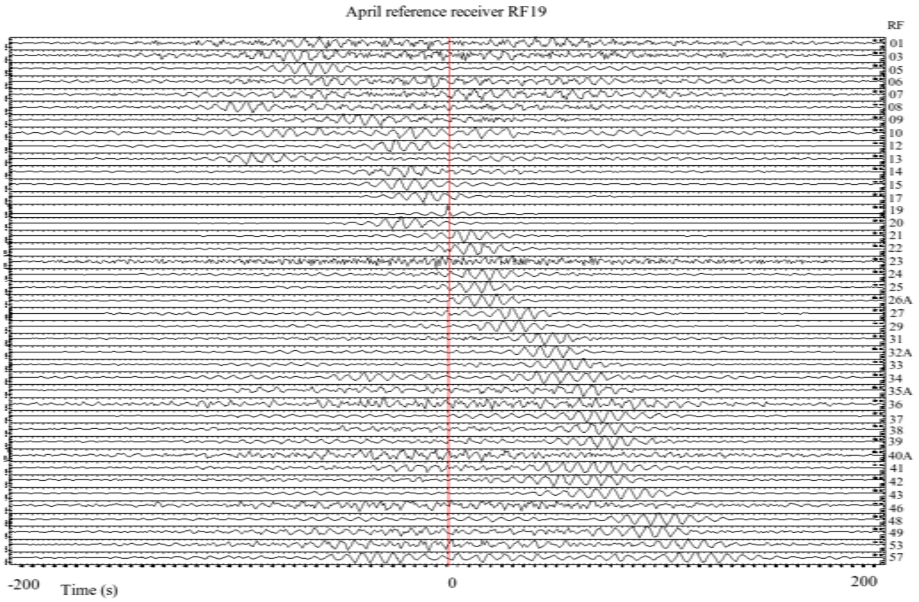

Figure B.7 Green’s function for the month of April. Virtual source location at RF19.

Month of May 2003

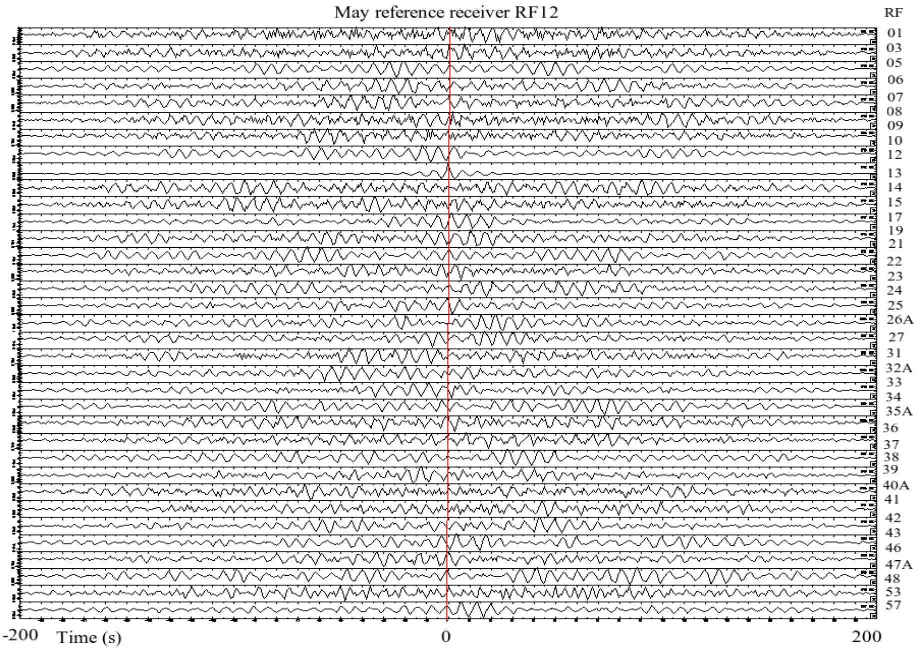

Figure B.8 Green’s functions for the month of May. Virtual source location at RF12.

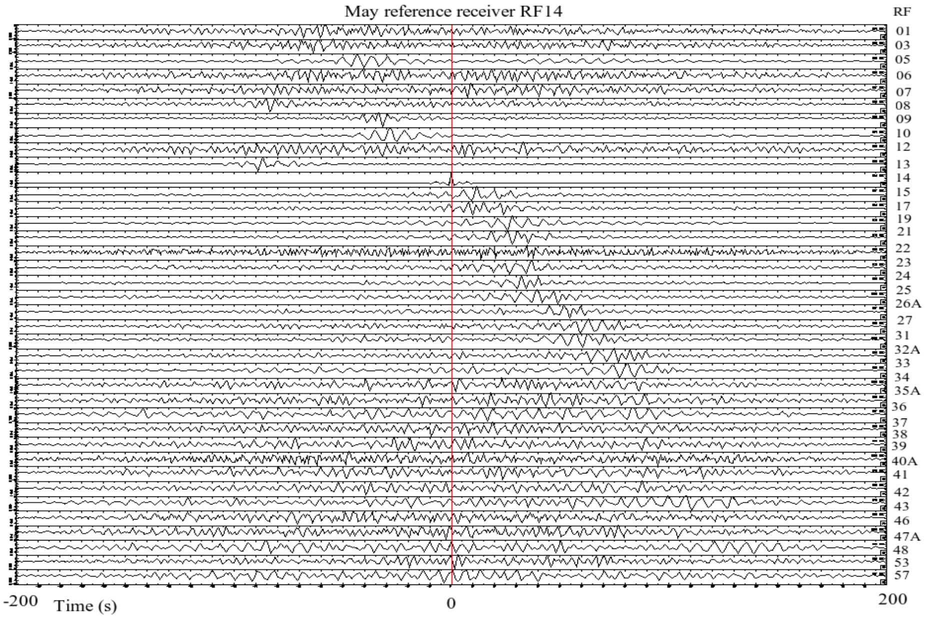

Figure B.9 Green’s function for the month of May. Virtual source location at RF 14.

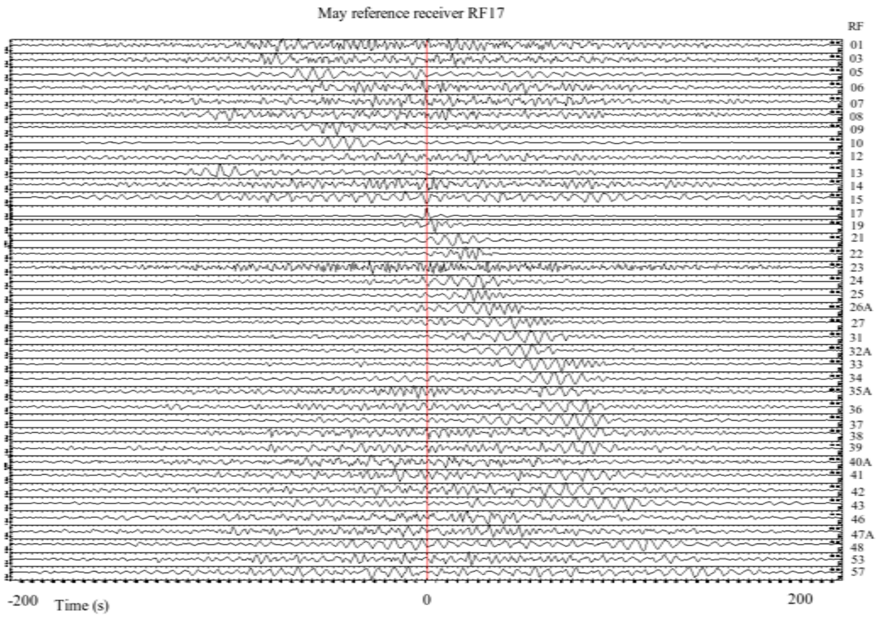

Figure B.10 Green’s function for the month of May. Virtual source location at RF17.

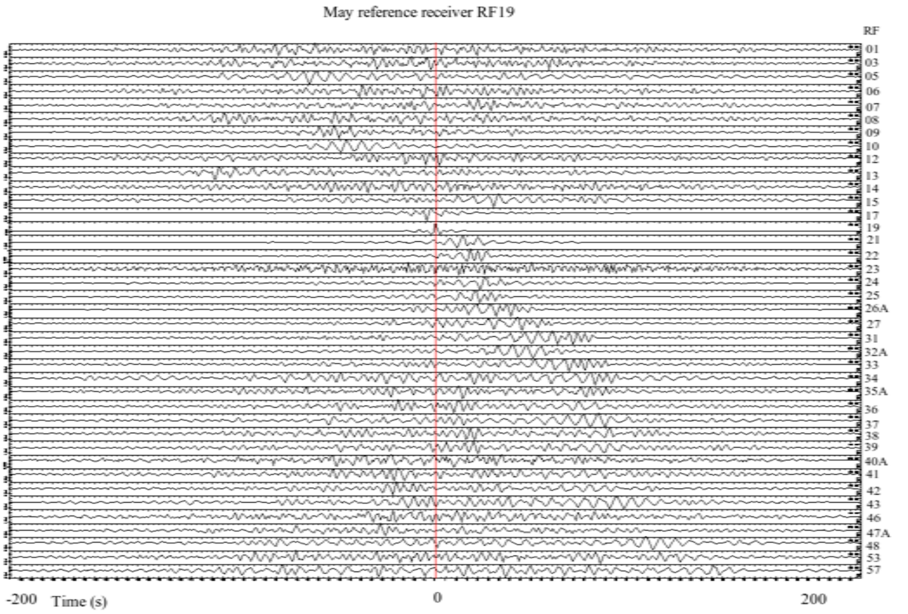

Figure B.11 Green’s function for the month of May. Virtual source location at RF19.

Month of June 2003

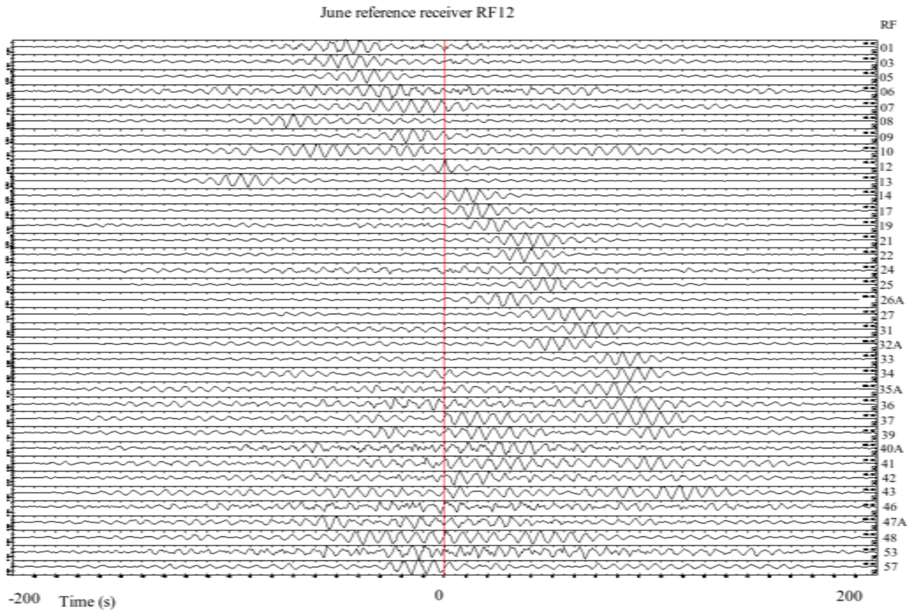

Figure B.12 Green’s function for the month of June. Virtual source location at RF12.

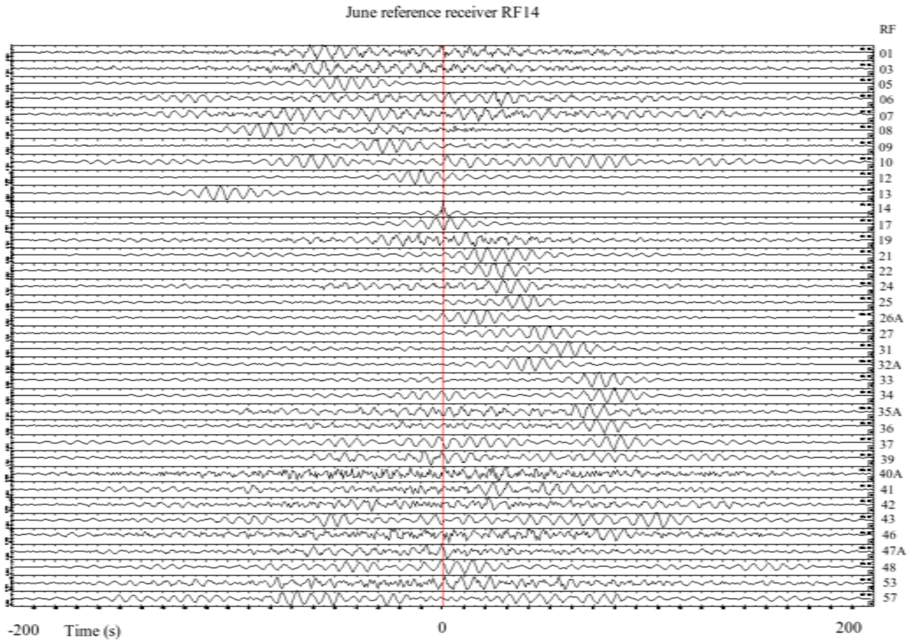

Figure B.13 Green’s function for the month of June. Virtual source location at RF14.

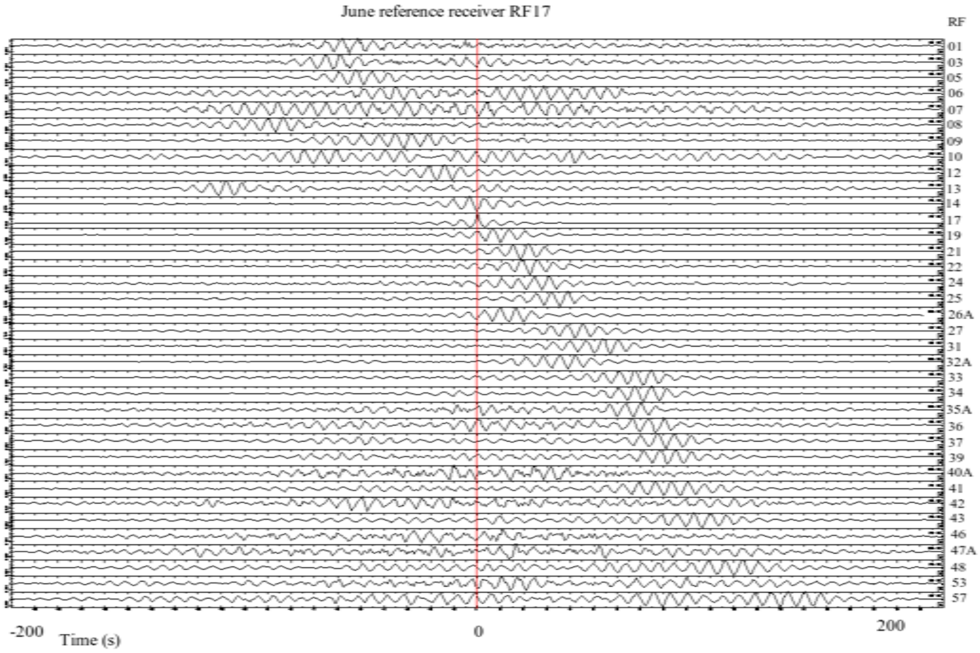

Figure B.14 Green's function for the month of June. Virtual source location at RF17.

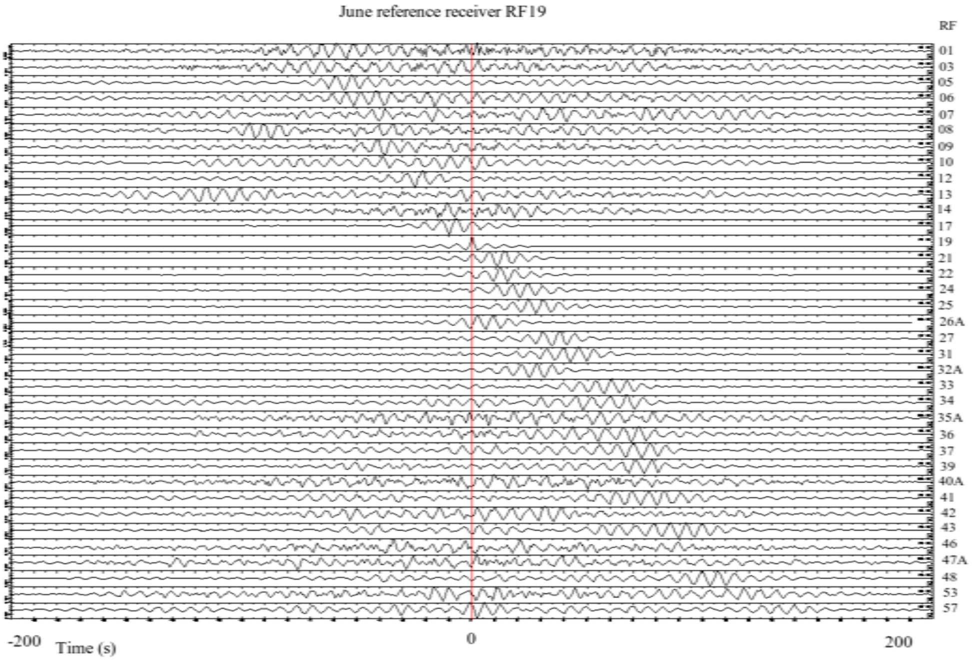

Figure B.15 Green's function for the month of June. Virtual source location at RF19.

Month of July 2003

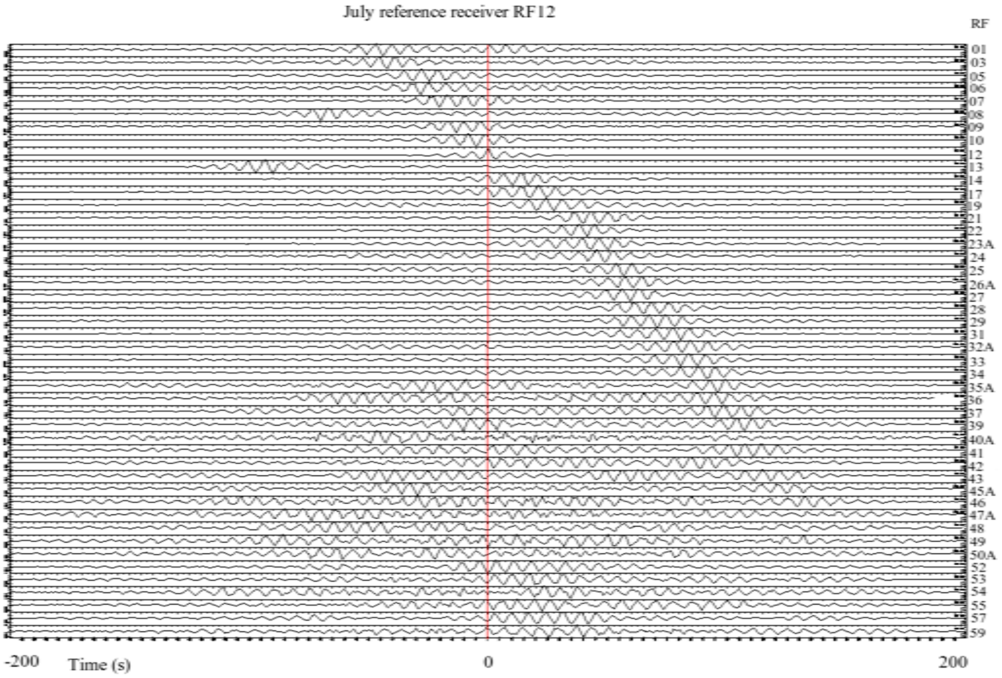

Figure B.16 Green’s function for the month of July. Virtual source location at RF12.

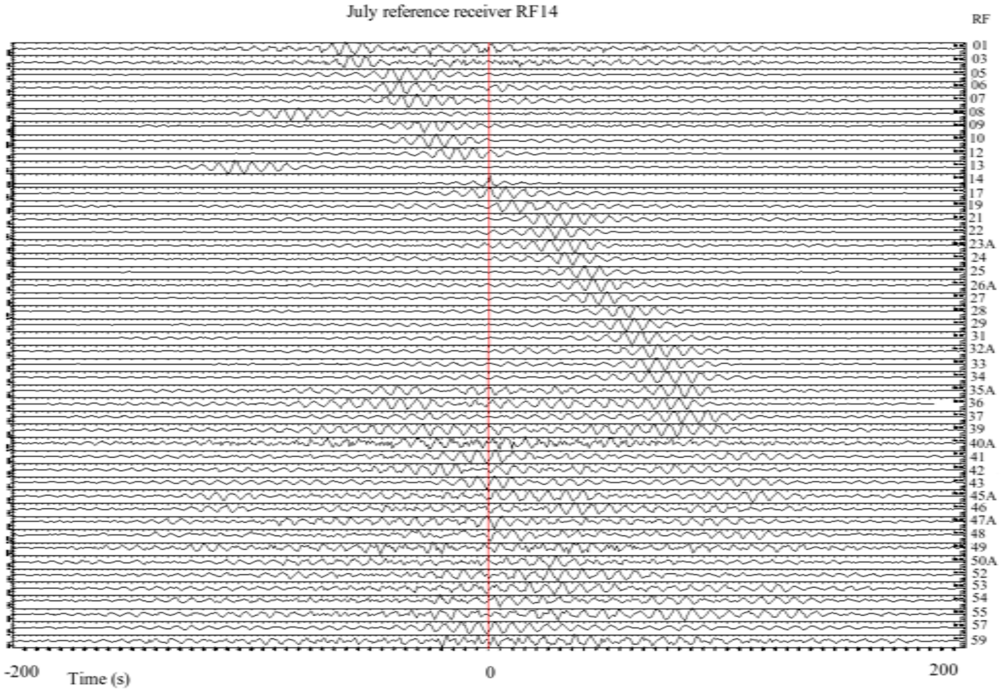

Figure B.17 Green’s function for the month of July. Virtual source location at RF14.

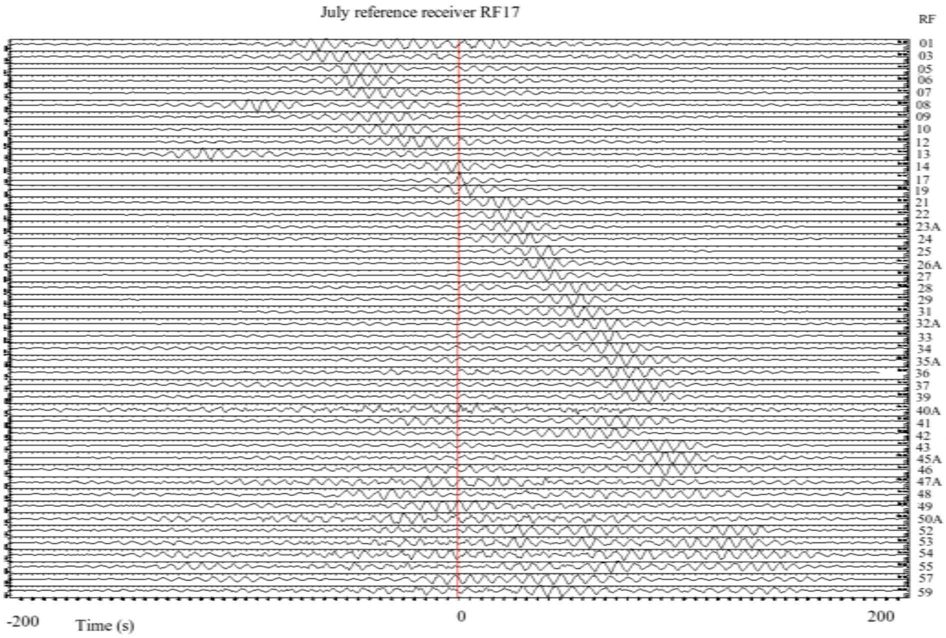

Figure B.18 Green’s function for the month of July. Virtual source location at RF17.

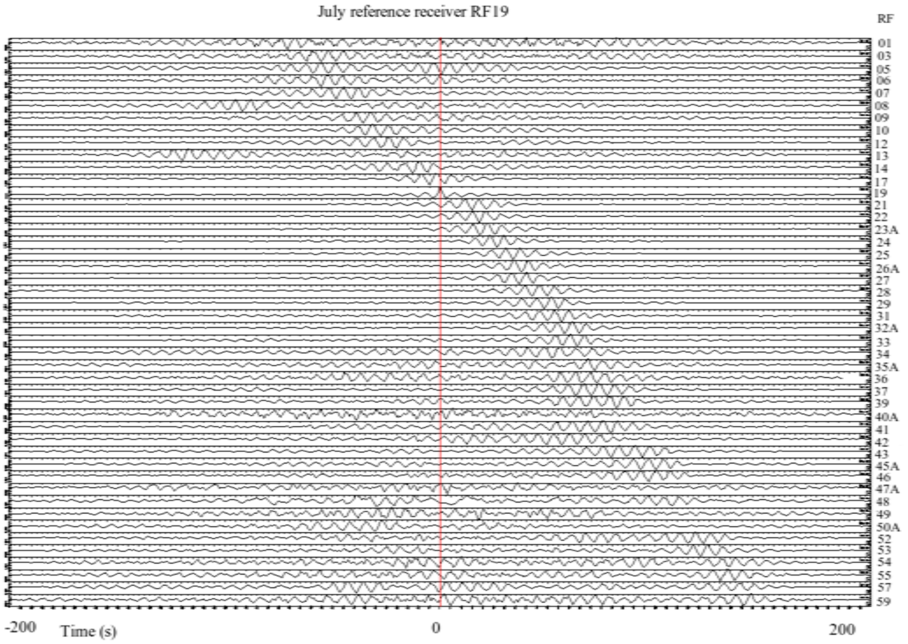

Figure B.19 Green’s function for the month of July. Virtual source location at RF19.

Month of August 2003

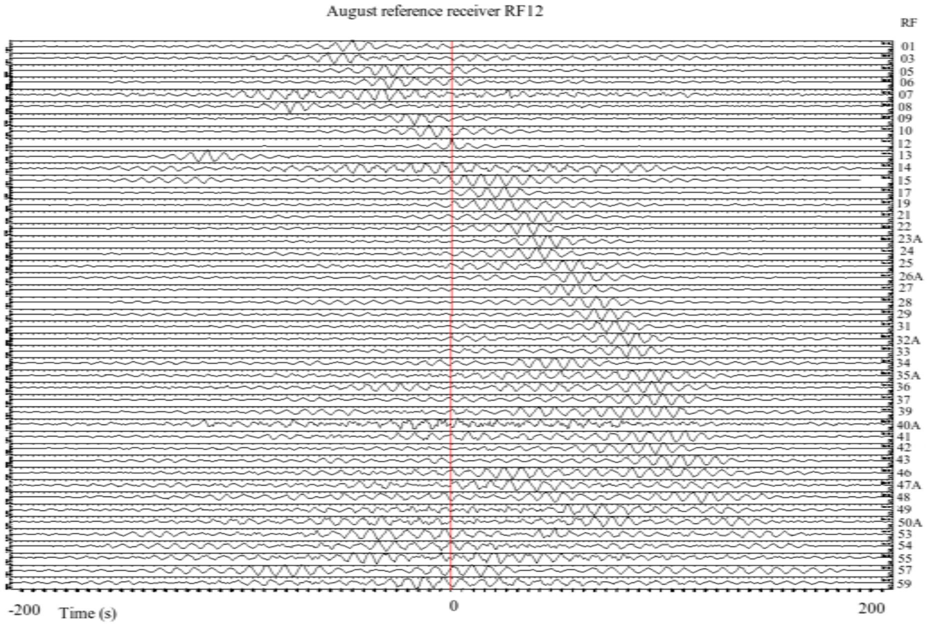

Figure B.20 Green’s function for the month of August. Virtual source location at RF12.

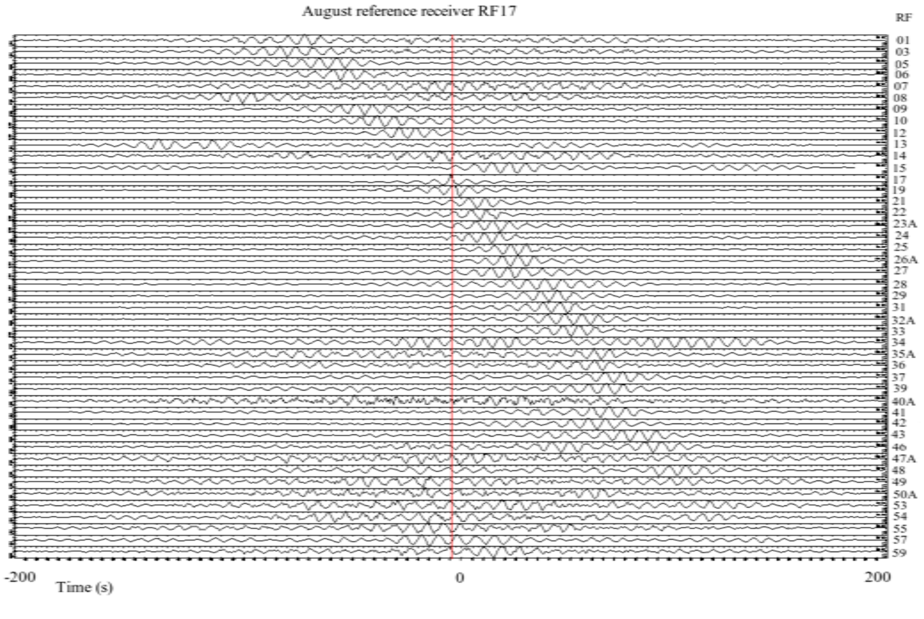

Figure B.21 Green’s function for the month of August. Virtual source location at RF17.

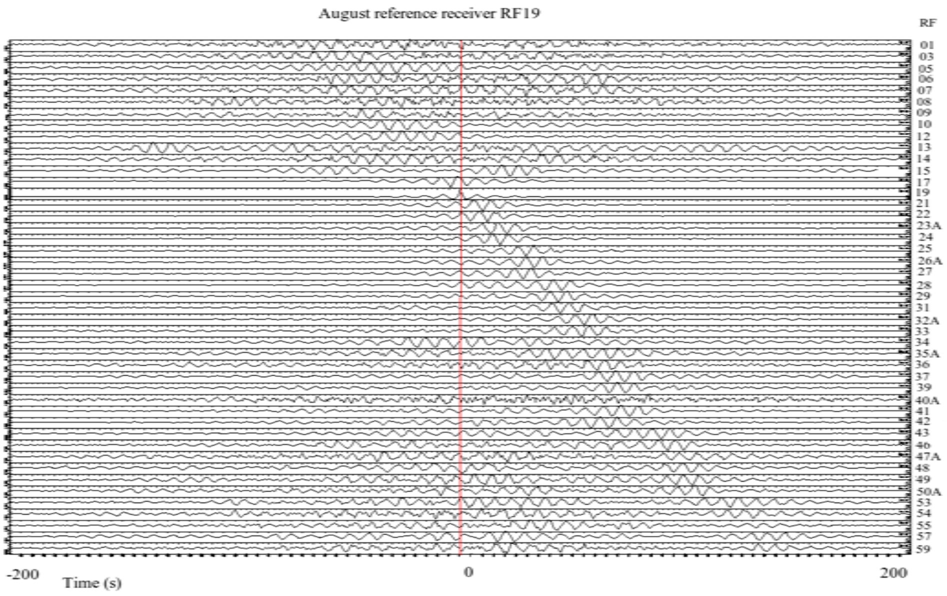

Figure B.22 Green’s function for the month of August. Virtual source location at RF19.

Puna Plateau

Month of April 2003

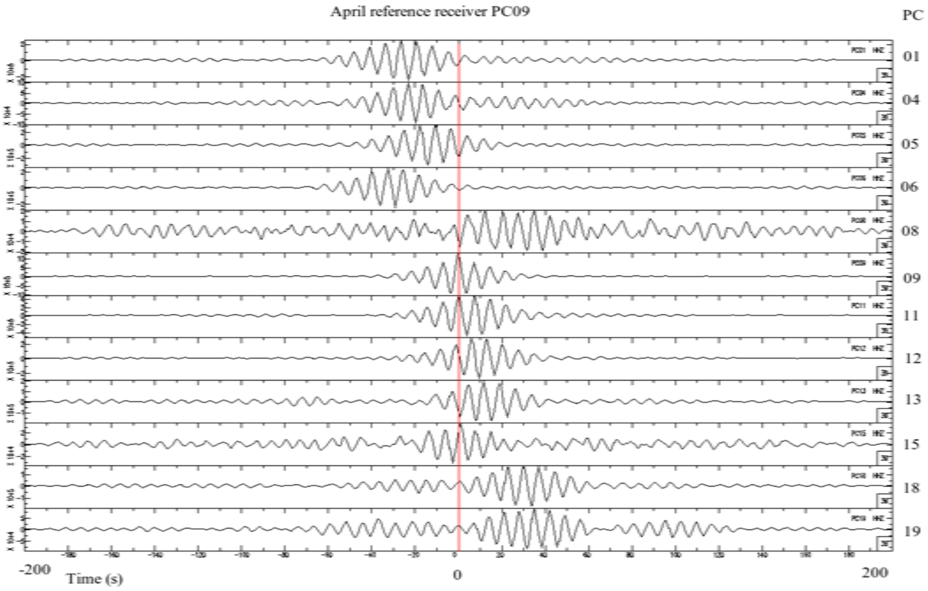

Figure B.23 Green’s Function for the month of April. Virtual source location at PC09.

Month of May 2003

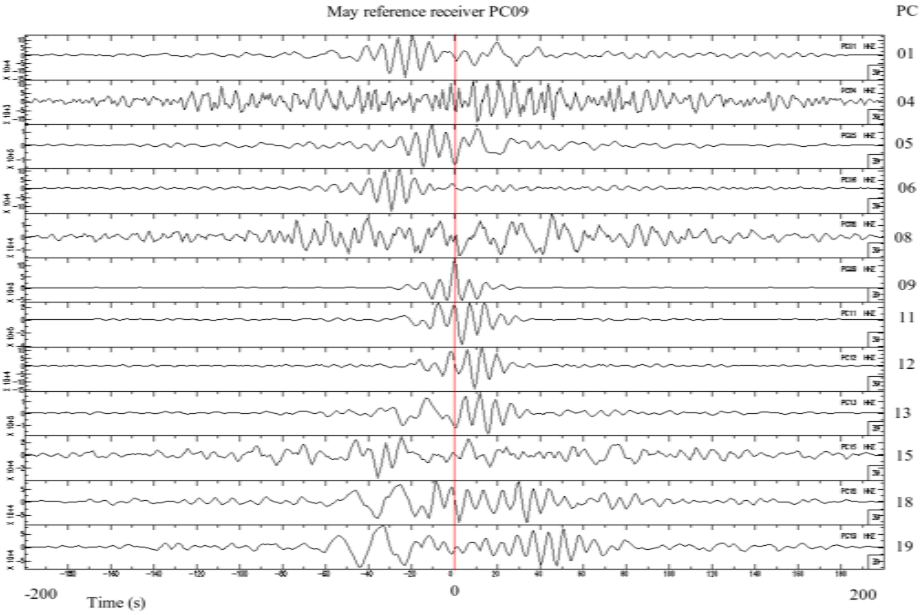

Figure B.24 Green’s function for the month of May. Virtual source location at PC09.

Month of June 2003

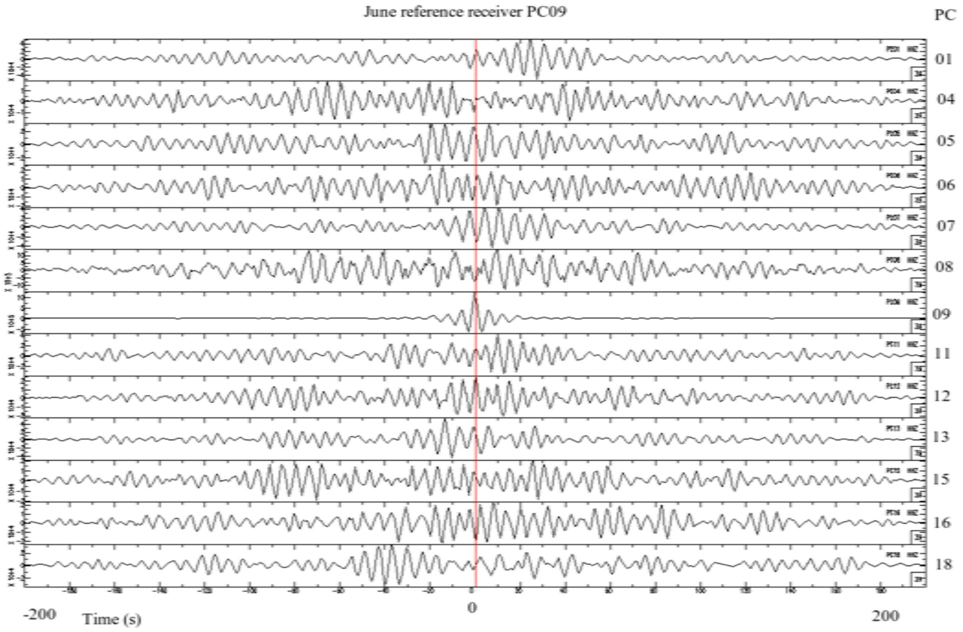

Figure B.25 Green's function for the month of June. Virtual source location at PC09.

Month of July 2003

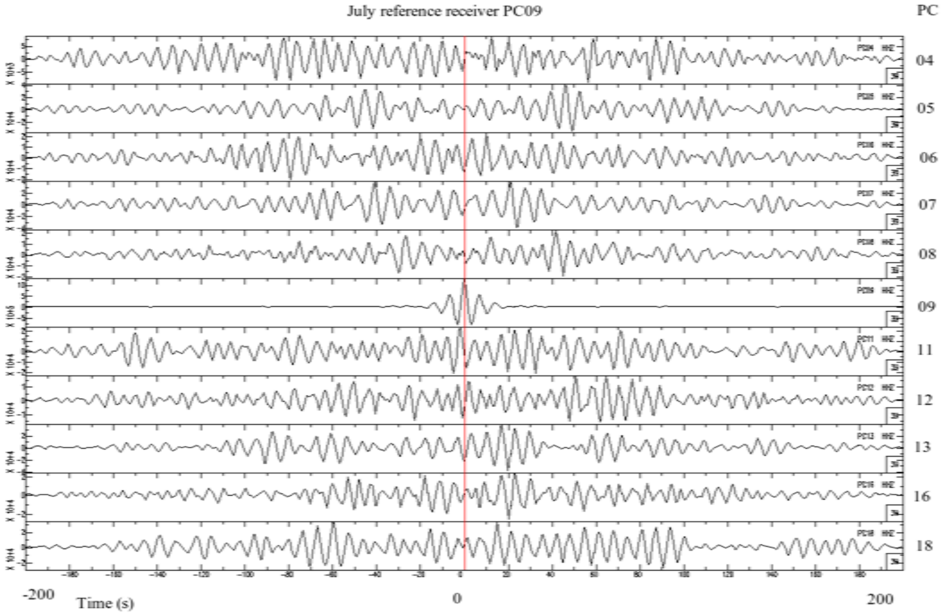

Figure B.26 Green's function for the month of July. Virtual source location at PC09.

Month of August 2003

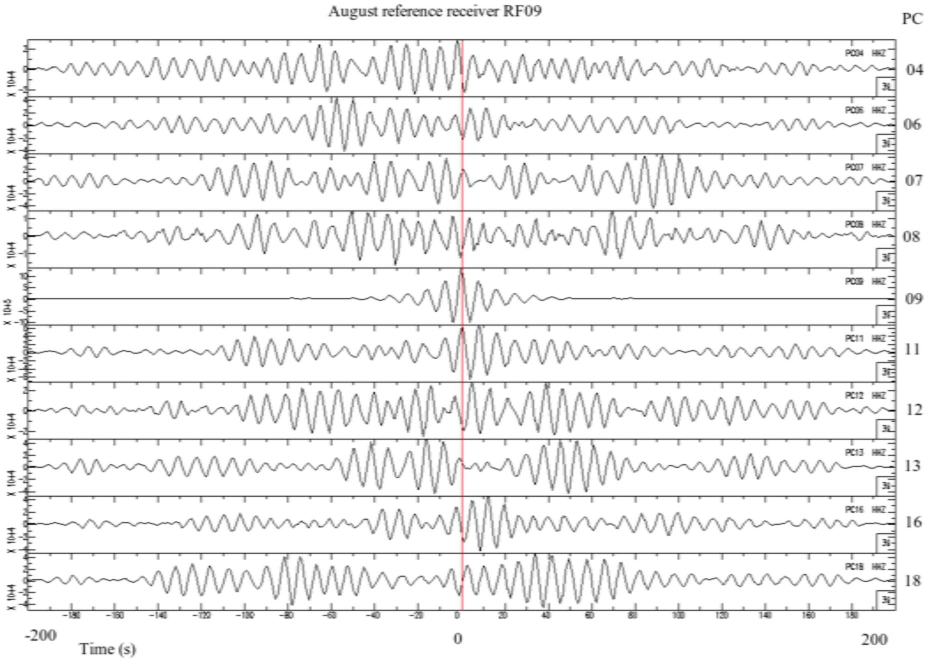

Figure B.27 Green’s function for the month of August. Virtual source location at PC09.

Results for six months of data

The following showed plots that correspond to the test results obtained from the six months of data, given that they include a summation over the whole six-month time period.

Altiplano plateau (21°S)

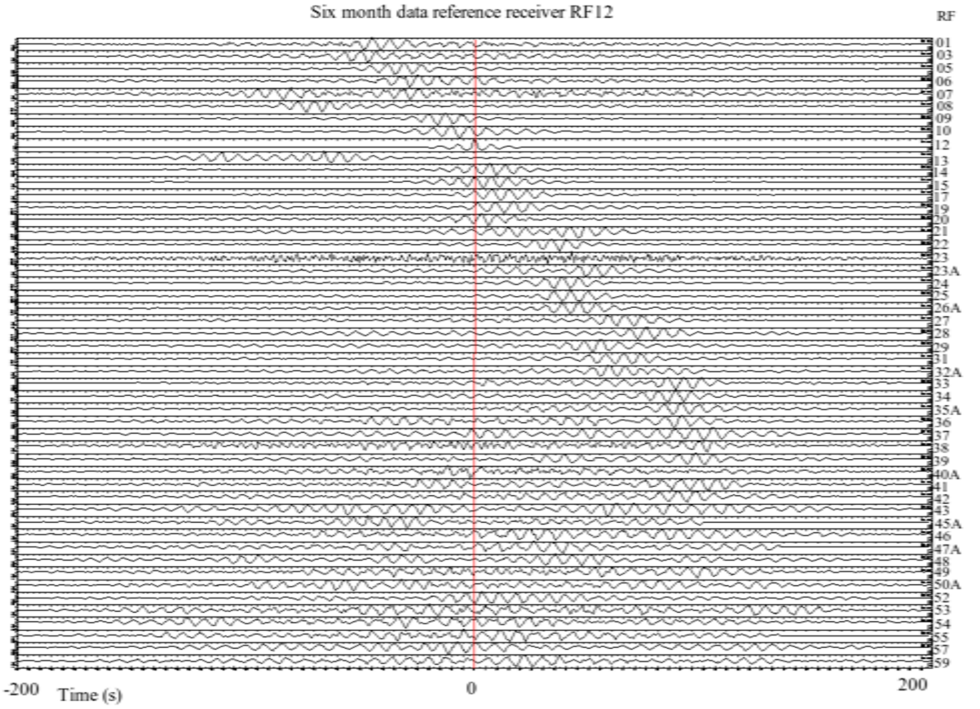

Figure B.28 Green's functions. Virtual source location at RF12.

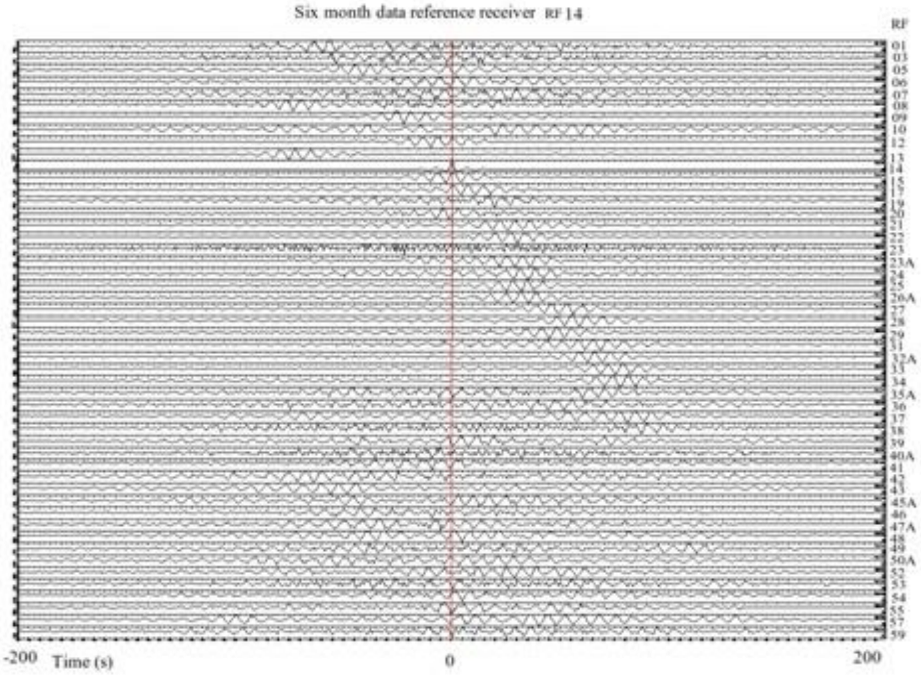

Figure B.29 Green’s functions. Virtual source location at RF14.

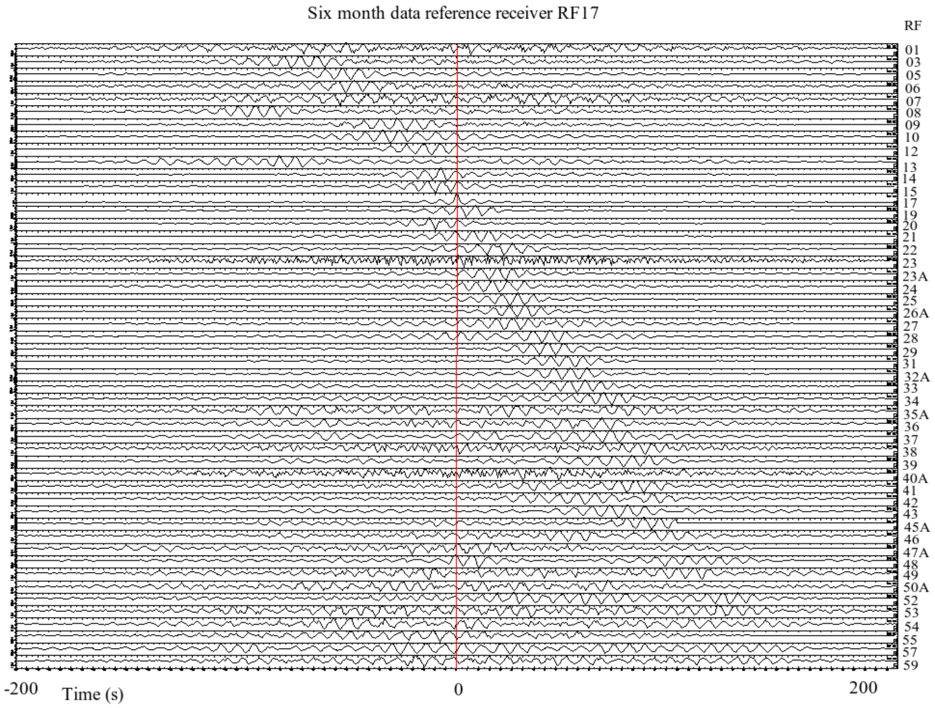

Figure B.30 Green’s functions. Virtual source location at RF17.

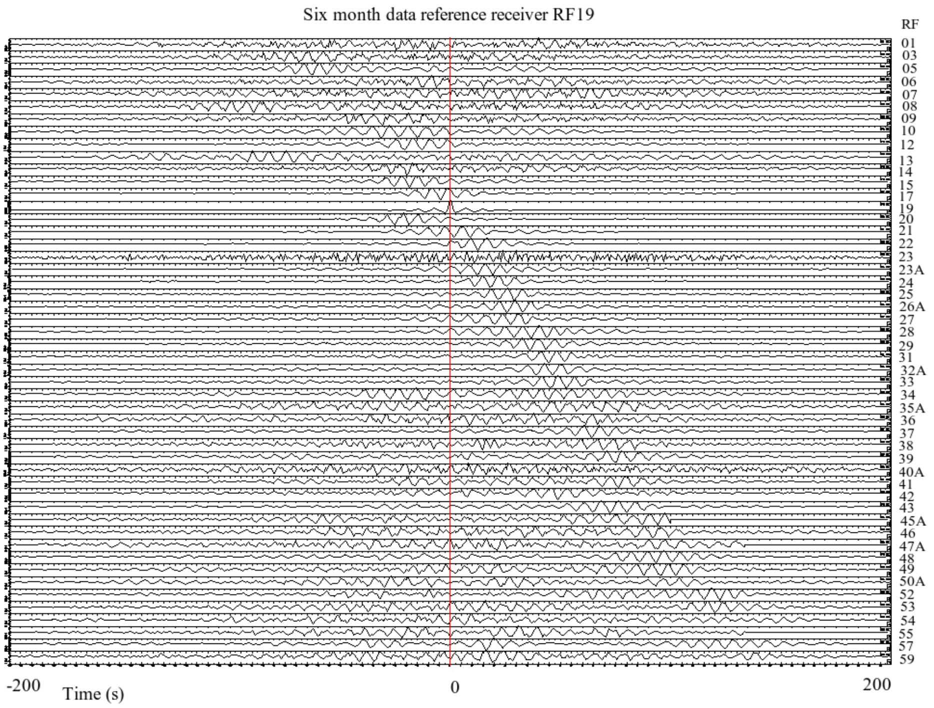

Figure B.31 Green's functions. Virtual source location at RF19.

Puna plateau (25.5°S)

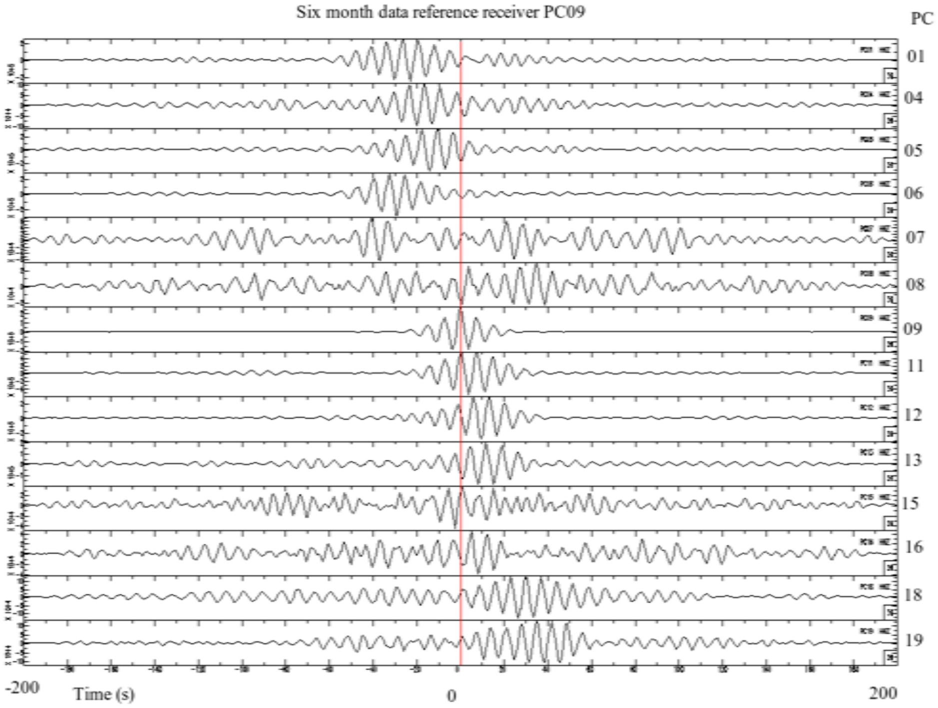

Figure B.32 Green's functions. Virtual source location at PC09.